



Université Claude Bernard



Lyon 1

N° d'ordre NNT : 2020LYSE1305

THÈSE DE DOCTORAT DE L'UNIVERSITÉ DE LYON

opérée au sein de
l'Université Claude Bernard Lyon 1

École Doctorale 52
(Physique et Astrophysique)

Spécialité de doctorat: Physique

Soutenue publiquement le 16/12/2020, par :
Alexis Forestier

Physical Response of Graphene Layers at Extreme Pressure

Devant le jury composé de :

Catherine Journet, Professeur, Université Lyon 1	Présidente
Laurent Alvarez, Maître de Conférences, Université de Montpellier	Rapporteur
Pascal Puech, Maître de Conférences, Université Toulouse III	Rapporteur
David Dunstan, Professeur, Queen Mary University of London	Examineur
Florence Garrelie, Professeur, Université Jean Monnet Saint-Étienne	Examinatrice
Laëtitia Marty, Chargée de Recherche au CNRS, Institut Néel Grenoble	Examinatrice
Antonio Gomes de Souza Filho, Professeur, Universidade Federal do Ceará	Examineur
Alfonso San Miguel, Professeur, Université Lyon 1	Directeur de thèse
Colin Bousige, Chargé de Recherche au CNRS, LMI Lyon	Co-directeur de thèse
Denis Machon, Maître de Conférences, Université Lyon 1	Co-directeur de thèse

Université Claude Bernard – LYON 1

Administrateur provisoire de l'Université	M. Frédéric FLEURY
Président du Conseil Académique	M. Hamda BEN HADID
Vice-Président du Conseil d'Administration	M. Didier REVEL
Vice-Président du Conseil des Etudes et de la Vie Universitaire	M. Philippe CHEVALLIER
Vice-Président de la Commission de Recherche	M. Jean-François MORNEX
Directeur Général des Services	M. Pierre ROLLAND

COMPOSANTES SANTE

Département de Formation et Centre de Recherche en Biologie Humaine	Directrice : Mme Anne-Marie SCHOTT
Faculté d'Odontologie	Doyenne : Mme Dominique SEUX
Faculté de Médecine et Maïeutique Lyon Sud - Charles Mérieux	Doyenne : Mme Carole BURILLON
Faculté de Médecine Lyon-Est	Doyen : M. Gilles RODE
Institut des Sciences et Techniques de la Réadaptation (ISTR)	Directeur : M. Xavier PERROT
Institut des Sciences Pharmaceutiques et Biologiques (ISBP)	Directrice : Mme Christine VINCIGUERRA

COMPOSANTES & DEPARTEMENTS DE SCIENCES & TECHNOLOGIE

Département Génie Electrique et des Procédés (GEP)	Directrice : Mme Rosaria FERRIGNO
Département Informatique	Directeur : M. Behzad SHARIAT
Département Mécanique	Directeur M. Marc BUFFAT
Ecole Supérieure de Chimie, Physique, Electronique (CPE Lyon)	Directeur : Gérard PIGNAULT
Institut de Science Financière et d'Assurances (ISFA)	Directeur : M. Nicolas LEBOISNE
Institut National du Professorat et de l'Education	Administrateur Provisoire : M. Pierre CHAREYRON
Institut Universitaire de Technologie de Lyon 1	Directeur : M. Christophe VITON
Observatoire de Lyon	Directrice : Mme Isabelle DANIEL
Polytechnique Lyon	Directeur : Emmanuel PERRIN
UFR Biosciences	Administratrice provisoire : Mme Kathrin GIESELER
UFR des Sciences et Techniques des Activités Physiques et Sportives (STAPS)	Directeur : M. Yannick VANPOULLE
UFR Faculté des Sciences	Directeur : M. Bruno ANDRIOLETTI

Remerciements

Ce travail n'aurait pu voir le jour sans le concours de nombreuses personnes à qui ces lignes sont dédiées. En premier lieu, ma profonde gratitude va à Alfonso San Miguel qui a dirigé mon travail de master puis cette thèse. C'est à travers son expérience, son optimisme à toute épreuve et sa grande humanité que j'ai tant appris. Je remercie ensuite Colin Bousige, grand manitou de R, maître de l'efficacité : il m'a d'abord formé avec patience puis accompagné, conseillé, aiguillé et encouragé tout au long de ces années. Denis Machon, complétant cette triade de direction, m'a beaucoup apporté par son regard critique aiguisé. Ses questionnements et remarques salutaires ne furent pas à dose homéopathique malgré la distance continentale qui nous séparait.

Je souhaite vivement remercier Laurent Alvarez et Pascal Puech qui ont accepté de rapporter mon travail ainsi que pour leurs critiques qui l'ont l'enrichi et consolidé. Merci à David Dunstan, avec qui ce fut un plaisir de collaborer sur le chargement portatif à hélium, mais aussi pour nos riches discussions scientifiques qui ont ponctuées ses visites au laboratoire. Ma reconnaissance va également à Florence Garrelie et à Catherine Journet pour leur participation à mon jury et pour leur intérêt pour ce travail. Un grand merci à Laëtitia Marty pour les nombreux échantillons qu'elle et son groupe de recherche nous ont fournis, ainsi que pour ses retours sur ce manuscrit. Antonio Gomes de Souza Filho, qui vient compléter ce large jury, nous a en outre réservé un formidable accueil à Fortaleza. Je l'en remercie chaleureusement.

Je suis très reconnaissant à Ian Rodrigues do Amaral qui a donné un nouveau souffle à nos activités lors de son année à Lyon. Il est un expérimentateur de grande qualité avec qui j'ai beaucoup apprécié de travailler. Je voudrais saluer également Rafael Silva Alencar pour nos discussions scientifiques, pour son hospitalité lors de la conférence EnBraER à Belém et pour nous avoir guider au travers de la magnifique région du Pará, aux portes de l'Amazonie.

Dans les péripéties d'un projet, il arrive qu'une personne joue un rôle clé. Ce fut le cas de Jérémie Margueritat, qui lors de mes déboires a su m'apporter les moyens matériels et intellectuels nécessaires. Il a non seulement toute ma gratitude mais aussi mon admiration. Je souhaite aussi ardemment remercier Rémy Fulcrand, Agnès Piednoir, Matthieu Mercury et Fabien Vialla qui chacun, par leurs savoirs et expertises, ont contribué aux travaux présentés dans ce document. D'autres membres de l'institut Lumière Matière ont d'une façon ou d'une autre apporté à mon travail : merci à Sylvie Le Floch, Hatem Diaf, Elodie Roméo, Nicholas Blanchard, Ciro Oliva, Ruben Mascart, Vittoria Pischedda, Olivier Pierre-Louis, Marie-Ange Lebeault, Tristan Albaret, Christelle Machebœuf, Delphine Kervella, ainsi qu'à l'ensemble des membres de l'équipe de recherche SOPRANO. Je remercie également Jérôme Degouttes de l'INL qui a réalisé les découpes de substrats en silicium oxydé.

Comment ne pas mentionner les membres du « Happy Bureau », Gianpetro Cagnoli et Valérie Martinez : peut-on seulement imaginer meilleure compagnie pour partager un bureau, un café et un panettone ? Merci à vous deux.

Une mention spéciale pour mes collègues doctorants de l'iLM, compagnons victimes d'abord des turpitudes du plan Campus, puis des difficultés liées à la pandémie de Covid-19. En particulier, je remercie les acteurs de l'association Team'Doc pour avoir organisé moult événements scientifiques et festifs. Merci aussi aux nombreux stagiaires qui ont pris part aux besognes.

Je réserve un merci affectueux à mes amis, pour leurs encouragements et pour leur compagnie : Mathilde et Kévin, compères co-fondateurs du renommé Clan des Vastes au marathon de Madrid, Antoine le voltigeur, Marion la courageuse, Marina et Pierre les stars de M'Roc, Thomas le "Maltèque" des cimes, Camille l'authentique parisienne et Paul l'artiste. Un hommage tout particulier à Romain, acolyte de déjeuners et de méta-discussions scientifiques ou non, mais toujours riches et endiablées et ce depuis plus de quatre années !

Je remercie mes parents pour leur indéfectible présence, qui fut précieuse tout au long de mes études.

Floriane, comment te remercier à hauteur de ton soutien et de ta patience démesurés. Pour tout, merci infiniment.

Puisque hélas je risque d'oublier quelqu'un : merci à tous !

Contents

General Introduction	13
1 Graphene and its Raman Scattering Response at High Pressure	19
1.1 Introduction	20
1.2 Basics	20
1.2.1 Graphene among Carbon Materials	20
1.2.2 Graphene Mechanics	22
1.2.3 Graphene Electronic Properties	23
1.2.4 Graphene Stackings	25
1.3 Raman Spectroscopy in Graphene	26
1.3.1 Basics of the Raman Effect	26
1.3.2 The Raman Spectrum of Graphene	29
1.3.3 Effect of External Perturbations on Graphene's Raman Response	34
1.3.3.1 Probing Graphene Strain through Raman Spectroscopy	34
1.3.3.2 Effect of Charge Doping on Graphene Raman Signatures	35
1.3.3.3 Deconvolution of Strain and Doping Effects	36
1.4 From Graphite to Graphene at High Pressure	37
1.4.1 Strain in Graphene Layers at High Pressure: State of the Art	37
1.4.2 Pressure-Induced sp^2 to sp^3 Phase Transition	40
1.5 Conclusion	41
1.6 Summary	42
2 Experimental Techniques	45
2.1 Introduction	46
2.2 Preparation of Graphene Samples	46
2.2.1 Graphene Production	46
2.2.1.1 Mechanical Exfoliation from Graphite	46
2.2.1.2 Chemical Vapour Deposition (CVD)	48
2.2.2 2D-Materials Transfer Techniques	49
2.2.2.1 PMMA Sacrificial Layer Technique	49
2.2.2.2 Deterministic Dry Transfer set-up by PDMS-stamping	49

2.3	High Pressure Techniques	52
2.3.1	Diamond Anvil Cell Apparatus	52
2.3.2	<i>In situ</i> Pressure Calibration	55
2.3.3	Pressure Transmitting Media	56
2.3.3.1	Comparison of Pressure Transmitting Media	56
2.3.3.2	Diamond Anvil Cell Loading Techniques	58
2.4	<i>In situ</i> Raman Spectroscopy	60
2.4.1	MicroRaman set-ups	60
2.4.2	Experimental Issues related to Raman Spectroscopy at High Pressure . .	63
2.5	Conclusion	65
2.6	Summary	66
3	Isotopically Labeled Bilayer Graphene at High Pressure	69
3.1	Introduction	70
3.2	Isotopically Labeled Bilayer Sample and its Loading Procedure	72
3.2.1	Description of the Isotopically Labeled Sample and its Raman Response .	72
3.2.2	Characterization and Loading of the Sample in the Pressure Cell	73
3.2.3	SiO ₂ /Si Substrates in High Pressure Experiments	75
3.3	Raman Signature Evolution at High Pressure in Various Media	75
3.4	Discussion of the Results	83
3.4.1	Solid Pressure Transmitting Medium Case: Strain Mismatch Effect	83
3.4.2	Liquid Alcohol Pressure Transmitting Medium Case: Piezo-doping Mis- match Effect	87
3.5	Conclusion	90
3.6	Summary	91
4	Experimental Developments for High Pressure Studies on Suspended Samples	93
4.1	Introduction	94
4.2	Suspended 2D-Material Diamond Anvil Cell Loading Strategies	96
4.2.1	Drilled Diamond Anvil	96
4.2.2	Lithographed Substrates with Trenches	99
4.2.2.1	Focused Ion Beam Cutting of Lithographed Substrates	99
4.2.2.2	Mechanical Cleaving of Substrates	103
4.2.3	Holed SiO ₂ /Si Substrates Prepared by Focused Ion Beam	106
4.3	Preliminary Results on Suspended Nanographite at High Pressure	110
4.4	New Portative Helium DAC Loading Development	117
4.4.1	Existing Helium DAC Loading	117
4.4.2	The New Portative Design	118

4.5	Conclusion	123
4.6	Summary	124
5	Pressure-Induced Microscale Buckling in Thin Graphite Flakes	127
5.1	Introduction	128
5.2	Preparation and Loading of the Samples	129
5.3	The Mechanical Behaviour of Supported Nanographites at High Pressure	129
5.3.1	Sample Detachment from the Substrate at High Pressure	129
5.3.2	Effect of the Nature of the Pressure Transmitting Medium	130
5.3.3	Effect of the Sample Thickness	130
5.3.4	Raman G-band Evolution of the Nanographite Flakes at High Pressure .	134
5.4	Discussion	134
5.4.1	Formation of Wrinkles at High Pressure	136
5.4.2	Role of the Pressure Transmitting Medium	136
5.5	Conclusion and Perspectives	139
5.6	Summary	141
	General Conclusion	143
	Appendix	147
A	Raman Spectra Fitting Procedure	148
B	Isotopically Labeled Bilayer Graphene: Raman Spectra before and after the Pressure Cycle	150
	Résumé Substantiel en Langue Française	151
	Bibliography	169

General Introduction

In the laboratory, extreme values of pressure can be achieved using the diamond anvil cell apparatus [1]. Its use contributes to reveal the richness of the changes in matter with this thermodynamic parameter. In a compressed system, bringing atoms closer and closer leads to a considerable modulation of the physico-chemical properties, to structural transformations and to the emergence of new, sometimes exotic effects.

Scientific Context: High Pressures and Low Dimensional Materials

Pressure is by definition a three-dimensional concept. Low-dimensional materials appear then as very interesting systems to investigate in extreme pressure conditions, firstly because of their geometry [2]. Low dimensional systems are of nanometric size – ultimately of atomic scale – in at least one of the spatial dimensions, and thus are designated according to their geometry as being N -dimensional. They can take the form of nanoparticles or cages molecules with spherical topology (0D), of linear atomic chains or tubular structures (1D) as well as planar, atomically thin crystals (2D). Carbonaceous nanomaterials are central among them, due to the astonishing flexibility of the carbon-carbon bond leading to fullerenes (0D), carbon nanotubes (1D) or graphene (2D) allotropes, between many other structures.

Pressure application is able to change the geometrical shape of low dimensional materials. The radial collapse of carbon nanotubes into a two-lobe – peanut shape – cross-section is a pictural example of such pressure-induced geometrical transformation [3, 4].

An important aspect of low-dimensional materials lies in their strong interactions with their environment, since they are mostly (if not completely) composed of surface atoms. Extreme pressures are able to magnify these interactions. This is illustrated by the pressure-induced chemical bonding between host carbon nanotubes and their intercalants, or variations in charge transfer between them [5, 6]. These interactions can also manifest through mechanical effects, such as the reinforcement of carbon nanotubes when they are filled with water or fullerenes [4, 7]. When multiple low dimensional systems are assembled by weak van der Waals interaction, pressure may be able to induce covalent bonds between them. Typical examples are the polymerization of fullerenes at high pressure *via* cycloaddition mechanisms [8], or the transformation of graphite into diamond at high pressure and temperature through a reconstructive transformation [9]. Recently, the formation of "diamondene", a two dimensional analog of diamond obtained by high pressure application on bilayer graphene has been proposed [10–12].

Finally, their low dimensionality confers them very singular electronic, optical, mechanical, ther-

mal, surface, and chemical properties. Pressure application allows tuning these properties. The case of 2D-materials is interesting in that sense, because they can withstand very high levels of strain compared to bulk systems [13, 14], allowing to modulate their properties over wide ranges of values.

Through the above mentioned pressure effects, we see that the study of low dimensional systems at high pressure is an interesting subject from the fundamental point of view. In addition, there are tremendous perspectives for technological applications, for example in material mechanics (towards new composite, lightweight materials [15, 16]), tribology [17] or for the development of new devices for nano-electronics and nano-optics [18–20].

The reduction of dimensionality and size, coupled with extreme pressures, leads to a vast and rich domain of research encompassing mechanics, optics, surface physics, thermodynamics, electronics and chemistry – a domain that has been explored in our host research group at institut Lumière Matière (iLM) for the past 15 years.

This Work: Graphene Layers at Extreme Pressures

In this experimental work, we focus on the study of graphene and graphene stackings at extreme pressures using diamond anvil cells as pressure device. Raman spectroscopy will be our main technique to probe the system in *in-situ* conditions.

From the fundamental point of view, graphene at high pressure constitutes a paradox. Since it is of atomic thickness, how can a force be applied on its lateral surface? In most experimental works, the paradox is lifted thanks to the presence of a substrate on which graphene lays. In addition, the studied system is always immersed in a pressure transmitting medium. Graphene is thus embedded in a complex environment, sandwiched between a substrate and a pressure transmitting medium which can be of different nature, in fluid or solid state. In previous works, it has been shown that graphene undergoes a biaxial compression at high pressure, transferred by the substrate compression through interfacial adhesion [2, 21–24]. The interplay of the pressure-transmitting medium is not well understood. In previous works, bilayer graphene is reported to be more sensitive to a solidified pressure transmitting medium than monolayer graphene from the mechanical point of view [25]. Furthermore, contradictory information has been reported on a possible pressure-induced charge transfer with graphene when alcohol is used as pressure transmitting medium [22, 23]. Thus, in a first axis of this work, we focus on the impact of this complex environment (substrate, environing fluid or solid) on the physical response of graphene at extreme pressure. With that goal, we have studied an isotopically $^{12}\text{C}/^{13}\text{C}$ labeled bilayer graphene sample using different pressure transmitting media, allowing to deeply address the graphene interactions with this environment at high pressure using *in-situ* Raman spectroscopy.

A second, important component of this work focuses on new experimental developments for the study of *suspended* graphene at high pressure. Overcoming this technological lock is highly desirable in the field of 2D-materials at extreme pressure. Despite the clear interest of the community for this question [26], at the beginning of this thesis no clear study was published on this

subject – which highlights the technical difficulties inherent to the study of singled suspended graphene under high pressure. Some studies have reported measurements on graphene layers in suspension in the pressure transmitting medium, but flakes are likely to re-aggregate in such conditions [21, 27]. In 2020, a study reported *in-situ* measurements using Raman spectroscopy to probe a *single* and *suspended* graphene sample over cut gold grids in a diamond anvil cell [12]. Unfortunately, the authors have not detailed the sample loading technique, which is a very challenging part. Experiments in such conditions would help to overcome the difficulties of interpretation arising from the complex environment mentioned above. The suspended 2D crystal, only interacting with the pressure transmitting medium, constitutes the simplest possible experimental environment for hydrostatic compression. In that aspect, graphene even constitutes a model system for future studies on various other 2D-materials. In absence of substrate, the intrinsic strain response of an atomically thin crystal to hydrostatic compression becomes accessible. Finally, it should simplify the comparison of experiments with *ab-initio* modeling. For these reasons, we have developped various techniques with this challenging goal, which led to proof-of-concept experiments on suspended thin graphite samples of nanometric thickness (that we call "nanographites").

We have mentioned that supported graphene undergoes a biaxial compressive strain at high pressure, which is transferred by the compressed substrate [2, 22–24]. A third aspect explored in this work lies in the strain relaxation mechanisms in play when the sample is mechanically driven by the substrate at high pressure. In previous works, it was observed experimentally that the substate's strain is not *entirely* transferred to graphene through adhesion, thus the strain transfer is only *partial* [2, 22–24]. The physics leading to this partial strain transfer remains unclear, and is very difficult to address experimentally in *in-situ* conditions. Therefore, by the use of contrast-enhancing substrates and nanographite samples that are stiffer than single layer graphene, it was possible to vizualise and investigate the out-of-plane displacements and curvature effects that are induced in the thin graphite membranes by extreme pressure, while such effect has never been observed in thinner, single layer samples.

Organization of this Manuscript

In the **first chapter**, we present graphene, its physical properties and graphene stackings. The Raman scattering effect is described, as well as how it can be used to probe strain and doping perturbations in our samples compressed at extreme pressure. Finally, the state of the art of high pressure studies on samples ranging from graphite to graphene is introduced.

The **second chapter** is dedicated to the experimental techniques. Graphene production and transfer methods are described. The high pressure techniques are presented, centered on the diamond anvil cell apparatus. The Raman experimental set-up is presented in detail as well as the practical implications of *in-situ* Raman spectroscopy at high pressures.

In a **third chapter**, we present experimental results obtained on the $^{12}\text{C}/^{13}\text{C}$ isotopically labeled bilayer graphene at high pressure. The use of this particular sample allowed probing deeply the

role of the pressure transmitting medium on the graphene physico-chemical response at high pressure.

Our experimental developments for the study of *suspended* graphene systems at high pressure are presented in the **fourth chapter**, with emphasis on the specific challenges that such experiments represent. Preliminary results obtained on suspended nanographites at extreme pressures are presented.

The last, **fifth chapter** presents our experimental campaign performed on supported nanographite flakes at high pressure, exploring buckling, wrinkling and detachment effects observed in these systems.

The main results of this thesis work are then briefly summarized in the **conclusion** part.

1

Graphene and its Raman Scattering Response at High Pressure

Contents:

1.1	Introduction	20
1.2	Basics	20
1.2.1	Graphene among Carbon Materials	20
1.2.2	Graphene Mechanics	22
1.2.3	Graphene Electronic Properties	23
1.2.4	Graphene Stackings	25
1.3	Raman Spectroscopy in Graphene	26
1.3.1	Basics of the Raman Effect	26
1.3.2	The Raman Spectrum of Graphene	29
1.3.3	Effect of External Perturbations on Graphene's Raman Response	34
1.3.3.1	Probing Graphene Strain through Raman Spectroscopy	34
1.3.3.2	Effect of Charge Doping on Graphene Raman Signatures	35
1.3.3.3	Deconvolution of Strain and Doping Effects	36
1.4	From Graphite to Graphene at High Pressure	37
1.4.1	Strain in Graphene Layers at High Pressure: State of the Art	37
1.4.2	Pressure-Induced sp^2 to sp^3 Phase Transition	40
1.5	Conclusion	41
1.6	Summary	42

1.1 Introduction

In this first chapter, we introduce the main objects and concepts used throughout this work. Graphene, its mechanical and electronic properties are described, as well as how graphene layers can be stacked. Raman scattering, the effect allowing us to probe the response of graphene to high pressure, is introduced theoretically. We discuss in details the physical origin of the Raman signatures of graphene, since it will be very important for the interpretation of changes in these signatures during *in-situ* experiments. We emphasize how Raman spectroscopy is used for graphene characterization. Importantly, we describe the Raman sensitivity to graphene's external perturbations such as strain and charge transfers, allowing to probe these effects. In the aim to show how our work fits into the discipline, we present the pre-existing work on graphene at high pressure, with emphasis on dimensionality effects.

1.2 Basics

1.2.1 Graphene among Carbon Materials

The carbon-carbon bond is extremely versatile, and can form both macroscopic and nanometric systems. Its multiplicity leads to a wide variety of materials that can be dense or porous, ordered or disordered, electrical conductors or insulators, transparent to light or highly absorbant. This richness arises from the different types of hybridizations that carbon forms in its covalent bonds. Carbon electronic structure writes $1s^2 2s^2 2p^2$. Due to the small energy difference between the valence $2s$ and $2p$ states, the $2s$ and n $2p$ orbitals can mix to form hybrid sp^n orbitals [28]. The sp , sp^2 and sp^3 hybridizations leads to structures that are locally linear, planar, and tetragonal, respectively. Pure sp^3 structuration forms a diamond crystal, while pure sp^2 hybridization forms graphite, the stable carbon allotrope at ambient conditions. Graphene, at the heart of this work, is the building block of sp^2 -hybridized systems: it consists in a 2-dimensional crystal formed by a honeycomb network of carbon atoms, as pictured in figure 1.1(a).

The stacking of graphene layers (interacting by van der Waals forces) leads to the graphite 3-dimensional structure (figure 1.1(b) shows a three layers graphite system), while its wrapping around an axis leads to a carbon nanotube, a quasi-1-dimensional nanosystem (see figure 1.1(c)). Fullerenes, commonly designed as 0-dimensional systems, are cage molecules that can be seen as closed graphene sheets where pentagonal defects allows for the spherical topology (see figure 1.1(d)). Interestingly, these carbon nanostructures were discovered in a different order, first with C_{60} fullerenes in 1985 [29], single-wall carbon nanotubes in 1993 [30, 31], and graphene in 2004 [32]. The low dimensionality of these systems gives them astonishing mechanical, electronic, optical and chemical properties that are at the center of a very important research effort, both from the fundamental point of view and for technological applications. Indeed, the concept of dimensionality does not limit to the designation of systems shape: it is at the origin of their atypical physico-chemical properties and responses to external perturbations.

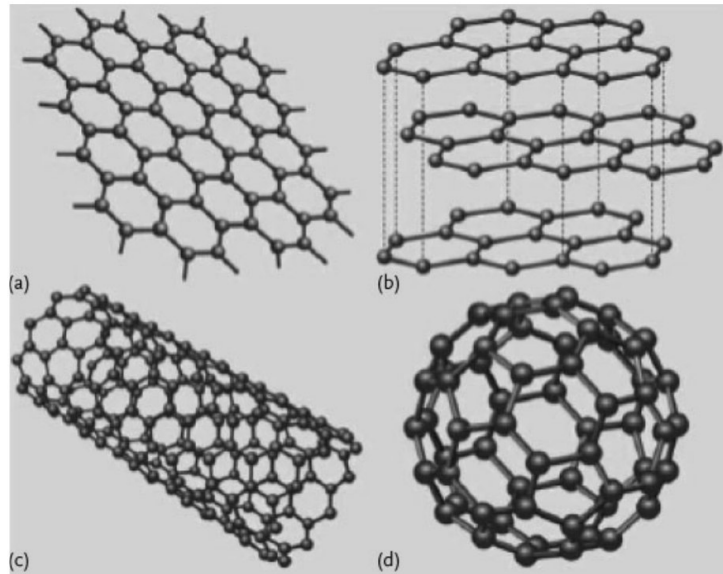


Figure 1.1 – Various examples of sp^2 -hybridized carbon materials. (a) A graphene layer, (b) three-layer graphite, (c) a carbon nanotube, (d) a C_{60} molecule, commonly called fullerene, including 12 pentagons and 20 hexagons in its structure. Figure taken from [28].

Graphene crystal structure can be described as shown in figure 1.2(a), where \mathbf{a}_1 and \mathbf{a}_2 are the unit vectors of the triangular lattice. Combined with a basis containing two carbon atoms per unit cell (the two non-equivalent carbon atoms are indicated as A, and B in figure 1.2(a)), it leads to the graphene hexagonal structure, where the equilibrium distance between atomic neighbors is $a_{CC} = 1.42 \text{ \AA}$.

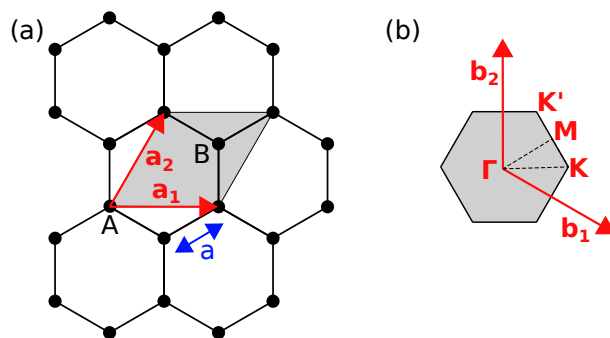


Figure 1.2 – (a) Honeycomb structure of graphene. The black circles represent carbon atoms. The unit cell is highlighted in grey. (b) First Brillouin zone (in grey) plotted in graphene reciprocal lattice. High symmetry points are indicated. Dotted lines correspond to the directions commonly used to plot dispersion diagrams, including in this work.

In order to later describe the electronic and vibrational properties of graphene, we define the first Brillouin zone (BZ) of the graphene lattice, shown in grey in figure 1.2(b). The reciprocal lattice vectors, \mathbf{b}_1 and \mathbf{b}_2 are represented in red and verifies $\mathbf{a}_i \cdot \mathbf{b}_j = 2\pi\delta_{ij}$. High symmetry points Γ , at the zone center, M , on the middle of the BZ edges, and the two inequivalent K and K' at BZ corners are indicated.

1.2.2 Graphene Mechanics

Despite the simplicity of graphene, its mechanical description through continuum mechanics laws remains challenging due to its atomic thickness. In order to handle quantities expressed in force per unit surface (GPa) comparable with values for bulk materials, it is common to introduce a graphene thickness equals to the interlayer spacing of graphite, $h = 3.35 \text{ \AA}$. It is also considered to describe graphene using "macroscopic" models [33]. However, graphene's thickness is in fact ill-defined [34]. In a two-dimensional universe, graphene elasticity would be described only with two elastic constants: its extensional in-plane stiffness (in N/m) and its in-plane Poisson ratio, since the elasticity of the 2D hexagonal lattice is isotropic [35]. The in-plane covalent bonds in graphene are very short and strong, thus, graphene in-plane stiffness $E^{2D} \simeq 340 \text{ N.m}^{-1}$ is very high. This value has been determined through experiments where graphene is strained in the perpendicular direction with an atomic force microscope (AFM) tip [13] (as pictured in 1.3(c)) consistently with other experiments (*e.g.* tensile strain experiments in ref. [36]). Using $E^{2D} \simeq 340 \text{ N.m}^{-1}$, we obtain a "three-dimensional" Young modulus of $E^{3D} \simeq 1 \text{ TPa}$ using $h = 3.35 \text{ \AA}$. Such value is consistent with the in-plane linear compressibility observed in high pressure experiments on bulk graphite [37]. Graphene's in-plane Poisson ratio is often considered similar as in graphite, $\nu \simeq 0.13$ [38]. However, a wide spread of values was found using various methods, ranging from $\nu \simeq 0.1$ to 0.4 (see ref. [33]). Interestingly, the reduced dimensionality of graphene allows to experimentally reach very high strain rates (up to $\sim 25\%$) before fragile fracture [13]. Indeed, its intrinsic strength is limited by atomic bonds strength rather than defects as it is the case for bulk materials [13].

As a matter of fact, graphene stays in a three-dimensional space where it can bend or undulate in the perpendicular direction. Thus, two supplementary elastic quantities are needed: the bending stiffness of graphene D , and a second Poisson ratio specific to bending [33]. Graphene is an highly flexible system with $D \sim 1.7 \text{ eV}$, value obtained from experiments on the pressure induced collapse of carbon nanotubes, in good agreement with first-principles calculations [3]. Similar values (in the $0.8 - 2 \text{ eV}$ range) were found using various other methods [33]. Therefore, we emphasize the fact that thanks to this high flexibility, in-plane compressive strain in graphene can easily be relaxed by rippling and wrinkling of the membrane, as observed in numerous experimental works on graphene as well as other 2D-materials when compressed through a flexible substrate [39–44]. Such out-of-plane effects are explored in this work, as they play an important role on the graphene mechanical response at high pressure.

High Pressure among Graphene Mechanical Studies

Various techniques exist for graphene mechanical straining. Some are illustrated in figure 1.3. Out-of-plane (OP) techniques are based on the deformation of a suspended graphene layer in the OP direction through various means (see (a,b,c) in figure 1.3). In the case of in-plane (IP) techniques, graphene's deformation is in general transferred through adhesion on its substrate. The transferred strain can be uniaxial, for example by mechanical flexion of the substrate ((d) in figure 1.3), or biaxial through substrate flexion as well [45], but also through substrate thermal

expansion [41, 42], or by using a piezo-electric substrate [46], ((e) in figure 1.3). It has been shown that strain can have a significant effect on the electronic properties of graphene, opening the path for "straintronics", *i.e.* the modulation of electronic properties of 2D-materials through mechanical strain [18].

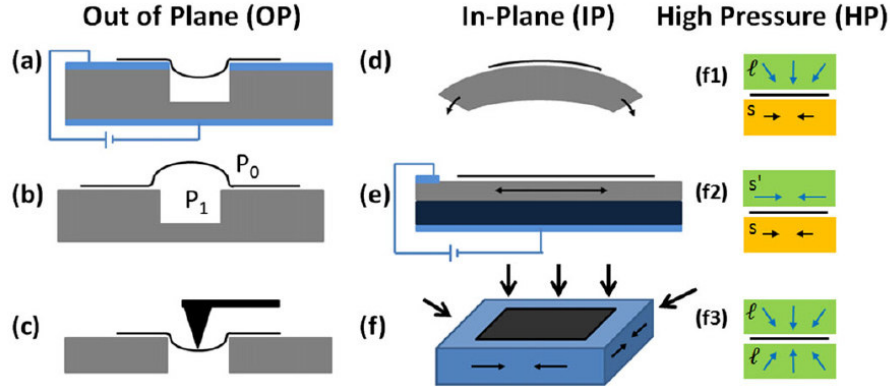


Figure 1.3 – Various experimental techniques used in the literature for graphene deformation. In (a), (b) and (c), graphene is strained in the out-of-plane (OP) direction by (a) electrostatic deflection [47], (b) pressure difference [48–50], (c) an atomic force microscopy tip [13]. (d), (e) and (f) shows configurations where in-plane (IP) strain is applied through (d) a flexible substrate [18, 39, 45, 51] or (e) a piezo-electric material substrate [46]. In (f), a biaxial strain is applied to supported graphene by high pressure compression. Three high pressure experimental configurations are depicted: (f1) supported graphene in a liquid environment, (f2) supported graphene in a solid medium, and (f3) suspended graphene in a liquid environment. Figure taken from ref. [25].

Supported graphene at high pressures in the GPa-range ((f) in figure 1.3) can be included in biaxial IP techniques, since the compressed substrate transfers strain – at least partially – to the graphene system by surface adhesion [21, 22, 24]. However, high pressure is pretty singular among these techniques, since a strong perpendicular stress component arises from the pressure transmitting medium (PTM). Intuitively, such perpendicular stress may increase the strain transfer from the substrate, allowing to reach high strain values. Additionally, the system is in close interaction with the PTM, which can be liquid and hydrostatic ((f1) in 1.3) or solid ((f2) in 1.3). We will see that this non-trivial environment plays an important role on the graphene physical response to high pressure. Finally, high pressure compression in suspended configuration is depicted in (f3) in figure 1.3.

Raman spectroscopy plays a central role in all these studies since it is a very sensitive strain probe, and a powerful non-destructive characterization technique. In the context of high pressure experiments, it is the technique by excellence since only optical *in situ* probes are possible.

1.2.3 Graphene Electronic Properties

Graphene electronic structure can be described approximately through the tight binding method, which is in general efficient to describe covalent systems. The electronic wavefunctions are expressed on a basis of Bloch states based on isolated carbon atomic orbitals. The relevant

atomic orbitals determining graphene electronic and optical properties are the remaining $2p_z$ orbital beside the sp^2 hybridized states, that produce the π bonds in graphene. Considering the interaction between first neighbors atoms only, the energy $E_{\pm}(\mathbf{k})$ of the π bonding and π^* anti-bonding electronic states (corresponding to + and - signs, respectively) can be calculated, leading to the band structure plotted in figure 1.4(a). Figure 1.4(b) shows a plot of the same function, $E_{\pm}(\mathbf{k})$, along the high symmetry directions indicated by dotted lines in figure 1.2(b). A detailed calculation of $E_{\pm}(\mathbf{k})$ is given in ref. [52].

In first approximation¹, close to the \mathbf{K} and \mathbf{K}' points of the BZ, the dispersion relation is linear with \mathbf{k} such as

$$E_{\pm}(\mathbf{k}) = \hbar v_f ||\mathbf{k}|| \quad (1.1)$$

where $\hbar = h/2\pi = 1.0545718 \times 10^{-34} \text{ m}^2.\text{kg.s}^{-1}$ and $v_f \sim 10^6 \text{ m.s}^{-1}$ is the graphene Fermi velocity [28, 55]. This relation leads to a conic band structure near the \mathbf{K} and \mathbf{K}' points, known as Dirac cone (see figure 1.4(c)). The valence band (π) and the conduction band (π^*) are symmetric and meet at \mathbf{K} and \mathbf{K}' points, at the Fermi level of intrinsic graphene (set as the energy origin). Intrinsic graphene is thus a zero-gap semi-conductor, in other words a semi-metal.

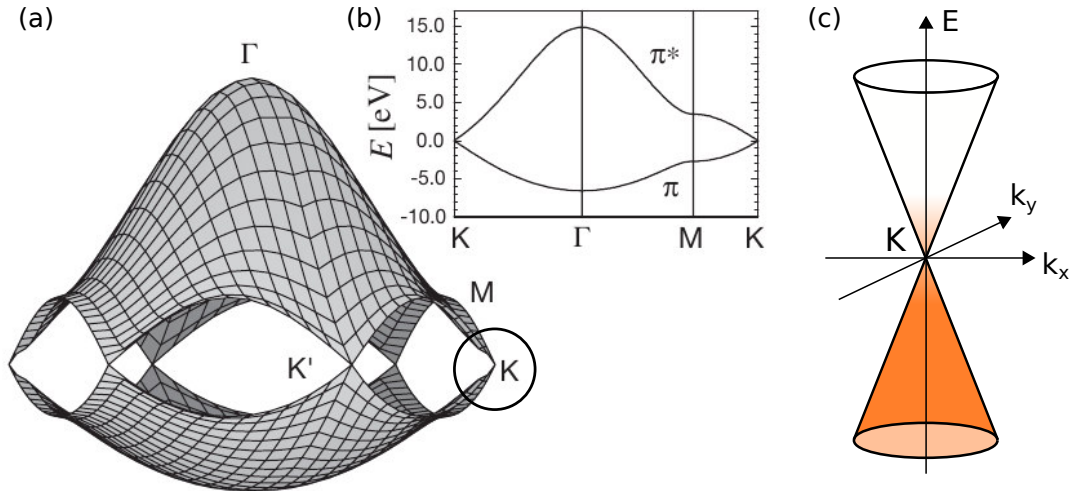


Figure 1.4 – (a) Electronic dispersion relation obtained through the tight binding approach plotted in the two-dimensional BZ of graphene [28]. High symmetry points are indicated. (b) The same electronic dispersion relation plotted along high symmetry directions in the graphene BZ. (c) Plot of a Dirac cone, corresponding to the linear dispersion relation near the \mathbf{K} and \mathbf{K}' points of graphene BZ (see circled region in (a)). Occupied states at finite temperature are schematically represented in orange for intrinsic graphene. Figure adapted from [28].

This unusual linear dispersion relation, first identified by P. R. Wallace in 1947 in his graphite band structure description [56], has a similar form to the photons dispersion relation in vacuum. Therefore, π electrons in graphene can be seen as a 2D massless Dirac fermions gas [57]. We

¹Note that beyond this first order approximation of the graphene band structure, the trigonal wrapping effect can be taken into account, especially for the proper description of interaction of graphene with photons in the visible spectrum [53, 54].

will see that this electronic band structure plays an important role in the optical properties of graphene, in particular in its Raman scattering response.

From equation (1.1) can be deduced the density of electronic states in the conduction band, $\rho(E)$, accounting for the spin and valley (\mathbf{K} and \mathbf{K}' Dirac cones) degeneracies:

$$\rho(E) = \frac{2\Sigma}{\pi} \frac{|E|}{(\hbar v_f)^2} \quad (1.2)$$

We can see that $\rho(E)$ is linear with E , instead of being constant for the usual parabolic dispersion electron gas in two dimensions. $\Sigma = 3\sqrt{3}a^2/2$ is the area of graphene's unit cell. In neutral graphene, the Fermi energy E_F is zero, while in case of n or p doped graphene, E_F is related to the surface electron concentration n through

$$E_F = \text{sgn}(n)\hbar v_f \sqrt{\pi|n|} \quad (1.3)$$

where $\text{sgn}(n)$ is the sign of n (negative in the case of p doping). Graphene charge concentration values of the order of $n \sim 5 \times 10^{12} \text{ cm}^{-2}$ can be induced experimentally by the electric field effect, such as in the pioneer works from K. Novoselov *et al.* [32, 57]. Higher doping values (up to 10^{14} cm^{-2} – corresponding to $E_F \sim 1 \text{ eV}$) can be reached by electro-chemical gating [58], and through atoms and molecules adsorption on graphene surface [59, 60]. We will see that due to electron-phonon coupling, doping has a significant effect on the Raman response of graphene. This allowed us to probe doping effects in our graphene samples at high pressure.

Note on Graphene Optical Properties

Graphene light absorption from the mid-infrared to the ultraviolet spectral range is dominated by interband transitions [61], that is, transitions of electrons from the valence to the conduction band in the Dirac cones by photons absorption. The probability of such event can be calculated, in first approximation for the linear electronic dispersion, zero temperature and zero doping, leading to the "universal" optical absorbance of graphene $\pi\alpha = 2.3\%$ (where α is the fine structure constant) [61, 62]. We note that in that first approximation, light absorption in graphene is independant on the wavelength. Experimentally, it increases beyond $\pi\alpha$ in the near-ultraviolet due to the saddle point at the \mathbf{M} point in the band structure, and excitonic effects [38, 61]. This large absorption value for an atomically thin layer allows to distinguish graphene samples by optical microscopy. The real part of the refractive index of graphene can be deduced from experimental data and its value was found to be $n \simeq 3$ [63]. We note that graphene light emission is weak, since it has no electronic gap [61].

1.2.4 Graphene Stackings

Various graphene stacking orders are possible, in which graphene sheets interact through weak van der Waals forces. In graphite, the layers are most of the time arranged following the Bernal (ABABA...) structure, but rhombohedral (ABCABCA...) stackings can also be found [64]. These two stacking orders are represented in figure 1.5(a) and (b), respectively, for two and

three adjacent layers. In graphite, as well as in artificial multilayer graphene systems, twisted stackings (also called turbostratic configurations) can be present with any angle between the adjacent lattices (an example is shown in figure 1.5(c)). In graphite, such configurations may be considered as stacking faults/disorder.

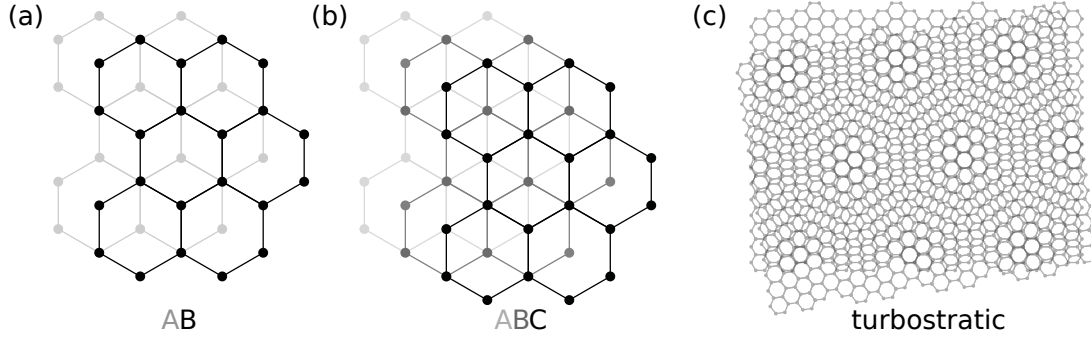


Figure 1.5 – Representations of various stacking orders in multilayer graphene systems, where the lowest layers are shown with the lowest opacity. (a) Bernal stacking (AB) bilayer system, (b) rhombohedral stacked (ABC) trilayer system, (c) turbostratic stacking of two graphene layers, showing a moiré effect.

The interlayer distance in graphite is $h = 3.35 \text{ \AA}$, much larger than the in-plane interatomic distance $a_{CC} = 1.42 \text{ \AA}$. This illustrates the strong anisotropy of graphite physical properties in directions colinear to graphene planes (in which cohesion arises from the strong in-plane σ bonds of graphene) and perpendicular to the planes. Graphite’s electrical conductivity, as well as its elastic stiffness, are much larger in the graphene planes than perpendicular to it. By stacking graphene layers, new electronic bands appear and depend strongly on the stacking order [55]. We will see that this reflects in the Raman response of the system. In twisted systems, interesting effects can appear such as Van Hove singularities, as well as flat bands leading to unconventional superconductivity at low temperature (in the “magic angle” configuration) [65, 66]. Such effects are examples belonging to the emergent field of “twistronics”, *i.e.* the study of the relation between electronic properties and the twist angle in 2D-materials stackings.

1.3 Raman Spectroscopy in Graphene

1.3.1 Basics of the Raman Effect

The Raman effect is the inelastic scattering of light by vibration modes in a crystalline or molecular systems. Some of its characteristics can be captured in a classical picture [67]. Let’s consider an incident electric field $\mathbf{E} = \mathbf{E}_0 \cos(\mathbf{k}_i \cdot \mathbf{r} - \omega_i t)$ illuminating our sample (in our case this monochromatic light is produced by a laser source). An oscillating polarization \mathbf{P} is induced such as $\mathbf{P} = \chi \mathbf{E}$, where χ is the electrical polarizability of our sample (in general, χ is a second-rank tensor, but we will consider an isotropic medium in which χ is scalar for convenience). The electrical polarizability χ fluctuates due to thermally populated phonons in the system. Thus,

χ can be developed around its equilibrium value χ_0 such as $\chi = \chi_0 + \chi' \mathbf{Q}$ where

$$\chi' = \left(\frac{\partial \chi}{\partial \mathbf{Q}} \right)_0 \quad (1.4)$$

and $\mathbf{Q} = \mathbf{Q}_0 \cos(\mathbf{q} \cdot \mathbf{r} - \omega t)$ are the atomic displacements of a normal mode of vibration of energy $\hbar\omega$ and wavevector \mathbf{q} . Thus, the resulting polarization in the material writes:

$$\begin{aligned} \mathbf{P} = (\chi_0 + \chi' \mathbf{Q}) \mathbf{E} = \chi_0 \mathbf{E}_0 \cos(\mathbf{k}_i \cdot \mathbf{r} - \omega_i t) &+ \frac{1}{2} \chi' \mathbf{Q}_0 \mathbf{E}_0 \cos[(\mathbf{k}_i - \mathbf{q}) \cdot \mathbf{r} - (\omega_i - \omega)t] \\ &+ \frac{1}{2} \chi' \mathbf{Q}_0 \mathbf{E}_0 \cos[(\mathbf{k}_i + \mathbf{q}) \cdot \mathbf{r} - (\omega_i + \omega)t] \end{aligned} \quad (1.5)$$

The scattered radiation originates from this induced polarization in the material, which is modulated in frequency by the atomic vibrations. The first term in eq. (1.5) corresponds to Rayleigh scattering, which is an elastic process. The two other terms are Raman scattering (inelastic) processes, corresponding to the creation (Stokes process) and annihilation (anti-Stokes process) of a phonon of energy $\hbar\omega$ in the medium. Thus, the energy of the scattered light is decreased (increased) by the energy of the excitation created (annihilated) such as energy and impulsion are conserved:

$$\hbar\omega_s = \hbar\omega_i \pm \hbar\omega(\mathbf{q}) \quad (1.6)$$

$$\hbar\mathbf{k}_s = \hbar\mathbf{k}_i \pm \hbar\mathbf{q} \quad (1.7)$$

where $\hbar\omega_s$ and \mathbf{k}_s are the energy and wavevector of the scattered light, respectively, and the \pm symbol holds for the Stokes ($-$) and anti-Stokes ($+$) processes. Raman spectroscopy consists in the energy-resolved measurement of the scattered light $\hbar\omega_s$, so that the sample excitations energies can be deduced through the plot of the scattered light intensity as a function of $\hbar\omega_i - \hbar\omega_s$ (usually called "Raman Shift" and expressed in cm^{-1}). Our Raman experimental set-up will be presented in chapter 2. We must precise the following points on the Raman effect:

- Looking at equation (1.5), it is clear that χ' must be non-zero in order to observe the Raman scattering effect. Thus, only phonon modes that induce changes in the electrical susceptibility tensor can produce Raman signal. Additionnal selection rules related to the polarization of the light and the symmetry of the vibration modes exist, the interested reader can refer to ref. [67].
- For visible light, the wavevector \mathbf{k}_i is of the order of $\sim 2\pi/\lambda$ where $\lambda \sim 500 \text{ nm}$, while phonons wavevectors in the BZ are of the order of $2\pi/a$ with $a \sim 1 \text{ \AA}$. Thus, photons wavevectors are very small with respect to phonons wavevectors, and only zone center phonons (*i.e.* $\mathbf{q} = \mathbf{\Gamma}$) can be probed *via* one-phonon Raman scattering (due to the conservation equation (1.7)).
- Multi-phonons Raman scattering is possible and very important to understand the Raman spectrum of graphene. It can be described by expanding the electrical susceptibility χ up to higher order terms as function of the atomic displacements (one speaks then of n -th order Raman scattering). In that case, the last term in equations (1.6) and (1.7) must be replaced by a sum over all phonons involved in the process. Therefore, zone center phonons are not the only ones that can contribute since the selection rule becomes $\sum_a \mathbf{q}_a \sim 0$, where

the summation runs over all phonons involved. It leads to the observation of combination (*e.g.* $\mathbf{q}_a + \mathbf{q}_b \sim 0$), difference ($\mathbf{q}_a - \mathbf{q}_b \sim 0$) modes as well as overtones ($\mathbf{q}_a - \mathbf{q}_a \sim 0$).

- Since the scattered signal arises from oscillating dipoles, its intensity varies like ω_s^4 . Furthermore, the Stokes and anti-Stokes signal intensities are not equivalent for a given phonon mode: the Stokes signal intensity I_S is proportional to $n + 1$ while the anti-Stokes signal $I_{aS} \propto n$, where $n = 1/[\exp(\hbar\omega/kT) - 1]$ is the average population of the phonon mode of energy $\hbar\omega$ given by the Bose-Einstein statistics at temperature T . Therefore, the Stokes signal is easier to measure since $I_S/I_{aS} = \exp(\hbar\omega/kT)$, and in this work, we will focus on Stokes signals. Interestingly, we may note that this last relation can be used to evaluate the local temperature in a sample [68] (this is correct only in the case of non-resonant Raman scattering, see later).
- A Raman peak does not take the form of a Dirac function, but shows a defined linewidth Γ_a containing informations on the lifetime of the phonon mode, as well as on the inhomogeneities existing in the sample at the laser spot scale (for example, strain inhomogeneities at the submicron scale in graphene). In general we represent the Raman signatures with Lorentzian lineshapes containing three fitting parameters, A_a , Γ_a and ω_a for the phonon mode a such as²

$$I(\omega) = \frac{A_a}{1 + \left(\frac{\omega - \omega_a}{\Gamma_a}\right)^2} \quad (1.8)$$

We should highlight that the incident energy of the laser, $\hbar\omega_i$, does not necessarily match any electronic transitions in the sample. In the particular cases where $\hbar\omega_i$, or $\hbar\omega_s$ matches an electronic transition in the system, the process is said *resonant*. We will see that resonant Raman scattering is central to describe the Raman response of graphene and of sp^2 -hybridized carbon nanosystems. In the quantum picture of Raman scattering using perturbation theory, one can express the Raman intensity $I(\hbar\omega, E_L)$ for a one-phonon Stokes process of energy $\hbar\omega$ and laser energy $\hbar\omega_i = E_L$ in the form³

$$I(\hbar\omega, E_L) \sim \left| \sum_{m, m'} \frac{\langle i | H^{e-l} | m' \rangle \langle m' | H^{e-ph} | m \rangle \langle m | H^{e-l} | i \rangle}{(E_L - \hbar\omega - E_{m'i} + i\gamma)(E_L - E_{mi} + i\gamma)} \right|^2 \quad (1.9)$$

The Raman mechanism described through this equation starts with the system in initial electronic state i and follows the sequence: (i) the incident photon of energy E_L excites the system in the intermediate state m through the electron-light interaction term $\langle m | H^{e-l} | i \rangle$, (ii) the electron is scattered by emitting a phonon of energy $\hbar\omega$ and the system is left in intermediate state m' (this step corresponds to the electron-phonon interaction term $\langle m' | H^{e-ph} | m \rangle$), and (iii) the system makes the transition from m' to the final state which is identical to the initial electronic i state, through the last term $\langle i | H^{e-l} | m' \rangle$, and emits a photon of energy $\hbar\omega_s$. The quantity γ is introduced to describe the broadening of the resonance window, related to the lifetime of the intermediate electronic states. The energies $E_{m(i)} = E_{m'} - E_i$ are the transitions energies

²An example of experimental spectrum fitting using Lorentzian spectral lineshapes is shown in appendix A.

³Rigorous treatments using this formalism can be found in refs. [28, 67]. Herein, we simply highlight the resonance mechanism through eq. (1.9).

from the i to the m' state: we see clearly in eq. (1.9) that the scattering cross-section increase drastically when $E_L \sim E_{mi}$ or $E_L - \hbar\omega \sim E_{mi}$. These two cases corresponds to incoming and outgoing resonance, respectively. The distinction between non-resonant and resonant processes is shown in the pictural energy diagram in figure 1.6. In the case of non-resonant scattering, the intermediate electronic states are said "virtual" states.

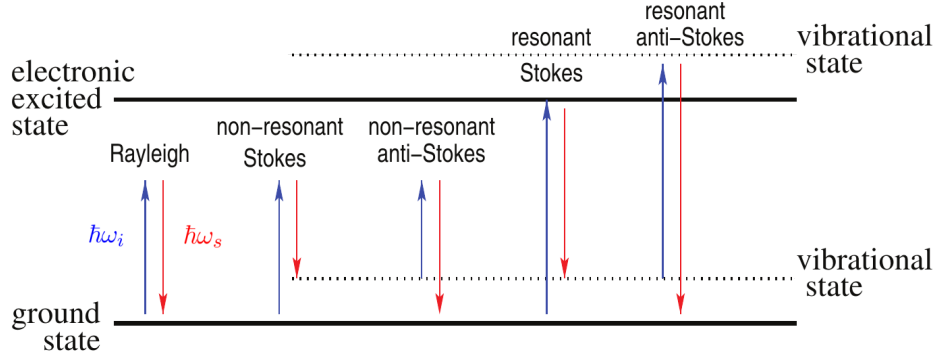


Figure 1.6 – Energy diagram of the system studied by spectroscopy Raman. The incident and scattered photons are represented in blue and red, respectively. Rayleigh scattering, non-resonant Raman and resonant Raman scattering are depicted. Figure from supplementary informations of ref. [69].

We have seen that in general, resonant Raman scattering leads to the exaltation of the Raman intensity. This is the reason why Raman scattering from individual carbon nanosystems such as an unique graphene monolayer or a carbon nanotube can be measured, despite the extremely low quantity of matter excited by the incoming light. In the case of graphene, its zero-gap electronic band structure as well as its linear electron dispersion near \mathbf{K} and \mathbf{K}' provide resonance conditions for any E_L in the visible. However, we may note the sum on every possible intermediate states in eq. (1.9). In some cases, the individual terms of the sum can add up with different phases leading to destructive (or constructive) quantum interferences [70, 71]. Finally, we mention that it is possible to adapt eq. (1.9) for multi-phonon scattering by adding supplemental matrix elements in the numerator (corresponding to the additional elementary scattering events), and the associated energy differences at the denominator. Thus, multiple-resonance effects can be observed.

1.3.2 The Raman Spectrum of Graphene

Figure 1.7 shows the Raman spectrum of monolayer graphene, along with spectra of other sp^2 -hybridized carbon systems for comparison. We will describe the origin and characteristics of the principal Raman bands of graphene. Throughout the description, we will emphasize how the Raman signatures of graphene can be used for its characterization. We may underline that Raman spectroscopy for the study of graphene and sp^2 carbon materials is a vast and rich subject, relatively well understood in comparison to its use on *e.g.* other 2D-materials discovered

recently. This is mainly because it benefits from more than 50 years of researches, first on graphite and later on carbon nanotubes. We may note that our description herein holds for ^{13}C graphene as well as for usual ^{12}C graphene, except for phonons energies which vary as $M^{-1/2}$ where M is the atomic mass. Therefore, the phonon energy spectrum of ^{13}C graphene undergoes a global decrease by a factor $\sqrt{12/13}$ due to heavier ^{13}C atoms.

G-band

The G-band, clearly visible in the graphene spectrum at $\sim 1582\text{ cm}^{-1}$ corresponds to the in-plane vibration of sp^2 hybridized C-C bonds. It is a Raman band observed in all sp^2 -hybridized carbon systems (see figure 1.7). The G-band arises from first-order Raman scattering by the degenerated, zone-center ($\mathbf{q} \sim 0$) longitudinal and transverse optical (LO and TO) phonon modes, visible in the graphene phonon dispersion plotted in figure 1.8. A representation of a Raman process responsible for the G-band is shown in the electronic energy diagram of graphene near \mathbf{K} in figure 1.9. We should insist on the fact that such diagram is pictural and a large number of pathways across the whole BZ of graphene contributes to the G-band intensity, although many of these pathways cancel by destructive interference in neutral graphene [70, 71]. The atomic displacements corresponding to the G-band mode are represented in figure 1.8 (see right spectrum). The energy of these in-plane vibrations is directly related to the strength of the sp^2 bonds, and is very sensitive to strain [72]. Thus, the spectral position of the G-band ω_G will be our main strain probe throughout our high pressure experiments on graphene (the effect of strain on the Raman bands will be detailed in subsection 1.3.3.1). The G-band position ω_G as well as its full width at half maximum $\text{FWHM}_G = 2\Gamma_G$ (through eq. (1.8)) depends also strongly on the carrier concentration n in doped graphene, see section 1.3.3.2 for details. The G-band linewidth Γ_G is inversely proportional to the G-band phonon lifetime in graphene, thus, it contains contributions from all possible interactions that may scatter the excited G-phonon. In general,

$$\Gamma_G = \Gamma_G^{ph-ph} + \Gamma_G^{e-ph} + \Gamma_G^h \quad (1.10)$$

where Γ_G^{ph-ph} is the phonon-phonon interaction term due to the interatomic potential anharmonicity (this term is small, $< 1.5\text{ cm}^{-1}$, but always present), Γ_G^{e-ph} is the electron-phonon interaction term contributing in zero-gap systems where the G-phonon can decay into an electron-hole pair [73]. Finally, Γ_G^h is a broadening that we introduce phenomenologically to account for heterogeneities at smaller scales than the excitation laser spot size (in terms of *e.g.* strain, doping...). For Bernal stacked multilayer graphene, the G-band intensity is increasing step-by-step consistently with the number of layers [74]. The G-band intensity can vary drastically in specific cases, such as highly doped graphene [70, 75] or in multilayer systems with specific twist angles [76].

2D-band

The 2D-band of graphene (previously called G'-band in literature) is the most intense Raman feature in the pristine graphene Raman spectrum (figure 1.7), observed near 2700 cm^{-1} (de-

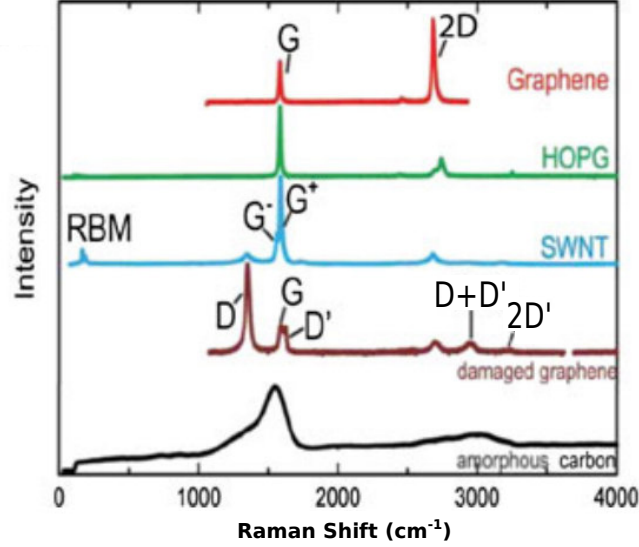


Figure 1.7 – Raman spectrum of graphene (red), of graphite (HOPG for highly oriented pyrolytic graphite, in green), of a single wall carbon nanotube (SWCNT, in blue). In brown is plotted the spectrum of damaged graphene (for details on combination band labels, see *e.g.* refs. [69, 77]), and in black a spectrum of amorphous carbon. Figure adapted from ref. [38].

pending on the excitation laser energy). The 2D-band originates from second-order Raman processes involving two TO phonons of opposite wavevectors ($\mathbf{q}_1 \sim \mathbf{K}$ and $\mathbf{q}_2 \sim -\mathbf{K}$) in order to conserve momentum. It is the overtone of the TO phonon at point \mathbf{K} of the BZ. The atomic motions of this mode corresponds to the breathing of hexagons. Two resonant (doubly, and triply-resonant) processes that contribute to the 2D-band signal are pictured in figure 1.9 [78, 79]. Through these mechanisms, one can see that the 2D-band is dispersive, *i.e.* its spectral position ω_{2D} varies with the incident laser energy E_L [69]. This is a direct consequence of both (i) the multiple-resonance effect in the electronic structure of graphene near \mathbf{K} , and (ii) the Kohn anomaly in the phonon dispersion near \mathbf{K} , which corresponds to a phonon softening due to electronic screening at BZ edges [80]. The 2D-band intensity, position, and shape are sensitive in a non-trivial way to external perturbations such as charge doping [38], as well as on the stacking order for multilayer systems. In the case of Bernal or rhombohedral multilayer stackings, the 2D-band lineshape can be used for number of graphene layer determination (monolayer is clearly identifiable with respect to two or more stacked layers) [81]. Indeed, the number of lorentzian components in the 2D-band in multilayer graphene reflects its electronic structure, *via* resonant Raman processes involving the supplemental electronic bands in multilayer systems as intermediate electronic states [54, 81]. Combined with the Kohn anomaly in the phonon spectrum at \mathbf{K} , it lead to slightly different phonon energies for each process, explaining the splitting into multiple components. For example, in Bernal stacked bilayer graphene, four components are observed contrarily to the single lorentzian lineshape for monolayer graphene [54]. Such layer-counting method does not hold for twisted stackings in which a single lorentzian 2D-band is observed [76]. The electronic structure of such turbostratic system is highly dependant on the twist angle between adjacent layers [65]. Considering any stacking order, the dermination of the number of layer by Raman spectroscopy solely is ambiguous [74, 82].

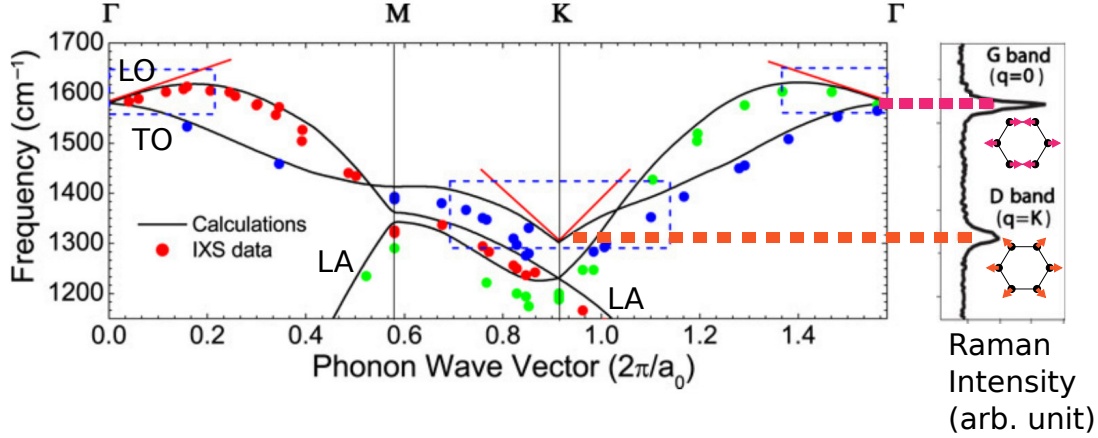


Figure 1.8 – In-plane optical phonons dispersion in graphene. Solid lines corresponds to *ab-initio* calculations from ref. [80], while coloured dots to experimental data obtained by inelastic X-rays scattering [83]. On the right part is projected the Raman spectrum of graphene in the corresponding energy range. Normal modes atomic displacements are shown for the G-band and the D-band. Red lines highlight the Kohn anomalies in the optical bands. Figure adapted from references [38, 73].

D-band

Graphene's D-band originates from the same TO phonon of wavevector $\mathbf{q} \sim \mathbf{K}$ as the 2D-band which is its overtone. The D-band is not observed in pristine graphene since \mathbf{q} is different from zero and momentum must be conserved in the process. The D-band is observed in damaged graphene (see figure 1.7) close to 1350 cm^{-1} , depending on E_L . Indeed, it is a second order process involving a structural defect, mathematically modeled by a "particle" of wavevector $-\mathbf{K}$ and of zero energy [69]. Doubly-resonant processes contributing to the D-band are shown in figure 1.9. For the same reasons as for the 2D-band, the D-band position depends on E_L . Since the D-band is observed only in damaged samples, it is very useful for crystallinity characterization: through the measurement of the intensity ratio I_D/I_G and Γ_G , the evaluation of the size and type of defects in the graphene crystalline structure is possible [84, 85]. We may note that the D-band can be observed at graphene edges. Furthermore, the D-band signal can also be observed in the case of non-chemical defects such as in graphene folds [86].

Other bands

On the spectrum corresponding to damaged graphene in figure 1.7, other Raman bands are visible. The D'-band, observed at 1626 cm^{-1} (depending on E_L), also needs the presence of crystalline defects to be active, and involves the LO phonon branch. Other combination and difference modes such as $D+D'$, may appear in defected graphene [69]. The $2D'$ -band, corresponds to two-LO-phonon processes and is observed in pristine graphene at $\sim 3240 \text{ cm}^{-1}$. Interestingly, the $2D'$ -band has been proposed for strain assessment in graphene since it is insensitive to doping, while the discrimination between strain and doping effects can be tedious using the G and $2D$ -bands [87]. However, its intensity is much lower than the principal bands described before.

In the case of multilayer stackings, we mention the existence of interlayer vibrations modes that

can be observed by low frequency Raman spectroscopy. The C-band corresponds to interlayer shear vibrations and may be used for number of layer determination [68]. However, the C-band is very difficult to measure, due to substrate effects and to the Raman modes of ambient air showing up in the same frequency range (the C-mode is observed at $\sim 31 \text{ cm}^{-1}$ for bilayer graphene [68]). Furthermore, layer breathing modes (LBMs) can be observed in turbostratic multilayer systems [88].

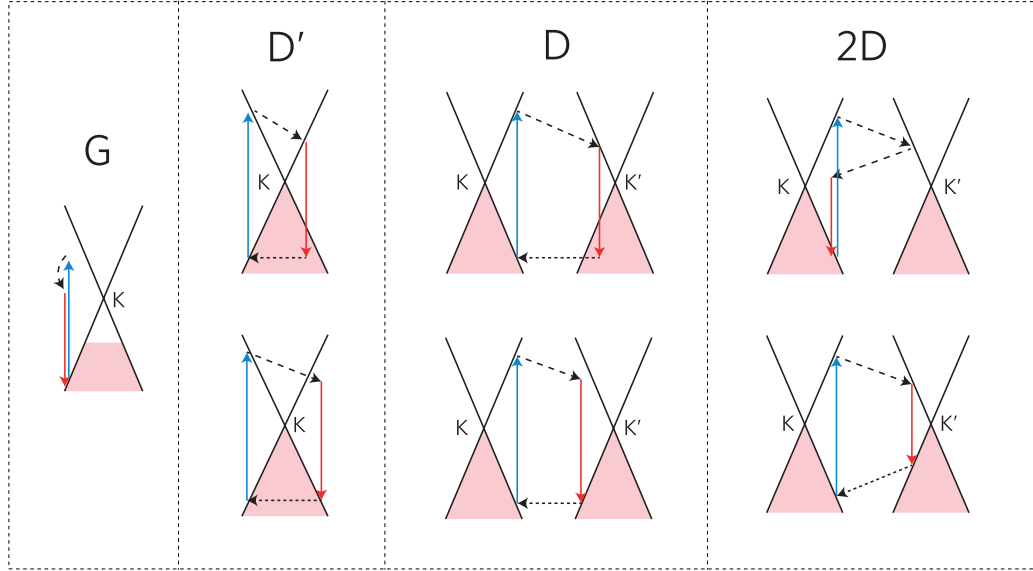


Figure 1.9 – Representations of Raman scattering processes contributing to the G, D, D' and 2D-bands plotted in the electronic band structure of graphene (shown as Dirac cones at points \mathbf{K} and \mathbf{K}' of the BZ). In the case of the 2D-band, double and triple-resonance processes are shown, the latter being the most probable. Filled areas corresponds to occupied electronic states. Photon absorption (the first elementary process of the inelastic scattering, leading to the creation of an electron-hole pair) as well as photon emission are represented as blue and red vertical arrows, respectively. Phonon emissions are shown as loosely dashed black arrows. Densely dashed horizontal black lines corresponds to electron scattering events on defects (with zero energy exchange). Figure adapted from ref. [69]. For more details on the Raman scattering processes, see reference [69].

Comparison with Raman Spectra of other sp^2 -hybridized Materials

In graphite, the G-band is still present as in all sp^2 carbon materials, while the 2D-band shows a particular lineshape related to the evolution of the electronic structure with number of layer increase [89]. Interestingly, in single wall carbon nanotube (SWCNT), the G-band is splitted into two components (usually labeled G^+ and G^-) due to the curvature of the tube. Indeed, such curvature lifts the degeneracy between LO and TO phonons at the Γ point. We will see that uniaxial strain can lead to a similar splitting. In the low frequency range ($50 - 300 \text{ cm}^{-1}$) of SWCNTs spectra, one can observe Raman modes corresponding to the radial breathing vibrations of the tubes (labeled RBM for radial breathing mode in figure 1.7). The energy of such mode depends on the tube diameter. We note that RBMs constitutes a very interesting mechanical probe for the pressure-induced collapse of nanotubes at high pressure [3, 90]. Finally, the Raman spectrum of amorphous carbon in figure 1.7 shows a broad Raman signature in the region of the D and G-band, which is explained by an important disorder.

1.3.3 Effect of External Perturbations on Graphene's Raman Response

1.3.3.1 Probing Graphene Strain through Raman Spectroscopy

In this section, we will outline how graphene in-plane strain can be measured through Raman spectroscopy in our high pressure experiments. Logically, the starting point is to examine how such in-plane strain changes the energy of a given phonon mode, in our case, the G-band of graphene. The description starts with the dynamical equation for carbon atoms in the graphene lattice, in which is introduced the effect of strain. For small strain, this equation writes [28]

$$-M \frac{\partial^2 Q_i}{\partial t^2} = M \omega_G^0 Q_i + \sum_{k,l,m} \frac{\partial K_{ik}}{\partial \varepsilon_{lm}} Q_k \quad (1.11)$$

where Q_i are the spatial components ($i, k, l, m = x, y$ coordinates) of the relative atomic displacement between the two atoms of the unit cell, M is the carbon atomic mass, and ω_G^0 the G-band energy for unstrained graphene. The last term in equation (1.11) introduces the effect of the two-dimensional strain tensor ε_{lm} . The $\partial K_{ik}/\partial \varepsilon_{lm}$ term is a fourth rank tensor quantifying the change in the sp^2 -bonds spring constant K with strain in the 2D space. Eq. (1.11) can be solved to determine ω_G , the vibration frequency in presence of strain. Such derivation is given in details in the literature, *e.g.* references [28, 91], and leads to the relative strain-induced shift

$$\frac{\Delta \omega_{G^\pm}}{\omega_G^0} = \frac{\omega_{G^\pm} - \omega_G^0}{\omega_G^0} = \gamma_G (\varepsilon_l + \varepsilon_t) \pm \beta_G (\varepsilon_l - \varepsilon_t) \quad (1.12)$$

where we have defined $\gamma_G = (\partial K_{xx}/\partial \varepsilon_{xx} + \partial K_{xx}/\partial \varepsilon_{yy})/(4M\omega_0^2)$, the G-mode Grüneisen parameter, and $\beta_G = (\partial K_{xx}/\partial \varepsilon_{xx} - \partial K_{xx}/\partial \varepsilon_{yy})/(4M\omega_0^2)$, its shear deformation potential [28, 72]. The Grüneisen parameter is a measure of how the graphene σ -bonds spring constant evolves with strain. In the case of tensile strain, the G-band softens, while it hardens with compression. Signs \pm shows that for uniaxial strain conditions (such as $\varepsilon_l = \varepsilon$ and $\varepsilon_t = -\nu\varepsilon$), the G-band splits into two components, G^+ and G^- as observed in carbon nanotubes due to the curvature. The notations l and t indicates the longitudinal direction (parallel to the applied strain), and the transverse direction (perpendicular to it), respectively. The G-band splitting was observed in different experimental works using flexible substrates to deform the graphene flake [51, 91]. Interestingly, such splitting coupled with polarized Raman spectroscopy can be used for the determination of the crystalline orientation of graphene samples [51, 91]. We may also note that uniaxial strain changes the electronic structure of graphene [51].

We will now focus on the biaxial strain situation, since it is central for high pressure Raman experiments interpretation. When $\varepsilon_l = \varepsilon_t = \varepsilon$, eq. (1.12) reduces to

$$\Delta \omega_G = 2\omega_G^0 \gamma_G \varepsilon \quad (1.13)$$

where we have defined ε *positive* for compressive strain. Multiple experimental works using various biaxial straining techniques (such as graphene bubbles [49], flexible and piezo-electric substrate [45, 46], high pressure [24]) converge towards a biaxial strain induced G-band slope of $\sim 57 \text{ cm}^{-1}/\%$, corresponding to $\gamma_G \simeq 1.8$. Thus, using a Raman spectrometer with 1 cm^{-1} spectral resolution, biaxial strain in graphene can be measured with an excellent sensitivity of

$\sim 0.02\%$. Concerning the 2D-band evolution, an equation similar to eq. (1.13) holds with a larger Grüneisen parameter $\gamma_{2D} \sim 2.6$, although there are some discrepancies in the reported values [38]. Finally, we should highlight the ω_G^0 dependance in eq. (1.13) which leads to a slightly lower $\Delta\omega_G(\varepsilon)$ slope evolution for a graphene layer made of ^{13}C than of ^{12}C .

1.3.3.2 Effect of Charge Doping on Graphene Raman Signatures

The Raman signatures of graphene, and especially the G-band, are highly sensitive to changes of the Fermi level, *i.e.* to charge doping. This allows to measure the surface charge concentration n in graphene through the positions of the Raman peaks. One first contribution to the doping-induced G-band shift is intuitive and varies as follows: n doping leads to the G-band softening since it populates the π^* antibonding band (decreasing bonds force constants), and conversely, p doping leads to the G-band hardening (solid blue line in figure 1.10(a)). This contribution is the adiabatic contribution that can be computed within density functional theory (DFT) (ref. [92]). In this calculation, the variation of the in-plane lattice spacing due to charge concentration changes is taken into account, since it also contributes to the softening (or hardening) of the G-mode (dashed blue line in figure 1.10(a)) [92].

A second, larger contribution to the doping-induced G-band shift arises from the strong electron-phonon coupling (EPC) that exists in graphene. The EPC manifests through the Kohn anomalies in the optical phonons dispersion at points Γ and \mathbf{K} of the BZ (indicated by red lines in figure 1.8) [80]. It corresponds to a renormalization of the phonon energies due to the EPC in metallic systems, where the phonon can decay into virtual electron-hole pairs [28]. This process depends on the Fermi level: it leads to a symmetric stiffening of the G-band when graphene is n or p doped (see figure 1.10(a)). The description of this effect requires to go beyond the Born-Oppenheimer approximation, that is, electrons cannot be considered to relax instantaneously in their ground state during the atomic motion due to the G-phonon. This has been treated theoretically with time-dependant perturbation theory within DFT [92–94] and observed experimentally in various works on both gate doping and chemical doping [58, 93, 95, 96]. Therefore, Raman spectroscopy can be used as a doping probe, not only on graphene but also on other nanocarbons such as carbon nanotubes [97–99]. Since ^{13}C graphene was used during this work, we have also calculated the G-band evolution for this isotope (shown in figure 1.10). However, the difference due to the heavier ^{13}C ions is very weak, inferior to 1 cm^{-1} for $|n| < 4 \times 10^{13} \text{ cm}^{-2}$.

The evolution of the electron-phonon interaction contribution to the G-band linewidth, $2\Gamma_G^{e-ph}$ with charge doping is plotted in figure 1.10(b) according to the model from ref. [92]. For both n and p doping, a symmetric, strong drop is observed. This effect is due to the Pauli blocking of the G-phonons decay into electron-hole pairs. Indeed, at $T = 0 \text{ K}$, when the Fermi level $|E_F|$ exceeds half the energy of the G-band phonon, $\hbar\omega_G/2$, the decay into electron-hole pair is impossible due to Pauli principle (the electronic states with suitable energy for such decay are occupied). This leads to the increase of the G-phonon lifetime. As for the G-band shift, this effect has been observed in numerous works [58, 93, 95, 96]. At room temperature, the drop is smoother but is still clearly observable. Thus, it can be used to identify doping effects

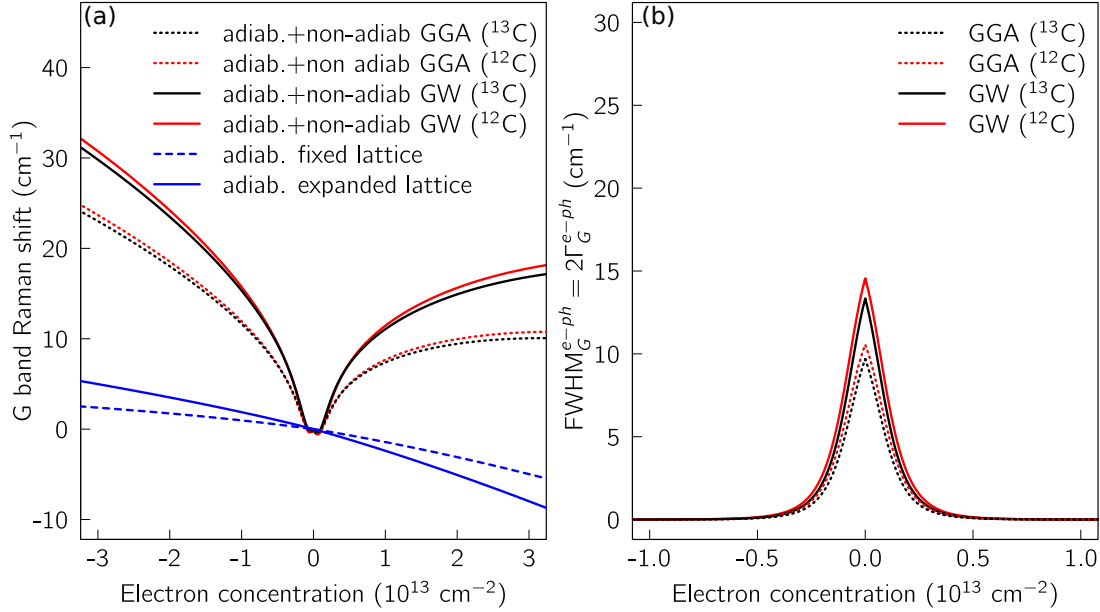


Figure 1.10 – (a) Evolution of the G-band position with electron concentration considering the model from Lazzeri *et al.* at temperature $T = 300$ K (calculated using eq. (6) of ref. [93]). Curves labeled "adiab.+non-adiab" includes the lattice expansion contribution. The EPC value is taken from ref. [92] (GGA) or from ref [94] (GW). Both ^{12}C and ^{13}C are considered. (b) Evolution of the G-band FWHM (electron-phonon contribution solely) with the electron concentration at temperature $T = 300$ K. The curves are computed using eq. (14) of ref. [92], using the two reported EPC values and for both isotopes. Note the different x-axis scale between (a) and (b).

in experiments. We mention that this effect is also responsible for the very broad G^- band observed in neutral metallic SWCNTs [100].

The 2D-band evolution with doping is less clear and still subject to discussions [38]. We simply mention that its intensity decreases monotonically with both n and p doping [101]. We underline that if doping and strain are present in a sample, both will impact the G-band evolution. In that case, the 2D-band evolution is useful to separate the two effects. This is the topic of the next section.

1.3.3.3 Deconvolution of Strain and Doping Effects

In order to deconvolute the concomitant effects of strain and doping on the Raman spectrum of graphene, Lee *et al.* [102] have shown that the use of the correlation diagram between the 2D and G-band positions can be used. In absence of doping for different biaxial strain applied, a linear evolution of $\Delta\omega_{2D}/\Delta\omega_G \simeq 2.2$ is found (see figure 1.11) [102]. Conversely, in absence of strain and for different hole doping levels, a different slope of $\Delta\omega_{2D}/\Delta\omega_G \simeq 0.7$ is observed [102]. In the case of n -doping, an even smaller slope of ~ 0.2 is observed (at low doping levels) [58].

Knowing the origin $(\omega_{2D}^0, \omega_G^0)$ in the Lee diagram for a given sample, one can project a given experimental observation $\mathbf{x} = (\omega_{2D}, \omega_G)$ on the non-orthogonal basis defined by the pure strain

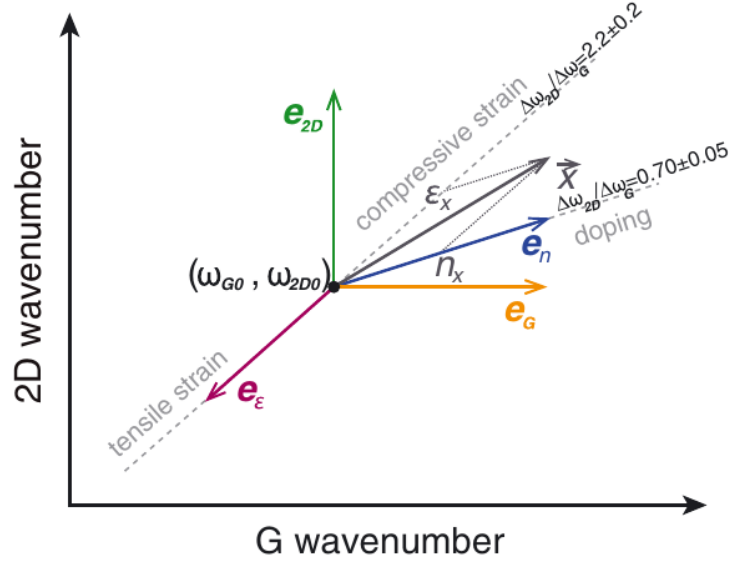


Figure 1.11 – Correlation diagram ω_{2D} as function of ω_G (Lee’s diagram). Evolutions for pure tensile and compressive biaxial strain are illustrated (dotted line). Unit vectors of the non-orthogonal basis are shown in red for biaxial strain, in blue for p -type doping. An example of projection is shown for a given vector \mathbf{x} corresponding to strain ϵ_x and charge (hole) concentration n_x . Figure taken from reference [38].

vs. pure doping evolutions, and obtain quantitatively the strain and doping present in the sample (this procedure is illustrated in figure 1.11). Without knowing the origin, one can however analyze *variations* in terms of doping and/or strain. A refined analysis can be applied when shear strain is present [103].

1.4 From Graphite to Graphene at High Pressure

We have introduced the physical properties of graphene, its Raman signatures origins, and how it can be used as a probe for structural, mechanical and electronic effects. In the light of these tools, we will outline the state of the art on high pressure experiments on graphite and graphene that underlies this work, highlighting effects related to the reduction of dimensionality.

1.4.1 Strain in Graphene Layers at High Pressure: State of the Art

In experiments, the biaxial strain in graphene layers is measured *in-situ via* the G-band shift, and pressure is measured independantly using a pressure gauge. Graphite has been studied at high pressure using a diamond anvil cell in a work by Hanfland *et al.* by Raman spectroscopy on a single-crystal [37]. The authors found a G-band pressure slope of $\partial\omega_G/\partial P = 4.7 \text{ cm}^{-1}.\text{GPa}^{-1}$ at low pressure, with a clear sublinearity of ω_G with pressure. Interestingly, Sun *et al.* have recently proposed that this sublinearity arises from the large out-of-plane strain due to the small out-of-plane stiffness of graphite [27]. Other authors reports slightly smaller values of $4.1 \text{ cm}^{-1}.\text{GPa}^{-1}$ using the same pressure transmitting medium (methanol-ethanol mixture), probably due to

the sublinearity averaged in a single linear slope value [104]. Finally, F. Balima have studied graphite samples at high pressure using argon and paraffin oil as pressure transmitting medium and found values of $4.0 \text{ cm}^{-1}.\text{GPa}^{-1}$ and $4.7 \text{ cm}^{-1}.\text{GPa}^{-1}$, respectively [105]. Using the graphite in-plane linear bulk modulus $\beta_{bulk} = -r\partial P/\partial r = 1250 \text{ GPa}$ found by Hanfland *et al.* by X-ray diffraction [37], and $\partial\omega_G/\partial P = 4.7 \text{ cm}^{-1}.\text{GPa}^{-1}$, we find the G-band shift with biaxial strain in layers $\partial\omega_G/\partial\varepsilon = \beta_G \times \partial\omega_G/\partial P \simeq 58.8 \text{ cm}^{-1}/\%$, consistently with values obtained for strained graphene using various techniques (subsection 1.3.3.1). Within the $0 - 10 \text{ GPa}$ range, no significant variations are observed in the G-band FWHM with pressure, but all authors observed an important broadening of the G-band beyond $\sim 10 \text{ GPa}$. This broadening is in general interpreted as the onset of a structural phase transition towards a more stable, sp^3 -hybridized structure induced by pressure: this will be discussed later, and we first concentrate on the low pressure regime. We may mention the work of Clark *et al.* on multilayer graphene (about seven-layers systems) at high pressure: the G-band follows a similar evolution than for graphite indicating a bulk response to pressure [106].

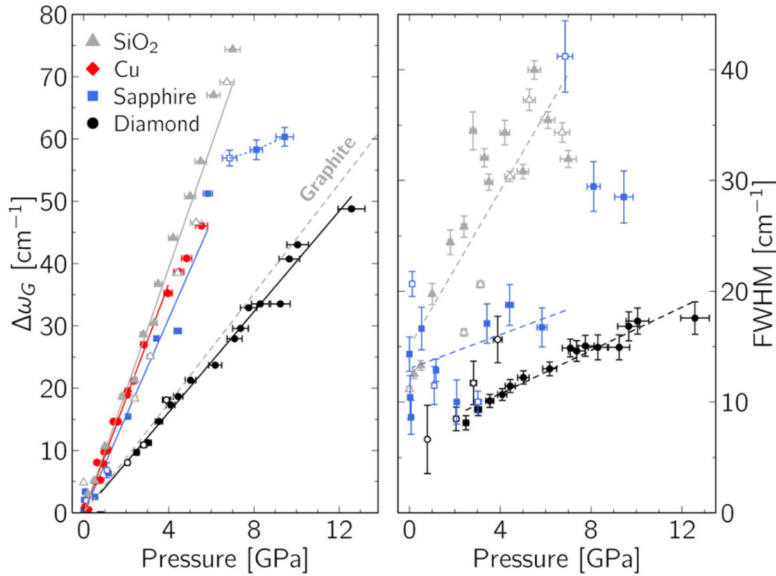


Figure 1.12 – G-band pressure shift (left panel) and FWHM (right panel) as function of pressure observed for monolayer graphene supported on various substrates (see legend). Figure from ref. [24].

Reducing the dimensionality to a single graphene sheet, the picture is different. Proctor *et al.* as well as Nicolle *et al.* have performed the first experiments on monolayer graphene samples at high pressure, supported on oxydized silicon substrates [21, 22]. In both works, a strong G-band shift (ranging from ~ 8 to $\sim 16 \text{ cm}^{-1}.\text{GPa}^{-1}$) was observed with pressure, much higher than in the case of graphite. This is explained by a strain transfer from the substrate to graphene through the adhesive van der Waals force between them. Indeed, the substrate contracts significantly at high pressure following its own pressure-volume equation of state, which drives graphene in biaxial compression (the substrate is always more compressible than graphene, except for diamond substrate for which it is comparable). Bousige *et al.* have explored this strain transfer by varying the substrate material (and thus its compressibility), confirming and formalizing the mechanism of strain transfer [24]. Figure 1.12 shows the G-band pressure shifts and FWHM as function of pressure for the different substrates used in this work, highlighting the important

role of the substrate. The strain transfer can be total, or partial, such as $\varepsilon_G(P) = \alpha \varepsilon_S(P)$ where ε_G and ε_S are the biaxial strain in graphene and at the substrate surface⁴, respectively, and α is a phenomenological "strain transfer efficiency" such as $0 < \alpha < 1$. The physical meaning of α is proposed to be related to the formation of an inhomogeneous strain field due to rippling, buckling or/and sliding of graphene, providing partial dissipation of the strain imposed by the substrate [24]. Supporting this hypothesis, a significant broadening of the G-band is observed with pressure from the beginning of the compression (see right panel in figure 1.12), contrarily to the bulk case of graphite, suggesting that nanoscale strain inhomogeneities are averaged over the Raman probe size, *i.e.* $\sim 1 \mu\text{m}^2$. In the case of diamond substrate (see figure 1.12), the strain transfer is total ($\alpha = 1$). This may be related to (i) the very low compressibility of diamond and/or (ii) its very low surface roughness compared to other substrates. In chapter 5 of this work, we explore new insights on the physical meaning of α . The coefficient α is observed being constant with pressure, apart from possible abrupt drops that are interpreted as slippage or detachment of graphene from the substrate [23, 24]. After such event, a smaller slope of $\sim 5.6 \text{ cm}^{-1}.\text{GPa}^{-1}$ was observed by Filintoglou *et al.* for graphene on copper [23]. Hadjikhani *et al.*, also using copper substrates, have observed a similar slope value from the beginning of the compression [107]. This may be explained by a lower degree of adhesion of graphene on the copper substrate in their case.

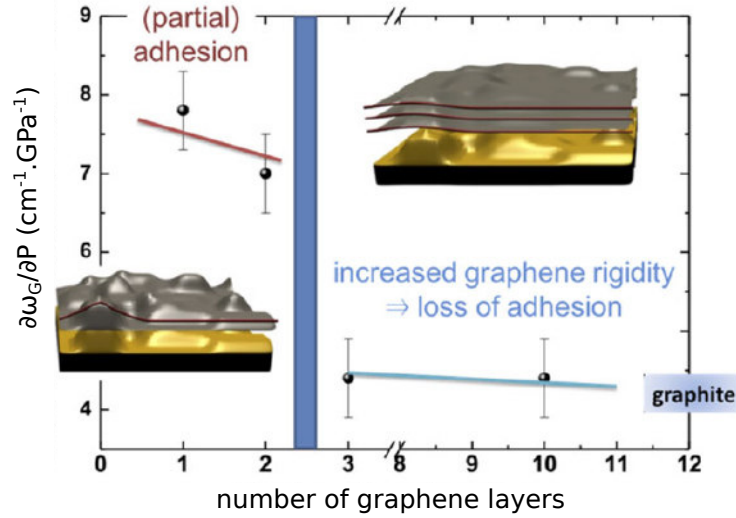


Figure 1.13 – G-band pressure slope as function of the number of graphene layers observed in experiments. The transition between the partial adhesion regime and the bulk regime is indicated between two and three layers. Illustrations represent the conformation state of the system on the rough substrate for monolayer and trilayer graphene. Figure taken from reference [25].

Increasing the number of layers, the graphite bulk response is recovered from three layers [22]. Figure 1.13 summarize the G-band pressure slope values as function of the number of graphene layers. The different pressure response between mono/bilayer systems and thicker systems is explained by a transition of the adhesion state of the sample, due to the increase of the bending

⁴The biaxial strain at substrate surface ε_S can be retrieved from the substrate bulk modulus $B_S(P)$ through $\varepsilon_S(P) = \exp\left(-\int_0^P \frac{dP'}{3B_S(P')}\right) - 1$ for isotropic materials. If $B_S(P)$ can be considered constant with P , we have $\varepsilon_S(P) = \exp\left(-\frac{P}{3B_S}\right) - 1$.

rigidity with the number of layers [22]. The competition between the adhesion energy of the system on a rough substrate and the bending energy required to conform on it leads to an unbinding for three layers and thicker systems [22, 108]. This effect is illustrated in figure 1.13 for monolayer and trilayer systems. Consistently, in experiments on MoS₂ single-layer at high pressure (MoS₂ having a larger bending rigidity than monolayer graphene), an intermediate "bimodal" adhesion state on the substrate was observed [109].

The role of the pressure transmitting medium (PTM) on the response of graphene is little known. First we remark that the sudden drop of α observed by Filintoglou *et al.* was observed in non-hydrostatic conditions, in a solidified PTM (fluorinert) [23]. Nicolle *et al.* reports a pressure-induced doping effect when the alcohol mixture PTM is used, while Filintoglou *et al.* does not [22, 23]. Mechanically, the bilayer system seems to be more sensitive to the PTM than monolayer [25]. We will address the effect of the PTM in details in chapter 3, through our experiments on the isotopically labeled bilayer graphene at high pressure.

In experiments on monolayer graphene, the strain ε_G and the pressure P are directly measured, but the stress on graphene σ_G is unknown and difficult to access. Bousige *et al.* propose to retrieve σ_G using the graphite in-plane bulk modulus such as $\sigma_G = \beta_{bulk}\varepsilon_G$ [24]. Pakornchote *et al.* consider that the stress on graphene is the sum of the frictionnal stress arising by adhesion on the substrate, and the "exterior" stress related to the intrinsic response of the 2D-material to pressure P [110]. Interestingly, Francisco-López *et al.* states that the intrinsic in-plane response to hydrostatic pressure should be zero for 2D-materials [111]. As explained in the introduction, experiments on suspended monolayer graphene are needed to apprehend the question of the intrinsic response of a 2D-materials at high pressure. More insight will be given in chapter 4 where we present our experimental developments in that goal.

1.4.2 Pressure-Induced sp^2 to sp^3 Phase Transition

As mentionned earlier, the broadening of the graphite G-band at pressures > 10 GPa observed in several works [37, 105] is attributed to a structural phase change towards a sp^3 -hybridized carbon structure. It is known that diamond can be synthesized by high pressure – high temperature process (HPHT) from carbon materials. The cold compression (at room T) of graphite requires very high pressures to transform (10 – 25 GPa) and does not lead to the diamond crystal structure: numerous other sp^3 structures have been proposed (see ref. [112] and references therein). The high pressure phase shows a very high hardness, an increased resistivity as well as optical transparency [112, 113]. By Raman spectroscopy, Lu *et al.* observed a transformation in graphene "nanoplates" (1 – 5 nm thick) similar to the graphite case [114], while Clark *et al.* propose that the limited number of layer in few-layer samples disfavors the transformation [106].

Recently, Martins *et al.* have suggested the formation of "diamondene" by cold compression of bilayer graphene (with turbostratic stacking) at pressures as low as 5 – 10 GPa in water [10]. In this work, a dispersive G-band is observed after the transition, which suggests the presence of sp^3 bonds [10]. In diamondene, hydrogen and hydroxyl groups favors the transformation

by bonding with the obtained sp^3 -hybridized monolayer, consistently with other experimental observations [11, 12]. A recent work reports the formation of a sp^3 -hybridized system even without pressure application, by exposure of bilayer graphene to hydrogen, highlighting the role of the environment of the sample when dimensionality is reduced [115]. Other authors have observed a new superhard phase by compression of multilayer graphene using an AFM tip [116]. Finally, Ke *et al.* reports a transition in trilayer graphene by *in-situ* resistivity and optical absorption measurements at high pressure in a diamond anvil cell [117].

1.5 Conclusion

We have introduced graphene and its mechanical properties, as well as graphene stackings. We have presented its electronic properties since it plays an important role in its Raman response. Raman spectroscopy is introduced in details, and we outline its role in this work, being (i) a versatile graphene characterization tool, and (ii) an sensitive *in-situ* optical probe for strain and doping in graphene layers.

We have described the state of the art of high pressure physics on graphite and graphene studied by Raman spectroscopy. The pressure response of thinner samples (of one or two graphene layers) is very different from the response of graphite. What emerges from previous work is that the high pressure response of graphene is guided by its complex environment, especially by the substrate on which graphene lays, while the role of the PTM is not clear. Graphene is a 2D-material, but we see that the third dimension is important as graphene interacts with neighboring atoms. Furthermore, it can bend, ripple, buckle in the out-of-plane direction to relax high strain levels imposed by the compressed substrate. In bilayer structures, a few research groups have suggested phase transitions towards sp^3 -hybridized layers by compression, where strong bonds in the third dimension are created.

Through the review of existing works, we believe that the need for (i) the clarification of the role of the PTM on graphene at high pressure, (ii) new, challenging experimental work on suspended samples, (iii) the exploration of the relaxation mechanisms in play when graphene is strained by the substrate at high pressure, appears clearly. These elements are at the centre of this work.

1.6 Summary

Synthetically, here are the important messages of this first chapter:

- Graphene is a two-dimensional material made of carbon in sp^2 hybridization, arranged in a honeycomb lattice. It is mechanically very strong but also flexible. The stacking of graphene layers following the Bernal structure leads to graphite, but other stackings are also possible.

- Raman spectroscopy probes vibrations in graphene through inelastic light scattering. The G-band is the in-plane vibration of the sp^2 carbon-carbon bonds. Due to the particular electronic band structure of graphene, its Raman spectrum exhibits resonance effects as well as multi-phonon scattering. This richness allows to use Raman spectroscopy for graphene characterization in terms of: number of layers, stacking order, crystallinity and type of defects, and even carbon isotopic composition.

- Importantly, Raman spectroscopy is an optical probe for the in-plane strain in graphene through its effect on the optical phonons energy (especially on the G-band). Furthermore, the energy of the G-band is also affected by doping due to electron-phonon coupling, allowing to measure the Fermi level. The two concomitant effects can be deconvoluted.

- When submitted to high pressure, monolayer and bilayer graphene exhibits stronger in-plane compression than for three layer and more. This different response at low dimensionality is explained by a strain transfer effect from the substrate to thinner samples by adhesive forces. The role of the pressure transmitting medium, as well as the intrinsic response of graphene to pressure are little known.

2

Experimental Techniques

Contents:

2.1	Introduction	46
2.2	Preparation of Graphene Samples	46
2.2.1	Graphene Production	46
2.2.1.1	Mechanical Exfoliation from Graphite	46
2.2.1.2	Chemical Vapour Deposition (CVD)	48
2.2.2	2D-Materials Transfer Techniques	49
2.2.2.1	PMMA Sacrificial Layer Technique	49
2.2.2.2	Deterministic Dry Transfer set-up by PDMS-stamping	49
2.3	High Pressure Techniques	52
2.3.1	Diamond Anvil Cell Apparatus	52
2.3.2	<i>In situ</i> Pressure Calibration	55
2.3.3	Pressure Transmitting Media	56
2.3.3.1	Comparison of Pressure Transmitting Media	56
2.3.3.2	Diamond Anvil Cell Loading Techniques	58
2.4	<i>In situ</i> Raman Spectroscopy	60
2.4.1	MicroRaman set-ups	60
2.4.2	Experimental Issues related to Raman Spectroscopy at High Pressure	63
2.5	Conclusion	65
2.6	Summary	66

2.1 Introduction

In this chapter, we present the experimental techniques at the heart of our work on graphene at high pressure. In further chapters, specific protocols and experimental developments can be found, but they rely on the central techniques presented herein. First are described methods for graphene synthesis and its transfer on suitable substrates for high pressure compression. Next are presented the experimental techniques for (i) the perturbation of the graphene sample (high pressure application), and (ii) measuring its response (*in situ* Raman spectroscopy).

The first section focus on graphene synthesis by micromechanical cleavage and chemical vapour deposition (CVD), the two techniques used to produce our samples. Then, we present graphene transfer methods with emphasis on sample suspension. More attention is given to the PDMS-stamping transfer method, since we have implemented it at our lab. Afterwards, we present the high pressure techniques centered on the diamond anvil cell (DAC) apparatus, extensively used in this work to produce high pressures. The method used to evaluate the applied pressure *in situ* is explained in details. Particular attention is given to the characteristics of the various pressure transmitting media in which graphene is compressed. Indeed, as we will see, graphene is very sensitive to its environment especially at GPa-range pressures. In a last part, the Raman spectrometer mounted and used for our experiments is described in details. Specific experimental features and limitations of *in situ* Raman spectroscopy at high pressure are highlighted in the context of samples of the graphene family.

2.2 Preparation of Graphene Samples

2.2.1 Graphene Production

2.2.1.1 Mechanical Exfoliation from Graphite

The first and simplest method for graphene synthesis is the mechanical exfoliation from graphite crystals. This micromechanical cleavage technique was reported by K. Novoselov and A. Geim in their famous work in 2004 [32]. The principle relies on the strong anisotropy of graphite, in which weak van der Waals forces hold the layers together while stronger bonds ensure coherency within layers. It can be exfoliated several times using scotch tape to separate the constituent layers by cleavage. The graphite source must be of high purity: in general, synthetic Highly Oriented Pyrolytic Graphite (HOPG), or very high quality natural crystals are used. In our case, we have choosen natural graphite crystals provided by NGS naturgraphit GmbH. These crystals present very large monocrystalline domains, which make them ideal for graphene preparation. We have used commercial polydimethylsiloxane (PDMS) thin films instead of scotch tape for mechanical exfoliation since it is cleaner. The flakes from successive exfoliations are deposited on a substrate, where one can find randomly distributed thin crystals of various thicknesses (see figure 2.1(a)).

It should be mentioned that the same technique applies to produce other 2D-materials from their layered-bulk counterparts, such as transition metal dichalcogenides (TMDs), hexagonal boron nitride (hBN), or phosphorene, among others [118].

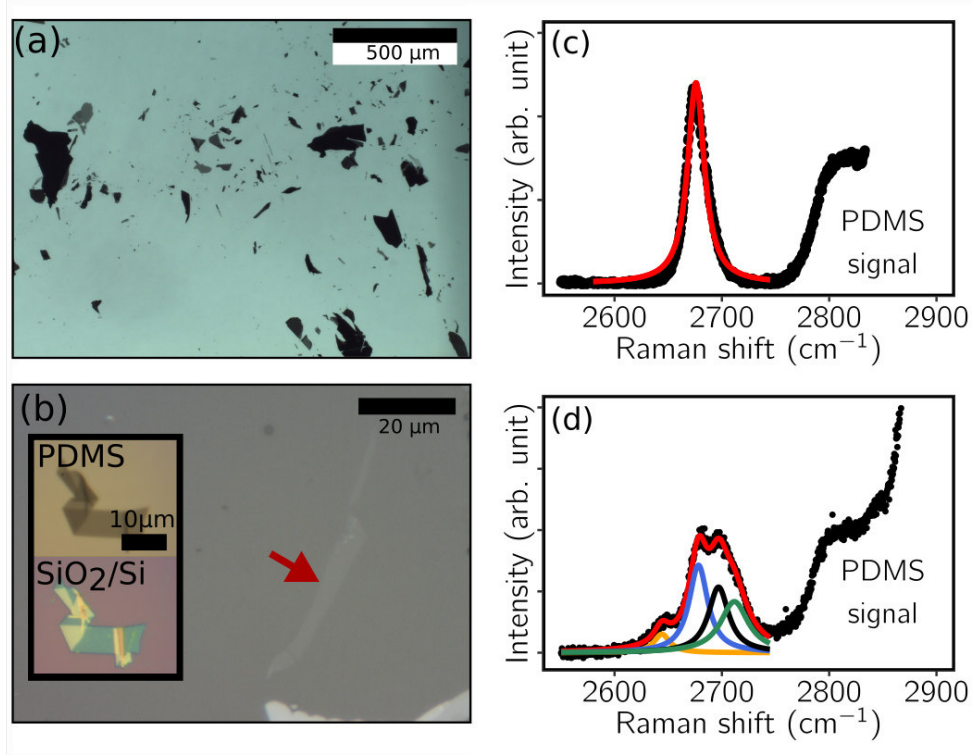


Figure 2.1 – (a) Optical micrograph of typical flakes resulting from graphite exfoliation. (b) Optical micrograph of a monolayer graphene flake obtained by exfoliation (indicated by a red arrow), on a PDMS substrate. The inset in (b) shows a folded multilayer sample on PDMS and on a SiO₂/Si substrate for the sake of comparison. (c) and (d) show the Raman 2D-band of monolayer and bilayer graphene on PDMS, respectively. Fitting functions are superimposed with the Raman spectra: a single Lorentzian in the case of monolayer graphene, and a four Lorentzian components lineshape for the bilayer sample. The Raman excitation wavelength is 532 nm.

Inherently to the micromechanical cleavage technique, interesting samples must be searched for by optical microscopy on the substrate (see figure 2.1(a) and (b)). It can be performed on various substrates (figure 2.1(b) shows a monolayer graphene sample on PDMS), but specific SiO₂/Si substrates are frequently used in that goal. This type of substrates consists in a thin layer of thermal silicon oxide (300 nm) at the surface of a bulk crystalline silicon wafer. It is very useful and widely used for optics and spectroscopy experiments on graphene, since it allows for (i) an excellent optical contrast under the microscope [119], and (ii) the sample's Raman signal enhancement [120]. These two effects result from optical interferences when multi-reflected light beams on the underlying silicon wafer are in phase while leaving the oxyde surface [119]. The electric field is enhanced at the sample location due to these constructive interferences (the maximum enhancement is close to 532 nm for 300 nm oxyde thickness). This in turns increases the sample absorption, enhancing both optical contrast and Raman intensity. The inset in figure 2.1(b) shows a folded multilayer sample on PDMS and on SiO₂/Si where the interference effect is clearly visible.

Flakes spotted by optical contrast can later be characterized in terms of number of layers using Raman spectroscopy through the 2D-band lineshape, as explained in chapter 1. In the case of monolayer and bilayer samples, the determination of the number of layer is unambiguous (figures 2.1(c) and (d) shows the 2D-band spectra of a monolayer and a bilayer graphene flake on PDMS substrate, respectively).

The micromechanical cleavage method has the advantage to produce high quality, monocrystalline graphene samples. In general, multilayer samples present Bernal or rhombohedral structure since the probability to find a turbostratic stacking in the graphite source is low. The method does not require any expensive equipments or sophisticated machinery. However, the lateral size of the obtained samples rarely exceed 50 μm . Furthermore, sample research is time consuming, since flakes must be found and characterized one by one. It is not suitable for large scale studies, but is adapted for proof-of-concept works. We will see that large flakes are in general not required for high pressure experiments. During this work, exfoliation was frequently used to produce samples on demand, essentially for our experimental developments on suspended samples at high pressure and our studies on supported nanographites. We should note that no other graphene production technique is available at iLM.

2.2.1.2 Chemical Vapour Deposition (CVD)

During this work, we have also used graphene grown by chemical vapour deposition (CVD). It mainly concerns the isotopically labeled bilayer graphene system (studied at high pressure in chapter 3), since it is not possible to produce this kind of sample by other means [121]. It was synthesized in M. Kalbac's research group at the Heyrovsky Institute of Physical Chemistry in Praha, Czech Republic. CVD graphene was also used in our work on suspended graphene at high pressure, outlined in chapter 4. In that later case, samples were synthesized in the group of N. Bendiab's at Institut Néel in Grenoble, France.

There are several variants of the CVD technique, based on the same principle: a carboneous precursor is decomposed at high temperature up to ~ 1000 $^{\circ}\text{C}$ in a reaction chamber *via* a metallic catalyst. The precursor consists in small molecules such as methane or ethylene, while the most common catalysts are Ni and Cu. In our case, Cu catalysts were used. Since the solubility of carbon in copper is very low, carbon atoms interact and organize into a monoatomic sheet of graphene on the copper surface. The growth is mediated by adsorption on Cu, contrarily to the Ni catalyst case in which carbon is solubilized *in* the metal [122]. The advantage is that the growth is self-limiting, resulting mainly in monolayer graphene on the Cu foil [123]. It can later be transferred from the copper to a choosen target substrate using the PMMA-assisted technique described in the next section.

The interest of CVD samples lies in their large size and uniformity. They are polycrystalline with a typical grain size of tens of microns. However, they commonly present crystalline defects, as well as wrinkles [123]. Many other techniques exists for graphene production. The interested reader can refer to refs. [124–127].

2.2.2 2D-Materials Transfer Techniques

In the aim to compress 2D-materials in a diamond anvil cell (DAC), one needs to transfer the sample from its synthesis location to a substrate to be loaded in the DAC. We will see that the main requirement is the small size for such support (in general $< 100\text{ }\mu\text{m}$ in all dimensions). During this work, the target substrates were designed depending on the experiment goals, and will be described specifically in each chapters. We will focus on the transfer techniques used during in this work: the reader interested in a larger panel of 2D-materials transfer techniques can refer to the review in ref. [128].

2.2.2.1 PMMA Sacrificial Layer Technique

CVD-grown samples can be transferred from the copper catalyst to a target substrate using a sacrificial poly(methyl methacrylate) (PMMA) layer. The PMMA layer is coated on the graphene surface, and copper is dissolved by chemical etching. Next, graphene along with the PMMA layer are deposited on the target substrate. The remaining PMMA is finally rinsed out with acetone. This was the technique used by M. Kalbac's group to transfer the isotopically labeled graphene layers on SiO_2/Si substrates. Interestingly, the target substrates can include holes intended for graphene suspension. In that case, the solvent drying must be performed at supercritical state to prevent applying capillary forces on suspended graphene regions. Indeed, these forces can induce the collapse of the fragile suspended samples [128]. This technique is implemented in Institut Néel for the preparation of suspended samples (see chapter 4).

The advantage of this technique is the ability to transfer very large CVD samples (a few millimeters in size). On the other hand, it requires wet chemistry steps which may induce slight pollution of the samples [128].

2.2.2.2 Deterministic Dry Transfer set-up by PDMS-stamping

Castellanos-Gomes *et al.* [129] have developped in 2014 a transfer method based on visco-elastic stamping [129]. The principle is sketched in figure 2.2. Two XYZ micromanipulators are arranged under a microscope: the first is used for the target substrate positionning (denoted "sample stage" in figure 2.2(a)), while the second is used for stamp positionning ("stamping stage" in figure 2.2(b)). The stamp consists in a PDMS 1 mm-thick layer on which 2D-material flakes have been previously exfoliated (or transferred by other means). The back of the stamp adheres on a transparent microscope slide. This slide is turned upside-down under the microscope, and the interesting flake on the stamp is aligned with the target substrate. To transfer it, the stamp is approached and pressed against the target substrate before being removed very slowly (see sketches in figure 2.2(b)). Thanks to the visco-elastic properties of the PDMS stamp (which is elastic at short time-scales but viscous at longer time-scales) the flake stays in adhesion on the target substrate after the stamp removal. This relies on the condition that the adhesion energy between the flake and the target is sufficient. The microscope must be equipped with a

long working distance objective (in our case 20 mm) in order to have sufficient space for the microscope slide and the PDMS stamp. Figure 2.3 shows a picture of the stamping transfer set-up we have mounted at iLM.

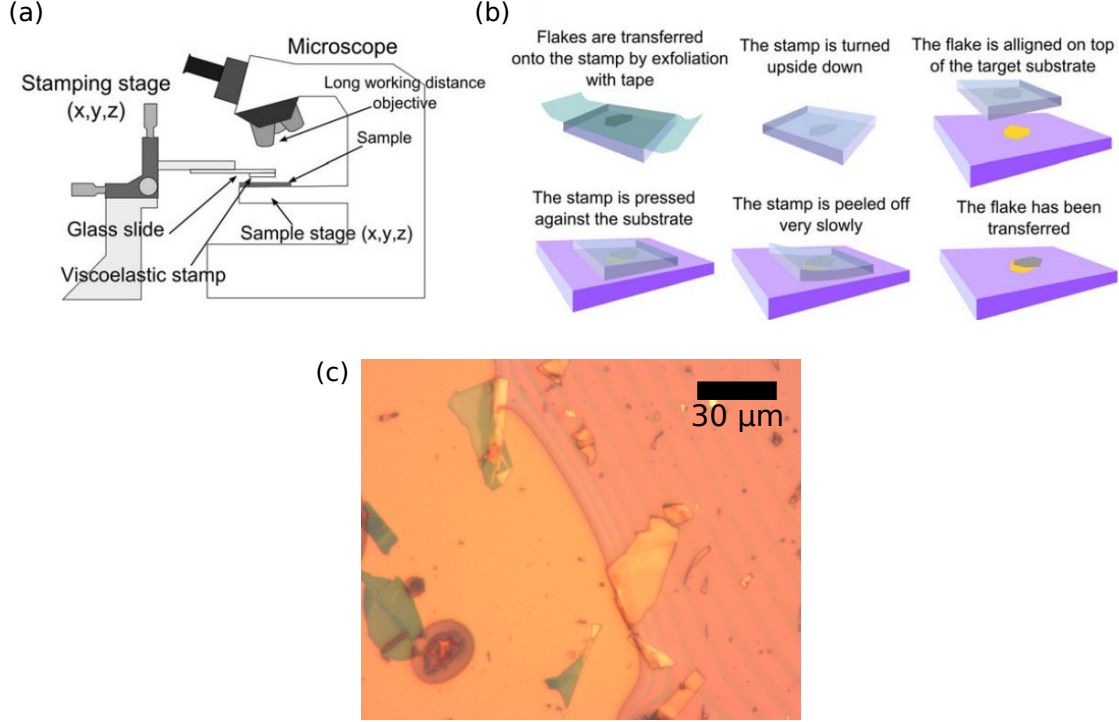


Figure 2.2 – (a) Sketch of the deterministic dry-transfer set-up. Two XYZ stages are arranged beneath the microscope equipped with long working distance objectives. (b) Sketches of the transfer steps. Figures reproduced from Castellanos-Gomes *et al.* [129]. (c) Optical micrograph obtained during the transfer of thin graphite flakes on a SiO_2/Si substrate. The contact front between the PDMS and the substrate is visible, as well as interference fringes in the right part, where the stamp is not yet in contact with the target substrate. Note that the SiO_2/Si substrate contrast enhancement is clearly visible in transferred flakes region, on the left part of the micrograph.

Compared to the PMMA-assisted method presented earlier, the PDMS stamping has the advantage to be deterministic and completely dry. It is beneficial for sample suspension since no capillary forces are involved. In that case, the target substrate includes a hole or a trench previously designed for flake suspension. No chemistry step is required, and it is relatively fast to perform.

The transfer process is precisely controlled by looking at the contact front between the PDMS stamp and the target substrate through the microscope. Interference fringes are visible in regions where the stamp is very close to the target, since it forms an air wedge (see figure 2.2(c)). The Z axis screw of the stamping stage is operated accordingly. In the case of sample suspension, the stamp should be removed extremely slowly to prevent flake breakage. A large proportion of the flake must belong to a supported region around the hole or trench, bringing sufficient adhesion for the successful transfer. The size and shape of the flake to transfer, as well as the substrate trench geometry are thus very important.

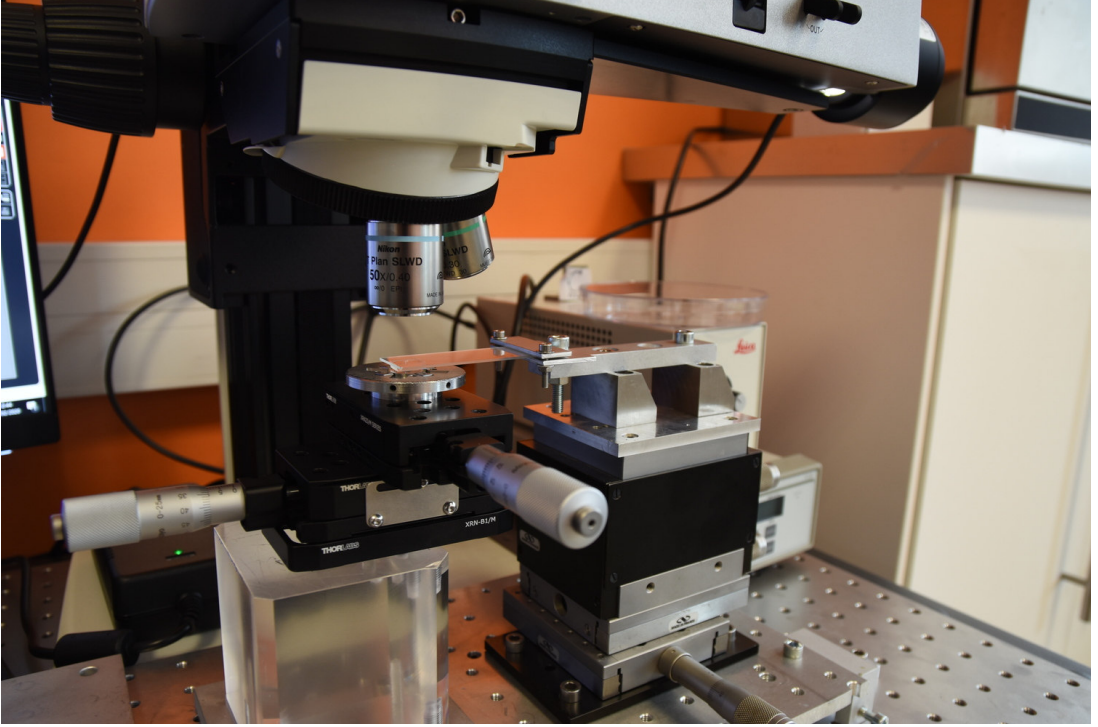


Figure 2.3 – Picture of the transfer set-up we have implemented at iLM. Under the microscope objective, the glass slide is inserted with the PDMS facing the diamond, in order to perform a flake transfer on a substrate installed on the diamond anvil.

The PDMS stamps are prepared in clean room by mixing liquid PDMS with a reticulant (10:1 proportions). The mixture is centrifugated, then pumped in a vacuum chamber to prevent any air bubbles in the resulting PDMS stamp. The mixture finally stays 24 hours in an oven at 70°C for reticulation in a large Petri box. Multiples squares of $\sim 1 \text{ cm}^2$ are then cut in the PDMS layer and used as transfer stamps.

With a few variations, this stamping method was used for the preparation of suspended monolayer 2D-material "drums" resonators [130], to build van der Waals heterostructures (hybrid stacking of different 2D-materials) [131], and even artificial twisted stackings (turbostratic stackings of the same 2D-material with a deterministic moiré angle) [66, 128, 132]. It is commonly used for 2D-materials encapsulation in hexagonal boron nitride, a strategy to improve electronic and optical performances of these systems [133, 134]. Such new hybrid structures are of great interest, due to the opportunity to design their physical properties by choosing their atomically thin constituents one by one [135]. In the high pressure context, the study of such devices is a very promising perspective. Indeed, GPa-range pressure is able to considerably tune the interaction between these constituent layers. We have implemented this stamping technique at iLM (i) considering the scope of new researchs unlocked with it for high pressure studies, and (ii) since combined with exfoliated samples, it allowed us to be autonomous for sample production and transfers at iLM. We have extensively used it for our developments in the aim of the study of suspended flakes at high pressure. This work is presented in chapter 4.

We have presented the synthesis and transfer techniques used to prepare samples. The next part presents the experimental set-up used for high pressure application on these samples.

2.3 High Pressure Techniques

2.3.1 Diamond Anvil Cell Apparatus

The diamond anvil cell (DAC) is an apparatus allowing to study samples at very high pressures, in the tens or even hundreds of GPa range. It is based on a simple principle: pressure is a force by unit surface. Consequently, reducing the surface on which the force is applied leads to pressure multiplication, at the expense of the study of very small samples. This limited size constitutes the main experimental constraint in the design of the sample's substrate.

In practice the DAC is a Bridgman anvil cell made of diamond, the hardest known macroscopic material. The sample is compressed in a closed pressure chamber through a pressure transmitting medium (PTM). This experimental volume is delimited by the two opposites diamond anvils culets (0.2 to 1 mm in diameter) and a sealing metallic gasket (see figure 2.4). The gasket confines the sample and the PTM in the experimental volume. Hydrostaticity (stress isotropy) in this chamber is maintained as long as the PTM stays liquid. A pressure calibrant is also placed in the DAC, which in our case is a small ruby chip (the pressure calibration method is detailed in part 2.3.2).

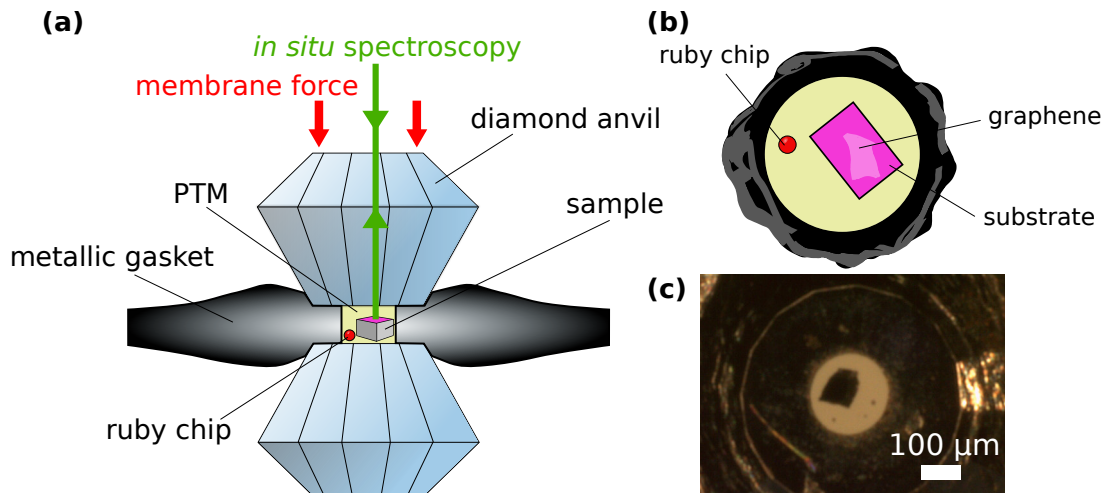


Figure 2.4 – (a) Sketch of the diamond anvil cell set-up. (b) Sketch of the pressure chamber where the sample consists in supported graphene over a SiO_2/Si substrate (top view). (c) Micrograph of a real DAC loading with the sample and three small rubies.

In order to increase the pressure in the chamber, one anvil is fixed while the other is mounted on a mobile piston where is applied the driving force (see red arrows in figure 2.4). The force can be applied by various means such as mechanical screws, arm levers, or by a hydraulic or pneumatic system [136]. In our case, a pneumatic system developed by R. Letoullec *et al.* is used: the piston is driven by a deformable metallic membrane which is inflated with helium gas by a dedicated setup [137]. With this technique, the force is uniformly applied on the piston and is precisely varied through the microvalve that controls the helium pressure in the membrane. This pressure is monitored by a digital manometer on the gas supply. The order of magnitude of

the applied force is a few thousands of newtons. A sketch and a picture of the most used DAC during this work is presented in figure 2.5(a) and (b), respectively (the membrane is visible in figure 2.5(b)). A picture of the gas supply set-up is shown in figure 2.5(c).

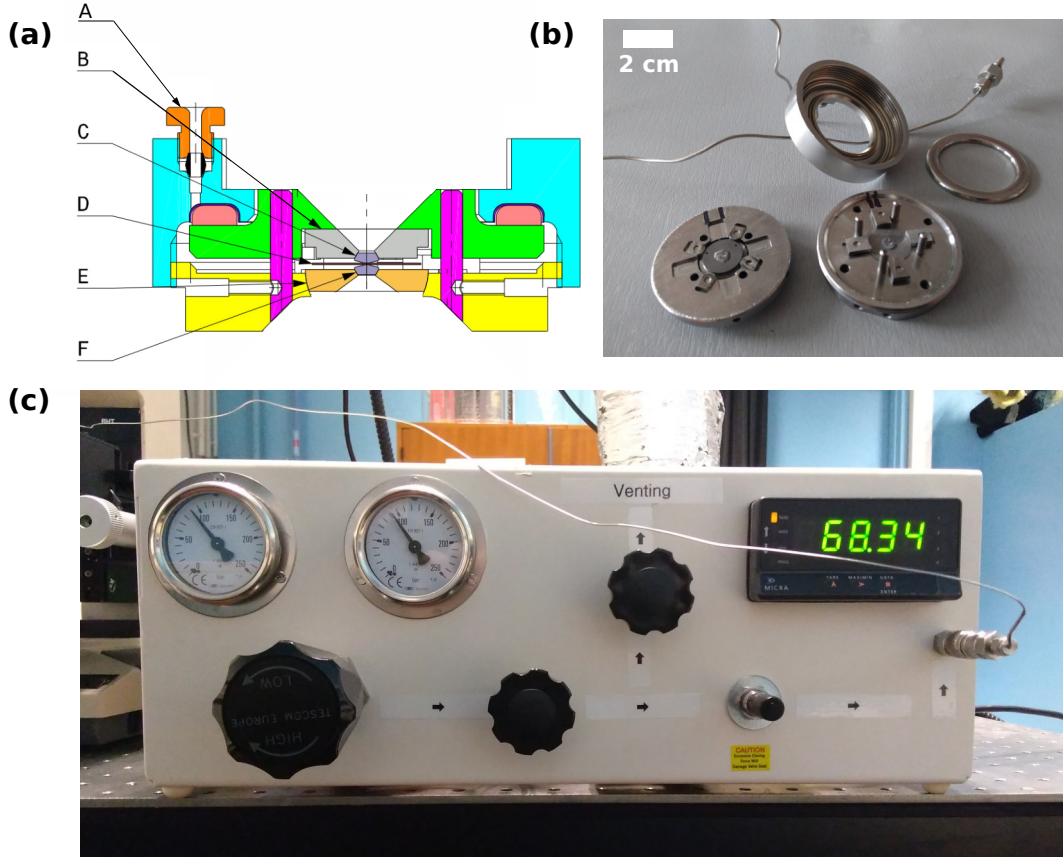


Figure 2.5 – (a) Sketch of the DAC called PROXIMA 1. A: outlet for the capillary of the deformable membrane, B and E: tungstene carbide anvil seats, C and F: diamond anvils, D: metallic gasket. (b) Picture of the piston and the body of the PROXIMA 1 DAC. The metallic deformable membrane is also visible as well as its capillary. (c) Gas supply set-up used to inflate or deflate the membrane through the capillary, allowing to control the force on the DAC. Such gas supply set-up is connected to a small helium bottle.

When the driving force is increased, the gasket plastically deforms and extrudes while the pressure increases in the pressure chamber [138]. After the force adjustment, it is important to wait for stabilization of this plastic process in order to reach a stable pressure in the DAC and before starting the *in situ* measurements (most of the time 10 – 30 minutes are sufficient).

At high pressures, stresses on anvils are distributed on the diamond culet but also on its surrounding region: this corresponds to Bridgman's principle of massive support which is a optimized situation to avoid diamond breakage. Diamonds seats are made of tungstene carbide (WC), a very hard material in order to withstand the load at the diamond-seat interface. The WC pieces need to be polished near to optical quality to ensure a proper contact area. The cell itself is made of maraging steel.

In order to decrease the pressure in the DAC and return to ambient conditions, the membrane pressure is lowered. The decompression process does not follow the same path than the compression since the plastic deformation of the gasket is not a reversible mechanism. Indeed, a consequential decrease of the membrane pressure is needed to lower the *in situ* pressure. Consequently, it is more difficult to precisely vary the pressure in the DAC at the decompression. The pressure decrease mechanism is not very clear yet, but it has been proposed that the DAC leaks [138]. In some of our experiments during the decompression, we have observed tinny channels in the gasket surface around the hole, reinforcing the leakage hypothesis.

Diamonds are not only used for their very high hardness and compressive strength, but also because of their transparency to a wide range of electromagnetic radiations (from infrared to hard X-rays, passing by deep ultraviolet). Such optical access was in fact a turning point in high pressure science at the birth of the DAC in the late 1950s. It allows for numerous *in situ* experiments such as Raman spectroscopy in our case, but also optical absorption, fluorescence, X-rays diffraction or spectroscopy techniques, etc [1]... Naturally, the optical observation of the pressurized sample is straightforward through a optical microscope. In our work, the direct observation of the samples and the substrates in the pressure chamber gave us a lot of information on the physical processes involved during compression. Diamonds used are single crystals with very low impurities, birefringence and fluorescence. They are cut from rough gems with the culet being the (100) crystal plane for highest strength [139].

The DAC showed in figure 2.5, called PROXIMA, has been developed in the laboratory and extensively used in this work. It is a very flat DAC: it is possible to focus light in the pressure chamber with a 100x magnification objective of 10 mm working distance. This objective is designed to compensate spherical aberrations introduced by the optical path through the diamond, in such a way that the spot in the focal plane is diffraction limited *in* the DAC (see part 2.4.2 for more details). The PROXIMA DAC uses Boehler's geometry for the anvils cut [140], helpful for such a flat design.

In a DAC, the alignment of the two diamonds is crucial in terms of culet superimposition as well as parallelism. A proper alignment prevents from high stress concentration at the anvil edges, thus from brittle failure of anvils. Tiny screws in the DAC design allows for the precise X-Y alignment, as well as the tilt between the two culets. The latter is achieved looking at interferences fringes at the air wedge between the two anvils. When no fringes left and a characteristic white pale colour is observed, the angle between the two culets is less than 5 arc minutes.

Prior to a high pressure experiment, the gasket is at first a simple metallic disk and is prepared in two steps: (i) preindentation of the gasket, and (ii) hole drilling. The gasket is preindented by compression in the DAC, which leaves the two anvil prints of a well controlled thickness (see sketch in figure 2.4). This preindentation provides hardening of the gasket, as well as an improved massive support for the anvils and the gasket itself. Then, the hole is achieved using a electro-erosion drilling machine.

The maximum achievable pressure with a DAC results from the size of the culet, the gasket

strength, indentation depth and hole diameter, as well as the PTM compressibility [138]. Gaskets are generally made of copper, copper beryllium, stainless steel or even rhenium to reach the highest pressures. In our case, within the 0-10 GPa range we have used copper-beryllium and stainless steel gaskets. The initial indentation thickness and hole diameter defines the dynamics of the pressure chamber compression, and are chosen with care. Usually the best performances are achieved with thickness at indentation of $\sim \phi/10$ where ϕ is the culet diameter, and a hole diameter of $\sim \phi/3$ [138]. However, the sample size is an important issue: the sample should be reasonably smaller than the hole in order to leave space for ruby chips and the PTM. Moreover, while pressure increases, the distance between the two anvils decreases and at some point the sample can end up crushed between the anvils. The remaining distance can be evaluated measuring the vertical displacement between microscope focus on the top diamond surface and the sample surface.

In this work, we have studied graphene samples deposited on SiO₂/Si substrates of 50 μm thickness using diamonds with $\phi = 400 \mu\text{m} - 600 \mu\text{m}$ depending on the experiments. As a consequence, we worked with gaskets of 75 – 100 μm initial thickness. Despite this precaution, some of our experiments ended because of the above mentioned experimental limit and thinner substrates should be considered for future experiments.

2.3.2 *In situ* Pressure Calibration

The determination of the pressure in the DAC can be achieved by various methods. In diffraction experiment, it is common to use the equation of state of a NaCl crystal placed in the DAC. The high frequency edge of the first order Raman spectrum of diamond can also be used [141, 142]. In our studies, we have used the most common method in spectroscopy experiments: measuring the spectral position of the narrow red fluorescence doublet of a ruby chip (Al₂O₃: Cr³⁺) placed in the DAC (see figure 2.4). Ruby chips are positioned in the pressure chamber by hand, using a thin polished tungstene tip while looking at the operation in a binocular. The fluorescence doublet redshifts while pressure increases, the R1 line (most intense line) being the most sensitive to pressure [143]. Then, pressure is evaluated using the relation

$$P = \frac{A}{B} \left[\left(\frac{\lambda}{\lambda_0} \right)^B - 1 \right] \quad (2.1)$$

where P is pressure in GPa, λ and λ_0 are wavelengths of the maximum of R1 fluorescence line at P and at atmospheric pressure, respectively, and $A = 1876 \pm 6.7$ GPa, $B = 10.71 \pm 0.14$ [144]. Two representative spectra are presented in figure 2.6 showing the pressure-induced redshift, with corresponding pressure values determined through equation (2.1). We have evaluated that except for very low pressures, we measure P with a relative uncertainty of 5% or better. The width of the two fluorescence peaks are indicators of the hydrostaticity of stresses in the cell: the width increases if shear stress exists on the ruby chip [143]. The energy separation between the two lines can also be used for non-hydrostaticity monitoring.

In practice, the fluorescence measurement is done directly on the microRaman set-up. Because

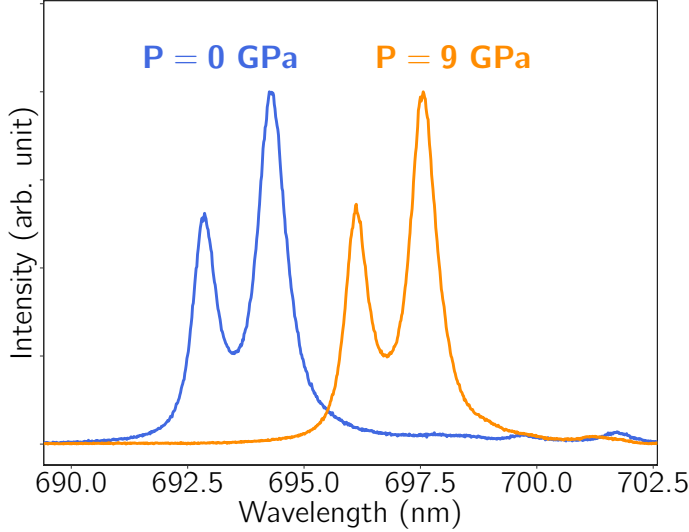


Figure 2.6 – Example of fluorescence spectrum of a ruby chip at atmospheric pressure ($\simeq 0$ GPa) (blue) and at 9 GPa (orange), showing clearly the redshift of the doublet with pressure.

this fluorescence signal is very intense compared to usual Raman signals, a very low laser power as well as a very short acquisition time (~ 100 ms) is used in order to avoid saturation of the CCD camera of the spectrometer.

In the next part, we will describe the properties of the pressure transmitting media used and how to load them in the DAC experimentally.

2.3.3 Pressure Transmitting Media

2.3.3.1 Comparison of Pressure Transmitting Media

During this work, we have observed that graphene is highly sensitive to the PTM nature and physical state. Indeed, a graphene monolayer has only surface atoms thus the entire material is in interaction with the PTM, interaction enhanced by pressure. Such system can be strongly affected by structural changes of the PTM in its vicinity, or even by chemical interactions with it. As a result, to properly interpret spectroscopic datas on graphene at high pressure, it is very important to consider the hydrostaticity of the different PTM used, as well as their reported phases transitions and recrystallizations at high pressures. This section is dedicated to these PTM characteristics.

In the pressure cell, conditions are hydrostatic if there is no shear stress at any point of the pressure chamber. This situation is achieved when the PTM has no shear strength at all, *i.e.* when it is liquid. Hydrostaticity is generally a desirable situation for the study of materials at high pressure, since it prevents any pressure gradient on the sample and the concomitant inhomogeneities in the interesting signatures. Non-hydrostaticity can promote or suppress phase transitions or even lead to pressure-induced amorphization of crystalline samples [145, 146]. When the PTM is non-hydrostatic, it should be noted that reproducibility in experiments (as

well as reversibility) is not guaranteed, since the geometry of the pressure chamber will drive the compression and eventual plastic flows in the solid PTM system. All PTMs undergo solidification with pressure at some point, and it is important to know how close they are to the pure hydrostatic conditions beyond this point. Another element to take into account is the chemistry of the PTM: depending on its nature, it can react with or even dissolve the sample [146]. In high pressure science, a wide variety of PTM are used such as rare gas, nitrogen, water, alcohol mixtures, fluorocarbons, and oils depending on the goal and specificities of the experiments [146, 147]. Here, we will restrict the description to PTM used in this work and related works on graphene: rare gas, nitrogen, water, and the 4:1 methanol-ethanol mixture. The latter is widely used for its remarkable property of remaining liquid up to 10.5 GPa, ensuring hydrostaticity in this pressure range.

In figure 2.7 we report the standard deviation σ of the pressure values given by a few ruby chips in the DAC as function of the mean pressure for different PTM (panel (a) for 4:1 methanol-ethanol mixture, panel (b) for helium, neon, argon and nitrogen). These measurements, published by Klotz *et al.* [147], have been carried out in order to characterize the hydrostaticity of various PTM since σ gives a quantified estimation of the hydrostaticity of the medium. When $\sigma = 0$, all rubies give the same pressure value and the PTM is hydrostatic. While σ deviates from 0 with pressure, the medium is less and less hydrostatic.

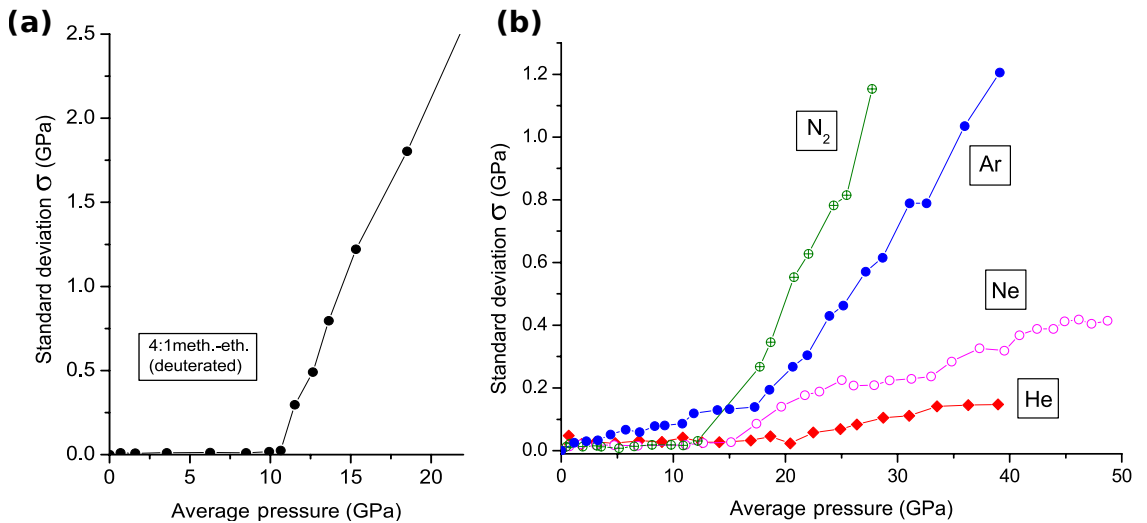


Figure 2.7 – (a) Standard deviations of pressure values given by a few rubies in the cell using 4:1 methanol-ethanol mixture as PTM, as function of the mean pressure. (b) Same plot for helium, neon, argon and nitrogen. Note the different y-scale between (a) and (b). After Klotz *et al.* [147].

In figure 2.7(a), we can see that the 4:1 methanol-ethanol mixture is hydrostatic in the 0 – 10.5 GPa range, as mentioned. We may note that, despite its liquid state, its viscosity can reach very high values at high pressure (of the order of 10^{11} Pa.s at 10 GPa) [148]. Helium is undoubtedly the best PTM even for the high pressure range, followed by neon (see figure 2.7). Counterpartly, their loading in the DAC is challenging due to their low boiling point (see next part for details on the techniques used to load the PTM in the DAC). At iLM, we were involved in the development of a new portable technique for helium loading. The concept and progress of this project is

described in section 4.4, the interested reader can refer to this section.

Due to the difficulty of the helium loading and since we have worked in the 0 – 10 GPa range, we have mainly used nitrogen and 4:1 methanol-ethanol PTM. We note that nitrogen is more hydrostatic than argon in the 0 – 10 GPa range (see figure 2.7(b)).

Only few data are available concerning the hydrostaticity of water as PTM. A broadening of the R1 fluorescence line of the ruby chip has been reported at pressure as high as 9.2 GPa[149]. In a more recent work, the onset of non-hydrostaticity is observed at ~ 2 GPa by looking at the energy separation between the R1 and R2 line of the ruby chip (Supplementary information of ref [10]). However, water solidifies in ice VI phase at pressure as low as 1 GPa, and it recrystallizes to ice VII near 2.1 GPa. Thus, H₂O is strictly hydrostatic only at pressures lower than 1 GPa.

We have compiled data on the different PTM in table 2.1. The reported hydrostatic limit corresponds to the pressure where a first insight of non-hydrostaticity is observed experimentally. In the case of ref. [147] it corresponds to an increase in σ , whilst in ref. [146] it corresponds to the broadening of the X-ray diffraction lines of a test quartz monocrystal in the DAC.

	He	Ar	N ₂	4:1 meth.-eth.
solidification pressure (GPa)	12.1 [147]	1.15 [150]	2.4 [151, 152]	10.5 [147]
transition/recryst. pressure (GPa)		*	4.8 [151, 152]	
hydrostatic limit (GPa)	23 [147]	1.9 [146, 147]	3 [146]	9.8 [146]
chemistry	inert	inert	inert	-OH

Table 2.1 – Solidification and phase transition/recrystallization pressures of various PTM. The hydrostatic limit corresponds to the first insight of non-hydrostaticity observed experimentally (see text). * In the case of solid argon, different authors have reported its recrystallization in one or a few crystals each time the pressure varies sufficiently, allowing the solid PTM to conform to the pressure chamber [150, 153–155].

2.3.3.2 Diamond Anvil Cell Loading Techniques

The PTM loading is the last step of the preparation of a high pressure experiment. The key point is that the PTM must be trapped with high density, in order to provide sufficient bulk modulus in the pressure chamber. If it is not the case, the compressibility of the PTM is too high and the pressure chamber will collapse when the driving force increases. Nitrogen or argon can be loaded at liquid state relatively easily, whilst helium requires a liquid helium cryostat and specific designs to immerse the DAC. A very high pressure loading apparatus can also be used at ambient temperature (see section 4.4 for details on the existing techniques for helium loading). In the case of PTM which are liquid at room temperature such as oils, water or the alcohol mixture, the loading is easier.

In the latter case of 4:1 methanol-ethanol, frequently used in this work, a drop of the mixture is directly deposited by using a syringe in the pressure chamber, where the sample and rubies are

arranged. The cell is then closed fastly, before the drop evaporation. The technique is simple in principle but many failures are possibles: the sample can move when the drop is deposited, or a ruby can be lost (this is the reason why more than one ruby are used most of the time). When the sample consists in supported graphene, an additionnal risk is that the substrate can flip and the interesting area (where graphene is) may become optically unaccessible. Oftenly, more than one try is required for succesful loading. The success can be confirmed by the observation of the Raman signal of ethanol and methanol in the DAC (its Raman spectrum is shown on figure 2.11). Sometimes, an air bubble can be observed (see figure 2.8(a)), sign of the presence of the PTM. For the loading of water PTM, the procedure is the same.

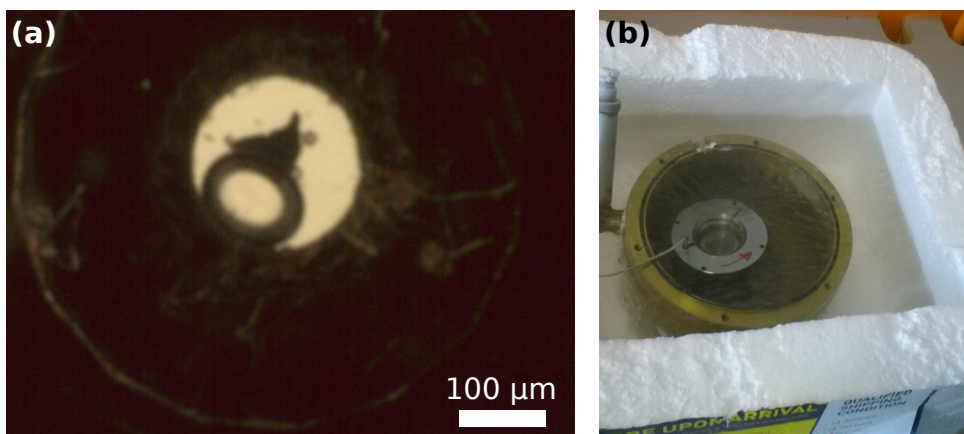


Figure 2.8 – (a) Micrograph of an air bubble in the pressure chamber during the loading of the DAC with 4:1 methanol-ethanol PTM. (b) Picture of the DAC immersed in liquid nitrogen during the loading.

Nitrogen loading requires a liquid nitrogen bath. The DAC, prepared with the sample and the ruby calibrants, must be slightly open and immersed in the bath (see figure 2.8(b)). Once the DAC is thermallized at 77 K and nitrogen is stabilized, the cell is fastly removed from the bath and closed by hand using cryogenic gloves in order to trap the PTM in the pressure chamber. Then, after placing the DAC back in liquid nitrogen, the membrane pressure is increased by a few bars in order to safely trap the PTM and avoid any leaking problem at the gasket level. The cell is finally retired from the bath again and heated up to room temperature: a precise control of the membrane pressure using the microvalve is required while the DAC warms up to compensate the membrane pressure increase. As in the case of alcohol, the sample may move during the loading, or the ruby calibrants can be lost. The presence of liquid nitrogen in the cell can be confirmed using Raman spectroscopy, searching for its molecular vibron at $\sim 2330 \text{ cm}^{-1}$. In the case of argon, the procedure is very similar except that argon is liquified in a container surrounded by liquid nitrogen (which boils at a temperature a few kelvin lower than the boiling temperature of argon). Since argon does not have any Raman signature, the presence of the PTM can be confirmed by measuring the pressure in the cell using the ruby fluorescence technique: a few kbar should be observed in the cell if it is loaded properly.

In our experiments, a common issue concerning all these loading processes is the capillary force created by the PTM when it is inserted in the DAC. For the study of suspended 2D-materials, this force may cause the sample collapse or displacement.

2.4 *In situ* Raman Spectroscopy

2.4.1 MicroRaman set-ups

To perform Raman experiments, one needs a monochromatic source of light, an efficient optical system to collect and disperse the different wavelengths of the scattered radiations by the sample, and a light detector. In the pioneer experiments by C. V. Raman in the late 1920s, the light source was an emission line from a mercury gas discharge lamp, and the scattered light was dispersed by a prism based spectrograph on photographic plates. Nowadays, laser lines make very stable and chromatically pure sources and diffraction gratings based spectrographs are used to record the Raman spectrum on a CCD device.

The Raman effect is generally very low, 10^4 to 10^6 weaker than the excitation light [67], therefore two features are needed: (i) an excellent stray light rejection in the spectrometer¹ or notch/edge filters to limit the elastically scattered light entering the spectrometer, (ii) a CCD detector with high quantum efficiency.

Our principal set-up is based on a Princeton Instruments Acton SP-2500i spectrometer. At my arrival at iLM, the existing Raman set-up was designed with usual holographic notch filters for Rayleigh filtering (cut-off frequency about 120 cm^{-1} from the Rayleigh line), and did not include any visualization system: it was dedicated to high pressure Raman spectroscopy on bulk samples or powders. For Raman studies on single nanomaterials such as graphene, visualization of the sample is essential. An imaging set-up coupled to the Raman system allows to visualize the precise position of the excitation laser spot on the sample, supported on a substrate or suspended. We have decided to upgrade the existing set-up in this goal, with the will of building an optical platform dedicated and optimized for high pressure studies on 2D-materials. A microscope unit has been implemented with transmission and reflexion imaging, as well as Volume Bragg Grating (VBG) filters in order to bring the ability to measure the high pressure evolution of interesting Raman modes very close to the Rayleigh line². The cut-off frequency is at $\sim 10\text{ cm}^{-1}$ from the Rayleigh line. Moreover, the laser excitation power on the sample (which is an important parameter for Raman spectroscopy on graphene) can now be measured easily. Our microRaman set-up is sketched in figure 2.9, and a picture is shown in figure 2.10. The mounting and use of this Raman platform was very appropriate, since our experiments has an important exploratory aspect that requires a permanent, fast, and flexible use of Raman microspectrometry to perform various verifications, and high pressure attempts.

The set-up is in backscattering geometry. The beam from the 532 nm laser source (a diode pumped solid state laser) is used as Raman excitation source. At the laser output, a metallic neutral density gradient filter is installed in order to control the laser power used for the Raman

¹To improve the stray light rejection ratio, it is also very common to use multiple dispersion stages in series [67].

²During this work, attempts have been made to follow the low frequency shear vibration mode between layers in multilayer graphene [68] at high pressure, with no success due to lack of signal relative to the low energy signal arising from the PTM.

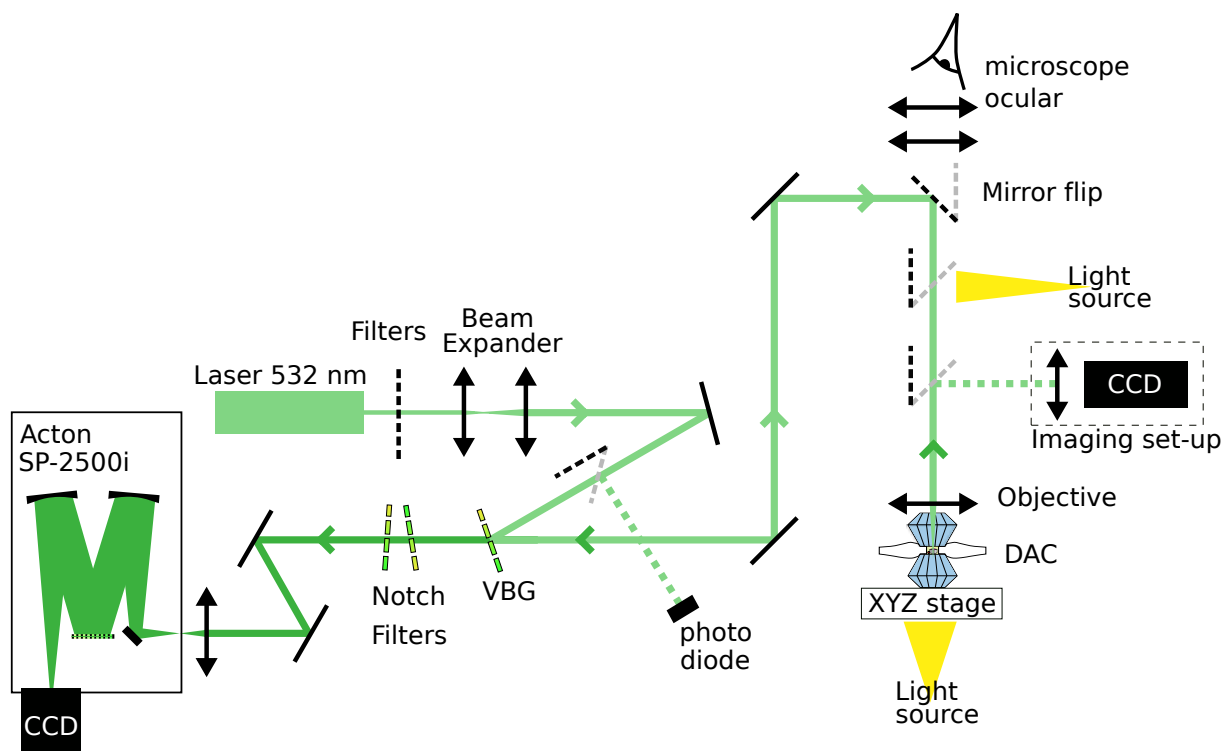


Figure 2.9 – Optical scheme of the high pressure Raman set-up. Flipping elements are represented in their two possible positions: in black for Raman measurements, in grey for visualization or laser power measurement.

measurement. The beam is then expanded to a diameter of ~ 4 mm, and reflected exactly at the Bragg angle of the VBG beam-splitter in order to be focused on the sample by the microscope objective. In general for high pressure experiments, long working distance objectives (> 10 mm) are needed to be able to focus the light in the DAC (see next section for more details on the microscope objectives used). The scattered light including Rayleigh and Raman signals is collected through the same objective and follow the inverse optical path (darker green arrows in figure 2.9). When the scattered light reaches the VBG beam-splitter, only wavelengths that matches the Bragg conditions are diffracted again: it corresponds to a very narrow spectral bandwidth of less than 20 cm^{-1} around the laser line. The Rayleigh line is thus rejected with 90% efficiency while the Raman signals are 90% transmitted. Two ultra-narrow notch filters are used in series to reject the laser line with an optical density superior to 4 each. Two mirrors and a lens allow for the precise focalisation through the spectrometer slit, opened at $100 \text{ }\mu\text{m}$. The lens is chosen regarding the $f/6.5$ aperture of the spectrometer, with a focal length of 25 mm for a ~ 4 mm spot diameter. The spectrometer is in Czerny-Turner geometry, equipped with a 1800 grooves/mm diffraction grating with blaze wavelength at 500 nm. The light is finally collected on the Princeton Instruments Pixis CCD camera of 1340×100 pixels, cooled at $-75 \text{ }^\circ\text{C}$ by a Peltier system for improved quantum efficiency. The spectrometer and the CCD are connected to a computer from which we can plot and save the data through the software Winspec32. The position of the diffraction grating can be controlled directly from the computer. The vertical CCD binning is limited to a few hundreds of micrometers, which combined with the slit creates a relative confocality. The whole experimental set-up is mounted on a pneumatic isolated table

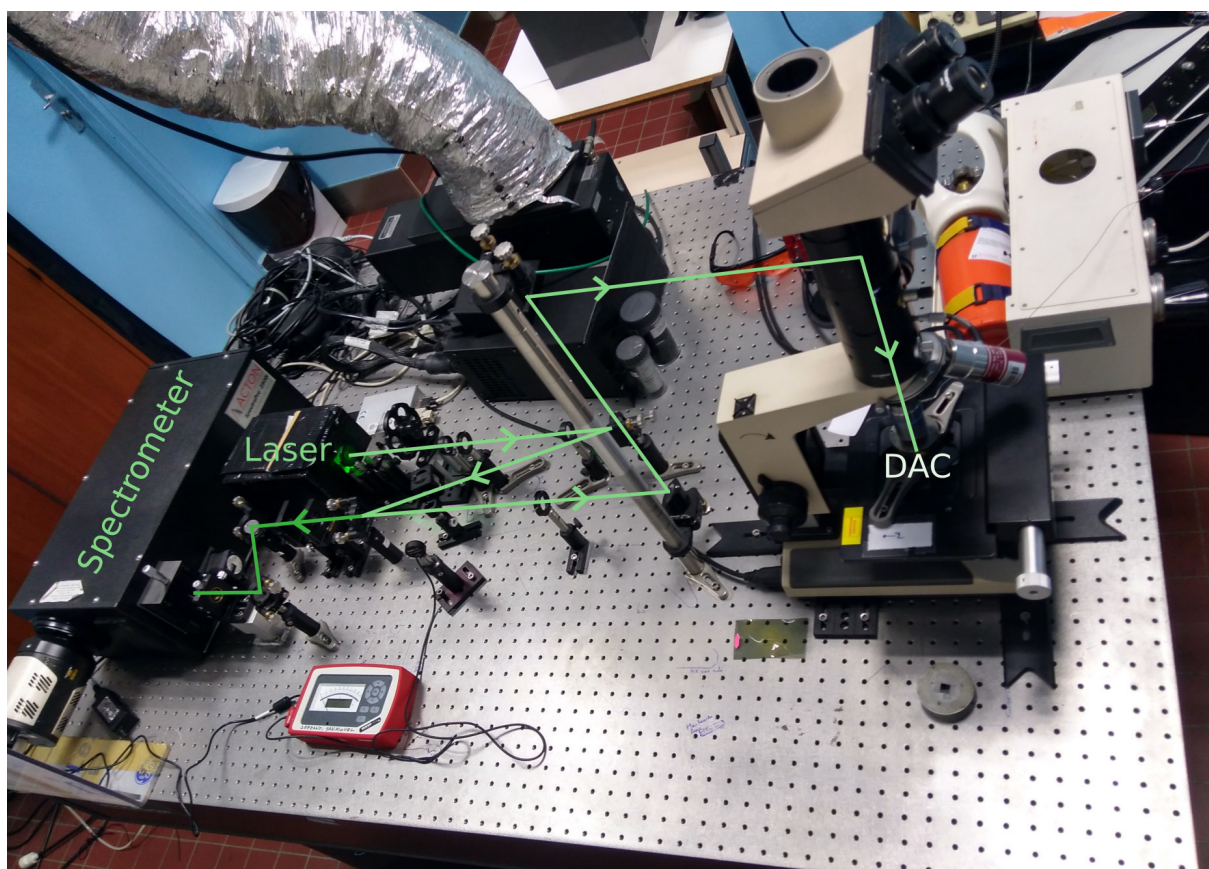


Figure 2.10 – Picture of the homemade microRaman set-up mounted and used during this work. The laser beam is symbolized by the green lines.

to ensure stability.

The sample (or the DAC) is fixed on the XYZ stage of the microscope (right side of figure 2.9), at the bottom of the microscope tower. Two flip 50:50 beam-splitters can be inserted, the first to illuminate the sample through the objective and the second to send the image on a CCD camera thanks to a tube lens. Back-illumination is also possible for transmission imaging. The Raman spot can be visualized at its exact position along with the sample image. Such image can also be seen directly through the microscope ocular by flipping the top mirror, in that case without the laser spot.

The excitation laser power at the sample can be measured, and calibrated with the power measured before the reflection on the VBG filter (see the position of the photodiode in figure 2.9). This is done at the beginning of an experiment. It is then possible to evaluate the incident laser power on the sample without removing it or change the focus, using the powermeter connected to the photodiode at the position shown in figure 2.9.

Often, the spectrometer is recalibrated using the two atomic lines from an spectral mercury lamp at 546.075 nm and 579.067 nm. We have chosen these two lines because of their spectral proximity with the Stokes Raman signal of carbon sp^2 -hybridized materials using the 532 nm excitation laser. The accuracy of the wavenumber along the spectral window is $\sim 2 \text{ cm}^{-1}$, and the resolution have been evaluated inferior to 2 cm^{-1} . The calibration is checked before experiments measuring the TO mode of a reference silicon crystal and/or the G-band of a graphite single-crystal.

2.4.2 Experimental Issues related to Raman Spectroscopy at High Pressure

The principal requirement is the use of long working distance objectives to focus and collect the light through the top anvil. Most of the time, a 50x magnification objective with $\sim 0.4 - 0.5$ numerical aperture is used. The use of 100x magnification with higher numerical aperture is unlikely: with most of DAC designs, the working distance would be too short to focus the light into the pressure chamber. Another important drawback is the introduction of optical aberrations due to the presence of the diamond anvil in the optical path. These aberrations arise because the beam is not collimated but convergent while passing through the diamond (1.44 mm thickness with ~ 2.42 refractive index³ [156]), leading to spherical aberrations and astigmatism. A specific ultraflat DAC design, called PROXIMA, has been developed at iLM: coupled with a dedicated pre-compensated 100x magnification objective custom-made by Mitutoyo, these aberrations can be corrected. The objective has a numerical aperture of 0.7 with a 10 mm working distance, leading to a near diffraction limited spot size of $\sim 1 \text{ }\mu\text{m}$ on the sample *inside* the DAC (at 532 nm). This set-up was first designed and characterized for *in situ* single nanoparticle absorption spectroscopy at high pressure, using spatial modulation techniques which requires a narrow and well defined spot intensity profile [157, 158]. In our work, we have used this design for the study of suspended thin layer samples at high pressure: it is very helpful to guarantee the precise positioning of the Raman spot on the suspended area which is only

³The pressure variation of the diamond refractive index is weak, less than 1% in the 0 – 20 GPa range [156].

a few microns wide. It also improves slightly the Raman signal to noise ratio thanks to the higher numerical aperture providing wider light collection. By the way, the pre-compensated objective contains more lenses than usual objectives and absorption/reflexion losses in these optics balances the signal gain. In the case of fully supported samples, there is no need for such pre-compensated objective and usuals 50x long working distance microscope objectives were used.

In all experiments using diamond anvil cells, Raman modes from diamond are observed due to the laser excitation in the top diamond anvil (see figure 2.11, blue spectrum). Even if this problem can be reduced using confocal Raman set-ups, the first order diamond Raman band at $\sim 1333\text{ cm}^{-1}$ is always very intense and overlaps with the spectrum of the sample. On figure 2.11 is also shown the Raman spectrum of a monolayer graphene sample (black dashed line), in order to compare how the diamond signals can hide the interesting signatures of graphene. Primarily, the defect related D-band of graphene (very weak peak at $\sim 1350\text{ cm}^{-1}$ on figure 2.11) is inaccessible *in situ*, masked by the prominent diamond Raman peak. It should be noted that in a study on carbon nanotubes, the D band has been measurable for pressures beyond 15 GPa thanks to its higher blue-shift than the sharp peak from diamond with pressure [159]. The second order Raman feature from diamond at ($\sim 2500\text{ cm}^{-1}$) is always observed but its intensity is low (it is multiplied by a factor 100 compared to its first order peak on figure 2.11 for clarity). Even if this signal partly overlaps with the 2D-band of graphene, it is usually possible to follow the 2D-band evolution at high pressure if care is taken during the deconvolution analysis. When these limitations are too cumbersome, an alternative is the use of anvils made of a different material than diamond: sapphire, or moissanite (SiC). Their Raman modes are located at lower energy and are not bothering for experiments on high energy Raman bands of sp^2 carbon materials, but their hardness and strength are significantly lower than diamond, as well as the maximum pressure achievable, accordingly. During this work, we have occasionally used a sapphire anvil cell.

Raman signals from the PTM are also observed and overlaps with the sample signatures: the spectrum of the 4:1 methanol-ethanol mixture is shown in orange in figure 2.11. During experiments following the G-band of graphene with pressure, it is common to observe the broad peak close to 1450 cm^{-1} , more or less intense depending on the precise focus at the sample surface. Furthermore, the low-energy wing of the PTM high energy peaks near 2800 cm^{-1} can also produce a background in the sample 2D-band spectrum. In every cases, the PTM and anvils signals must be taken into account when fitting the experimental datas using lineshapes functions. The PTM can also presents fluorescence signal, especially if it has been stored in a plastic bottle (likely due to a small amount of impurities from the plastic bottle that have diffused into the PTM). The alcohol mixture must be stored in a glass bottle.

Nitrogen presents only a very sharp peak at 2330 cm^{-1} corresponding to its molecular vibron. However, since the loading is done by immersion (see previous part), a small amount of oxygen can be present in the PTM and characteristic sharp peaks can be observed in the 1550 cm^{-1} region [160]. Monoatomic PTM such as argon or helium does not present any Raman modes at liquid state. Even at solid state, no high energy peaks can be observed since there is no strong bonds

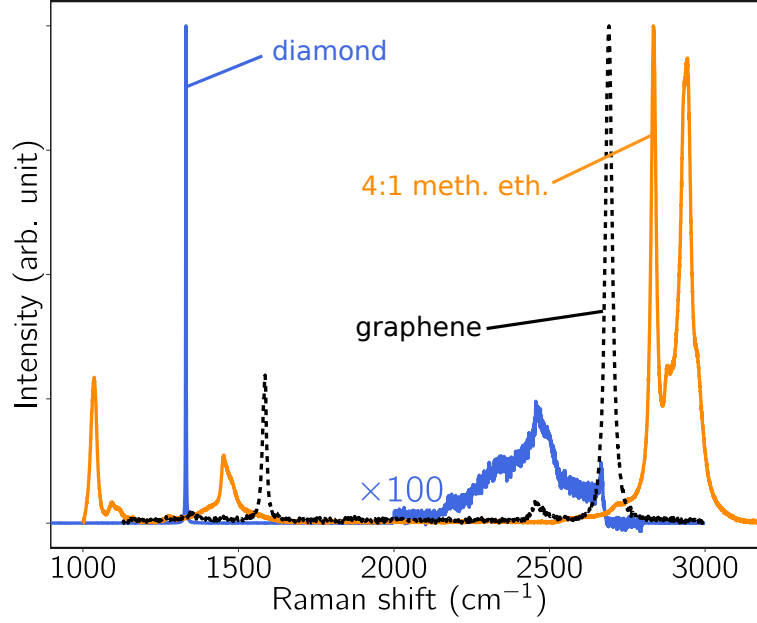


Figure 2.11 – Experimental Raman spectra of monolayer graphene (dashed black line), diamond (blue line) and 4:1 methanol-ethanol mixture (orange line). Please note that each spectrum is normalized to its most intense band, thus intensity comparison between the different spectra makes no sense.

between atoms.

One challenge is to keep exactly the same measurement position on the sample at any pressure. A technique that can be used is to avoid any XY displacement of the stage and to measure the ruby fluorescence by defocalisation of the excitation laser. However, high pressure experiments can last a few days long and it is difficult to avoid any displacement drift of the stage during such a long time. Furthermore, the sample contracts under pressure and the precise location of the Raman measurement at low pressure may thus slightly moves when pressure increases. In our case, we have drawn patterns of recognizables features around the sample on the microscope pictures, allowing to retrieve the reference position. However, measuring the sample exactly at the same position for every pressure was not possible in our work thus we measured the spectrum only in the same region of the sample (a few microns wide).

2.5 Conclusion

During this work, we have used exfoliated graphene samples as well as CVD-grown systems. These samples can be transferred by using the PMMA-assisted method (for CVD samples) or by using the PDMS-stamping set-up that we have implemented at iLM. We have seen that *in situ* Raman spectroscopy on graphene at high pressure implies various issues, essentially arising from (i) the limited size of the sample for DAC loading, (ii) the presence of a diamond anvil on the excitation beam optical path, and (iii) the oftenly complex high pressure phase diagram of the PTM. In the next chapters, (i) is addressed in details for the use of suspended samples since it has demanded numerous substrate developments. Concerning (ii), a very promising perspective

is the use of another material than diamond for the anvil (such as sapphire or SiC). This should bring new insight on graphene high pressure physics in the near future. In our work, we have also addressed (iii) in details, through our study on the isotopically labeled bilayer graphene (presented in the next chapter).

2.6 Summary

In this chapter, we have presented our samples and the principal experimental techniques used during this work.

- Graphene and thin graphite samples were produced by mechanical exfoliation and chemical vapour deposition (CVD).

- These samples can be transferred from their synthesis location to suitable supports for later high pressure runs. Specific substrates designs depend on the experiment goals and will be shown specifically in the next chapters.

- The diamond anvil cell (DAC) is used to compress graphene at GPa-range pressures, immersed in a pressure transmitting medium (PTM). The principal experimental constraint is the small size required for the samples and their substrates.

- The Raman spectrometer mounted during this work is used to measure the graphene optical phonons response during the high pressure sollicitation. *In-situ* Raman spectroscopy at high pressure implies several limitations, such as the overlap of the Raman signal from the diamond anvil and from the PTM with the signatures from the sample.

- Various pressure transmitting media can be used. They can solidify and present phases transitions at high pressure. In that case, the sample is not compressed in strictly hydrostatic conditions anymore.

3

Isotopically Labeled Bilayer Graphene at High Pressure

Contents:

3.1	Introduction	70
3.2	Isotopically Labeled Bilayer Sample and its Loading Procedure	72
3.2.1	Description of the Isotopically Labeled Sample and its Raman Response	72
3.2.2	Characterization and Loading of the Sample in the Pressure Cell	73
3.2.3	SiO ₂ /Si Substrates in High Pressure Experiments	75
3.3	Raman Signature Evolution at High Pressure in Various Media	75
3.4	Discussion of the Results	83
3.4.1	Solid Pressure Transmitting Medium Case: Strain Mismatch Effect	83
3.4.2	Liquid Alcohol Pressure Transmitting Medium Case: Piezo-doping Mismatch Effect	87
3.5	Conclusion	90
3.6	Summary	91

3.1 Introduction

In this chapter, we present our original high pressure study on the isotopically labeled bilayer graphene system. The sample consists of a bilayer structure which is the stacking of two graphene layers made of different carbon isotopes (the bottom layer contains the natural occurrence of carbon, *i.e.* mostly ^{12}C , while the top layer is made of ^{13}C). Figure 3.1 shows a schematic of the bilayer system on its substrate loaded in a DAC, representing the situation of our experiments.

At the heart of our work is the comprehension of the physical processes involved during graphene high pressure compression. The isotope labeling is thus of key interest, since it allows for separating the Raman signal of the top graphene layer (in contact with its environment) from the one of the bottom graphene layer in contact with the substrate and supposedly screened from the interaction with the environment. Indeed, according to the nucleus mass dependance of phonons energy, all the Raman bands of the ^{13}C top layer are red-shifted following

$$\omega^{top} = \sqrt{\frac{12}{13}} \omega^{bot} \quad (3.1)$$

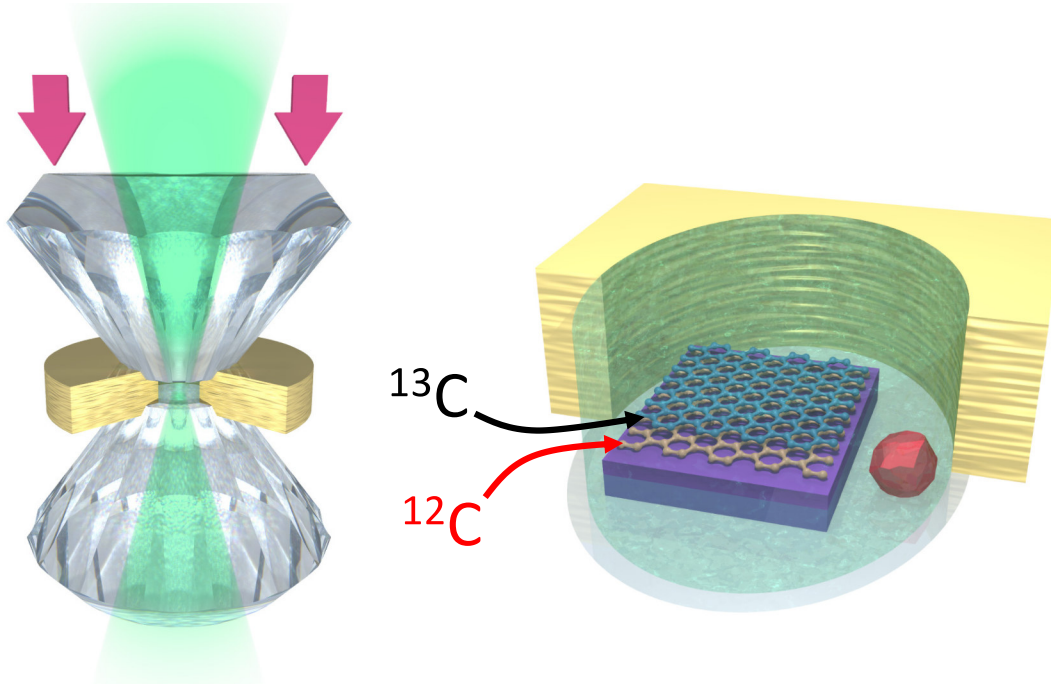


Figure 3.1 – Experimental set-up used in the Raman experiments showing the sample loaded in the diamond anvil cell. The applied force (red arrows) on the diamonds compresses the experimental cavity delimited by the two diamonds and a metallic gasket – opened to show the sample volume. The laser light illuminates the sample and the Raman signal is collected in backscattering mode. The sample volume is shown at the right and consists of a supported isotopically labeled BLG immersed in a PTM. A ruby chip (red crystal) is used for *in situ* pressure calibration.

If the role of the substrate has already been addressed for supported graphene compression [24, 25], the role of the environment – *i.e.* the PTM – is still subject to discussions. The study presented here is an attempt to elucidate the following questions:

- Can we quantify the mechanical role of the PTM in high pressure graphene compression? Since numerous PTMs solidifies at high pressure, it can transfer strain to the graphene as a substrate does: this was already observed in ref. [25] using conventional bilayer graphene at high pressure. Does PTM discontinuous phase transitions reflects in the mechanical strain of the bilayer system? In the literature, at our knowledge, there is only one study of the isotopically labeled bilayer graphene in compression, in which the system is compressed between two sapphires without any PTM [161].
- Is there any graphene doping effect using the 4:1 methanol-ethanol mixture as PTM, *i.e.* is there any charge transfer between this PTM molecules and graphene? If it exists, how such effect depends on pressure? There is controversial informations in the litterature: Nicolle *et al.* [22] have reported a doping effect based on the higher G-band pressure slope observed with this particular PTM in regard to argon, while Filintoglou *et al.* [23], using a metallic substrate, did not found any doping effect.
- Can chemical bonds form between graphene and the PTM and between the two graphene sheets? Several groups have reported a pressure induced re-hybridization of multilayer graphene into an sp^3 -hybridized structure where dangling bonds are closed by OH- groups from the environment [10–12]. Do we observe any signature of such transition by Raman spectroscopy in our experiments?
- Is it possible to generate, or observe any asymmetries between the two layers in terms of strain or doping, *i.e.* different strain or charge carrier concentration in each layer? Would a possible doping be limited to the top layer in direct contact with the PTM? Such effects have never been observed in high pressure experiments. However, strain and doping asymmetries have been observed as function of the system temperature [162]. Interestingly, in a study on double wall carbon nanotubes (DWCNTs) at high pressure, a splitting of the Raman G-band was observed corresponding to different stresses in the inner and the outer nanotube [163]. In another work on doped DWCNTs, it was shown that only the outer tube G-band shifted due to the non-adiabatic doping contribution, while the inner tube G-bands shift was only due to lattice contraction [164].

Beyond these fundamental consideration, answering these questions may have interesting outcomes from the technological point of view. The observed effects offer new opportunities for the development of an *asymmetric straintronics* able to modulate opto-electronic properties taking advantage of induced asymmetries between 2D-system layers. In addition, the observed effects can bring interesting elements to better understand and engineer graphene-based composite materials.

In this chapter, we show that a strain asymmetry (or mismatch) can be induced between the two layers at high pressure when using a solid PTM. In the case of 4:1 methanol-ethanol, we have identified an asymmetrical piezo-doping effect. These observations comfort isotopic bilayer graphene as a benchmark system for the study of asymmetric effects in devices or composite surfaces.

The organization of the chapter is as follows. First, the sample properties, its ambient pressure

Raman spectrum and its preparation techniques are presented. Then, high pressure results using nitrogen, argon and 4:1 methanol-ethanol PTM are shown. The discussion of the results follows in a dedicated section. By convention, and for convenience, all strain quantities ε introduced in the chapter are considered *positive* for compression.

3.2 Isotopically Labeled Bilayer Sample and its Loading Procedure

3.2.1 Description of the Isotopically Labeled Sample and its Raman Response

As mentioned in chapter 2, the isotopically labeled graphene system was produced by our collaborators from the group of M. Kalbáč at the Heyrovský Institute of Physical Chemistry in Praha, Czech Republic. Two independent CVD growths on copper, using either $^{12}\text{CH}_4$ or $^{13}\text{CH}_4$ as precursors were performed to prepare the two graphene layers separately. The two layers were transferred (using the PMMA-assisted technique) successively on a 50 μm thin SiO_2/Si wafer, the ^{12}C layer being the bottom layer (in contact with the substrate), and the ^{13}C the top layer deposited above (see the sketch of the sample in the DAC, figure 3.1). Details on the synthesis can be found in ref. [121].

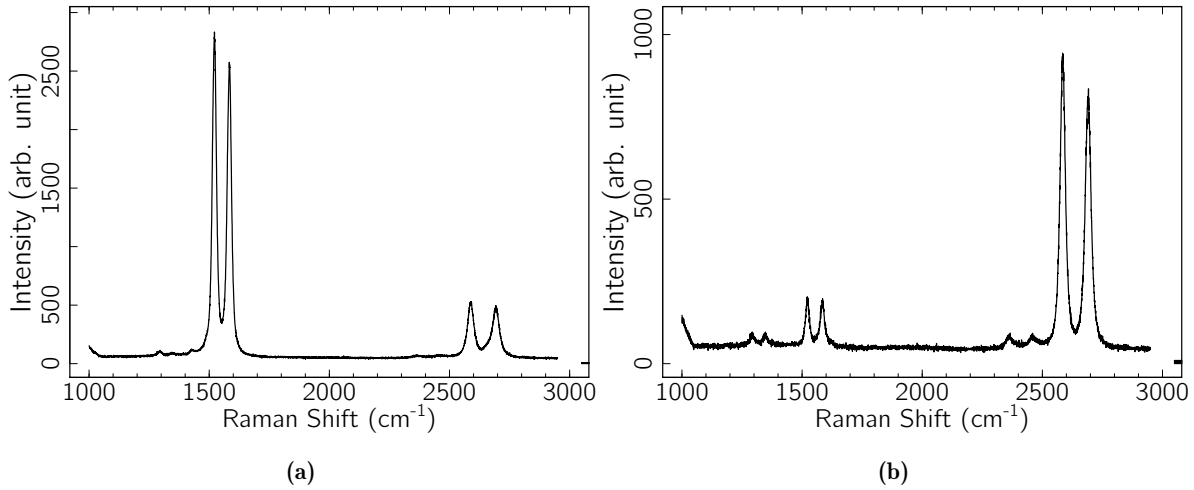


Figure 3.2 – Two representatives Raman spectra of the isotopically labeled bilayer graphene sample at ambient pressure, using a 532 nm excitation wavelength. (a) and (b) are obtained at two different locations of the sample on the wafer.

Typical Raman spectra obtained in two different regions of the sample are shown in figure 3.2(a) and (b). Two G-bands and 2D-bands are clearly resolved thanks to the isotopic substitution, as well as very weak D-bands indicating low concentrations of structural defects in the graphene sheets [73]. The ^{12}C bottom layer G-band is observed at $\omega_G^{\text{bot}} \simeq 1582 \text{ cm}^{-1}$, and the ^{13}C top layer G-band at $\omega_G^{\text{top}} = \sqrt{12/13} \times \omega_G^{\text{bot}} \simeq 1520 \text{ cm}^{-1}$ at ambient pressure. The observation of two separated 2D-bands (at $\omega_{2D}^{\text{bot}} \simeq 2690 \text{ cm}^{-1}$ and $\omega_{2D}^{\text{top}} \simeq 2584 \text{ cm}^{-1}$) indicates that our sample presents turbostratic stacking: in the case of Bernal (AB) stacking, a unique eight-component 2D-band should be observed resulting from four double-resonant Raman contributions for each

isotope [165]. Turbostratic stacking is indeed expected in our sample: CVD graphene is usually polycrystalline since during the growth, grains growing from several nucleation points will finally meet, forming grain boundaries. Consequently, the final two-layer stacking presents different regions with random stacking angles.

The spectacular difference in 2D and G-bands intensity ratios between figures 3.2(a) and (b) originates from different twist angles in the two probed regions. Indeed, the 2D-band intensity, position and FWHM depends on the moiré angle between the layers [76], while the G-band positions and FWHM are unaffected [76]. Contrariwise, the G-band intensities strongly depend on the twist angle, especially when the angle is close to its critical resonant value for a given excitation wavelength [76, 166]. In our study, we cannot control the twist angle of the sample which will be studied at high pressure. The determination of that angle would require various Raman excitation wavelengths [76], or scanning tunneling microscopy characterization [65] before the pressure cycle, the latter being not possible when the substrate is placed on the diamond anvil. Despite this limitation, we have always studied turbostratic samples, since the 2D-bands are separated and easier to monitor [165]. The deconvolution of spectra and interpretation of results are thus facilitated compared to the Bernal case.

For this study, we have mostly used the LabRAM HR Evolution Raman set-up available at iLM. Its optical set-up is very close to our design described in chapter 2. The laser wavelength is 532 nm and the system is equipped with super-notch filters, as well as an adjustable confocal hole. On this Raman spectrometer, the spectral accuracy and resolution are both about 1 cm^{-1} . In the specific case of measurements using argon as PTM, experimental data have been collected by our collaborator F. Balima at the ENS Physics lab in Lyon, using another LabRAM spectrometer equipped with a 514.5 nm argon laser as Raman excitation.

3.2.2 Characterization and Loading of the Sample in the Pressure Cell

The isotopically labeled graphene layers lays on a SiO_2/Si substrate. The use of such substrate is beneficial at every step of our protocol described hereafter: from the identification of a interesting zone with graphene on the large substrate, to the improved *in situ* Raman signal-to-noise ratio when running the high pressure experiment.

The technique to load the sample in the DAC has been previously developped by our research team and used in numerous *in situ* Raman experiments on supported 2D-materials [22, 24, 25, 109, 167, 168]. We may note that this method is by principle applicable to any type of samples (exfoliated or CVD grown) as long as it is supported on a substrate.

Firstly, the whole SiO_2/Si substrate (centimeter wide, a section of the wafer) is inspected by microscopy and microRaman spectroscopy. The goal is to locate interesting positions where the bilayer system is present and with low defect concentration. This can be identified by the observation of the Raman spectrum : weak or inexistant D-bands are seeked for (see figure 3.2 for typical examples). Pictures with different magnifications as well as the corresponding Raman spectra measured are kept as reference, and very useful to retrieve an interesting zone for the

high pressure run.

When such zone is identified, the main challenge is to isolate it as a piece of sample (graphene plus substrate) adequately sized to be loaded in the DAC. This corresponds to pieces smaller than 100 μm in every direction¹. This is performed by mechanical cleavage of the substrate immersed in an ethanol bath, while carefully looking at the operation under binocular (10x magnification). The force is exerted by hand on a side of the substrate, using a very thin razor blade: a crack in the silicon substrate is then created along a favourable crystallographic direction. The alcohol bath prevents loss of samples during the cleavage (in air, pieces of samples may be projected because of the shock). It also helps to keep samples clean and to avoid contaminants which may produce fluorescence during the *in situ* measurements. By a few successive chops, a small piece with the required dimensions can be isolated. It is then handled and deposited on the bottom diamond anvil by hand, using a sharp tungstene tip of a few microns (the picture in figure 3.3 shows one of our sample deposited on the diamond anvil).

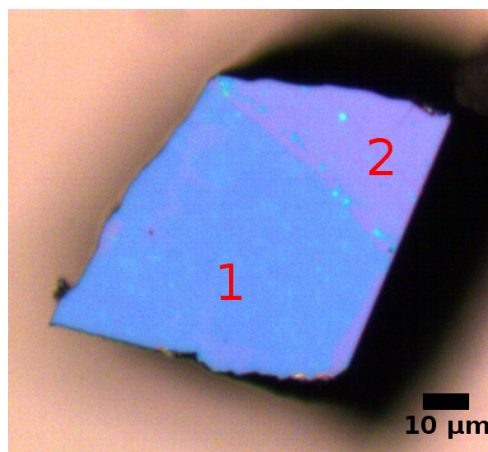


Figure 3.3 – Micrograph of a piece of substrate deposited at the center of the bottom diamond, illustrating the typical size of a sample ready for high pressure compression. The zone marked 1 is where the isotopically labeled bilayer graphene sample lays. In the zone labeled 2, no sample is present on the substrate. These two zones are clearly identifiable thanks to the substrate’s contrast enhancement.

The sample adheres to the tip thanks to electrostatic forces. Such sample handling using a very sharp tungstene tip is common in high pressure technology [169]. However, the small substrate needs to be deposited with suitable orientation (sample upwards for later Raman measurements). This requires to carefully manipulate the sample with the tip when it is already on the culet to get it well oriented. This sample loading technique is inexpensive and does not require elaborate machinery. However, the success rate is not 100% and training is needed, since the sample can be lost or damaged easily. It is worth mentioning that this method is easier when the sample consists of CVD graphene for which large exploitable areas can be found. When the sample is a small flake of exfoliated graphene, its precise isolation by successive chops of the substrate is very challenging. Another method, involving laser cutting of the substrate around the sample has been tested by J. Nicolle [167]. However, he reported that the cutting process creates pollution

¹Usual SiO_2/Si substrates are too thick to be load in the DAC: specific pre-polished SiO_2/Si substrates of 50 μm -thick were used.

over the sample (mostly silicon powder from the cut substrate, but also glue from the tape holder of the laser cutting bench he used) [167].

When the sample is correctly deposited on the DAC, the integrity of the sample is checked by Raman spectroscopy and optical inspection, to verify the absence of damage during the loading process. Ruby chips are then added and the PTM loaded following the protocol detailed precendently in chapter 2. The high pressure measurements can start. After the pressure run, measurements are taken again to compare the cycled sample with the initial one and obtain information on the reversibility of the compression cycle (corresponding spectra are shown in appendix B).

3.2.3 SiO₂/Si Substrates in High Pressure Experiments

Beyond their interesting benefits, SiO₂/Si substrates presents some drawbacks in high pressure experiments. We have repeatedly observed fractures and delaminations of the oxyde layer during compression, starting at pressures close to 4 GPa (see figure 3.4). Our observations agree with those reported by J. Nicolle during his PhD thesis: he observed a delamination process close to 4 GPa [167]. This effect can be understood considering the bulk modulus difference between the silicon wafer and its surface oxyde, leading to high stress concentration at the interface that eventually relax by fragile fracture of the oxyde layer when pressure increases. Interestingly, this delamination process was observed only when the 4:1 methanol-ethanol mixture was used as PTM.

Despite this substrate delamination problem, we have usually been able to follow the graphene Raman signatures beyond 4 GPa. If the oxyde layer was broken in some regions, as long as the measurement zone was stable, we have continued the *in situ* measurements. Care was taken during data analysis, remembering that some anomalies in the Raman data evolution could be linked to this phenomenon.

Another limitation when using SiO₂/Si substrates is the well-known crystalline phase transition of silicon at 11.2 GPa [170]. It transforms to the β – Sn phase, reducing its volume of 22%. Such transition has dramatic effects on the integrity of the substrate, and probably on the graphene laying on. The pressure of ~ 11.2 GPa thus constitutes an *a priori* experimental limit using silicon based substrate. In our studies, we did not exceed this pressure.

3.3 Raman Signature Evolution at High Pressure in Various Media

Figures 3.5, 3.6 and 3.7 show the Raman spectra of the isotopically labeled-BLG at different pressures using nitrogen, argon and the 4:1 methanol-ethanol mixture as PTM, respectively. In the case of argon and nitrogen PTM, the G-bands and 2D-bands have been measured at high pressures and are shown in left and right panels of figures 3.5 and 3.6. In the alcohol mixture case, only the G-bands could be followed at high pressure, and are shown in figure 3.7 for

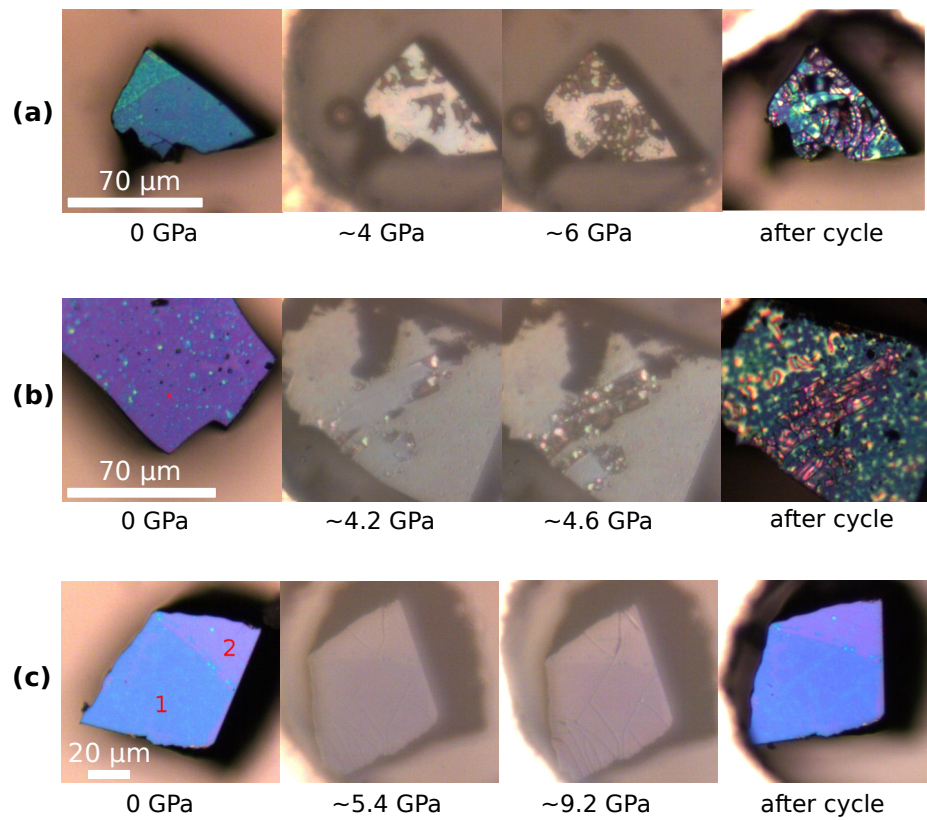


Figure 3.4 – (a-b) Micrographs of two different samples of the isotopically labeled bilayer graphene deposited on a SiO_2/Si substrate at various pressures using 4:1 methanol-ethanol as PTM. (c) Micrograph of another sample at various pressures, using nitrogen as PTM.

three different experiments done with that PTM. Indeed, the 2D-bands attenuated to become undetectable at very low pressure in all our attempts with the alcohol PTM: this effect is very clear in figure 3.8, showing the experimental spectra obtained with the same sample loaded in a sapphire anvil cell, using 4:1 methanol-ethanol and nitrogen successively². We will therefore focus the analysis primarily on the G-bands evolution with pressure.

All peaks blue-shift with increasing pressure, and their positions and width could be extracted by fitting either with Lorentzian or Voigt functions. The fitting components and their sum are shown in figures 3.5, 3.6 and 3.7, along with the raw Raman spectra. Voigt functions (convolution of a Lorentzian with a Gaussian lineshape) were found to better represent the data in the case of nitrogen and argon PTM. Indeed, these two PTM solidify at relatively low pressures and this introduces a spatial inhomogeneity in the system, that can be taken into account by a Gaussian distribution of the Raman response. However, we verified that the results were not significantly affected by this choice : deviations from pure Lorentzian fits are weak.

In order to analyze the pressure evolution of the Raman signatures, we define the pressure induced shift of the G-band with respect to its ambient pressure value, $\Delta\omega_G(P) = \omega_G(P) - \omega_G(0)$, and the difference in G-band positions between the two layers, $\chi(P) = \omega_G^{bot}(P) - \omega_G^{top}(P)$.

In figure 3.9(a) are gathered $\Delta\omega_G$ as function of pressure for the two layers in the three used PTMs. In graphene, the G-band position is sensitive to the strain in the system, but also to electron concentration changes (electron or hole doping) through electron-phonon coupling [38]. As explained in chapter 1, when supported graphene is compressed at high pressure in a DAC, the sample is subjected to a compressive biaxial strain due to the volume reduction of the substrate through adhesion, *i.e.* $\varepsilon = \varepsilon_l = \varepsilon_t$ (no shear strain) [24]. The shift of the optical G-band phonons as function of the biaxial strain ε reduces to

$$\Delta\omega_G = 2\gamma_G\omega_G(0)\varepsilon \quad (3.2)$$

where $\Delta\omega_G$ is the strain-induced shift of the G-band, and γ_G the Grüneisen parameter of the G mode [28]. Through equation 3.2, corresponding to a pure mechanical response, the Raman shift evolution is directly proportional to the sample's strain. As mentioned in chapter 1, it also depends on the isotopic weight through the $\omega_G(0)$ term which is different for each isotope.

The black solid line in figure 3.9(a) represents the expected G-band shift for the bottom layer in the ideal case of a total strain transfer from the silicon substrate. It is calculated using the high-pressure range of the silicon equation of state given in reference [171] and $\gamma_G = 1.8$ [24, 25, 49, 51]. Figure 3.9(a) shows that, in all cases, the data points are below this ideal adhesion line, meaning that the deformation of the substrate is not fully transmitted to the BLG: local buckling, wrinkling, and sliding of graphene manifest at local scales, resulting in an inhomogeneous strain field in the sample probed by the Raman laser which is of micrometer size

²Sapphire anvils were used in order to avoid the second order Raman peaks of diamond overlapping with the 2D-bands of the sample, and clearly observe its attenuation.

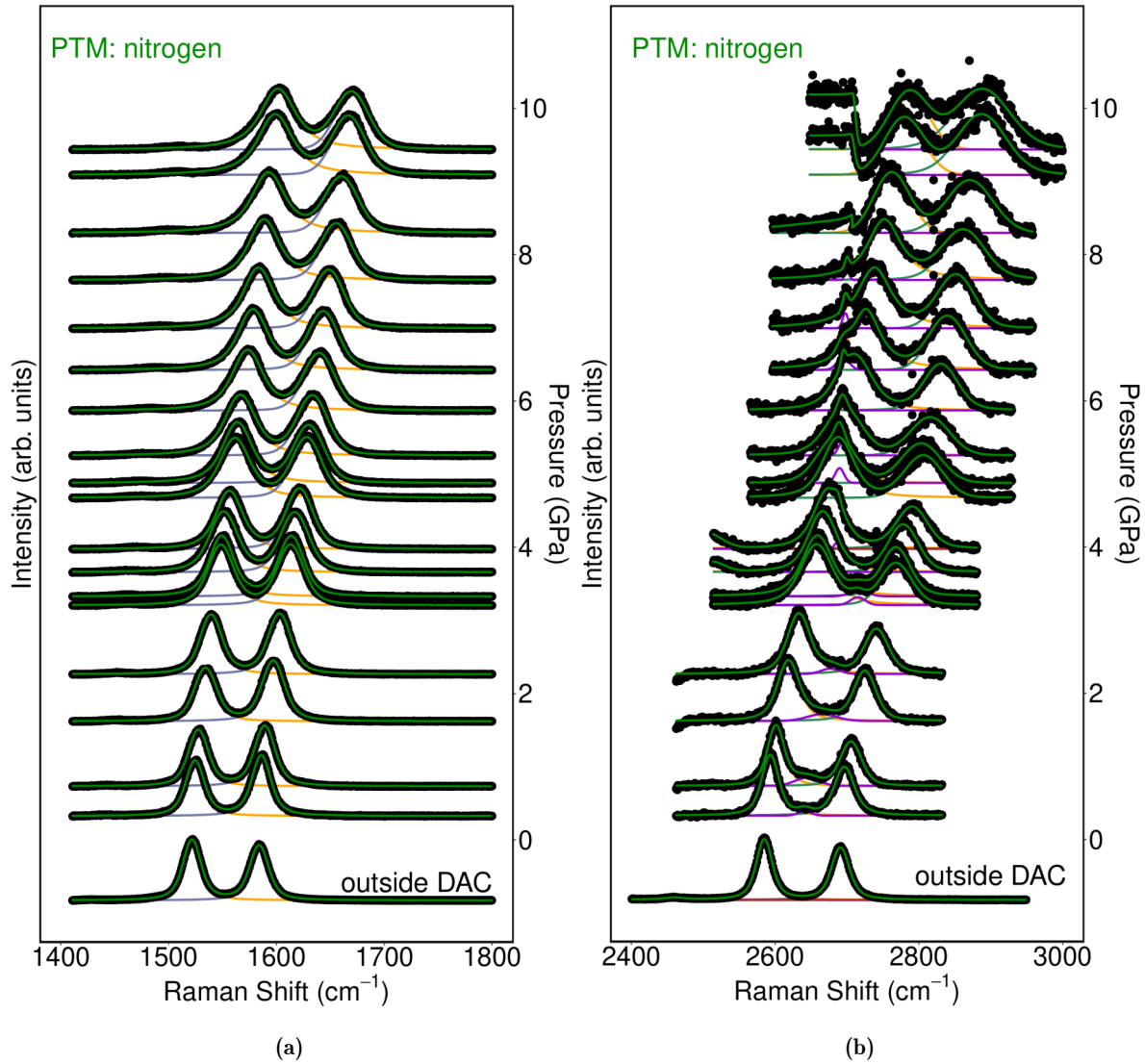


Figure 3.5 – Evolution of the Raman signatures as function of pressure using nitrogen PTM : (a) G-bands, (b) 2D-bands (black dots). The spectras are background corrected and normalized to the highest band, such as the baseline height corresponds to pressure (right axis). The spectrum located lower than the zero pressure position corresponds to the ambient pressure spectrum outside the DAC, downshifted for clarity. Each fitting components are represented with different colors along with the sum of all components in green. The small peak observed at high pressures around 2700 cm⁻¹ (overlapping the top layer's 2D-band) corresponds to the diamond anvil's second order Raman signal.

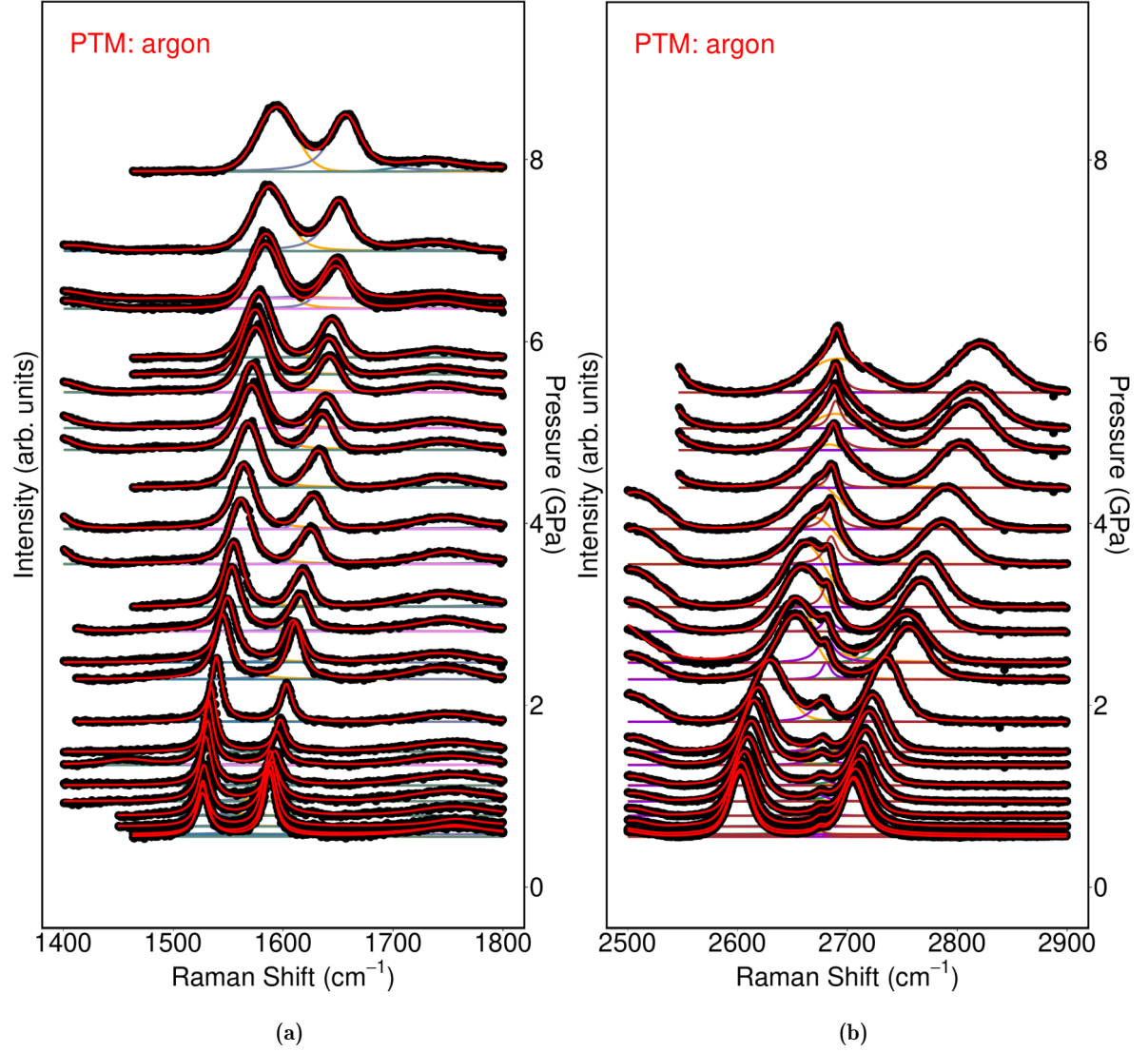


Figure 3.6 – Evolution of the Raman signatures as function of pressure using argon PTM : (a) G-bands, (b) 2D-bands (black dots). The spectras are background corrected and normalized to the highest band, such as the baseline height corresponds to pressure (right axis). Each fitting components are represented with different colors along with the sum of all components in red. The small peak osberved at high pressures around 2700 cm^{-1} (overlapping the top layer's 2D-band) corresponds to the diamond anvil's second order Raman signal.

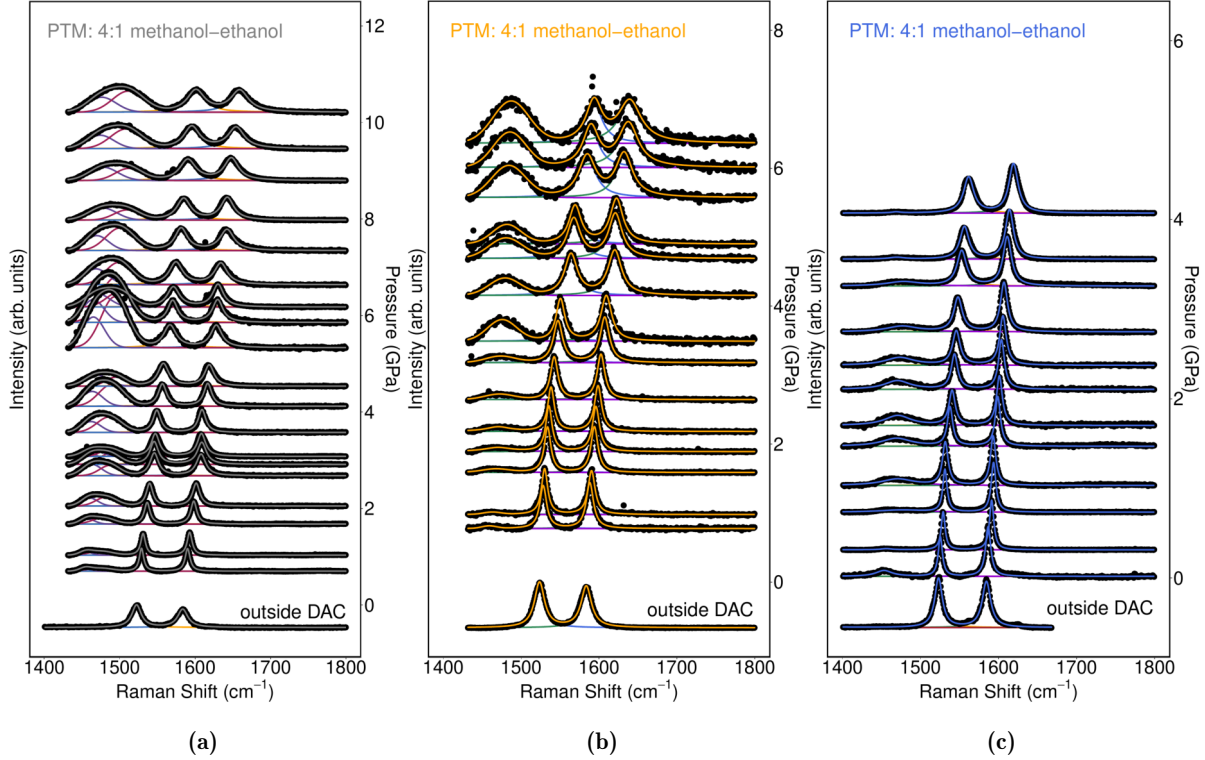


Figure 3.7 – Evolution of the Raman signatures as function of pressure using 4:1 methanol ethanol PTM (3 different experiments). Panel (a) corresponds to the black dots on figures in the main text, panel (b) to the orange dots, and panel (c) to the blue dots. The spectras are background corrected and normalized to the highest band, such as the baseline height corresponds to pressure (right axis). The spectrum located lower than the zero pressure position correspond to the ambient pressure spectrum (0 GPa), downshifted for clarity. Each fitting components are represented with different colors along with the sum of all components. The large peak oftenly observed around 1450 cm^{-1} corresponds to the 4:1 methanol:ethanol PTM Raman signals.

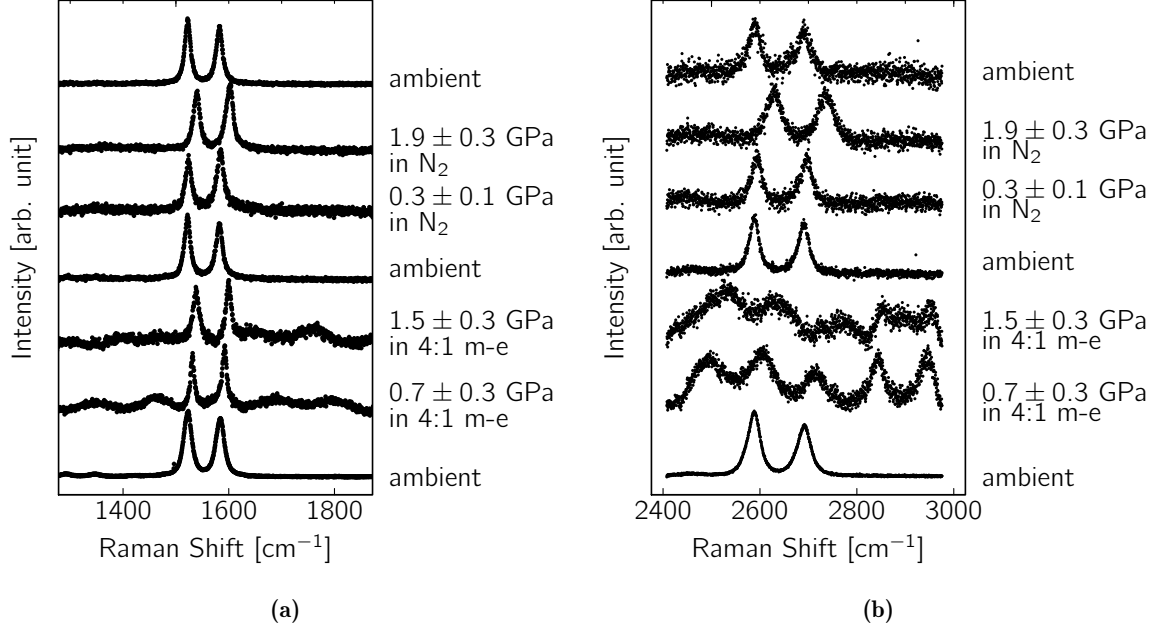


Figure 3.8 – Raman spectrum evolution of the isotopically labeled bilayer graphene at high pressure in the sapphire anvil cell loaded with alcohol and nitrogen PTMs successively. Panel (a) : G-bands, panel (b): 2D-bands. On panel (b), Raman signatures of the alcohol PTM are visible. All spectra are background corrected and normalized to the most intense band.

[24, 25]. This logically results into the G-band full width at half maximum (FWHM) increase with pressure (figure 3.9(b)). The black dashed line in figure 3.9(a) is the extrapolation of the low pressure G-band evolution for nitrogen and argon PTM in the liquid PTM pressure range. It is plotted considering a strain transfer efficiency of $\alpha_S \simeq 42\%$ from the substrate to graphene, calculated directly from fitting the liquid PTM-range data points for both layers. This projected evolution is also shown for comparison in the alcohol PTM case (figure 3.9(a)).

Figure 3.9(b) presents the pressure evolution of the G-bands FWHM for the different experiments. As mentioned, the G-band FWHM increases with pressure application for all PTMs, as expected for an increasing inhomogeneous strain field in the sample. However, for the alcohol PTM, there is a strong drop in the G-band FWHM at low pressure – roughly 5 cm^{-1} to 10 cm^{-1} depending on the experiment – that cannot be explained by a purely mechanical response.

Figure 3.9(c) shows the pressure evolution of the G-band shift difference between the two graphene layers *corrected* for the isotopic weight through the $\sqrt{13/12}$ term, such as

$$\Delta\chi^* = \Delta\omega_G^{bot} - \sqrt{13/12} \times \Delta\omega_G^{top} \quad (3.3)$$

The use of this corrected quantity is very useful since in the hypothesis where the BLG response is purely mechanical, we have directly $\Delta\chi^*(P) \propto (\varepsilon^{bot}(P) - \varepsilon^{top}(P))$. Interestingly, the evolution of $\Delta\chi^*(P)$ in figure 3.9(c) shows two opposite behaviors depending on the PTM nature: for the argon and nitrogen cases, the bottom layer has its G-band more blue-shifted than the top layer ($\Delta\chi^* > 0$), while we observe the opposite trend in the case of alcohol PTM ($\Delta\chi^* < 0$) in the three experiments performed.

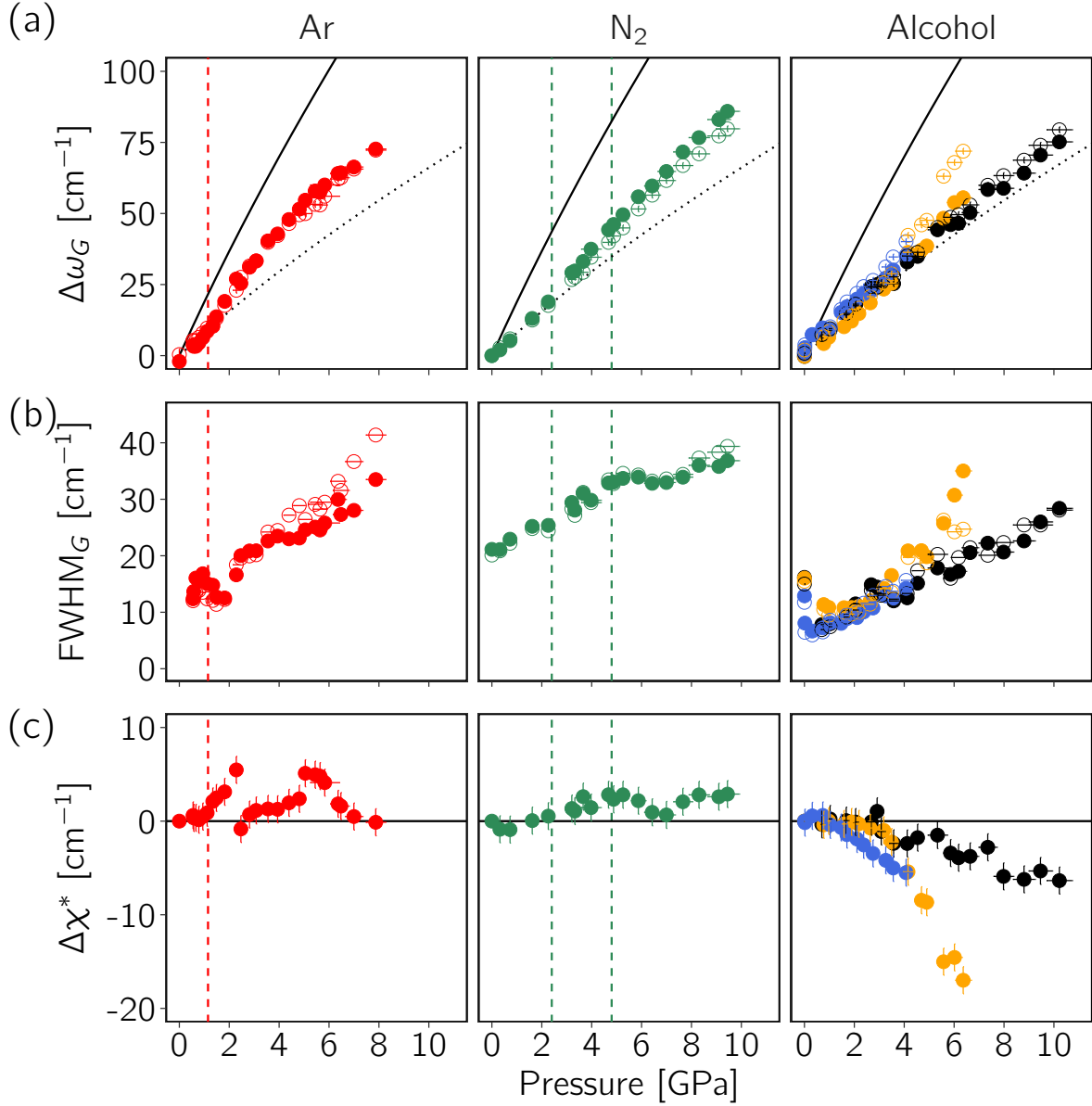


Figure 3.9 – Pressure evolution of the G-band shifts (a) and FWHM (b), for the top (empty symbols) and bottom (full symbols) graphene layers in argon, nitrogen and in a 4:1 methanol:ethanol mixture (alcohol). Panel (c) shows the corrected G-band shift difference between the graphene bottom and top layers, $\Delta\chi^*$. When using alcohol PTM (right column), three different experiments are presented (colors corresponds to the one used on figure 3.7 for the fit function). In panel (a), the expected ideal evolution in the case of perfect adhesion of the sample on substrate is plotted for the bottom layer as a black solid line. The black dashed line in (a) corresponds to the extrapolation of the low pressure data points for nitrogen and argon (before solidification), also shown for comparison in the alcohol case. PTM solidification and crystalline phase transitions pressures are indicated by vertical lines at 1.15 GPa for argon, and 2.4 GPa and 4.8 GPa for nitrogen [150–152]. Vertical error bars are given by the fit standard error when larger than spectral resolution. Pressure error bars are estimated at 5 % of the measured pressure.

3.4 Discussion of the Results

The discussion is splitted between experiments using (i) solidifying PTMs, *i.e.* argon and nitrogen, and (ii) alcohol PTM, liquid in all the studied pressure domain, discussed in the second instance. In (i), we will see that the bilayer system response can be understood through a purely mechanical effect, while in the case of alcohol (ii), a "piezo-doping" mechanism is observed. This will be justified in the corresponding sections.

3.4.1 Solid Pressure Transmitting Medium Case: Strain Mismatch Effect

A shift of the G-band can arise from (i) elastic strain, and/or (ii) a modification of the charge carrier concentration in the graphene layer. As detailed in section 1.3.3.3, Lee's correlation diagram is commonly used to deconvolute strain and doping effects [102, 103]. Indeed, the graphene 2D-band is less sensitive to doping than the G-band (affected by non-adiabatic effects), whilst in the case of strain, the 2D-band linearly shifts with its own Grüneisen parameter. The correlation diagram is plotted for the two graphene layers and the two PTM in figure 3.10. The dashed lines are the slopes obtained by linear fitting of the data in each cases. For nitrogen PTM we obtain values of $\partial\omega_{2D}/\partial\omega_G = 2.47 \pm 0.03$ for the top layer and 2.33 ± 0.03 for the bottom layer. In the argon PTM case, we obtain $\partial\omega_{2D}/\partial\omega_G = 2.31 \pm 0.09$ and 2.14 ± 0.05 for the top and the bottom layer, respectively. All these values are compatible with the reported value for pure biaxial strain, $\partial\omega_{2D}/\partial\omega_G = 2.2 \pm 0.2$ [38]. As a consequence, the data for nitrogen and argon PTM can safely be interpreted as a purely mechanical response to the applied pressure.

The black dashed line in figure 3.9.(a) corresponds to the extrapolation of the biaxial strain transmitted by the sole substrate to the bottom layer and considering the α_S coefficient, without any other contributions. In figure 3.9(a), after PTM solidification (indicated by vertical lines in figure 3.9), the data-points evolution is higher than the dashed line extrapolation, which is the signature of an additional stress from the solid PTM. Nevertheless, even after PTM solidification, all data-points are relatively close to this dashed line, which indicates that the substrate-induced biaxial compression is the dominant effect in the observed Raman response. These findings are in very good agreement with similar experiments with argon and water PTM performed on exfoliated non-isotopically labeled bilayer graphene, where a similar additionnal stress contribution is clearly observed [25].

It is also clear in Fig. 3.9.(c) that in the solid PTM domain, $\Delta\chi^*(P) > 0$ for argon and nitrogen, *i.e.* the solidification of the PTM leads to a differentiation of the layers Raman response. Since $\Delta\chi^*(P) > 0$, and the Raman response is purely mechanical, we can state that $\varepsilon^{bot} > \varepsilon^{top}$. It is worth quantifying the strain difference between the two layers. This calculation is straightforward since the strain difference is proportional to $\Delta\chi^*$ through the relation $\varepsilon^{bot} - \varepsilon^{top} = \Delta\chi^*(P) / [2\gamma_G\omega_G^{bot}(P=0)]$. The pressure evolution of the strain difference is presented in figure 3.12. At its maximum, this difference is $\varepsilon^{bot} - \varepsilon^{top} \simeq 0.1\%$ in the argon PTM case, and $\simeq 0.05\%$ in the case of nitrogen PTM. Since the pressure induced strain is different in each layer, we have

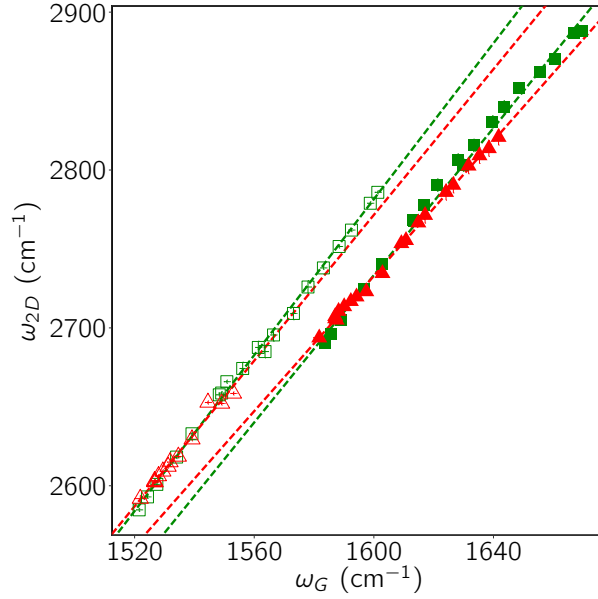


Figure 3.10 – Lee’s correlation diagram showing $\omega_{2D}(P)$ as function of $\omega_G(P)$ evolving with pressure for the two layers (same color convention as is 3.9, with filled symbols for the bottom layer and empty symbols for the top layer), in the case of argon PTM (red, triangles) and nitrogen PTM (green, squares). Dotted lines corresponds to linear fits of the dataset, see text for slopes values. In the argon PTM top layer case, higher pressure data points are not shown since the deconvolution of its Raman 2D-band with respect to the superimposed diamond signal was difficult and innacurate (it is very clear in figure 3.6).

denoted this observation as a ”strain mismatch” between the layers.

The observation that the bottom layer is the most strained is puzzling. Indeed, the solid PTM is very soft in regards to the silicon substrate and is expected to transfer a very high compressive biaxial strain to the top layer (see figure 3.11 showing the compressibilities of solid nitrogen, argon, and the silicon substrate for comparison). We then conclude that the strain transfer from the solid PTM to graphene is much weaker than from the substrate. We have developped a simple mechanical model, which despite its crudeness can describe this mechanical effect and even fix an upper limit for the strain transfer from the PTM to the sample. As introduced by Bousige *et al.* in ref. [24] and explained in the first chapter of this work, if we consider a supported monolayer graphene sample at high pressure, its strain ε can be described phenomenologically as $\varepsilon = \alpha_S \varepsilon_S$ where ε_S is the substrate surface biaxial strain and α_S the strain transfer coefficient between the substrate and the graphene laying on ($0 < \alpha_S < 1$). To describe our isotopically labeled bilayer sample at high pressure, we introduce the following equations

$$\varepsilon^{top} = \alpha_m \varepsilon_m + \alpha_{gg} \alpha_S \varepsilon_S \quad (3.4)$$

$$\varepsilon^{bot} = \alpha_S \varepsilon_S + \alpha_{gg} \alpha_m \varepsilon_m \quad (3.5)$$

where ε^{top} and ε^{bot} are the biaxial strain of the top and bottom layers, respectively. The quantities α_m and α_S are the strain transfer coefficient from the PTM to the top layer, and from the substrate to the bottom layer, respectively. These two quantities are considered constant with pressure in our model. The biaxial compressive strain of the substrate ε_S and of the medium

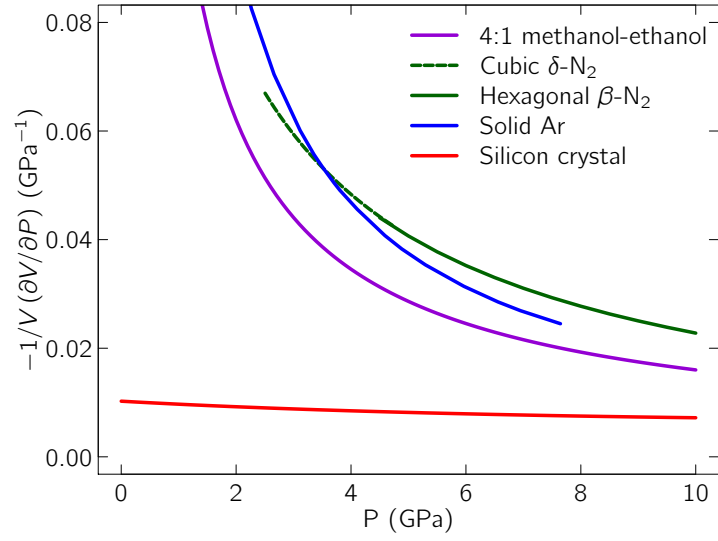


Figure 3.11 – Compressibilities of the silicon substrate [171] and of various PTM used during this work. For PTMs, the curves are Murnaghan equations of state [172] fitted on experimental data given in ref. [150] for argon, and in refs. [151, 173] for nitrogen. In the case of 4:1 methanol-ethanol, it corresponds to the Tait equation of state given in ref. [174].

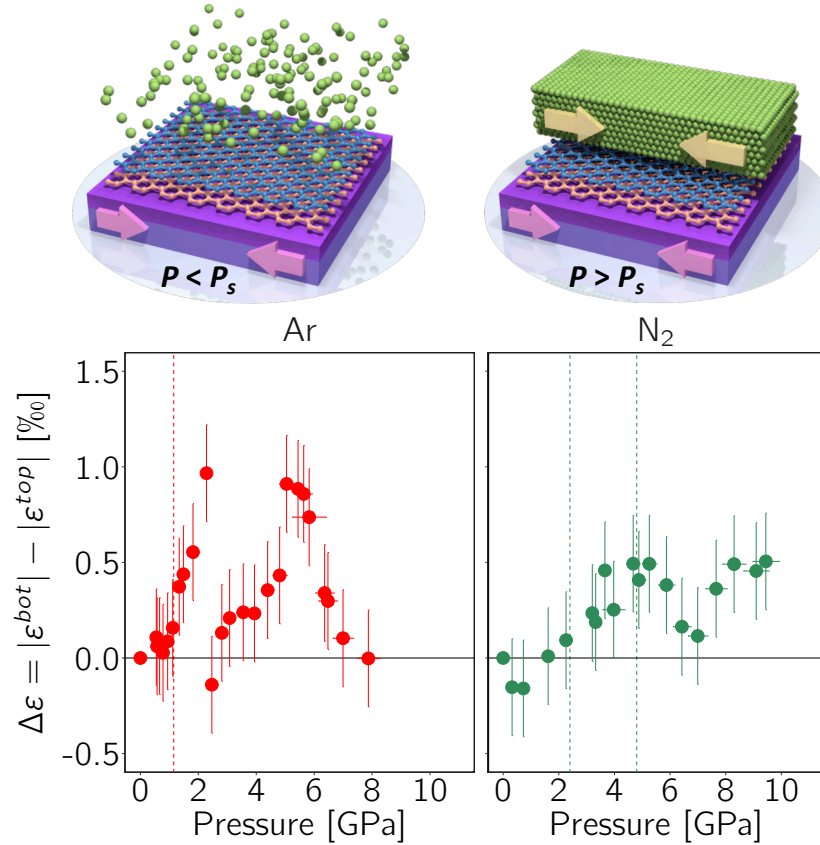


Figure 3.12 – Strain difference $\varepsilon^{bot} - \varepsilon^{top}$ between the two graphene layers as function of pressure for argon and nitrogen as PTM. Values are given in ‰. On top are shown schematically the two situations of the sample when the PTM is liquid ($P < P_s$) and when it is solid ($P > P_s$). The solidification pressure, P_s , corresponds to the first vertical dashed lines in both graphs.

ε_m are derived from their high pressure equations of state (figure 3.11) assuming tridimensional isotropy. The coupling α_{gg} represent the strain transfer between the two layers. It is also considered as not varying with pressure in our description.

In equations (3.4) and (3.5), it is clear that the strain in each layer is splitted in two contributions, transmitted from (i) the environment in direct contact with the layer, and (ii) through the other layer. Note that following equations (3.4) and (3.5), it appears that the maximum possible strain in both layers (when $\alpha_S = \alpha_m = \alpha_{gg} = 1$) is the sum of the strain of the PTM and of the substrate. This extreme scenario is intrinsically non-physical since if we consider a homogeneous compression such as $\varepsilon_S = \varepsilon_m = \varepsilon$, the expected strain in each layers is simply ε . Our model presented here would require refinements to take into account this aspect. In that goal, a better understanding of the physical significance of the strain transfer coefficients α would help. Finally, note that when $\alpha_{gg} = 0$, each layer follows mechanically its direct environment, corresponding to totally uncoupled layers.

In our experiments, aside from anomalies in the evolution of $\varepsilon^{bot} - \varepsilon^{top}$ which will be discussed later, we observe $\frac{\partial}{\partial P}(\varepsilon^{bot} - \varepsilon^{top}) > 0$, at least for pressures below 5 GPa. Considering this condition, we obtain

$$\frac{\alpha_S}{B_S} > \frac{\alpha_m}{B_m}(1 - \varepsilon_m) \quad (3.6)$$

where B_m and B_S are the bulk moduli of the PTM and the substrate, respectively (it is considered linearly varying with pressure for the PTM and constant – $B_S = 98$ GPa – for the bulk silicon substrate which is much more incrompressible). This leads to the following condition on α_m :

$$\alpha_m < \frac{\alpha_S B_m(P)}{B_S(1 - \varepsilon_m(P))} \simeq \kappa P \quad (3.7)$$

with $\kappa = 0.035 \text{ GPa}^{-1}$ using the equation of state of solid argon PTM and $\alpha_S = 0.42$ derived before. The quantity κP is therefore the maximum value of α_m possible such as $\frac{\partial}{\partial P}(\varepsilon^{bot} - \varepsilon^{top}) > 0$ at a given pressure P . It is worth insisting on the fact that α_m does not vary with pressure in our model for a given phase of the PTM. It is the κP maximum condition which depends on pressure through the PTM equation of state. Using solid nitrogen equations of state, we find $\kappa = 0.022 \text{ GPa}^{-1}$, less than for argon since solid nitrogen is more compressible beyond ~ 3 GPa (figure 3.11). Regarding the two PTMs beyond their solidification point, α_m takes a lower value than κP which leads to the observed $\Delta\chi^*(P)$ increase. The higher $\frac{\partial}{\partial P}(\varepsilon^{bot} - \varepsilon^{top})$ slope observed for argon is consistent with our description if we consider that α_m is identical for argon and nitrogen. However, we should mention here that quantitative differences between our two experiments may also arise from different mechanical coupling α_{gg} between the two graphene layers corresponding to different twist-angles of the samples. Moreover, as indicated in chapter 2, nitrogen is more hydrostatic than argon in the pressure range studied and this may also explain the slope difference.

We observe a number of accidents in the evolution of $\varepsilon^{bot} - \varepsilon^{top}$ and in the G-band FWHM (figures 3.12 and 3.9(b)) as pressure increases, anomalies that are not described through our rough model. These events can be associated with discontinuous transformations of the PTM. For nitrogen, it reflects its crystallization at ~ 2.4 GPa and the hexagonal to cubic phase transformation at

~ 4.8 [151]. For argon, we should underline its crystallization around 1.2 GPa, its hydrostatic limit at ~ 1.9 GPa [146] and its known recrystallizations at higher pressures [150, 154, 155]. These changes in the vicinity of the BLG surface should induce strain variations or relaxations in the bilayer system, leading to the observed anomalies. We can translate this effect in terms of discontinuous changes in ε_m , B_m , and more importantly in α_m , the latter being probably different for each phase or arrangement of PTM atoms on the top layer surface. Intuitively, for argon PTM at pressure near 5 GPa, the recrystallization of the PTM may induce an α_m discontinuous jump beyond κP , leading to the inversion of the $\varepsilon^{bot} - \varepsilon^{top}$ observed slope.

Consistently with our interpretations and our model, in the study published by E. Del Corro *et al.* on isotopically labeled BLG directly compressed between two sapphire crystals, $\varepsilon^{bot} - \varepsilon^{top}$ (observed as $\Delta\chi$) remained zero during the whole compression experiment [161], since $\varepsilon_S = \varepsilon_m$ in their case.

Measuring the strain difference between the two graphene layers of an isotopically labeled BLG system using Raman spectroscopy thus appears as an *extremely* sensitive probe of the mechanical characteristics of different PTMs. Our results are in quantitative agreement with the hydrostatic limits given in reference [146] (see also section 2.3.3.1 in chapter 2). Interestingly, these hydrostatic limits obtained *via* different experimental methods seem to remain valid even for an atomically thin sample. We underline the opportunity to use such type of isotopically labeled BLG samples for qualitative PTM hydrostaticity characterization.

3.4.2 Liquid Alcohol Pressure Transmitting Medium Case: Piezo-doping Mismatch Effect

In this section we discuss our results obtained using the 4:1 methanol:ethanol mixture as PTM. This mixture remains liquid up to its glass transition at 10.5 GPa [147], we may then expect similar results to the argon and nitrogen PTMs in their liquid phase (*i.e.* $\alpha_m = 0$, even if $\alpha_{gg} \neq 0$). It is not the case as for alcohol PTM: $\Delta\chi^*(P) < 0$ in the whole pressure range (figure 3.9(c)). The $\Delta\chi^*(P) < 0$ observation suggests that the BLG response to high-pressure application is not purely mechanical. As already mentionned, the 2D-bands signal could not be observed or only as a very weak signal at low pressures, not allowing its use for doping characterization through the ω_{2D} vs. ω_G correlation diagram.

Both n and p doping induce a blue-shift of the Raman G-band, a narrowing of its FWHM and the 2D-band intensity attenuation [38, 58, 73, 75, 92, 93, 95, 96]. These three effects are observed in our experiments using alcohol PTM, which is in favor of a pressure induced doping effect. Indeed, (i) the G-bands blue-shift on figure 3.9(a) is stronger than the dashed line extrapolation for liquid PTM when pressure increase, (ii) a G-band FWHM drop (equivalent for both layers) is observed at the beginning of the compression, and (iii) the 2D-bands signal disappeared at very low pressure.

Since $\Delta\omega_G$ increases with doping, $\Delta\chi^*(P)$ for the alcohol PTM probes the difference in charge carrier concentration between the two graphene layers. For all experiments, Fig. 3.9(c) shows

that $\Delta\chi^*(P) < 0$ with a monotonous decrease, meaning that the top layer is more doped than the bottom one, and that this difference increases with pressure. Such pressure-induced increase in the difference of charge concentration can be explained as follows: the graphene layer exposed to the alcohol PTM is the most susceptible to interact with it, and this interaction is increased by the reduction in PTM-graphene distance induced by pressure. Such asymmetrical doping at the layer scale has already been observed in gate induced doping experiments on twisted bilayer graphene immersed in an ion gel electrolyte [175]. In our case, we have called this effect "piezo-doping mismatch" since the charge carriers concentration increases with pressure and is asymmetrical between the two layers.

From the $\Delta\omega_G(P)$ evolution, it is possible to roughly evaluate the carrier concentration in each layer with alcohol PTM. We consider the black dashed line extrapolation on figure 3.9(a), corresponding to the partial adhesion on substrate observed in argon and nitrogen at liquid state, as the pure mechanical contribution to the G-bands shift $\Delta\omega_G^{mech}(P)$. The doping-induced Raman shift $\Delta\omega_G^{dop}(P) = \Delta\omega_G(P) - \Delta\omega_G^{mech}(P)$ can be translated in terms of charge carrier concentration through the DFT model proposed by Lazzeri *et al.* (see section 1.3.3.2 in the first chapter). Such approaches have been successfully applied to determine the doping levels in chemically doped graphene and graphite intercalated systems [96, 176].

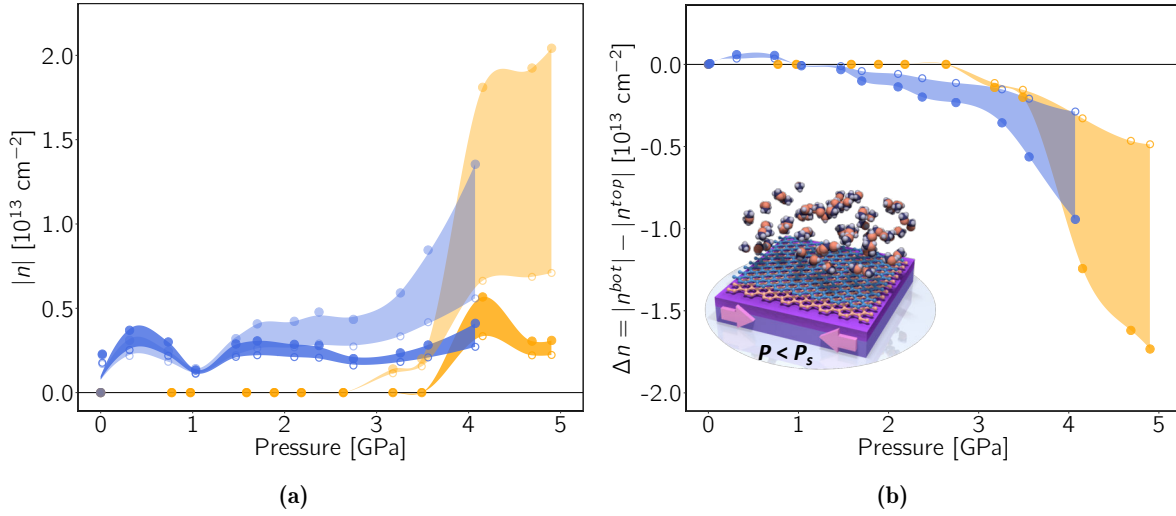


Figure 3.13 – Charge carriers concentration in each layer (a), and its difference $\Delta n = |n^{bot}| - |n^{top}|$ (b) as function of pressure using alcohol PTM. Filled circles correspond to the evaluated values using the electron-phonon coupling value from ref. [94] and considering hole carriers. The empty ones corresponds to electron-phonon coupling value from ref. [92] and electron doping. The areas in between cover the other two combinations. In (a), the lighter shade area corresponds to the top layer. The two colors corresponds to the two experiments in figure 3.9. The inset schematically shows the situation in the whole pressure domain where the alcohol PTM remains liquid.

Results for the two layers are given in figure 3.13(a) (data corresponding to the top layer are in lighter shade), considering two of our high pressure runs. The charge carrier concentration difference between the two layers, $\Delta n = |n^{bot}| - |n^{top}|$ as function of pressure is deduced and plotted in figure 3.13(b). One can appreciate that doping differences between layers of the order of 10^{13} cm^{-2} can be reached. In these graphs, we have considered the non-adiabatic contributions

either using LDA/GGA [92] or GW approximations [94] which define the shaded areas in the figures 3.13. We have considered the graphene lattice parameter evolution arising solely from the biaxial strain partially transferred from the substrate [24] and not from doping due to substrate pinning [96]. Due to the high symmetry of the G-band shift as function of charge concentration at low doping (figure 1.10), it is not possible to discriminate between hole or electron doping from the sole combination of experiments and models.

It appears clearly in figure 3.9(c) that the $\Delta\chi^*(P)$ difference is weaker in one of our alcohol PTM experiments (black symbols). This particular behavior may be explained due to the graphene-substrate unbinding [24] in this particular experiment leading to a lower value of $\Delta\omega_G^{mech}(P)$ through a lower value of α_S , consistently with our data on figure 3.9(a). We have clearly observed pressure induced unbinding in experiments with thicker samples (see experiments in chapter 5 on supported nanographite). Such partial unbinding would in turn involve a progressive exposure of the bottom graphene layer to the PTM and hence allow for the interaction of the PTM with the bottom layer too, leading to a reduction of the absolute value of $\Delta\chi^*(P)$ as observed. As $\Delta\omega_G^{mech}(P)$ is modified in this particular experiment with respect to all others, we did not evaluate its doping evolution with pressure and the corresponding points are not included in figure 3.13.

Additionally, we note that the G-band FWHM for one of alcohol PTM experiments in Fig. 3.9(b) shows an anomalous high value, in particular for the bottom layer. This may be related to the progressive delamination of the oxide layer observed in all alcohol PTM experiments (see figure 3.4), whereas it was absent for the argon or nitrogen PTM ones. To avoid such spurious contributions, we did not use the corresponding data points for the charge carrier concentration evaluation of figure 3.13. Finally, there is an overall good agreement between the two experiments in figure 3.13 with some differences which may arise from the different twist-angle between the two samples.

As mentionned in the introduction, values of $\partial\omega_G/\partial P$ were considered as a doping effect argument in an earlier work [22]. Nevertheless, subsequent works in references [23–25] showed the difficulties to use such parameter alone for doping characterization. In the case of the study presented in ref. [23], no doping has been observed using alcohol PTM for a monolayer sample on a copper substrate: a different substrate may have an influence on the piezo-doping mechanism observed during this work.

As we clearly show here, comparison of $\partial\omega_G/\partial P$ between experiment with various PTMs can be hazardous since additionnal strain and doping contributions can add to this slope value. This can lead to similar G-band slopes but from different physical contributions, especially if one uses non-isotopically labeled BLG for which the G-bands of each layer would be superimposed. Thanks to the use of isotopically-labeled BLG samples and through the observation of the inversion of the $\Delta\chi^*(P)$ evolution, we are able to disentangle doping and mechanical stress effects arising from the PTM.

Our work does not provide direct information on the piezo-doping physico-chemical mechanism associated with the use of alcohol PTM. Nevertheless, we may discuss different possibilities. As

mentioned in the introduction of the chapter, pressure studies of bilayer graphene in water PTM have proposed the formation of sp^3 bonds on the top layer with -OH groups leading at the same time to an sp^3 hybridization between the two graphene layers, a transition observed around 5-10 GPa [10, 11]. In our study, such a high-pressure onset hybridization hypothesis cannot be invoked since doping appears from the earliest pressure stages. Electronic doping of graphene by surface adsorbates [59] appears as a more favorable scenario. In fact, it has been shown that water, toluene or F4TCNQ, *i.e.*, polar molecules, show at ambient pressure such type of doping, whereas the non-polar molecule naphthalene, for instance, does not [60]. The dipolar nature of the molecule thus seems to be a factor favoring graphene electronic doping through surface adsorption. Pressure enhances the surface environment interaction and may exalt such doping effect. We should nevertheless underline that the graphene doping mechanism associated with the adsorption of atoms or molecules may be complex including red-ox interactions mediated by the presence of other molecules [59] and may also be affected by the incident Raman laser power [177].

Further work is needed to better understand the piezo-doping effect observed. We are now extending the study to other molecular fluids known to electronically dope graphene at ambient conditions [60], which could further enhance the effect, and bring interesting outcomes both from the fundamental point of view as well as for applications. Water PTM should be tested, since it consists of polar molecules. A key step forward will be to compare the high pressure Raman evolution of the sample using a 1:1 pentane-isopentane mixture as PTM, in regard with its alcohol version (1:1 pentane-isoamyl alcohol). This should confirm the role of polarity of the PTM molecules on the piezo-doping effect. Finally, combining such type of sample with the possibility to study suspended samples could allow to better explore the physico-chemical origin of piezo-doping effects.

3.5 Conclusion

Our work shows that the use of supported isotopically-labeled bilayer graphene at high pressure not only allows disentangling mechanical and chemical effects in a remarkable way, but also evidences strong asymmetries. While the bottom layer is mechanically strained by the substrate compression, the top graphene layer can exchange chemically or mechanically with the PTM environment. Experiments were done using three different pressure transmitting media: argon, nitrogen and 4:1 methanol:ethanol. We have shown that, as far as these media remain liquid, the measured mechanical strain is transferred solely from the substrate to the two layers without asymmetry. Conversely, the solidification of the pressure medium leads to a mechanical decoupling of the layers, leading to a strain mismatch of up to 0.1 %. We have been able to propose a crude model to describe this mechanical effect and obtain an upper limit for the strain transfer coefficient between the solid PTM and the top graphene layer. In the case of the 4:1 methanol:ethanol medium we have evidenced a remarkable piezo-doping effect on the graphene layer in contact with the alcohol molecules, which remain in their liquid state. The piezo-doping is strongly asymmetrical, with the top layer showing a charge concentration of the order of 10^{13} cm^{-2} above the lower one.

Asymmetric doping or strain between layers can bring opportunities in band structure engineering of two-layer systems [178, 179] with possible applications including devices, or composite materials optimization.

3.6 Summary

In this chapter is presented our study on the isotopically labeled bilayer graphene at high pressure. The key point of this experimental work is the ability to monitor the Raman response of each layer independantly thanks to the isotope labeling. It allowed us to indentify new physical mechanisms, showing the effect of the environment state and chemical nature on the high pressure response of graphene:

- When the PTM is an inert liquid, the substrate partially transfers its strain to the bilayer structure as a whole, and no mechanical mismatch is observed between layers.
- When the PTM solidifies, its strain is also partially transferred to the bilayer system. It leads to a strain differentiation between the two layers. Anomalies can be observed in this strain differentiation, related to high pressures phase transitions and recrystallizations of the PTM.
- In the case of the liquid 4:1 methanol-ethanol PTM, a pressure induced piezo-doping effect is observed. It is highly asymmetrical, the top layer in direct contact with alcohol molecules showing a higher charge doping effect. The identification of the physico-chemical mechanism in play, as well as the type of doping (p or n) would require further work.

These original results provide a better understanding of the PTM role in high pressure experiments on graphene. It also shows how to create strain asymmetries and doping mismatch in the two-layer stacking structure, which may have interesting implications for opto-electronic devices, and graphene nanomechanics.

4

Experimental Developments for High Pressure Studies on Suspended Samples

Contents:

4.1	Introduction	94
4.2	Suspended 2D-Material Diamond Anvil Cell Loading Strategies	96
4.2.1	Drilled Diamond Anvil	96
4.2.2	Lithographed Substrates with Trenches	99
4.2.2.1	Focused Ion Beam Cutting of Lithographed Substrates	99
4.2.2.2	Mechanical Cleaving of Substrates	103
4.2.3	Holed SiO ₂ /Si Substrates Prepared by Focused Ion Beam	106
4.3	Preliminary Results on Suspended Nanographite at High Pressure	110
4.4	New Portative Helium DAC Loading Development	117
4.4.1	Existing Helium DAC Loading	117
4.4.2	The New Portative Design	118
4.5	Conclusion	123
4.6	Summary	124

4.1 Introduction

This chapter presents our experimental developments in order to implement *in-situ* Raman spectroscopy on suspended graphene at high pressure. As we have mentioned in the general introduction, the study of suspended samples is very desirable in the field of 2D-materials at high pressure. Figure 4.1 pictures the ideal situation where a pressurized suspended graphene sample is probed by *in-situ* Raman spectroscopy. Such experiments would help to disentangle the effects arising from the substrate and from the PTM (we have seen the effect of such complex environment in chapter 3). The absence of strain transfer from the substrate would allow to determine the intrinsic strain response of an atomically thin crystal to hydrostatic compression (on the condition that a fluid and inert PTM is used). In suspended configuration, the 2D membrane is compressed between systems of identical chemical nature and compressibility on both sides. Furthermore, inhomogeneities of strain or doping related to the presence of a substrate are also suppressed in the suspended configuration [180]. Experiments performed in suspended configuration may also bring new insights on the sp^2 to sp^3 structural phase transition in bilayer graphene [10, 12].

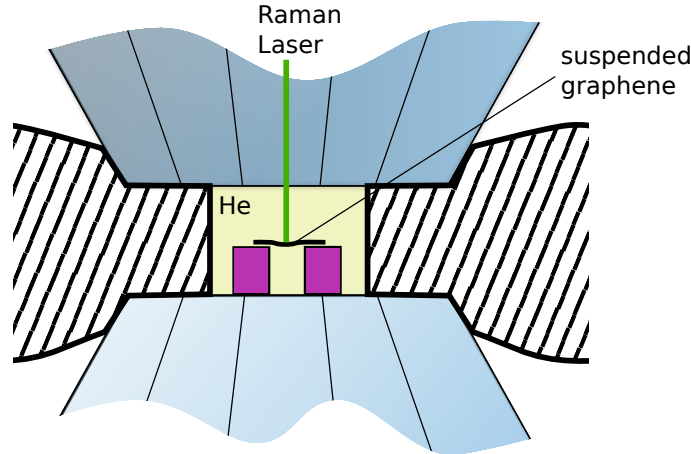


Figure 4.1 – Diagram illustrating ideal experimental conditions for the study of suspended two-dimensional materials under high pressure in a DAC *via* Raman spectroscopy. The ideal PTM is helium. On the diagram, the sample is hold by a specific substrate (pictured in purple) designed for sample suspension.

The question of the intrinsic strain response of a single graphene layer to hydrostatic compression is not trivial, and was rarely adressed in the literature. Proctor *et al.*, as well as Sun *et al.* have studied the G-band pressure evolution of unsupported graphene in solution using DACs, both reporting values of $\partial\omega_G/\partial P$ close to the values observed for bulk graphite ($4.7 \text{ cm}^{-1}.\text{GPa}^{-1}$ [37]) [21, 27]. The authors concluded that the in-plane strain response of monolayer graphene to hydrostatic pressure is similar to the one of graphite. The drawback of such experiments is that the Raman probed samples consists of multiple graphene flakes in solution, that are very likely to aggregates through van der Waals interaction. In fact, it is not possible to rely on commonly used Raman layer-counting indicators, namely the I_{2D}/I_G integrated intensity ratio, the FWHM of the 2D-band as well as its lineshape, since these characterization tools does not hold for non-

Bernal stackings [74, 76, 82]. Indeed, turbostratic stackings are most probably formed by layers aggregation. Thus, it is not surprising that the authors found similar results as for graphite in term of G-band pressure dependency since (i) multiple flakes of various thicknesses may contribute to the measured Raman G-band, and (ii) aggregation of flakes leads to the retrieve of the bulk, three dimensional mechanical response of the system to pressure. We should mention that Soldatov *et al.* have reported in a conference abstract dated 2012 [181] a G-band pressure slope of $5.6 - 5.9 \text{ cm}^{-1}.\text{GPa}^{-1}$ for a free-standing monolayer graphene sample at high pressure, but the authors have not published the results in an article since. Very recently, Tao *et al.* have reported high pressure experiments on single suspended monolayer and bilayer graphene in DAC [12]. The CVD graphene samples were transferred through PMMA-assisted method on pieces of Au grid loaded in the DAC, including holes where graphene suspends (such grid are priorly designed for transmission electronic microscopy). The authors report a pressure G-band slope of $\partial\omega_G/\partial P = 3.1 \text{ cm}^{-1}.\text{GPa}^{-1}$ for all samples studied, a value lower than the value observed for graphite. We see that this research field is little explored yet. Furthermore, different values for the G-band pressure evolution are reported, corresponding to different experimental conditions. Thus, an experimental campaign on well defined, single suspended graphene samples at high pressure is very desirable.

Similarly to the work of Tao *et al.* [12], in our experimental approach, the objective is to study single suspended nano-systems. In practice, a limited area of such flake is suspended while it is hold by a support appropriately designed for suspension (see figure 4.1). The advantage of such protocol is the ability for direct measurement of the Raman signatures both in the suspended and in supported regions. This will help to clearly compare the role of the substrate [26]. Main obstacles encountered are related to the manipulation of the small supports to be loaded in the DAC, to the extreme fragility of suspended 2D-materials over it, and to the small number of available samples due to their difficult preparation. We should mention the difficulty to load a liquid-state PTM in the DAC where a suspended graphene sample is installed, since capillary force are likely to induce sample's collapse. To overcome this problem, ideally, the DAC would be loaded with helium at supercritical state. Furthermore, we have shown that graphene (and nanomaterials in general) are very sensitive to non-hydrostatic conditions. Thus, during this work, we contributed to the development of a new portative helium DAC loading technique under implementation at iLM.

We did not yet achieved the ideal experimental conditions pictured in figure 4.1, for the study of monolayer or bilayer samples in helium PTM. However, we were able to approach it by studying thicker, less fragile suspended samples of a few dozens atomic graphene layers, using nitrogen and alcohol PTM. These experiments constitute proof of feasibility of the developed techniques. We should underline that the work presented here focus on graphene as a model 2D-material, but the outcomes are exploitable in the future to design experiments on other 2D-materials, and even complex combination of 2D-materials such as twisted stacking and Van-der-Waals heterostructures.

Different strategies for the loading of suspended graphene samples in the DAC have been designed during this work, believing that multiple approaches developped in parallel would increase the chances of success. It also diversifies financial and human ressources. First is presented a strategy

based on the machining of a trench in the diamond anvil of the DAC for graphene suspension. Later on, techniques involving intermediate holed substrates are presented. Preliminary results obtained on suspended nanographites samples are detailed and analyzed. Finally, our work on the development of the new portative helium DAC loading technique is presented.

4.2 Suspended 2D-Material Diamond Anvil Cell Loading Strategies

4.2.1 Drilled Diamond Anvil

Our first strategy presented here is straightforwardly using the diamond anvil of the DAC as target substrate, where samples can be suspended by PDMS stamping. Deterministic dry transfer of 2D-systems on diamond has already been performed in a recent study on supported WSe₂ at high pressure [111]. The additionnal challenge here consists in the suspension of the flakes. In this goal, we have designed a rectangular trench on the diamond anvil surface intended for sample suspension (see figures 4.2(a) and (b)). The trench has been machined using the Ga⁺ ion beam of a Focused Ion Beam set-up (FIB Zeiss NVision 40) available at the Mateis lab of INSA Lyon. The dimensions of the trench are $5 \times 30 \mu\text{m}$, with $\sim 10 \mu\text{m}$ depth. The width of the trench is of great importance: indeed, it must be sufficiently narrow to make the sample dry transfer easier, but larger than the Raman excitation spot size. This ensures that Raman measurements correspond to completely suspended regions of the sample. Figure 4.2(d) shows a picture taken during the dry transfer of a thin graphite sample for suspension over the holed diamond substrate. The resulting suspended sample is shown in figure 4.2(e) at ambient pressure, and in figure 4.2(f) loaded in the DAC at 6.5 GPa (the PTM was nitrogen).

Our interest for the development of this strategy is its simplicity. Graphene samples can be prepared by mechanical exfoliation from graphite, and since we have implemented the stamping transfer method at iLM, a complete autonomy is achieved. This was a serious advantage in order to perform numerous experiment attempts, as needed for such challenging experiments. The absence of any silicon substrate supporting graphene pushes the maximum pressure achievable higher, since it is no longer limited by the silicon β -Sn transition (~ 10.5 GPa), neither by its thickness (as explained in section 2.3.1). Counterpartly, in supported regions of the sample on diamond nearby the central trench, the Raman signal is not as intense as on oxydized SiO₂/Si substrates (no constructive interference condition is verified). Another drawback is the presence of a weak amorphous carbon Raman signal around $\sim 1600 \text{ cm}^{-1}$, which is more intense close to the trench (see figure 4.3 showing the anvil Raman spectra obtained at various distances from the trench). Inside the trench, this signal has a similar intensity to the diamond second order Raman feature. A pollution is observable through an increased light absorption near the trench (see the microscope picture shown in figure 4.2(c)). These observations are probably related to redeposition of amorphous carbon particles, or/and weak amorphization of the diamond surface due to the FIB milling. This broad Raman band may have to be taken into account for sample's G-band deconvolution since it is in the same spectral range and may slightly appears

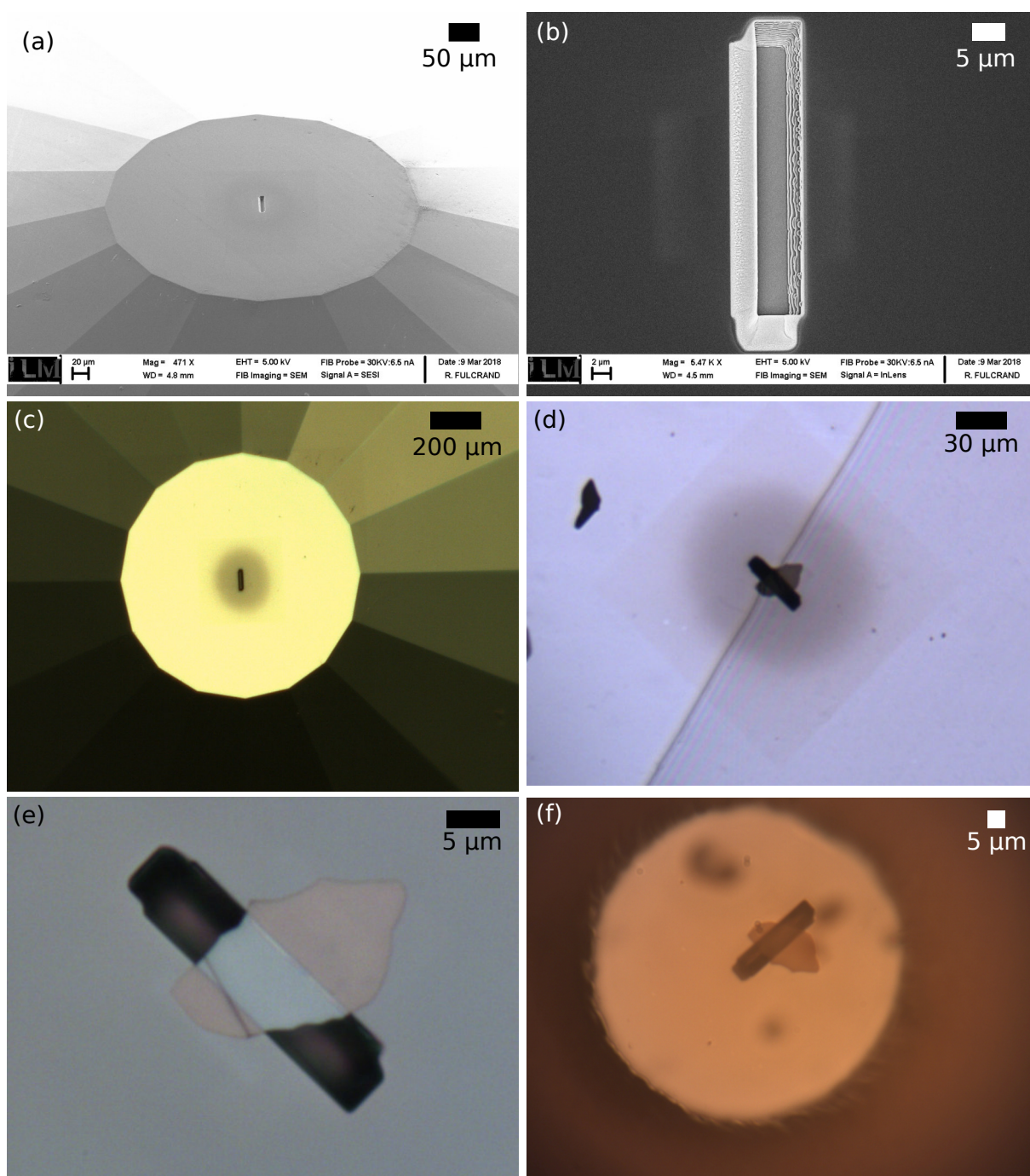


Figure 4.2 – (a) SEM image of the diamond anvil with the FIB milled rectangular trench at its center. (b) SEM image of the rectangular trench at the center of the diamond anvil (closer view). (c) Optical microscope image of the holed diamond anvil: increased light absorption is observed nearby the trench in the diamond anvil. (d) Optical micrograph of the holed diamond target during a thin graphite sample transfer for suspension: the contact front is visible as well as interference fringes in the region where the PDMS stamp is very close to the diamond (to the right of the contact front). (e) Optical micrograph of a thin graphite sample (40 nm thickness corresponding to approximately 120 graphene layers) suspended over the trench in the diamond anvil. (f) Optical micrograph of a suspended thin graphite sample loaded in the DAC with nitrogen as PTM. The pressure in the DAC was 6.5 GPa when this picture was obtained.

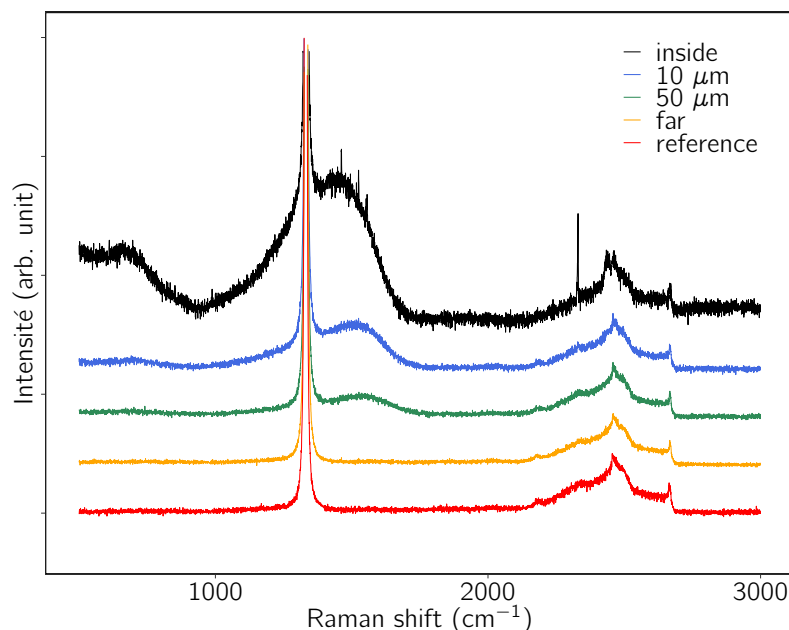


Figure 4.3 – Raman spectra of the diamond anvil measured at various distance from the central FIB trench (see legend). Spectra have been vertically shifted for clarity. The bottom red spectrum corresponds to pristine diamond.

in sample spectra.

Before transfer on the diamond, the PDMS stamp is carefully inspected searching for suitable flakes, following the protocol described in part 2.2.1.1. We should mention that monolayer and bilayer graphene flakes are hard to spot by optical contrast on PDMS and its research on centimeter wide stamps is time consuming.

Using the drilled anvil strategy presented here, we have performed proof-of-concept experiments on suspended thin graphite at high pressure (see for example the 40 nm-thick exfoliated sample loaded in the DAC shown in figure 4.2(f)). Preliminary results including Raman spectra obtained in these experiments are presented and analyzed in the dedicated subsection 4.3. After a few high pressure cycles beyond 10 GPa, the drilled anvil has cracked along the rectangular trench. This event hindered the continuation of our tests to reach experiments on monolayer or bilayer graphene with this strategy. Diamond machining, despite the small size of the trench with respect to the anvil size, seems to have mechanically weakened the diamond anvil. The position and geometry of the trench could have favoured fragile fracture in a particular crystallographic direction under stress. A path to pursue with this strategy could be the design of a smaller trench, taking into account the crystallographic orientation of the anvil. Along with the geometrical constraints imposed for flake suspension and Raman measurements, the goal would be to limit the negative impact of the trench on the mechanical strength of the diamond, for example by rounding off the edges of the trench. Furthermore, the diamond may be machined by laser cutting instead of FIB milling which seems to affect diamond widely nearby the trench (figures 4.2(f) and 4.3). We must note that during gaskets preparation, it needs to be indented using the holed diamond: this leads to supplemental stress cycles in the anvil. Another drawback of the drilled diamond technique lies in the fact that graphene is extremely hard to see on

diamond by optical contrast. Accordingly, its Raman signal in supported regions is very weak. The premature diamond breakage, and the high cost of a series of test on various trenches geometry (mainly in term of diamonds), led us to find other strategies. These new strategies use intermediate substrates for DAC loading of the suspended samples, and are presented in the next sections.

4.2.2 Lithographed Substrates with Trenches

4.2.2.1 Focused Ion Beam Cutting of Lithographed Substrates

To get rid of machined diamond breakage, another strategy implemented during this work is based on intermediate lithographed silicon substrates. Such substrates are designed in a "silicon on insulator" (SOI) wafer, including trenches for graphene suspension. It is pre-cut to make easier its isolation from the SOI wafer, as well as the challenging DAC loading step. Large polycrystalline CVD graphene sample have been transferred using the PMMA sacrificial layer technique on the surface of the wafer where substrates are lithographed. Lithography processes, as well as the CVD graphene growth and wet transfer are performed by our collaborators in Institut Néel (L. Marty and co-workers).

Figure 4.4(a) shows a Scanning Electron Microscope (SEM) images reconstitution of the SOI wafer (200 μm thickness) where numerous lithographed substrates are arranged in a lattice. The PMMA-assisted transfer of large CVD polycrystalline graphene sample (of millimeter size) is an interesting strategy, since the target substrates are not covered by the samples one by one but many at once. The area where CVD graphene lays after transfer on the SOI wafer is clearly visible on the SEM images in figure 4.4(a), as a darker shade. A zoom on one of the circular silicon substrates is shown in figure 4.4(b): it consists in a small disk of 90 μm diameter and 1 or 10 μm thickness, attached to the wafer by four silicon links around the disk. Each disk has five rectangular trenches of various sizes for graphene suspension. Such substrate along with the suspended graphene is intended to be detached from the wafer (as visible on the SEM image of figure 4.4(e)) and loaded in the DAC for high pressure Raman spectroscopy of the suspended sample.

Compared to the drilled diamond support technique, an additionnal transfer step is required. It consists in the intermediate substrate cutting from the wafer, including the fragile graphene suspended on it. In that goal, the first method described here uses a Focused Ion Beam (FIB) procedure to cut out the substrate, and a nano-manipulation step to drop it on the DAC anvil. Despite the fact that we encountered graphene damaging due to the FIB cutting nearby, the method is described here since it may be improved in the future (we propose a few paths in this purpose) and represent an important labour.

Before the cutting and loading procedure, the wafer is explored by optical microscopy and Raman spectroscopy for characterization purpose: substrates comporting sufficient suspended graphene areas, a measurable Raman signal and without defect related D-band are selected as candidates for high pressure runs. This represents approximately 5 – 10% of the substrates (a

dozen per wafer pieces prepared in Institut Néel). In general, the suspended samples do not show significative initial strain of doping levels. We may insist here on the fact that low laser excitation power (less than 1 mW) must be used to avoid any graphene heating during Raman measurements (in suspended configuration, no massive substrate provides heat dissipation as in the supported configuration).

The method for substrate cutting is performed in the vacuum chamber of the FIB-SEM. This set-up combines a vertical electron beam for SEM imaging, with a 54°-tilted Ga⁺ ion beam used for nanoscale milling and patterning. The experimental protocol can be summarized in four steps as follows:

1. Three out of the four links attaching the substrate to the wafer are cut using the focused Ga⁺ ion beam. During this first step, the wafer is 54°-tilted: the ion beam is therefore at normal incidence on the wafer while cutting. The ion beam is used only for milling, while the electron beam is always preferred for imaging in order to prevent graphene damage. The four links share the thickness of the substrate, *i.e.* 1 or 10 μm . In that later case, the cutting of one substrate lasts a few hours, while one hour is sufficient for thinner substrates.
2. Once the substrate is hold solely by the remaining link, a piezoelectric-based nanomanipulation tip available in the FIB-SEM is used. The tip is glued on the substrate using a system called Gas Injection System (GIS): a gas precursor is injected in the chamber, decomposes and forms a deposit under ion bombardment at the tip-substrate contact. This leads to the solidarization of the substrate on the tip by glueing. This operation must be performed without any wafer tilt, while the SEM is used for real time imaging.
3. The remaining link is finally cut, since the substrate is maintained by the nano-manipulator. The wafer is still oriented horizontally, therefore, the ion beam does not hit the wafer with normal incidence for this last cut. It is therefore more difficult to perform properly.
4. The substrate is detached from the wafer: it can now be carried using the nano-manipulator (see figures 4.4(c) and (d) where an isolated substrate is hold by the manipulator tip) and directly dropped on the bottom diamond anvil. Since the diamond surface is frequently charged by the SEM electron beam, the substrate is often projected and lost due to electrostatic forces. To overcome this problem, an intermediary copper piece with a central hole can be used to drop the substrate (figures 4.4(c) and (d)). That piece can later be adapted on the diamond anvil, and the substrate translated on the diamond by hand using a very sharp tungstene tip while looking the operation through the binocular.

We succeeded to drop substrates including suspended graphene on the anvil using this protocol (see figure 4.4(f) for an example). However, we encountered a stumbling problem of damaging of our graphene samples. This problem was observed through the graphene Raman spectrum after the deposition of the covered substrate on diamond. As a test experiment to identify the responsible protocol step for this deterioration, we have performed separated operations of FIB milling and GIS glueing on test supported graphene samples. Subsequently, Raman spectra were measured at various distance from the test FIB cut or from the cracked gas deposit on

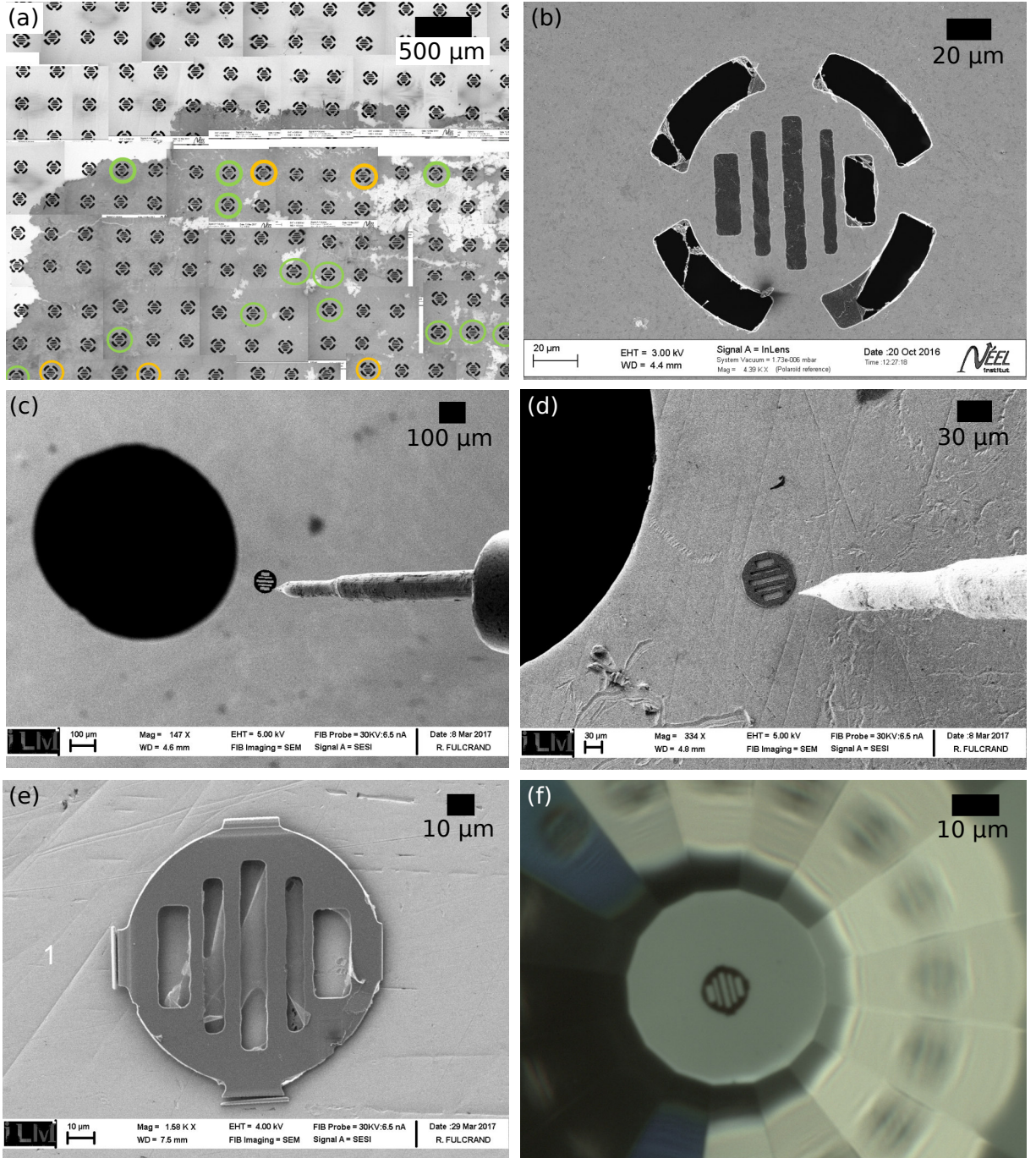


Figure 4.4 – (a) SEM images reconstitution of the wafer where numerous lithographed substrates are visible. (b) SEM image of a silicon substrate attached to the wafer *via* four links. Graphene is identifiable by contrast: four of the five trenches are covered with suspended graphene. (c) SEM image of a substrate attached to the nano-manipulator tip after substrate detachment by FIB cutting. (d) SEM image of the substrate just after the deposit on the intermediate copper piece (see text). (e) SEM image of an isolated substrate partially covered by suspended graphene, deposited on the intermediate copper foil. (f) Optical micrograph of a substrate deposited on the bottom diamond anvil of the DAC.

the graphene. This allowed us to identify that the FIB milling nearby graphene leads to its deterioration at long distance. Indeed, results presented in figure 4.5 shows that approaching the FIB cutting spot, first, narrow D and D'-band appears and increases in intensity, and secondly, the D and G bands broadens while the 2D-band disappears. We have evaluated the (corrected) intensity ratio $(I_D/I_G)E_L^4$ as function of FWHM_G for the four recorded spectra (inset of figure 4.5), in order to compare our values with the work from Cançado *et al.* [84] and identify the main defect type. The observed increase beyond 60 eV^4 while the G-band stays narrow suggests point defects rather than line defects in our samples. This results is expected: localized defects in the graphene lattice are created due to ion sputtering at long distance ($> 100 \mu\text{m}$ from the FIB cut). Closer to the FIB milling spot, disorder increases leading to the observed broadening of the Raman peaks (as well as the loss of the double resonance mechanism responsible for the 2D-band) [73]. A similar amorphization of graphene under ion bombardment has already been observed and described in reference [182].

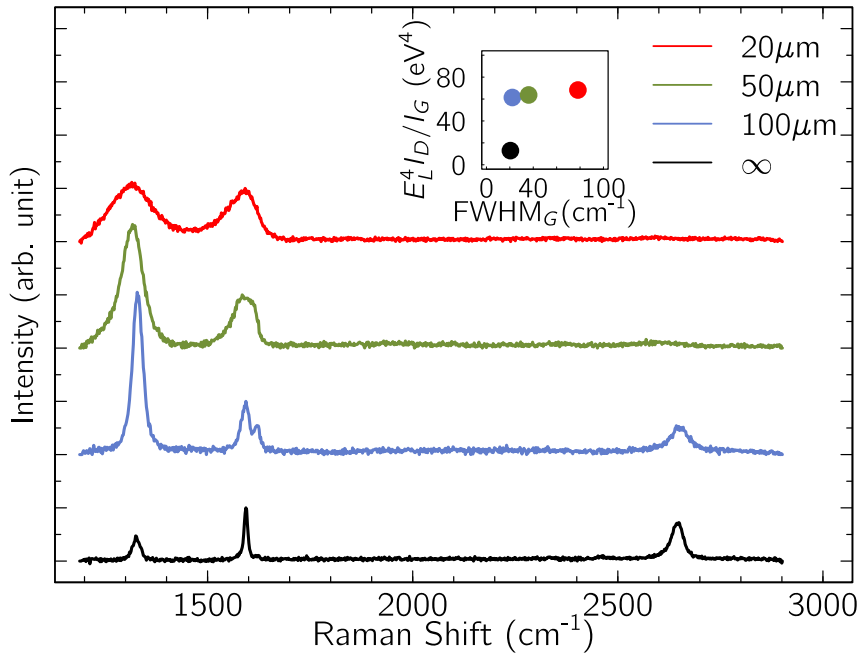


Figure 4.5 – Raman spectra of graphene measured at various distance from the FIB milling spot on a supported test sample. The ∞ symbol means that the spectrum was recorded far away from the milling area. The laser excitation wavelength was 633 nm, corresponding to $E_L = 1.96 \text{ eV}$. Inset: $(I_D/I_G)E_L^4$ as a function of the G-band FWHM for the four spectra with corresponding color.

The spatial extent of graphene damaging due to the FIB operations is striking: it hinders any experiment on a suspended sample since FIB operations takes place closer than $100 \mu\text{m}$ from the suspended graphene areas. After a few FIB cutting sessions, most of the samples belonging to the wafer piece were damaged. Decreasing the ion beam current would lead to a larger amount of time required to cut the silicon links, with finally equivalent consequences on the graphene samples. The use of thinner substrates ($1 \mu\text{m}$) was motivated by the shorter etching time required, but counterpartly, substrates becomes extremely fragile. Even with this extremely low thickness, the FIB procedure still damages the graphene samples. According to the literature, the annealing of damaged samples can lead to graphene self-healing [183]. However, the authors

of ref. [183] found that for their most damaged samples (still less than ours near the milling spot), the annealing is less effective.

Possible paths to overcome the graphene deterioration problem with this protocol may consist on (i) the use of an He^+ ion beam, instead of the Ga^+ ion beam set-up available in Lyon University, (ii) to use the smallest possible links in order to limit etching time required nearby graphene, and (iii) the use of a preliminary coated protection layer on graphene surface, which may be removed later once the substrate is on the diamond anvil. These three propositions could even be combined. In a recent paper, Cao *et al.* [36] have been able to perform FIB cutting directly on suspended graphene, using a Ga^+ beam with extremely low currents: their samples were not damaged. However, in our case, the current required for substrate cutting may be too important, even for narrowest possible links.

Beyond the graphene damaging issue, this protocole does not imply difficult hand-manipulations using the tungstene tip, which limit the risk of sample loss. On the other hand, the FIB and GIS operations are time consuming (a few hours for the loading of one substrate in best cases) and expensive. Pursuing this strategy through the mentionned suggestions would require a frequent access to a helium FIB, or/and a very large amount of samples to perform various attempts. Such samples are challenging to produce and to transfer on the lithographed wafers. Furthermore, in our case they require multiple site preparation, which makes all the procedure more difficult. The mentionned drawbacks combined with the risk of damaging many precious samples led us to modify the technique towards a simpler, faster, less expensive, and less demanding protocol. We have changed the lithography mask using a substrate geometry allowing its mechanical cleavage from the SOI wafer. This cleaving strategy is the topic of the next subsection.

4.2.2.2 Mechanical Cleaving of Substrates

We have modified the lithography mask such as the FIB cutting process is not needed anymore. Substrates can be separated from the wafer by mechanical cleavage by hand: a substrate is hold only *via* two weaks links (5, 10 and 15 μm width were tested), connecting it to the wafer. Counterpartly, substrates are thicker (50 μm) and has only one or two trenches (see figure 4.6(a) and (b) showing SEM images of the substrates along with suspended graphene membranes). This geometrical choice was motivated by the improvment of substrates mechanical resistance, reducing the risk of breakage of the substrate itself in favour of the breakage of the two weak links as wanted.

Various cleaving procedures have been tested, sharing the same central idea: the bottom diamond anvil is arranged directly beneath the wafer. The chosen substrate is aligned with the diamond culet. Then, weak links are cleaved using either (i) a 100 μm cylinder which can be precisely aligned over the substrate (see figure 4.6(c) for an illustration of the technique), or (ii) directly by hand using a tungstene tip, while looking the operation *via* binocular (figure 4.6(e)). In all cases, a perfored copper piece is prealably arranged over the DAC to support the wafer as illustrated in figures 4.6(c) and (e). The prealable alignement of the wafer with the diamond culet and the shape of the copper piece are intended to limit any further manipulations of the

substrate after cleavage (the less manipulations required, the less the risk of losing a sample). Ideally, the substrate falls directly near the center of the culet (see picture 4.6(d)).

Unfortunately, we did not succeed any high pressure run on suspended graphene using this technique neither. This is due to the following reasons: first, substrates are frequently projected away because of the mechanical shock when cleavage is performed (this problem is reduced for the smallest – most fragile – weak links of 5 μm). The hand cleavage using a tungsten tip frequently leads to graphene withdrawal if it enters in contact with the tip. Furthermore, substrates often fall upside down on the anvil, with graphene directly in contact against the diamond culet. Returning it using a tip is challenging and most of the time it leads to sample loss or deterioration. A geometric problem involved in these difficulties is the oversized thickness of the SOI wafer, which is the usual thickness of 200 μm . Lithographed substrates, 50 μm thick, are thus suspended too high above the diamond anvil culet: this leaves sufficient space for the substrate to flip over, or to attach to the wafer hole walls nearby *via* electrostatic forces.

We are currently working on improvements to use the protocol pictured in figure 4.6(f): here, the back side of the wafer is etched at each substrate's location to match the shape of the diamond anvil, as shown in figure 4.6(f). The DAC piston is mounted on a XYZ stage for its precise positioning before cleavage. Optimally, the substrate will be in direct contact with the diamond before breakage, preventing any projection or flipping. Another possible way to increase the loading success rate would be to weld a very thin gold wire on the substrate before cleavage: this may prevent sample loss. It could even be useful to maintain the sample later when the PTM is introduced. As mentioned, the cleaving technique is simple and inexpensive compared to the FIB and nano-manipulation processes, but highly hazardous for fragile suspended graphene membranes.

As mentioned, the cleaving technique requires many attempts to get a successful loading. It is therefore a very demanding method in terms of number of samples, that again cannot be produced on-site. Since we had numerous raw substrates (not covered by any sample and initially intended for cleaving practice training), we decided to perform PDMS-stamping transfers to suspend exfoliated samples over it (see figures 4.7(a) and (b)). Within this strategy, the PDMS-stamping is performed on the circular substrate before the cleaving procedure (as visible in figure 4.7(a)). However, the geometry of the trenches (especially its too large size) were not optimized for such transfers: it makes the transfer for suspension very difficult.

Moreover, problems encountered in the cleaving procedure are not bypassed through this new method since substrates must be cleaved after stamping. The flake research and PDMS transfer on the circular substrate are challenging and time consuming, while the cleaving technique is hazardous. Another important drawback (common to all strategies using raw silicon substrates), is that the optical contrast and the Raman signal in supported regions are weak, as in the case of diamond substrate.

Thus, we have developed a new intermediate substrate design, specifically intended for the loading of PDMS-stamped samples. The preparation of these SiO_2/Si substrates does not require

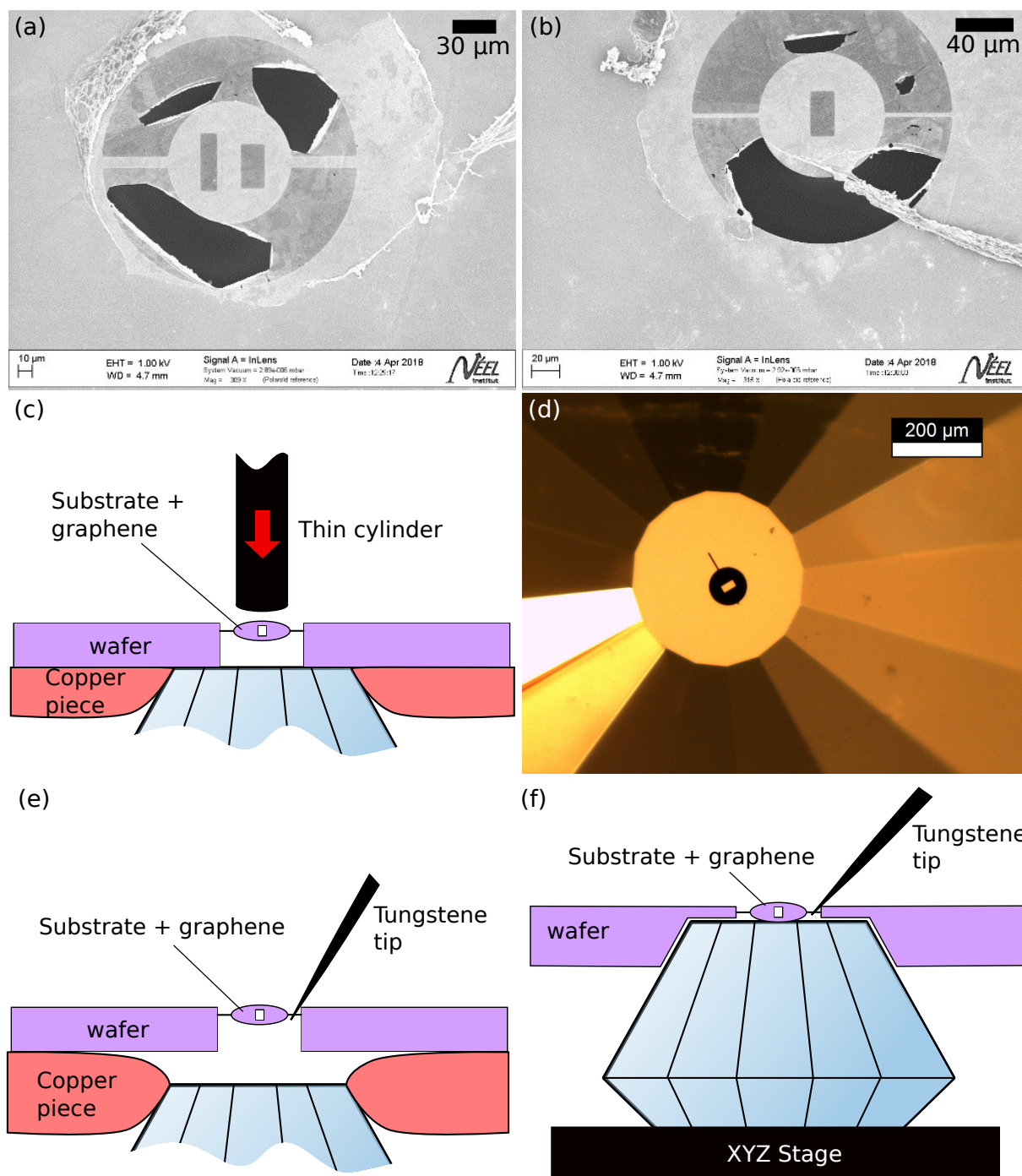


Figure 4.6 – (a) and (b), SEM images of two different substrates covered with CVD graphene, designed for mechanical cleavage of the weak links. (c) Scheme of the cleavage method using a narrow cylinder to break the weak links. (d) Micrograph of a blank substrate deposited on the bottom diamond anvil of the DAC, after cleavage. (e) Scheme of the cleavage technique using the tungstene tip. The shape of the underlying copper piece is intended to help the substrate falling directly on the diamond culet. (e) Scheme of the cleavage technique envisioned now: the wafer adapts directly on the bottom diamond anvil. The DAC is mobile on a XYZ stage.

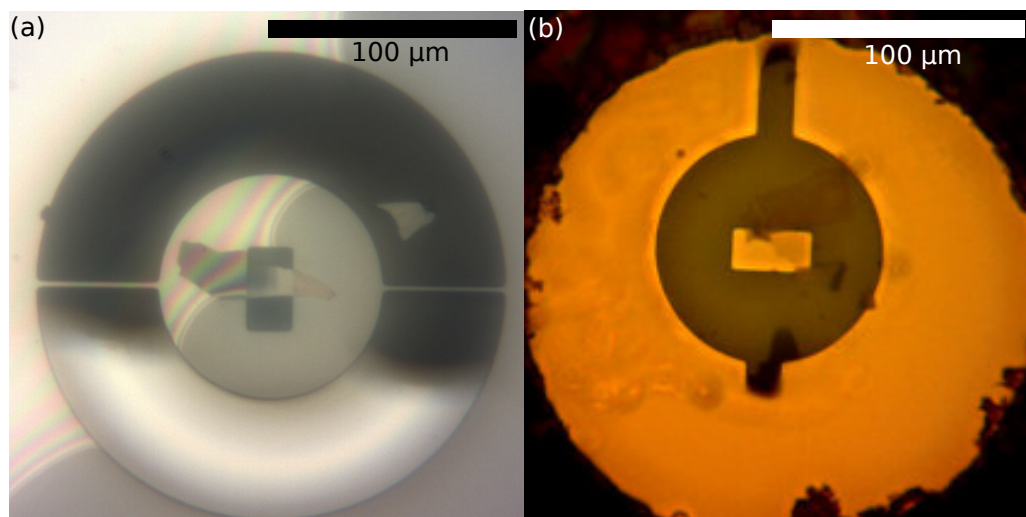


Figure 4.7 – (a) Optical microscope image obtained during the PDMS dry-transfer of a thin graphite flake on a pre-cut lithographed substrate. The contact front between the PDMS and the silicon surface is clearly visible, as well as interference fringes in regions where the PDMS is very close to the silicon wafer. (b) Optical micrograph of an exfoliated few-layer sample (priorly transferred by PDMS stamping), suspended over the trench of the lithographed substrate. The substrate along with the suspended flake are loaded in the DAC for high pressure measurements.

any lithography step and can be easily prepared on-site at iLM, in large quantity. Moreover, the loading does not require any cleaving procedure as we will see. Complete autonomy on-site at iLM was reached through this new strategy. It is described in details in the next section.

4.2.3 Holed SiO_2/Si Substrates Prepared by Focused Ion Beam

The new strategy also uses an intermediate holed substrate, but it is now *priorly* deposited on the diamond anvil as target for 2D-materials dry transfer. The key advantage of such approach is that no displacement or hazardous by-hand manipulations are required when the graphene flake is deposited for the high pressure run. It is transferred at the last moment on the substrate, just before the PTM loading. Substrates are cut out from SiO_2/Si wafers of 50 μm thickness using a dicing saw set-up (Disco DAD3220), in order to prepare small squares substrates of $\sim 50 \mu\text{m}$ by side that can be loaded in the DAC (see figure 4.8(a)). Before the cutting operation, the whole wafer is glued on scotch tape. Hundreds of substrates can be cut in a few hours. After cutting, substrates are machined by FIB in order to drill the central trench intended for samples suspension (see figure 4.8(b)). We have designed triangle trenches of $\sim 5 \mu\text{m}$ base and $\sim 30 \mu\text{m}$ height: this shape makes transfers easier since it can be performed on different locations along the triangle, thus over different trench widths. It also brings a relative flexibility in the flake positionning with respect to its size and shape. Just before the sample PDMS-stamping, the SiO_2/Si substrates can be cleaned with a O_2 plasma cleaner for $\sim 30\text{s}$, to remove small impurities on its surface and facilitate the transfer process.

Considering its size, a small square substrate can be detached from the tape and deposited on the diamond anvil by hand using a sharp tungstene tip, while looking at the operation

through binocular. This requires a bit of practice, but it does not constitute a problem since no sample is deposited on the substrate yet. There is no risks of sample degradation due to these manipulations (contrarily to the strategy presented in section 4.2.2.2).

This protocol presents several advantages: (i) the use of oxydized SiO_2/Si substrates allows for Raman signal and optical contrast enhancement in the supported regions of the deposited flake (see figure 4.8(e) and (f)), (ii) it allows, in the same experiment, for direct comparison between Raman responses in the suspended region of the sample versus the region supported on SiO_2/Si substrate, which is an already studied and well understood situation, and (iii) it can be applied for studies on fully supported samples using substrates without trenches (see for example the picture shown in figure 4.8(e), and our study presented in chapter 5). Indeed, this loading protocol for the sake of supported 2D-materials studies is cleaner and faster than the previous cleaving method used in our study on isotopically labeled bilayer graphene (chapter 3).

Prior to the flake transfer, the substrate must be attached to the anvil underneath, otherwise it would simply sticks to the PDMS stamp due to electrostatic forces. In order to overcome this problem, we have used an optical ultraviolet-curing glue (Norland Optical Adhesive 81). This specific glue has the right viscosity to deposit a very small drop ($\sim 100 \mu\text{m}$ diameter) at the center of the diamond anvil using the tungstene tip. The substrate can thus be dropped on this glue bubble with its oxydized layer upwards. Finally, the glue is cured in a few minutes under UV light (we have used the UV lines from a Hg discharge lamp). The bonding is sufficient to prevent the substrate from sticking to the PDMS stamp for the subsequent transfer. Another way to perform the manipulation is to drop the substrate upwards on any surface, without glue. Then, the stamping of the sample on the substrate is performed, but the substrate will actually stick to the PDMS where the flake is located. A drop of UV glue is placed on the center on the diamond, and the stamping stage is used to precisely install the substrate on it. The UV light is used to cure the glue for a few minutes, and the stamping stage can be finally lifted to terminate the transfer (the substrate remains bonded to the anvil). This second method has the advantage to facilitate the positioning of the substrate on the diamond culet, since the precise stamping stage is used in that goal. In general, ruby chips can be added before this manipulation, limiting the risk of sample loss. This glueing strategy also prevents the substrate (along with the sample on it) to get lost when the PTM is introduced.

The UV-curing glue does not present any optical absorption lines in the visible spectrum, neither luminescence signal. It shows a few Raman bands, but since it is localized far from the sample – under the substrate – its Raman signals do not polluate the sample spectrum. We have verified that once the glue is cured, it does not diffuse in the PTM loaded in the DAC during the high pressure run (even in the case of solvent PTMs such as the 4:1 methanol-ethanol mixture).

PDMS stamping on substrates with extremely limited area ($\sim 50 \times 50 \mu\text{m}^2$) such as our SiO_2/Si cubes are challenging. Indeed, when the target consists in an usual extended substrate, (i) the contact front progression at the PDMS-substrate interface is observable in advance, far from the precise location of the flake to be transferred, and (ii) the large contact area created prior to the flake contact provides mechanical stability in the system. Considering the case of

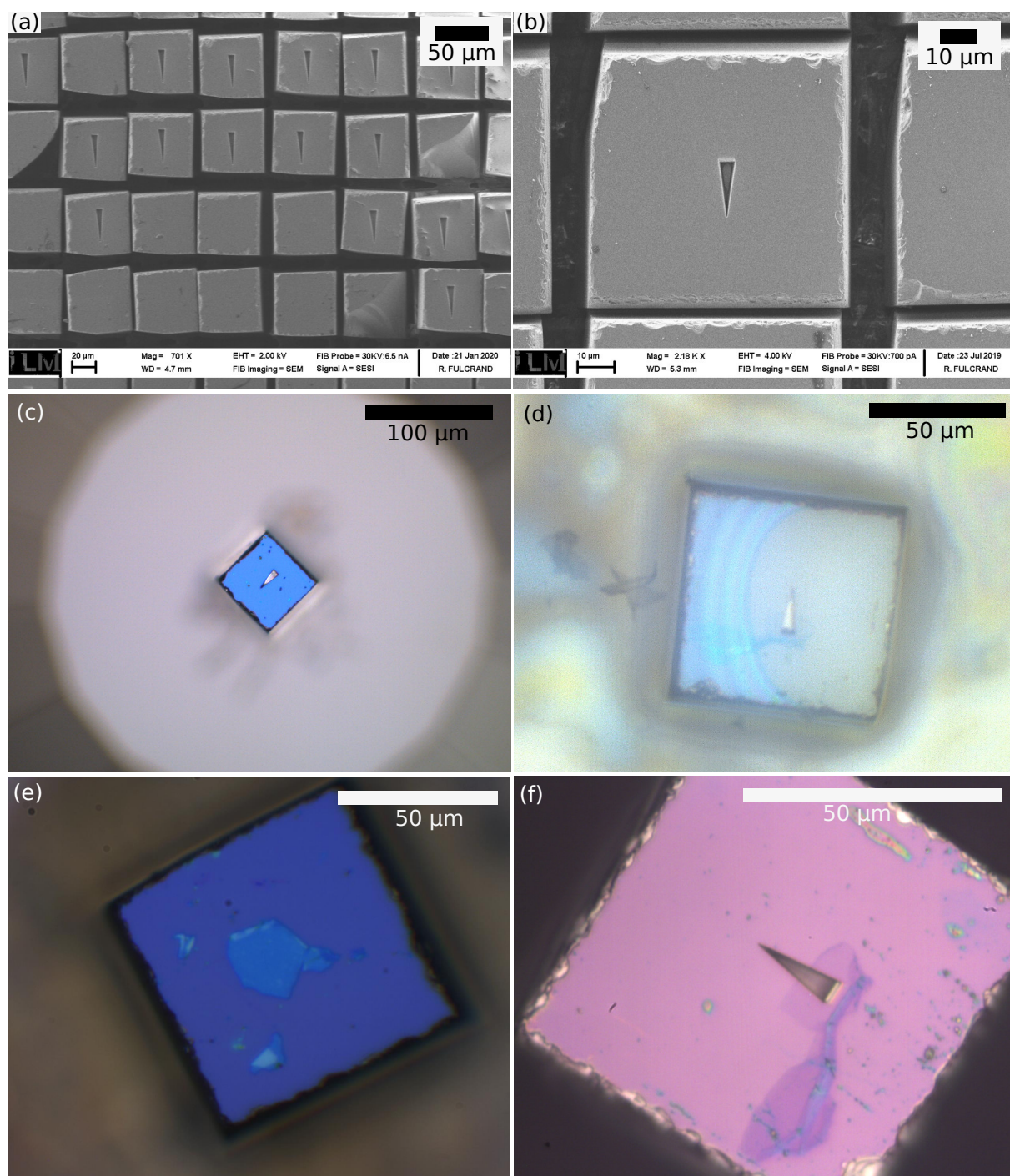


Figure 4.8 – (a) SEM image of cut-out squares SiO₂/Si substrates after FIB machining of triangle trenches on their surfaces. (b) SEM image (close view) of a single SiO₂/Si square substrate including a centered triangle trench. (c) Optical microscope image of a square substrate glued on the diamond anvil surface. (d) Optical microscope image obtained during a transfer of a graphene sample on the SiO₂/Si square substrate. The contact front between the substrate and the PDMS stamp is visible, as well as interference fringes where the stamp is very close to enter into contact with the target substrate (to the left of the contact front). (e) Optical microscope image of a thin exfoliated graphite flake supported on a square SiO₂/Si substrate without trench. (f) Optical microscope image of a bilayer graphene sample suspended over the trench of a square SiO₂/Si substrate. The substrate is glued on the diamond anvil.

extremely small targets as in our case, the Z axis screw of the stamping stage must be operated very softly while monitoring the transfer progress on the microscope screen in real time.

During our transfer attempts for monolayer samples suspension, we encountered the breakage of samples: the areas to be supported are transferred, while the suspended part breaks and remains on the PDMS. Recently, we have upgraded the PDMS-stamping set-up by adding a heating system, allowing to heat the target substrate up to ~ 110 °C. Combined with the use of a thin layer of polypropylene carbonate (PPC) spincoated on the PDMS stamp surface, this may help for the stamping of most fragile, thinnest samples (monolayer or bilayer) for suspension. Indeed, PPC is a thermoplastic material on which 2D-materials adhesion at room temperature is strong, while it decreases drastically beyond its glass transition temperature (40 °C) [184]. The heating system uses a heating resistor installed under the DAC piston for transfers, in order to heat the target substrate by conduction through the cell and the diamond anvil. Aluminium foils can be added for better conduction between the heater and the cell pieces. A resistive temperature sensor (TH100PT) is bonded to the DAC tungstene carbide seat using silver lacquer. It allows measurement and regulation of the temperature of the target substrate (which is assumed the same as the temperature of the WC seat, since thermal conductivity of diamond and of WC are very high). This heating system is also interesting for future experiments on van der Waals heterostructures [131].

We have been able to perform preliminary experiments on few-layer graphene samples using the protocol described here. The obtained results on these thick samples, presented in the next part, are unexpected and motivates to continue efforts towards suspended monolayer graphene experiments at high pressure. During our tries, we occasionally succeeded to suspend very thin samples (see for example the suspended bilayer graphene flake in figure 4.8(f)), but the introduction of the 4:1 methanol-ethanol PTM led to the peeling of the sample from the substrate. The capillary force created on suspended graphene during the PTM loading is a major challenge to overcome. Various attempts need to be performed: dinitrogen PTM should be tested since its surface tension at 77 K is more than 2.5 times lower than the 4:1 methanol-ethanol surface tension at ambient temperature [185, 186]. The impact of its loading on the fragile suspended membrane may therefore be reduced. An ideal experimental solution would be the use of helium as PTM, loaded at supercritical state. This would ensure the absence of any forces on the suspended membrane during loading, as well as hydrostaticity up to 12 GPa. We believe that it is the route to follow for future experiments. At our knowledge, two different experimental set-ups may provide the conditions needed for such He supercritical loading. We discuss these set-ups in a dedicated section of this chapter, section 4.4, especially the portative approach that we are developping at iLM.

4.3 Preliminary Results on Suspended Nanographite at High Pressure

Description of the Experiments

In this section, we present experiments performed on three different nanographites samples in suspended configuration. First, we note that what we call "nanographite" samples consist in graphite flakes of nanometric thicknesses. These samples are monocrystals obtained by exfoliation from natural graphite. Among the three samples studied, one was suspended on a holed SiO_2/Si substrate as explained in section 4.2.3, whereas the two other were suspended over the drilled diamond (section 4.2.1). Since the thicknesses of these samples cannot be determined by Raman spectroscopy, we have performed atomic force microscopy (AFM) scans in tapping mode to measure their thicknesses. This was done *after* the pressure cycle. AFM scans and profiles for the three samples are shown in figure 4.9, along with optical pictures of it at ambient and high pressure conditions. In figure 4.9, each sample is identified by its number of layers, determined by dividing its thickness by the interplanar distance of graphite $h = 3.35 \text{ \AA}$. Table 4.1 summarizes the informations on the three experiments carried out.

sample	34L	144L	123L
thickness (nm)	11.3 ± 0.4	48.4 ± 1.2	41.2 ± 0.3
suspension technique	holed SiO_2/Si substrate	drilled diamond	drilled diamond
PTM (hydrostatic limit in GPa)	4:1 methanol-ethanol (9.8)	nitrogen (2.4)	nitrogen (2.4)

Table 4.1 – Experimental conditions for the three samples studied at high pressure. The thicknesses were obtained by performing five AFM profiles measurements, and taking the mean value for each of the three samples. The reported errors corresponds to the standard deviation of these five measurements.

Results

For each sample, Raman spectra were recorded both in suspended and supported areas during the high pressure cycle. Spectra measured in the suspended regions are shown in figures 4.10, 4.11 and 4.12 for the 34L, the 144L and the 123L sample, respectively. We can see that the signal is clearly resolved, apart from the 2D-band of the thinner 34L sample in alcohol for which the signal-to-noise ratio is not excellent (the 2D-band signal was even lost beyond 4 GPa). Note that the laser power was kept near 1 mW in order to avoid heating of the sample. The 2D-band of graphite is composed of two components ($2D_1$ and $2D_2$), where the $2D_2$ band is the more intense component [73]. By least square fitting of Lorentzian lineshape functions, we have extracted the pressure evolution of the position and FWHM of the G-band, as well as the $2D_2$ -band position. Data obtained for suspended and supported areas are plotted in figure 4.13.

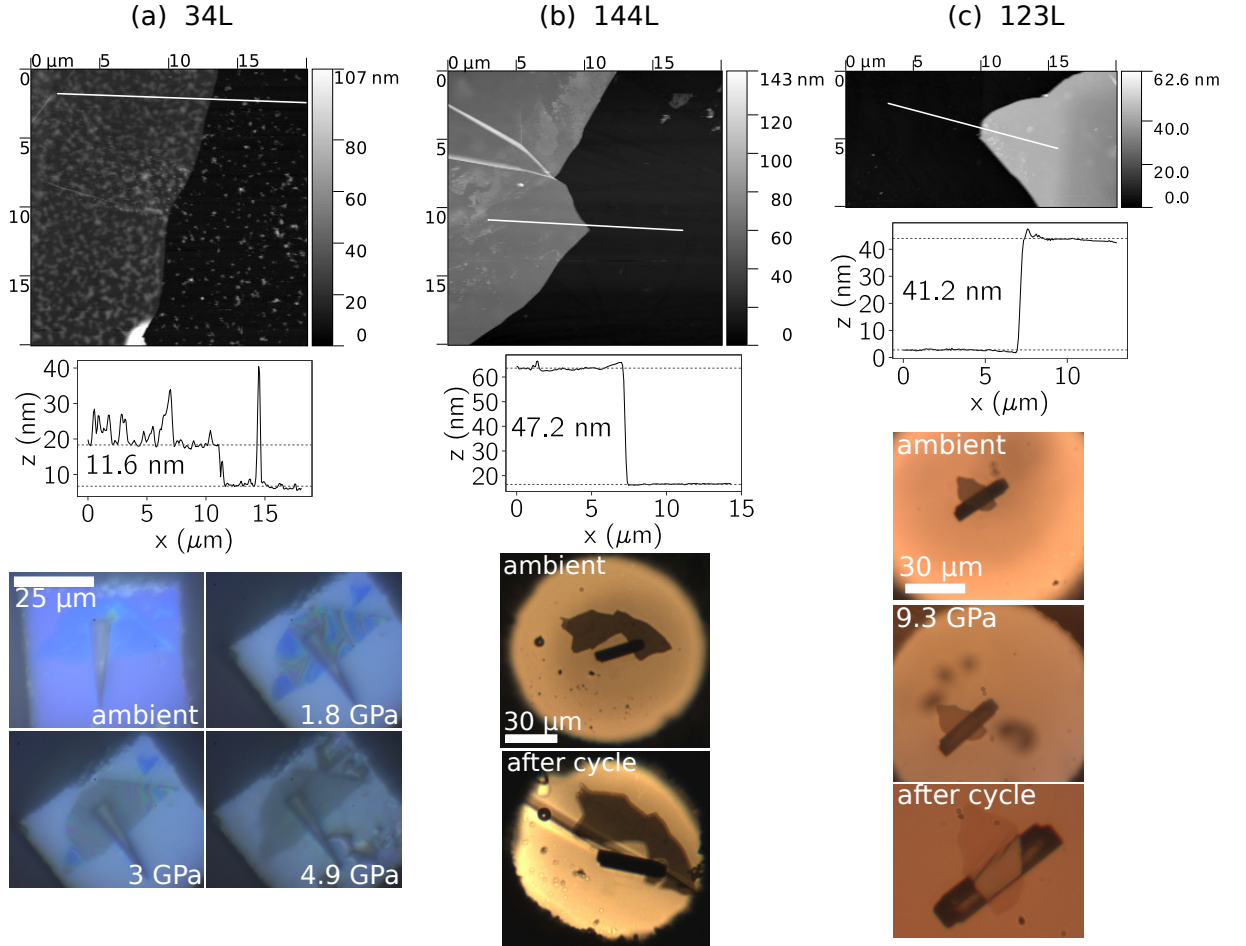


Figure 4.9 – Atomic force microscopy topographic images, profiles and optical micrographs of the suspended nanographite samples studied at high pressure. (a) column: nanographite sample of 34 ± 1 layers (34L) suspended over a SiO_2/Si substrate. (b) column: nanographite sample of 144 ± 4 (144L) suspended over the holed diamond. (c) column: nanographite sample of 123 ± 1 (123L) layers suspended over the holed diamond. For each samples, the height profile corresponds to the white line plotted on the AFM scan. In the optical picture in (b) after the pressure cycle, the crack in the diamond anvil is clearly visible.

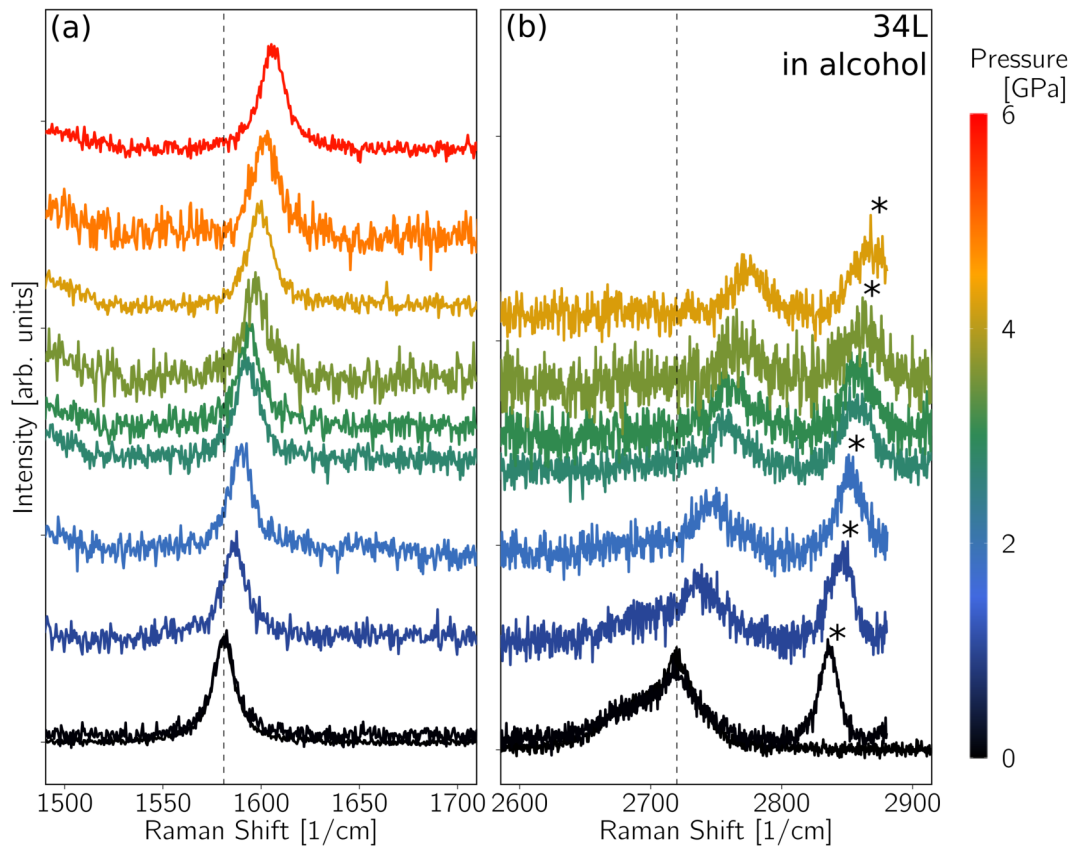


Figure 4.10 – Raman spectra obtained in the suspended region of the 34L nanographite sample at high pressure using 4:1 methanol-ethanol as PTM. (a) and (b) corresponds respectively to the G and 2D-band spectral regions. All spectra are background corrected and normalized such as the baseline height corresponds to pressure (colors and right pressure axis). In (b), the Raman peak from the alcohol PTM is indicated with the * symbol. The Raman excitation wavelength is 532 nm.

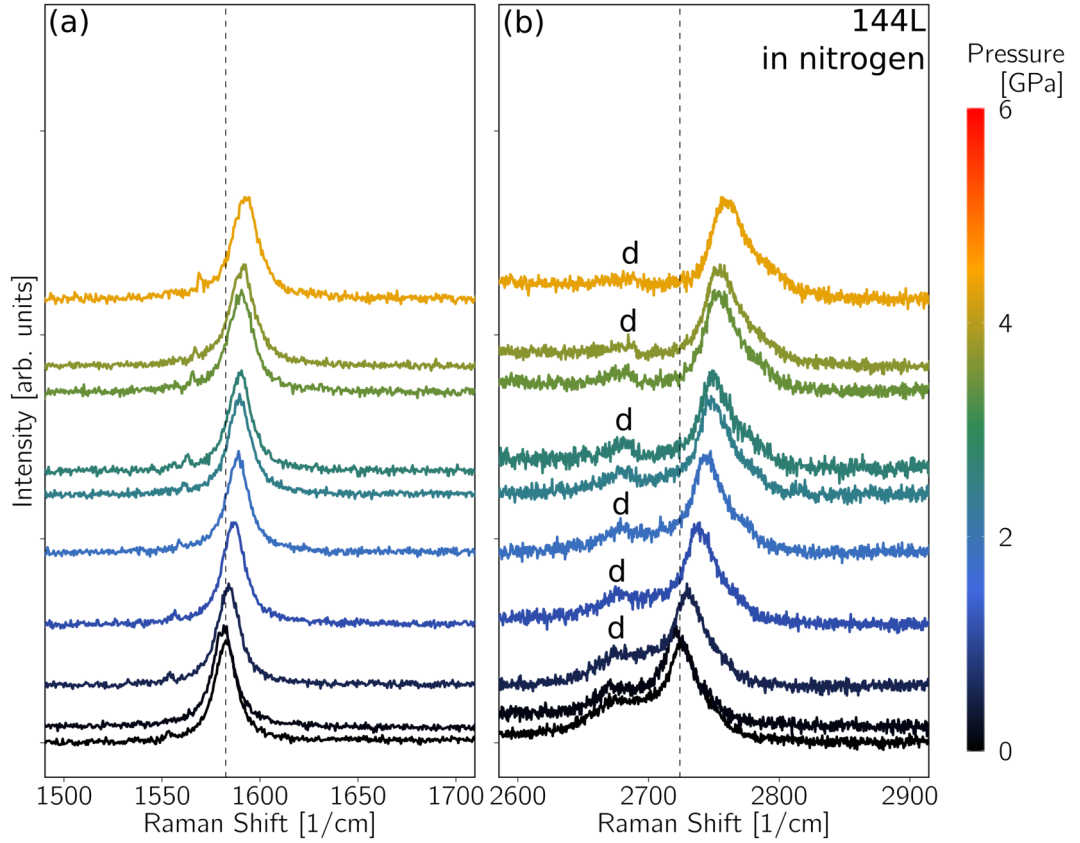


Figure 4.11 – Raman spectra obtained in the suspended region of the 144L nanographite sample at high pressure using nitrogen as PTM. (a) and (b) corresponds respectively to the G and 2D-band spectral regions. All spectra are background corrected and normalized such as the baseline height corresponds to pressure (colors and right pressure axis). In (d), features marked "d" corresponds to the Raman signal from the diamond anvil. The Raman excitation wavelength is 532 nm.

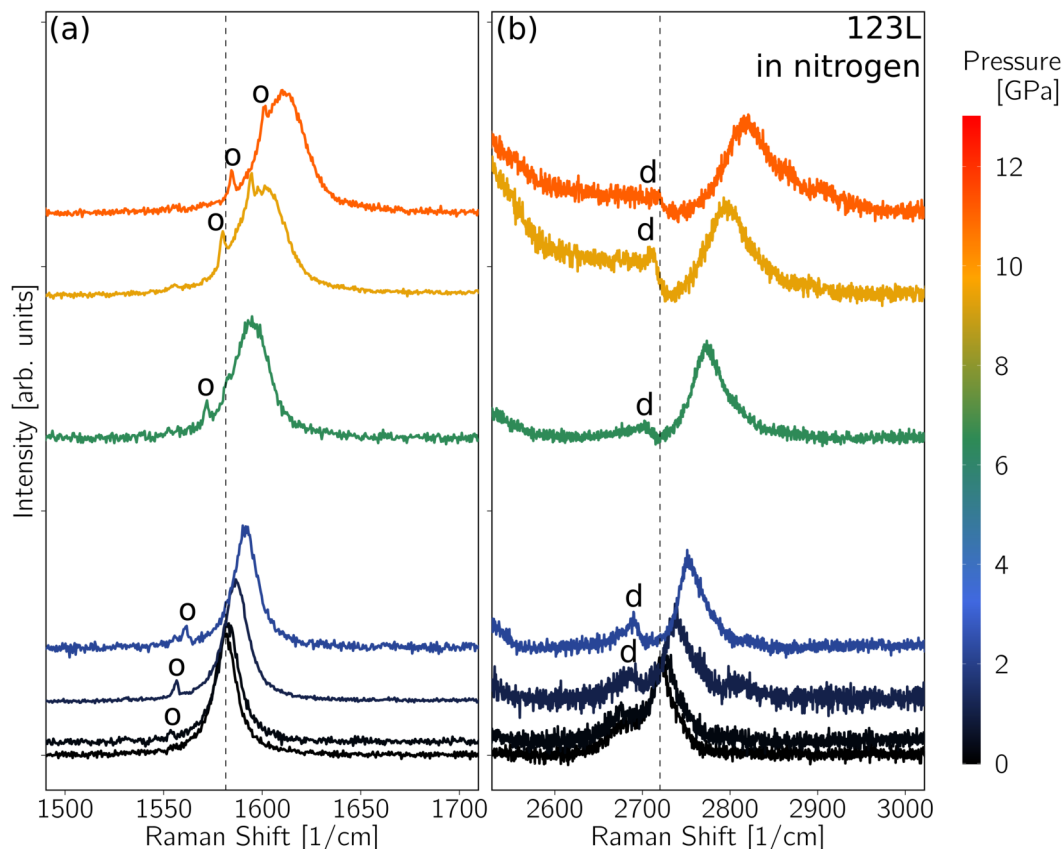


Figure 4.12 – Raman spectra obtained in the suspended region of the 123L nanographite sample at high pressure using nitrogen as PTM. (a) and (b) corresponds respectively to the G and 2D-band spectral regions. All spectra are background corrected and normalized such as the baseline height corresponds to pressure (colors and right pressure axis). In (b), features marked "d" corresponds to the Raman signal from the diamond anvil, while in (a), the "o" symbols indicates Raman peaks arising due to a small amount of oxygen present in the DAC [160]. The Raman excitation wavelength is 532 nm.

We should note that for the 34L sample, a progressive unbinding of the nanographite sample from the substrate was observed, until the sample was totally detached from it and appeared dark (microscope pictures in figure 4.9(a)). We will discuss this particular effect in details in chapter 5. Thus, for higher pressure points with the 34L sample, spectra were recorded in detached regions and were found identical to the ones obtained in the suspended region.

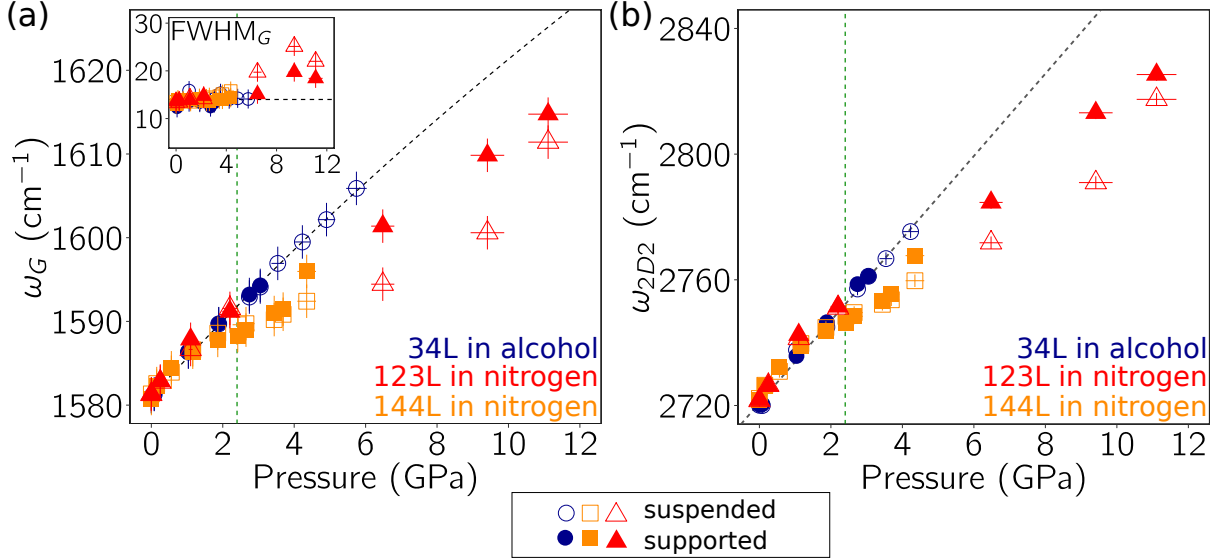


Figure 4.13 – (a) G-band and (b) 2D₂-band positions as function of pressure in the suspended region (open symbols) and supported region (filled symbols) for the three samples studied (blue circles: 34L in alcohol PTM, orange squares: 144L in nitrogen PTM, red triangles: 123L in nitrogen PTM). The topleft inset in (a) shows the pressure evolution of the G-band FWHM with pressure. In (a), the black dotted line corresponds to the bulk graphite evolution reported by Hanfland *et al.* [37]. In (b), the black dotted line corresponds to a linear fit of the 34L sample in alcohol PTM data (see text). The crystallization pressure of nitrogen (2.4 GPa) is indicated by the green dotted line in both graphs.

Looking at figure 4.13(a), one see clearly that for the 34L sample in alcohol, the G-band shift follows the bulk evolution (black dotted line) for both suspended and supported cases. Using nitrogen as PTM, the evolution is similar at lower pressures. However, beyond its solidification at 2.4 GPa, (i) an important softening is observed with respect to the bulk evolution for both samples (144L and 123L), and (ii) this softening is stronger in suspended regions of these samples. This observation is puzzling, since for the suspended 123L sample at ~ 10 GPa, the shift of the Raman G-band – thus, the compressive in-plane strain in the material – is even lower that what it would be if it was bulk graphite at half this pressure. To our knowledge, such effect has never been observed before. The 2D₂-band evolution follows a similar softening for nitrogen PTM at solid regime (figure 4.13(b)), confirming the observed trend. For the 34L sample using alcohol as PTM, a linear 2D₂-band pressure shift of $\partial\omega_{2D2}/\partial P = 13.1 \pm 0.8 \text{ cm}^{-1}.\text{GPa}^{-1}$ is found (black dotted line in figure 4.13(b)), close to value reported for HOPG under direct biaxial compression [187]. The FWHM of the G-band is nearly constant with pressure with a value of $\text{FWHM}_G = 14 \text{ cm}^{-1}$ (dotted line in inset in figure 4.13(a)), apart for the last points measured at higher pressures on the 123L sample for which a broadening of the G-band is observed.

Discussions

First, we should highlight that the concomitant observation of the softening effect in both the G-band and 2D₂-band evolution shows that it is of mechanical origin. Moreover, it appears clearly that the observed softening effect is related to the solid PTM regime.

We will develop here a first hypothesis in order to explain the experimental observations. Beyond the PTM solidification point, the suspended nanographite is sandwiched between nitrogen soft solids. In these conditions, the stress transfer mechanism is different than in the liquid PTM regime (in which the bulk evolution is observed). Here, stress is likely to be transferred by interfacial adhesion of the flake on the solid PTM (on both sides) as pressure increases. We have outlined in chapter 3 that the adhesion of graphene layers on such soft solids is weak. Therefore, the lower strain level observed in the solid PTM regime (observed through the softening of the in-plane optical phonons) may originate from a weak mechanical coupling between the nanographite sample and the PTM at solid regime. In supported regions, the effect is less pronounced. This may be related to the diamond anvil in contact with the nanographite sample on the bottom side. Concomitantly, the broadening of the G-band could be related to inhomogeneities in the stress transfer mechanism that we have pictured. Adding complexity, the solid PTM can be polycrystalline and different grain orientations may coexist in the vicinity of the nanographite sample. The lower G-band pressure evolution reported in ref. [12] for suspended samples over an Au grid with respect to bulk graphite could also be explained by this mechanical decoupling effect. Indeed, this lower slope value was observed in non-hydrostatic, solid PTM conditions (water and paraffin oil) [12].

We have an alternative hypothesis that can also account for the observations. In the solid PTM regime, the experimental results can be seen such as the sample is in relative in-plane tension with respect to its equilibrium interatomic distance at pressure P . We must consider that when the PTM solidifies, its molecules cannot diffuse in the pressure chamber anymore. Thus, the PTM volume trapped inside the trench *under* the suspended sample will continue to contract with pressure, following its equation of state. With increasing pressure, this contraction pulls the suspended nanographite system down, and creates a supplemental in-plane tensile strain in it. This tensile strain may be nearly uniaxial as in the 123L sample's geometry, or more complex (as in the case of 144L sample's geometry). The G-band broadening observed for the 123L can also be explained by this non-biaxial tensile strain developed in it. The relative tensile strain in the suspended region should have repercussions on the nearby supported regions of the material, explaining the lower but clear G-band softening observed in these areas. Indeed, in other experiments on *fully* supported nanographite at high pressure, no softening was observed at all.

Supporting this second hypothesis, we have observed the sample sagging in the trench after the pressure cycle in nitrogen. This is very clear on the AFM profile obtained after the pressure cycle, shown in figure 4.14(a), where one can see that the 123L sample is curved and sinks ~ 300 nm into the trench. The tensile effect can have induced the slippage of the sample on the diamond nearby the trench, leading to the remaining sinking after the compression. In the case of the 144L sample, the tensile effect even led to the sample's tearing, visible on the scanning electron

microscope (SEM) image shown in figure 4.14. We should mention that after the pressure cycle, no irreversible changes are observed in the Raman signatures. The geometrical effect described should be observed even for suspended samples in a hypothetical, perfectly hydrostatic solid PTM, since the effect is inherent to the PTM solid state.

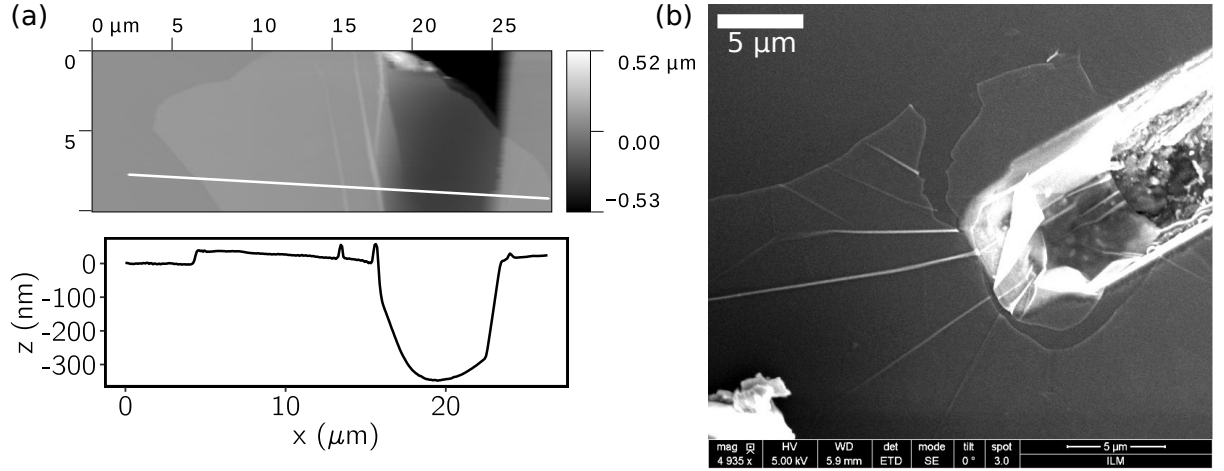


Figure 4.14 – (a) Atomic force microscopy topographic image and profile of the suspended sample (123L) after the pressure cycle, showing its sagging into the trench. The profile is obtained along the white line on the AFM image. (b) Scanning electron microscope image of the 144L sample over the trench evidencing its sagging into the trench and its tearing.

We have proposed hypotheses to account for the experimental results obtained. In all cases, the solid state of the PTM plays a central role. The proposed effects could even coexist. We have seen that the geometrical arrangement of the suspended sample can play a role in its response under compression in a solid environment. In complex non-hydrostatic conditions, the individual graphene layers constituting the nanographite system could even decouple and thus present different compressive strain levels (we have discussed such effect for bilayer graphene at high pressure in chapter 3, showing a strain mismatch effect).

In order to further explore the phenomenon, new experiments are desirable. An interesting path would be to study samples of different thicknesses in the same suspension conditions, in order to identify (i) from which thickness the bulk behaviour is retrieved, and (ii) ultimately, what happens for a monolayer system in these conditions.

In the light of these results, we insist on the need for a *fluid* PTM in order to study the intrinsic physical response of suspended graphene to high hydrostatic pressure.

4.4 New Portative Helium DAC Loading Development

4.4.1 Existing Helium DAC Loading

Helium is considered as the best pressure transmitting medium (see also part 2.3.3.1). Indeed, it is chemically inert, hydrostatic up to 12.1 GPa, and quasi-hydrostatic up to very high pressures

[147]. It is therefore frequently used for pressures experiments beyond 10 GPa. In the context of our studies on 2D-materials at high pressure, the use of helium as PTM is highly desirable for the following reasons: (i) we have shown in chapter 3 that graphene is very sensitive to the hydrostaticity of the medium, thus, the use of helium would reduce these effects and allow to explore the intrinsic response of graphene to pressure as high as 12.1 GPa, (ii) helium is inert, contrarily to the 4:1 methanol-ethanol which is hydrostatic up to ~ 10 GPa but shows a piezodoping effects with graphene (chapter 3), (iii) helium may be used to explore the response of graphene to higher pressures than in this work while maintaining quasi-hydrostatic conditions, (iv) fluid helium does not present troublesome low frequency light scattering modes (since it is monoatomic), thus, the *in-situ* Raman measurements of low frequency modes in multilayer graphene could be tested at high pressure [68, 88, 188], and (v) the DAC loading of helium at supercritical state would prevent any capillary forces on suspended graphene system during loading, as mentionned earlier in this chapter.

The main challenge for He DAC loading is the sufficient density required when trapping it inside the cell (as explained in section 2.3.3.2). Two techniques exist to achieve such loading. The first is a cryogenic method in which the DAC is immersed in liquid He at 4.2 K. Helium is trapped in the cell at liquid state, the cell being closed *via* a force applied by long metallic cables (the mechanism, similar to bicycle brake cables, is called Bowden cables) [189]. This technique is not compatible with the membranes DAC we use since the gas in the membrane would liquefy, leading to a sudden force drop on the DAC piston. With this strategy, the force must be applied from outside the cryostat through the Bowden cables. The second technique for He loading is performed at ambient temperature but in a high pressure environment, using a set-up called gas loading system (GLS). In that case, the membrane DAC can be used: it is introduced in a loading bomb which is pressurized with helium up to 1500 bar (in a volume of hundreds of mL) ! To trap the PTM inside the cell, the membrane pressure is increased slightly with respect to the loading bomb pressure, and the pressure difference is maintained during decompression to keep the DAC closed. The GLS can also be used to load other gas (argon, neon, xenon, krypton, nitrogen and hydrogen).

These two systems are expensive and not portative. In the cryogenic case, the method requires a liquid He cryostat. The GLS is an expensive set-up available only in a few labs in France. At iLM, we are developing a new helium loading technology intended to be low cost and portative. This project was launched in 2015 under the impulse of Prof. D. Dunstan and Prof. A. San-Miguel. It was thought to help the spreading of helium as PTM in labs equipped with DACs, since the technique does not require any He cryostat neither a GLS. If the technique is not yet fully implemented, progress have been made during this work and are described below. We mention that on this project, we have worked in collaboration with Prof. D. Dunstan, Prof. A. San-Miguel, H. Diaf, and M. Mercury who manufactured the parts at the iLM workshop.

4.4.2 The New Portative Design

The technique is based on a very small DAC that we will call the subcell (see figures 4.15(a-c)). Its diameter is of ~ 1 cm, and appart from the diamond anvils, it is made of aluminium. The

subcell cannot be operated by itself for pressure application, and must be inserted in a membrane based cell that we will call the main cell (a picture of the main cell is shown in figure 4.15(d)). On the other hand, the small size of the subcell make it possible to insert it in a narrow rod intended to be introduced in a helium dewar. This allow for the prior loading of helium at liquid state in the subcell, through a Bowden cables system inspired by the existing cryogenic technique [189]. Thanks to the very small size of the subcell, the use of a He dewar (that can be easily ordered and delivered to the lab) is possible instead of a dedicated cryostat.

The subcell is equipped with four small screws allowing to close it. It is also pierced with two holes for the passage of the two Bowden cables. The system used for the loading of helium is schematized in figure 4.16(a). The subcell is installed at the end of the Bowden cables, inside the rod immersed in liquid He. Before loading, the subcell is slightly open. The pneumatic circuitry allows to introduce gaseous helium in the rod (through the Bowden cables), and to pump it out of the rod. After a purging step, helium is introduced and condense inside the rod: then, the subcell is closed using the cables (it is tightened against spring restoring force, see red parts in figure 4.16(a)). This traps the PTM inside the subcell. A picture of the top-head from where cables are tightened and helium is inserted is shown in figure 4.16(b). Electrical carbon resistors are installed inside the rod in order to confirm condensation by measurement of the resistance (which increases with temperature drop). A control bladder is available on the pneumatic set-up in order to check the condensation process. After He trapping in the subcell, its four screws are tightened to keep it close, and it is removed from the Bowden cables mechanism to be installed in the main cell for the high pressure run.

For cost reasons, we have performed most of our tests using liquid nitrogen instead of helium which is much more expensive. It also allows to verify the presence of nitrogen in the subcell by observation of its Raman vibron. This is not possible with helium since it is monoatomic. We have been able to perform the gas condensation step by measuring the condensed volume (in terms of number of bladders of ~ 2 L) as function of the condensation time, and of the overpressure imposed in the rod. Results are shown in figure 4.17. The observed saturation volume of ~ 4 bladders corresponds to the immersed volume of the rod, thus the maximum condensed value possible. It is clear that the highest overpressure, as well as the longest condensation time (~ 20 min), provides the best conditions to liquefy the PTM in the rod. The rod overpressure can be cycled before subcell closure in order to remove possible gas bubbles in the sample's hole. We encountered difficulties in the next step, in order to trap the PTM in the subcell. During our various attempts, we could not observe the presence of PTM in the subcell after closing it *via* the four screws. By observation of the diamond-gasket contact after loading tentative, we observed a remaining space from where the PTM can leak. We suggest that the tightening of the subcell through the four screws is unbalanced leading to PTM leaks between anvils and the gasket. We are now developing new strategies in order to screw the subcell in a more balanced way to ensure that the subcell stays closed.

Independently, we have worked on the design of the specific tungstene carbide seats of the main cell (these pieces are visible in figure 4.15(d)). It is designed to withstand the mechanical stress

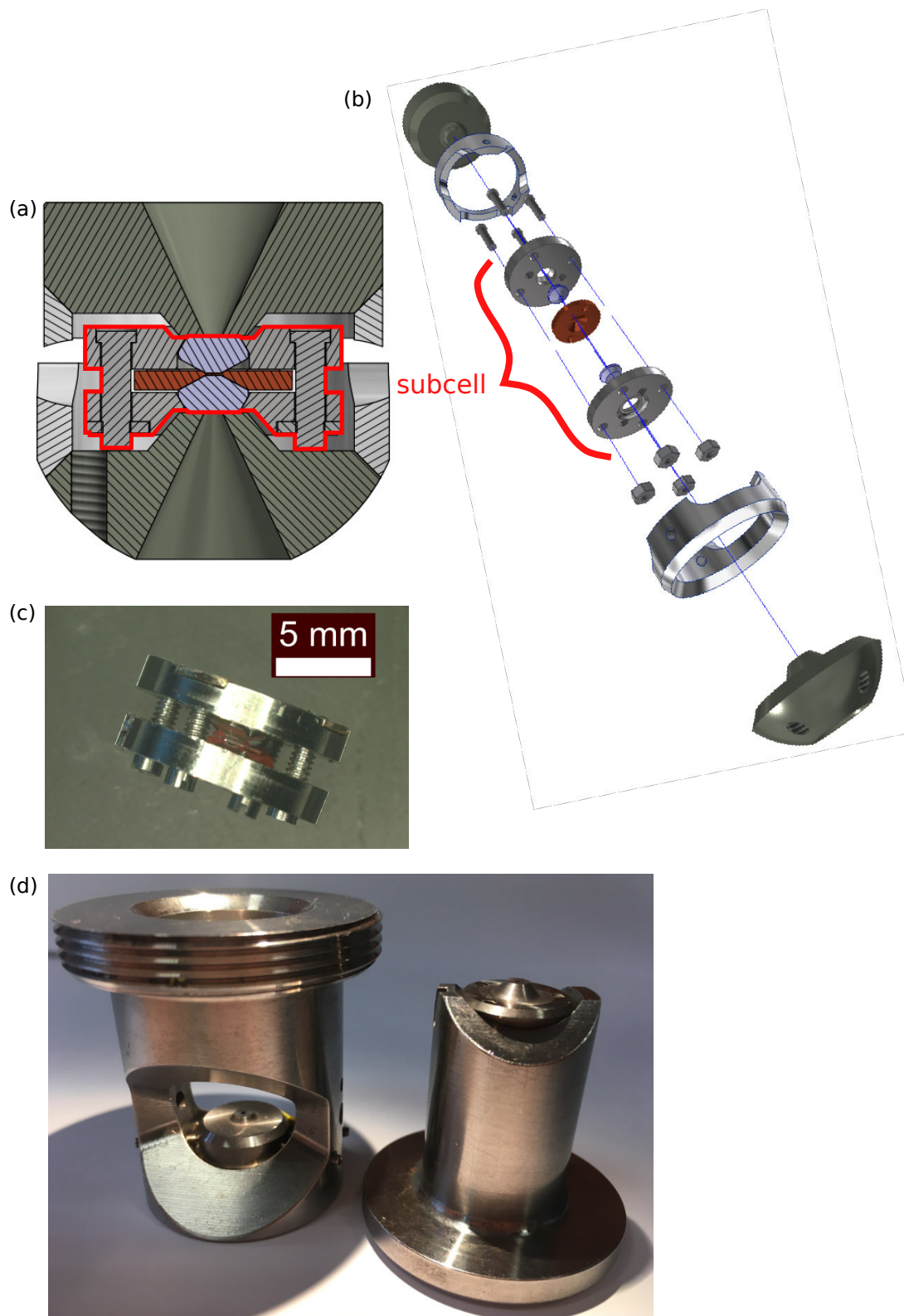


Figure 4.15 – (a) Mechanical drawing of the subcell (outlined in red) between the two tungstene carbide seats of the main panoramic cell. The adjustment crowns, fixed to the seats, are visible in a lighter shade around the subcell. (b) Exploded view of the subcell (indicated in red) and its four screws, along with the two seats of the main cell and the two adjustment crowns. (c) Picture of the closed subcell alone. (d) Picture of the main panoramic cell where the subcell can insert.

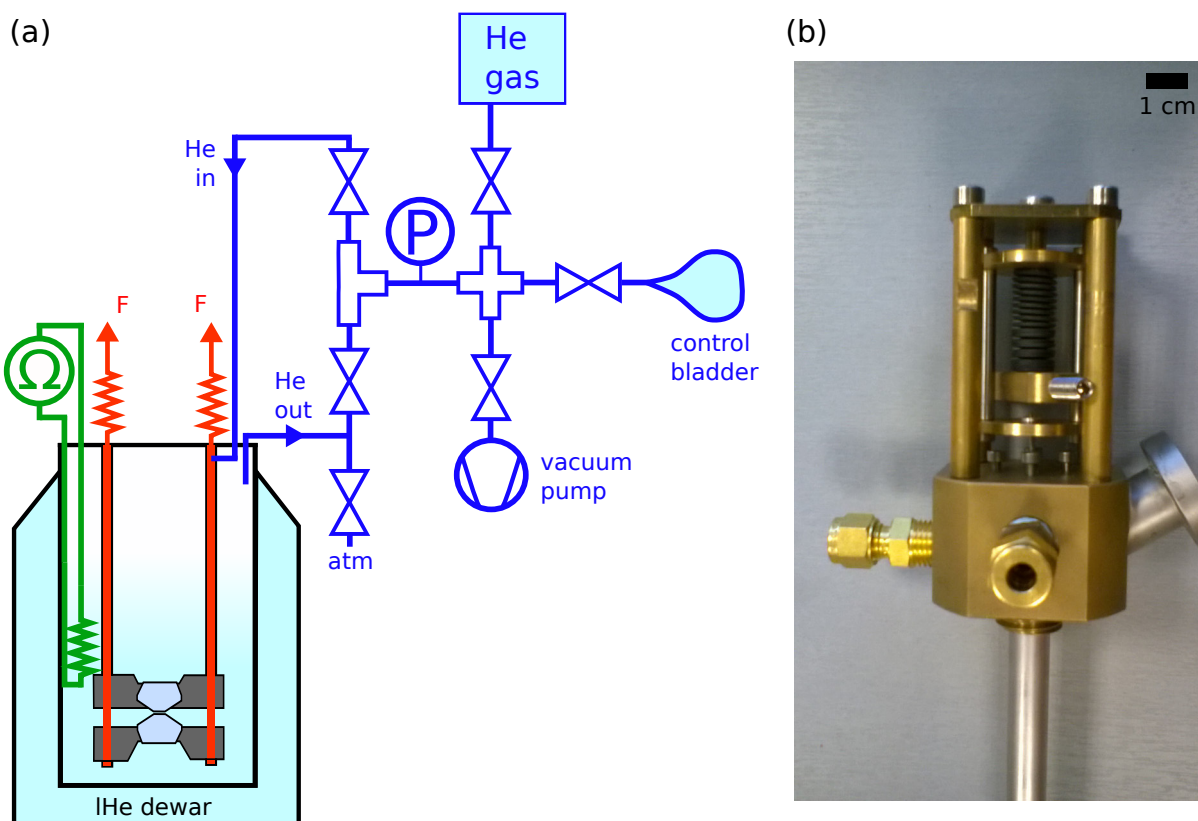


Figure 4.16 – (a) Schematics of the He loading apparatus. The subcell is installed in the rod which inserts into the liquid He dewar (lHe). Red elements corresponds to the mechanical part (Bowden cables and associated springs), green elements to the electrical part (temperature indication through carbon resistors measurement), and blue to the pneumatic apparatus for He loading. (b) Picture of the head of the rod, from where the two Bowden cables can be operated. Connections for He gas are visible.

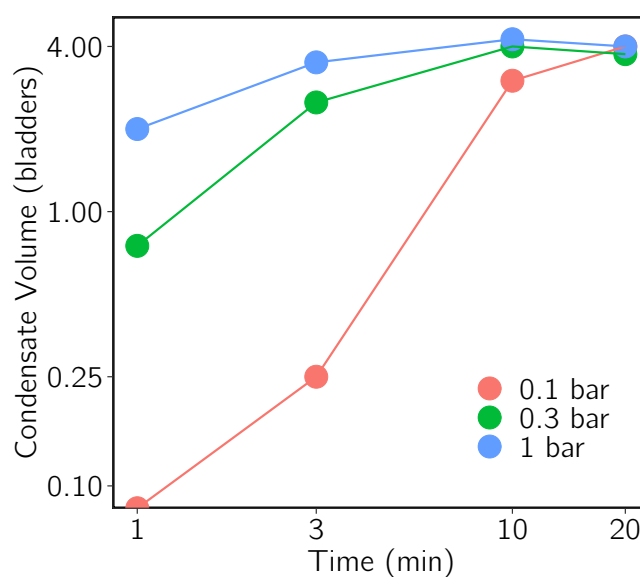


Figure 4.17 – Condensed nitrogen volume (expressed in bladders of ~ 2 L) as function of the condensation time for different nitrogen overpressures in the rod.

transmitted by the subcell's diamond anvils, as shown in the drawing of 4.15(a). Adjustment crowns mounted on the WC seats are intended to align the subcell correctly in the main cell for the high pressure run. Using silicon oil as test PTM, we performed a compression up to 4.5 GPa. A ruby chip was loaded in the subcell for pressure measurement. This has confirmed the correct functioning of the assembly: figure 4.18(a) shows the measured pressure as function of the membrane pressure of the main cell. We had to stop the compression near 4.5 GPa since the gaskets hole started to open up, as visible on figures 4.18(b,c) showing micrographs of the compression chamber at ambient conditions and at the maximum pressure achieved. This problem is probably due the very soft copper gaskets used. Indeed, usual gaskets could not be used with this assembly due to the very small size of the subcell, specific gaskets were prepared one by one at the workshop. Much higher pressure will be achievable with harder gaskets material (such as CuBe or stainless steel alloys) in the near future.

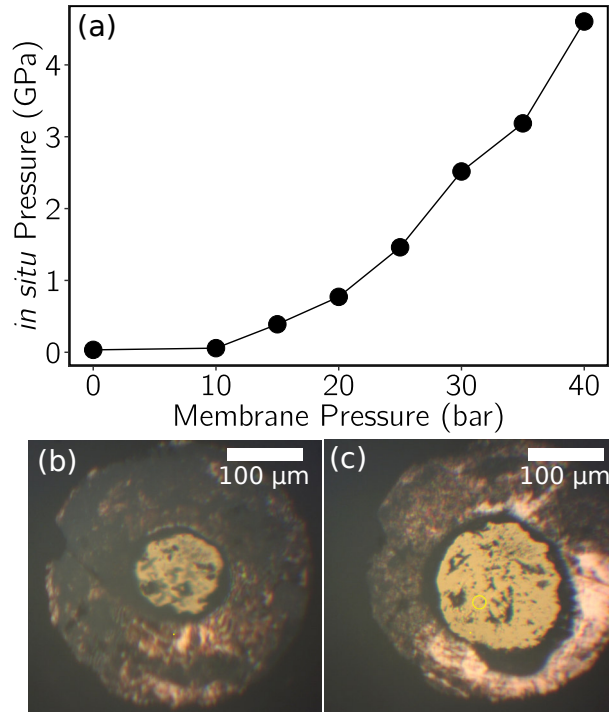


Figure 4.18 – (a) *In-situ* pressure as function of the membrane pressure during the test of the cell. Silicon oil was used as PTM. (b) and (c) are micrographs of the high pressure chamber at 0 and 4.5 GPa, respectively.

The next steps in the developpement is to successfully load the subcell with nitrogen and to perform the compression with it, then using helium. We should mention that this technique will be efficient to load other cryogenic fluids such as O₂, H₂, Ar, Xe and various mixtures.

Finally, as explained earlier, providing the best possible conditions for the study of suspended 2D-materials requires to load He at supercritical state. Helium critical point corresponds to the values ($T_c = 5.2$ K, $P_c = 2.24$ atm). While a pressure of 2.24 atm can easily be reached in the rod with our set-up, exceeding the critical temperature will require the use of a small heater resistor installed in the rod or on the subcell.

4.5 Conclusion

In this chapter are presented our developments for the study of suspended graphene samples at high pressure in DACs by *in-situ* Raman spectroscopy. Multiple strategies have been developed, based on holed supports where graphene can be suspended. We made attempts by machining a trench directly on the diamond anvil for graphene suspension, however, this has led to the diamond fracture. Thus, we focused our efforts on intermediate substrates designed for such suspension. We have identified that focused ion beam machining of pre-prepared substrates causes graphene damaging, while its mechanical cleaving for direct DAC loading is too hazardous for the fragile suspended sample. We have evolved our strategy in such way that the sample is transferred directly on a dedicated, holed SiO₂/Si substrates priorly installed on the diamond culet. This protocol allowed to reach (i) complete autonomy at iLM, and (ii) proof-of-concept experiments on thick samples of a few atomic layers. These preliminary experiments have brought unexpected results on the Raman signature evolution of suspended nanographites samples at high pressure. The success of these proof-of-concept experiments motivates to continue in the direction of thinner samples. We propose improvement paths for each techniques. Developments on the new portative helium loading will allow to study suspended 2D-materials in the best possible experimental conditions in the near future.

Interesting perspectives arise from our developed techniques. First, thanks to the aberration-corrected 100 \times microscope objective implemented on the Raman set-up, it will be possible to perform *in-situ* Raman mapping in the DAC. This will allow to compare Raman responses in suspended and supported regions, not only in terms of strain magnitude, but also in terms of strain inhomogeneities. This will bring new insights on the role of the substrate as well as a better understanding of the effect of high pressures on graphene, in both hydrostatic and quasi-hydrostatic environments. Possible bond changes in bilayer structures can be addressed in suspended configuration, with the opportunity to synthesized new nano-materials. Using intermediate substrates including through-holes, an eventual metastable bond change could be confirmed using *ex-situ* electron diffraction after the pressure cycle.

We emphasize that the techniques developed here can apply to other 2D-materials than graphene, as well as complex artificial stackings. Our loading protocols can be used for other *in-situ* experimental techniques, such as photoluminescence, optical absorption, electrical transport or even X-ray diffraction. As an example, pressure application on superconducting twisted bilayer graphene is able to tune its critical temperature [190]. The use of DACs in this context would allow to explore this effect up to much higher pressures. Investigations concerning the role of the substrate on the photoluminescence signal of monolayers TMDs at high pressure would be an interesting investigation. Indeed, in a work on WS₂ at high pressure, it was shown that the use of SiO₂/Si substrates leads to photoluminescence quenching at pressures as low as 4.5 GPa [191]. Finally, a very promising experimental perspective would be an optical absorption study of the pressure-induced collapse of a single suspended carbon nanotube, through *in-situ* spatial modulation spectroscopy [157, 192].

4.6 Summary

In this chapter are presented our experimental developments for the Raman study of suspended graphene at high pressure in DACs. Several strategies involving holed supports for graphene suspension were developed and tested.

- One of the strategies is based on the drilling of a small trench in the diamond anvil culet, intended for flake suspension by PDMS-stamping. This technique was used to study suspended nanographite samples at high pressure. However, the trench led to the mechanical weakening of the anvil, that have finally broke after a few pressure cycles.

- We have designed and used lithographed pre-cut silicon substrates including holes where graphene was priorly suspended by the PMMA-assisted method. Such systems proved to be very difficult to handle: while focused ion beam cutting of the substrates led to graphene damaging, its cutting by hand is too hazardous for the fragile samples suspended over it.

- Another strategy has been developed in which graphene is transferred by PDMS-stamping on holed SiO₂/Si substrate prorly installed on the DAC anvil. This technique proved to be efficient with experiments on thick samples as well.

Preliminary experiments on suspended nanographites shows the success of our methodology. Further works are needed to reach experiments on suspended monolayer graphene, that should focus on (i) the improvement of the dry transfer process for easier sample suspension, and (ii) the helium loading technique under development at iLM. We have contributed to the development of this new portative helium DAC loading system. Important milestones were reached, in particular on the proper functioning of the DAC designed for this loading method.

5

Pressure-Induced Microscale Buckling in Thin Graphite Flakes

Contents:

5.1	Introduction	128
5.2	Preparation and Loading of the Samples	129
5.3	The Mechanical Behaviour of Supported Nanographites at High Pressure	129
5.3.1	Sample Detachment from the Substrate at High Pressure	129
5.3.2	Effect of the Nature of the Pressure Transmitting Medium	130
5.3.3	Effect of the Sample Thickness	130
5.3.4	Raman G-band Evolution of the Nanographite Flakes at High Pressure	134
5.4	Discussion	134
5.4.1	Formation of Wrinkles at High Pressure	136
5.4.2	Role of the Pressure Transmitting Medium	136
5.5	Conclusion and Perspectives	139
5.6	Summary	141

5.1 Introduction

In this last chapter, we present experimental results obtained recently on supported nanographite samples at high pressure.

The idea behind these investigations is to study the out-of-plane deformations created in supported samples at high pressure. In chapter 1, we have mentioned that single and bilayer graphene undergo biaxial compression transmitted from the substrate by interfacial adhesion at high pressure [22, 24, 25]. Only a fraction of the substrate's pressure-induced strain $\varepsilon_S(P)$ is transmitted to graphene, such as $\varepsilon_G(P) = \alpha\varepsilon_S(P)$ where ε_G is the graphene in-plane biaxial strain and α is a phenomenological parameter that accounts for the incomplete strain transfer. The physical meaning of α is little known and very difficult to address experimentally. This quantity summarizes the graphene-substrate adhesion, friction, graphene bending and ripples formation, the difference in bulk moduli between graphene and its substrate, substrate's roughness and commensurability... α is a phenomenological parameter because the system is in fact too complex. The formation of an inhomogeneous strain field at the nanoscale due to rippling and/or sliding of graphene over the substrate has been proposed, providing in-plane strain dissipation [24] (see also section 1.4.1).

In the literature, graphene buckling and crumpling under compression have been reported in various works [15, 193]. Experiments where graphene is biaxially strained through thermal expansion mismatch with the substrate have shown the formation of buckling ridges [41, 42]. In ref. [41], the threshold buckling observed corresponds to a compressive strain of 0.21% on SiO₂. In high pressure experiments, such compressive strain value $\varepsilon_S(P) = 0.21\%$ at the SiO₂/Si substrate surface is achieved at pressure as low as ~ 0.7 GPa.

To assess such out-of-plane effects in supported graphene samples loaded in a DAC, only optical probes are possible – but they are intrinsically limited by the diffraction limit. Solely micrometer-scale and larger features can be observed by optical inspection and Raman spectroscopy, while buckling ridges and ripples in monolayer graphene are expected to be considerably smaller. Therefore, by optical inspection, such effects have never been observed in high pressure experiments on graphene. By studying thicker samples of nanometer thickness, that we call "nanographites", these out-of-plane deformations, wrinkles and buckling effects are likely to occur at a larger scale, primarily because of the larger bending stiffness of such systems. The use of SiO₂/Si substrate brings easier visualization of these displacements by optical inspection thanks to the contrast enhancement effect.

It is important to note that the interaction between n -layered graphene samples and the oxydized silicon substrate strongly depends on n [22, 108]. A transition takes place at $n > 2$, from which the bending modulus of graphene is large enough to avoid the conformation of the n -layered system [108]. All the studied thin graphite samples in this chapter correspond to the $n > 2$ case. In such conditions, the PTM is susceptible to wedge between the sample and the substrate surface, thus, the PTM plays an important role. This chapter is an exploration of the evolution of wrinkles, folds and other microstructures arising due to changes in the nanographite curvature

at high pressure. The interplays between these mechanical effects and the substrate, the PTM nature and state, as well as the thickness of the samples are studied. We try to provide a global picture explaining our experimental observations, and discuss the possible perspectives of this preliminary work.

The work presented here have been carried out in collaboration with I. Rodrigues do Amaral from the Universidade Federal do Ceará (Fortaleza, Brazil), who spent the present year to work at iLM in Lyon.

5.2 Preparation and Loading of the Samples

The thin graphite samples were obtained by mechanical exfoliation and deposited on a PDMS stamp for later inspection and transfer. Flake thicknesses were determined using AFM (Asylum Research AFM set-up) in tapping mode, performed directly on the flakes laying on the PDMS stamp (before transfer and high pressure runs). The number of layers is computed by dividing the measured thickness by $h = 3.35 \text{ \AA}$, the interlayer distance of graphite.

The DAC loading of the samples was performed *via* the protocol we have developped and described in section 4.2.3, with the difference that the substrate does not include any trench or hole. It consists in flat $50 \text{ }\mu\text{m}$ thick SiO_2/Si wafers cut into small pieces of $\sim 60 \text{ }\mu\text{m}$ by side using the dicing saw set-up (Disco DAD3220). The loading is performed in two steps: (i) a small square substrate is glued on the bottom diamond anvil using the UV-curing glue (see section 4.2.3 for details), and (ii) the priorly characterized nanographite sample is transferred on its surface using the PDMS-stamping set-up we have implemented. Finally, the PTM is loaded following the protocols described earlier, in section 2.3.3.2.

5.3 The Mechanical Behaviour of Supported Nanographites at High Pressure

5.3.1 Sample Detachment from the Substrate at High Pressure

Figure 5.1 shows pictures of a nanographite sample at various pressures up to 4.2 GPa . The PTM used was 4:1 methanol-ethanol. Multiple experiments were done on nanographite samples using 4:1 methanol-ethanol, giving similar results. We will describe in detail one of them. The measured sample thickness was approximately 17 nm – corresponding to ~ 51 layers (51L). The sample is easily spotted due to its darker blue appearance, arising from contrast enhancement provided by the SiO_2/Si substrate (see section 2.2.1.1 for details). Looking closely at pictures in figure 5.1 as pressure increases, one observes the progressive appearance of narrow lines with different contrast on the images. These lines correspond to regions where the sample starts to unbind from the substrate, probably due to the formation of wrinkles. The surface density of these wrinkles increases with pressure: the effect is particularly visible in the picture obtained

at 3.5 GPa where light interference effects are visible in the lower region of the sample. These interferences indicate the existence of narrow spaces between the sample and the substrate surface, with a thickness comparable with visible spectrum wavelengths. Ultimately at 4.2 GPa, the sample is completely detached. Indeed, the contrast enhancement arising from the SiO₂/Si substrate is not observed anymore and the flake appears dark. Moreover, the edges of the flake are folded on the last image obtained at 4.2 GPa. The sample unbinding from the substrate at high pressure is irreversible: during pressure decrease, it does not resettle back and continues to appear dark as observed beyond 4 GPa. Therefore, at the end of the high pressure run, the DAC opening often led to the sample loss or displacement. In some cases, the flake ended up lying on the diamond anvil surface. We should note the appearance of cracks on the substrate surface in the last micrograph of 5.1. This corresponds to the delamination effect of the substrate's oxide layer already discussed in section 3.2.3. Note that we have numerically improved the contrast in all micrographs presented here.

In order to identify whether the unbinding effect is observed using other pressure transmitting media, we have carried out supplemental experiments presented in the next section.

5.3.2 Effect of the Nature of the Pressure Transmitting Medium

Samples of comparable thicknesses (between 20 and 40 layers) were selected for experiments using nitrogen, distilled water, and paraffin oil as PTMs. Micrographs of the studied samples at various pressure are shown in figure 5.2(a), (b) and (c) for the three PTMs used, respectively. Surprisingly, no unbinding effect similar to the one observed with alcohol PTM is visible. Only in the case of distilled water PTM, subtle changes can be seen in the early stage of the compression, but not comparable with the spectacular detachment effect observed using alcohol PTM, despite the higher pressure value reached.

Since the unbinding effect was observed solely using the 4:1 methanol-ethanol mixture as PTM, we have performed experiments using (i) pure ethanol, and (ii) pure methanol as PTM. Samples of approximately 30 layers were studied. The obtained pictures are shown in figure 5.3. Interestingly, wrinkles formation is observed in both cases, but is clearly stronger in the case of pure methanol PTM, figure 5.3(b). Using ethanol PTM (figure 5.3(a)), the total unbinding of the sample is not observed up to 6.2 GPa, while for pure methanol the sample is completely detached at $P = 4.1$ GPa. Since pure methanol PTM seems to promote the observed detachment effect, we have continued to use this PTM in order to study the role of the sample thickness.

5.3.3 Effect of the Sample Thickness

Four samples of different thicknesses (9L, 30L, 60L and 110L) were studied at high pressure using pure methanol PTM. The optical micrographs obtained are shown in figure 5.4(a), (b), (c) and (d), respectively. As pressure increase, the development of wrinkles followed by the complete

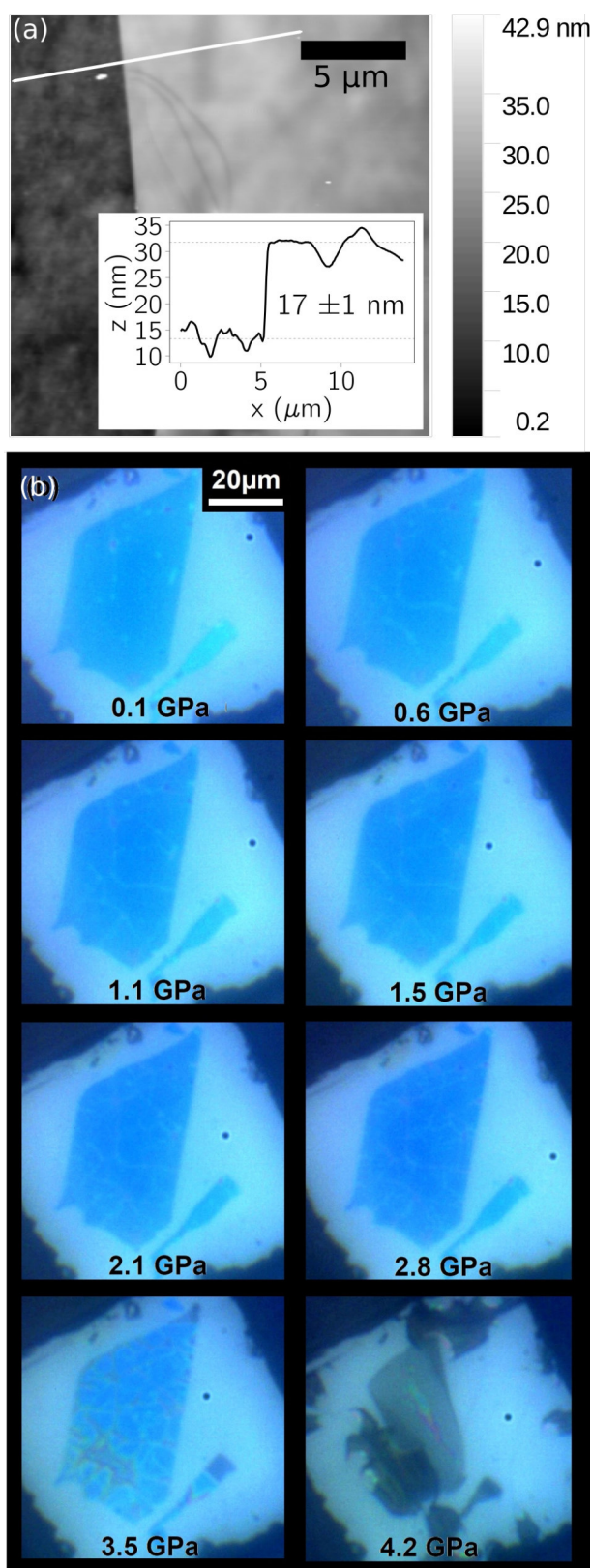


Figure 5.1 – (a) AFM topographic image at ambient conditions. The inset shows the height profile corresponding to the white line plotted on the AFM scan. (b) Optical micrographs of the supported 51L nanographite sample at various pressures using the 4:1 methanol-ethanol mixture as PTM. The progressive unbinding of the sample from the substrate is observed. At the highest pressure, the fracture of the oxyde layer is visible (see text). A long working distance (20 mm) 50 \times mitutoyo objective is used.

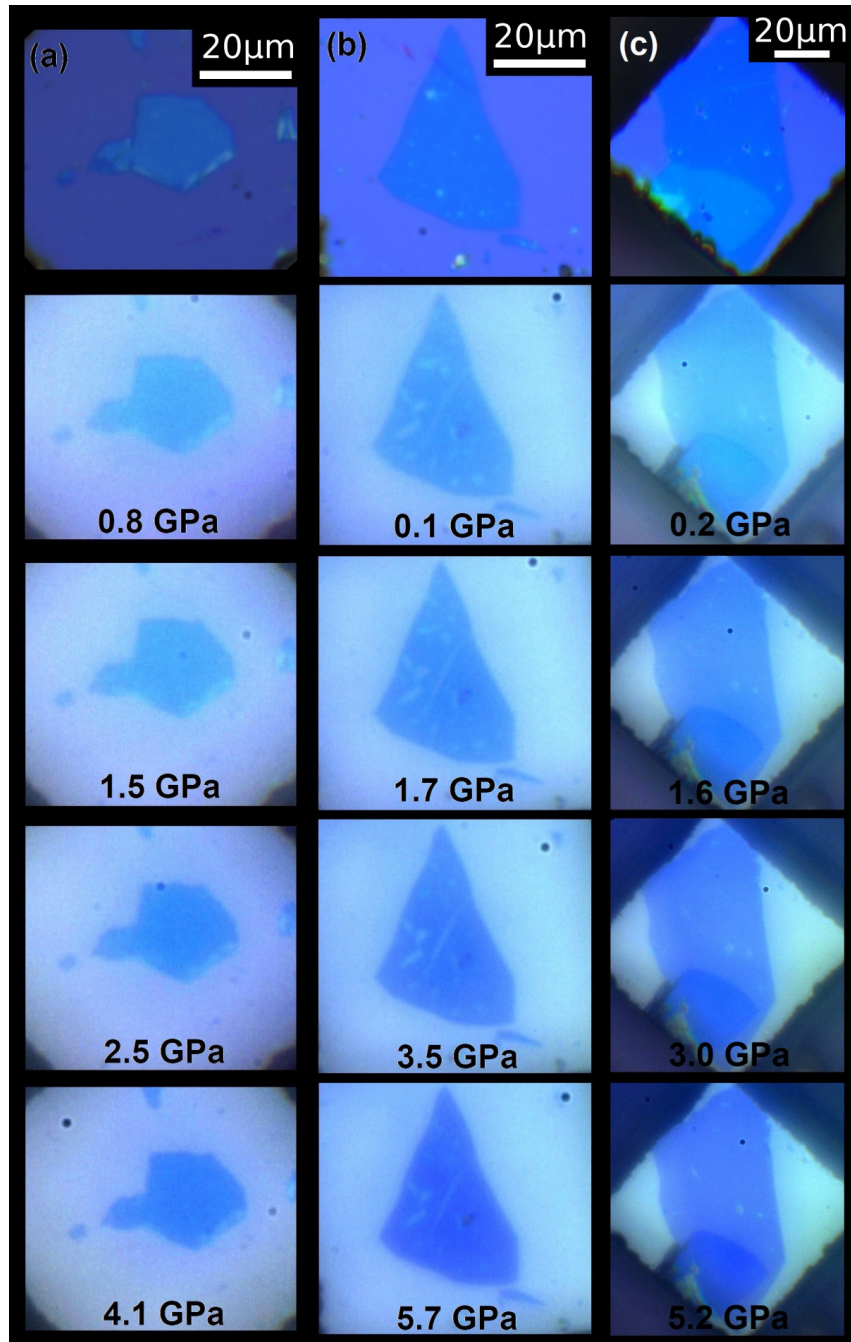


Figure 5.2 – Micrographs of nanographite samples at various pressures using (a) nitrogen PTM, (b) distilled water PTM, and (c) paraffin oil PTM. Samples thicknesses are respectively 24L, 30L and 21L.

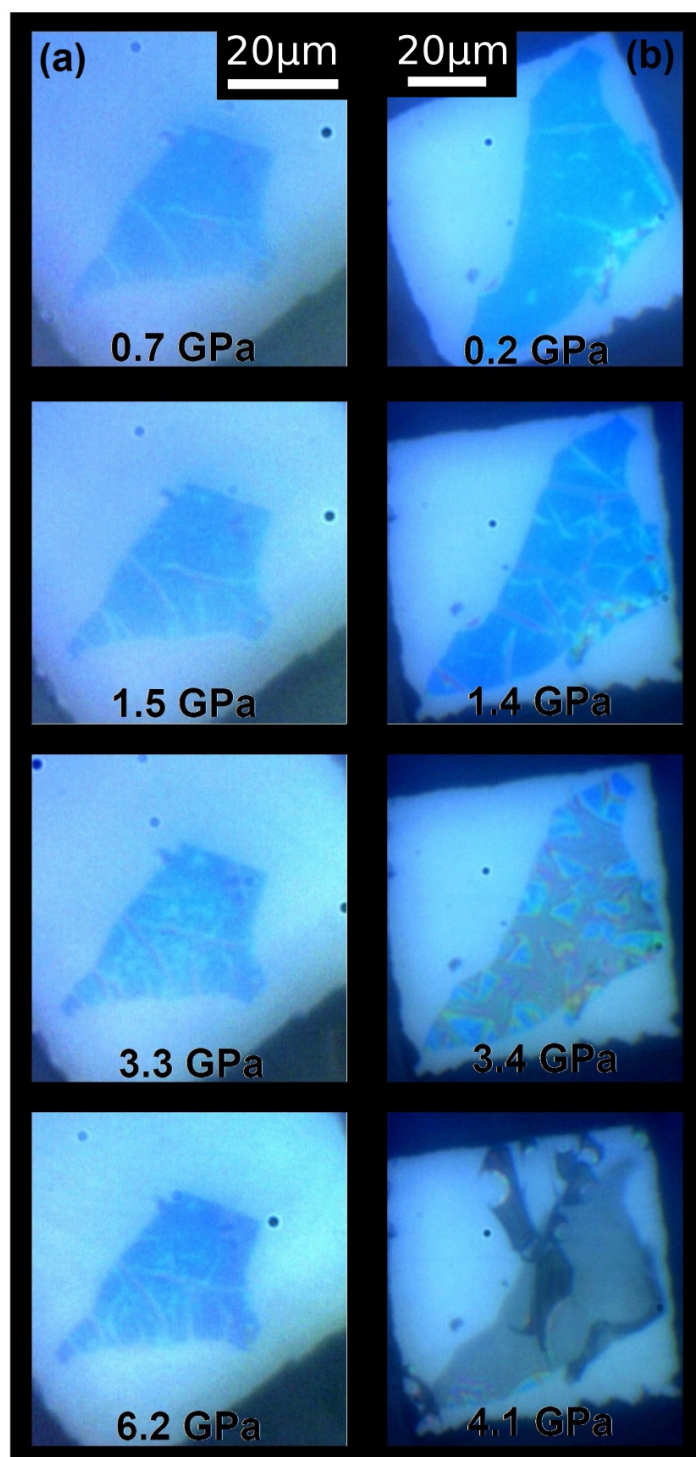


Figure 5.3 – Micrographs of ~ 30L nanographite samples using (a) pure ethanol PTM, and (b) pure methanol as PTM.

detachment of the sample are observed for all flakes studied. Two important conclusions emerge from figure 5.4: (i) the size of the individual channels observed between the flake and the substrate increases with sample thickness (ranging in width from $\sim 3 \mu\text{m}$ up to $\sim 10 \mu\text{m}$ for the 9L and 60L samples at $P \sim 3.5 \text{ GPa}$, respectively), and (ii) the final detachment is observed at $P \simeq 4 \text{ GPa}$ regardless of the sample thickness. For the thicker sample (figure 5.4(d)), the formation of very broad channels between the flake and the substrate leads to strong light interference effects.

5.3.4 Raman G-band Evolution of the Nanographite Flakes at High Pressure

Since we observed the formation of wrinkles, followed by the complete detachment of the sample using methanol PTM whilst these phenomena were not observed using the other PTMs tested, we have performed *in-situ* Raman measurements to investigate the mechanics of the nanographite samples at the interatomic bond scale. We have measured the Raman G-band evolution of a supported nanographite at high pressure using nitrogen and the 4:1 methanol-ethanol mixture PTMs for the sake of comparison. The sample thickness is approximately 8 nm, corresponding to ~ 24 layers. The G-band evolution observed with pressure is plotted in figure 5.5 for both PTMs used. The black solid line in figure 5.5 corresponds to the evolution reported for bulk graphite [37]. We have computed the expected G-band shift for a sample in total adhesion on the SiO_2/Si substrate. The $\varepsilon_S(P)$ evolution was deduced from the silicon equation of state from ref. [171], and was translated in terms of the G-band Raman shift considering a graphene layer with in-plane compressive biaxial strain $\varepsilon_G = \varepsilon_S$ through eq. (1.13) (see section 1.3.3.1 for details). The result is shown in figure 5.5 (black dashed line).

For both PTMs, the G-band frequency evolution of the sample is close to the evolution reported for bulk graphite (black solid line). Therefore, no significant strain transfer arises from the substrate to the nanographite flake. This result is expected since previous works have shown that strain transfer happens for single and bilayer samples only, while the bulk evolution is retrieved for flakes as thin as 3-layers graphene [22, 25] (see also section 1.4.1). The slightly larger shift observed with nitrogen PTM beyond its solidification point (2.4 GPa) may be related to a small strain transfer contribution from the solid PTM, as we have shown in chapter 3.

5.4 Discussion

In the case of pure methanol PTM, we have identified a progressive unbinding of the nanographite samples at high pressure, which starts by the formation of wrinkles. Flakes detached from the substrate near $\sim 4 \text{ GPa}$ regardless of the number of layers. This effect is unexpected, since high pressure application would intuitively lead to *increase* the sample-substrate interaction rather than to decrease it. The effect is observed in pure methanol PTM and using the 4:1 methanol-ethanol mixture, whereas no similar mechanism is visible with the three other PTMs tested (nitrogen, distilled water, and paraffin oil). Using pure ethanol PTM, wrinkles are observed but

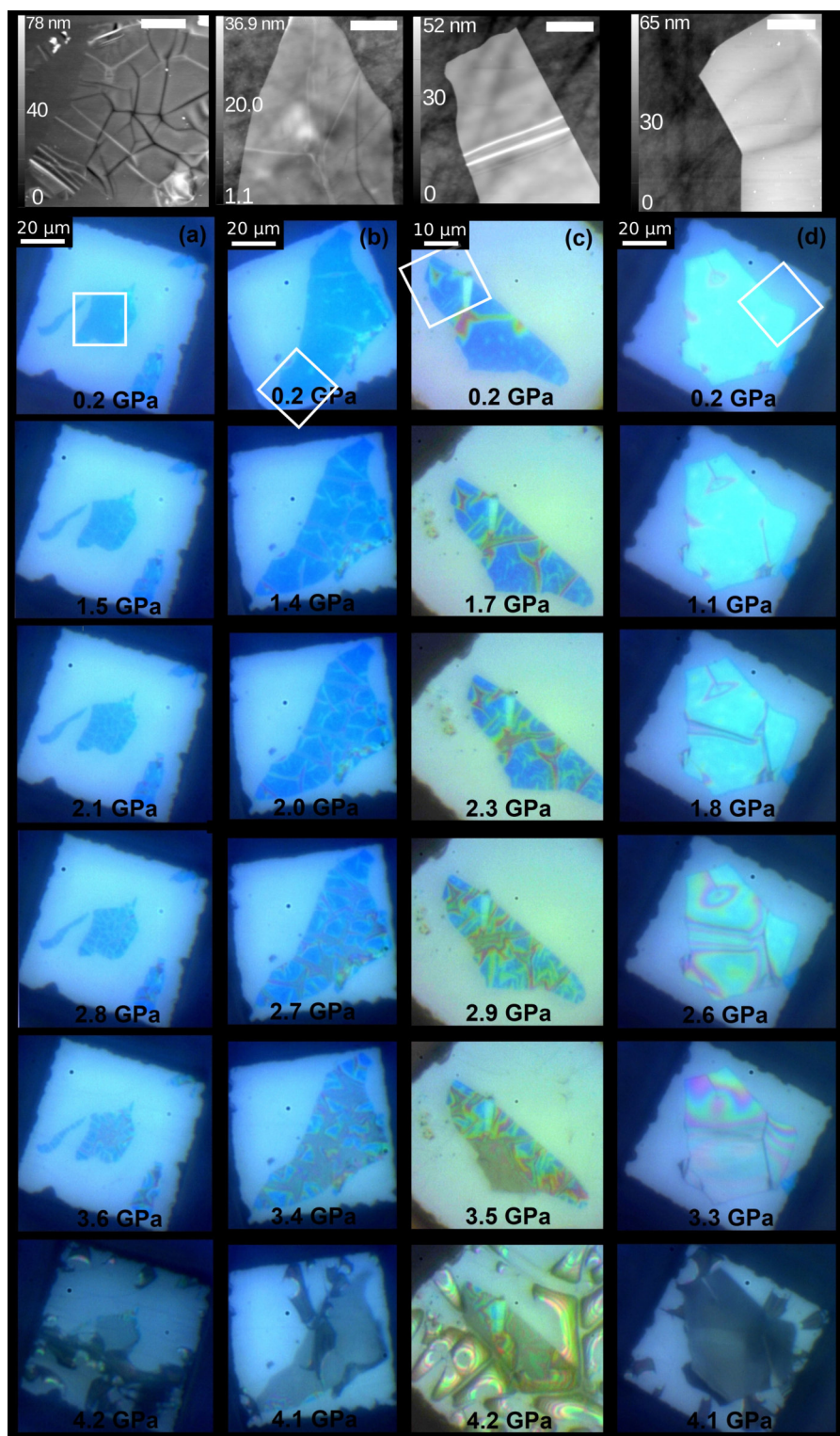


Figure 5.4 – AFM topographic images obtained at ambient conditions (scale bars correspond to 5 μm on every scans), and micrographs of the corresponding nanographite samples at various pressure in pure methanol PTM (locations of the AFM scans are shown as white frames in optical micrographs). Sample thicknesses are (a) 9L, (b) 30L, (c) 60L and (d) 110L. For all samples, the unbinding effect is visible. At the highest pressures, the fracture of the oxyde layer is observed as cracks on its surface. In (c), colors are different due to the use of the 100 \times aberration-corrected microscope objective with higher numerical aperture.

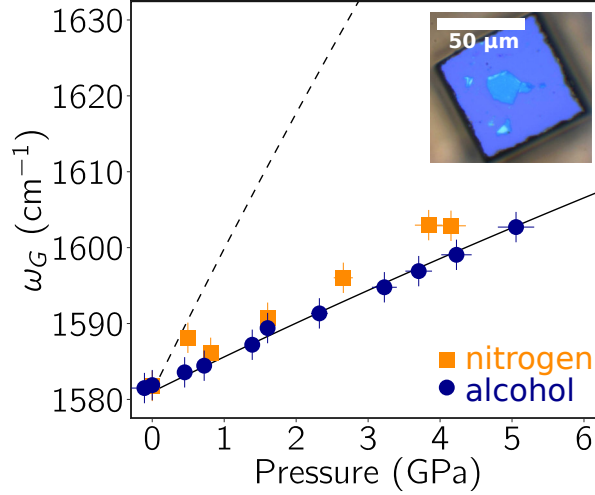


Figure 5.5 – Pressure evolution of the G-band frequency of a supported 24L sample using nitrogen (orange squares) and 4:1 methanol-ethanol (blue circles) as PTM. The inset shows a micrograph of the sample studied on the SiO₂/Si substrate. The black solid line corresponds to the bulk evolution reported by Hanfland *et al.* [37]. The black dotted line corresponds to the expectation for perfect adhesion on the SiO₂/Si substrate (see text).

no complete detachment of the sample is seen. In the following sections, we will try to propose explanations for the observed phenomena.

5.4.1 Formation of Wrinkles at High Pressure

By Raman spectroscopy, we observed that the G-band frequency evolution with pressure for our supported nanographite flakes is similar to the one of bulk graphite. However, the silicon substrate is much more compressible than graphite in the in-plane direction. More precisely, in the pressure range studied, we have $\varepsilon_S(P)/\varepsilon_G(P) \simeq 4$ where ε_S and ε_G are the substrate and nanographite in-plane biaxial strain, respectively. In other words, in our experiments, when a given distance at the substrate surface is compressed by a value δ , the interatomic distance in the nanographite sample is compressed by only $\sim \delta/4$. Therefore, the observed formation of wrinkles is not surprising: displacements imposed by the substrate contraction does not lead to compressive strain, but are completely dissipated through out-of-plane displacements of the membrane over it. These displacements are likely to be imposed from the substrate at very precise locations of the interface, where the sample is in direct contact with the substrate. Indeed, as mentioned before, thick membranes studied here do not conform on the nanoscale rugosities of the SiO₂/Si substrate's surface [22, 108].

5.4.2 Role of the Pressure Transmitting Medium

In regard with our proposed explanation for the formation of wrinkles, the effect of the PTM is puzzling. Why don't we observe wrinkles formation and detachment of the sample with the other PTMs studied (nitrogen, water, and paraffin oil)?

A first criterion to address the role of the PTM is its solidification at high pressure. Intuitively, the presence of a solid PTM at the top surface of the nanographite substrate may hinder the development of out-of-plane displacements in the flake. Furthermore, a solid PTM cannot diffuse inside the channels formed between the sample and the substrate by wrinkles: this could also limit the propagation of such channels. Pure ethanol, distilled water and nitrogen solidifies at pressures as low as 1.9 GPa, 1 GPa and 2.4 GPa, respectively [151, 152, 194, 195]. Paraffin oil is reported to solidify at higher pressures, near 5 – 7 GPa¹ [196]. Pure methanol is expected to solidify near 3.5 GPa, but is commonly found in a superpressed state beyond this pressure [197]. In our case, the methanol superpressed liquid state was always achieved, since no indication of solid formation (crystal or amorphous) was observed [197].

It appears clearly that the solid PTM hypothesis alone cannot explain the experimental results since the unbinding effect is not observed using paraffin oil PTM, although it remains liquid in the pressure range studied. Wrinkles and detachment are not observed neither in nitrogen PTM at liquid state ($P < 2.4$ GPa), whilst it is clearly observable in pure methanol in this pressure range (see figures 5.3 and 5.4). Therefore, the explanation does not lie in the PTM state only, and may be more related to the nature of the PTM-graphene interaction.

An interesting way to visualize the data obtained is to consider the quantity S_u/S_T , that is, the detached area S_u with respect to the total area S_T of the flakes as function of pressure. This plot is shown in figure 5.6 for all nanographite flakes studied, where the quantity S_u/S_T was evaluated by image analysis. The corresponding error bars were defined by different boundaries between suspended and supported zones. Interestingly, in figure 5.6, the pressure evolutions of S_u/S_T are similar for all flakes studied in pure methanol PTM (as well as the 4:1 methanol-ethanol mixture), regardless of their thickness. This suggests a surface effect, rather than a purely mechanical effect since the system's thickness does not play a significant role. The formation of an adsorption layer of PTM under the sample is favored by the wrinkles as entry points for the PTM molecules under the sample. This mechanism may explain our observations. Indeed, *ab-initio* calculations and experiments in the literature reports that the methanol-graphene interaction is stronger than the methanol-methanol interactions [198, 199]. This particularity is reported to lead to the formation of a complete adsorbed methanol monolayer before the development of supplemental adlayers [198, 199].

We have checked that the formation of wrinkles and the final unbinding effect is not observed by simple immersion at ambient pressure in methanol. The pressure increase plays therefore a preponderant role, at least in the initial formation of wrinkles. Our interpretation of the observed effect is the following: (i) the strain mismatch between the substrate and the nanographite sample leads to the formation of wrinkles and buckling as explained in section 5.4.1, (ii) methanol molecules diffuse in the channels created under the nanographite flake, (iii) due to the stronger interaction of methanol with graphite surface rather than with other methanol molecules, this intercalation tends to enlarge the channels, finally leading to the complete unbinding observed.

¹Using paraffin oil PTM, we did not observe any changes in the FWHM of the ruby fluorescence lines, nor in the spectral difference between the two lines R1-R2 that could have indicated the onset of non-hydrostatic conditions in the pressure range studied (up to 5.2 GPa).

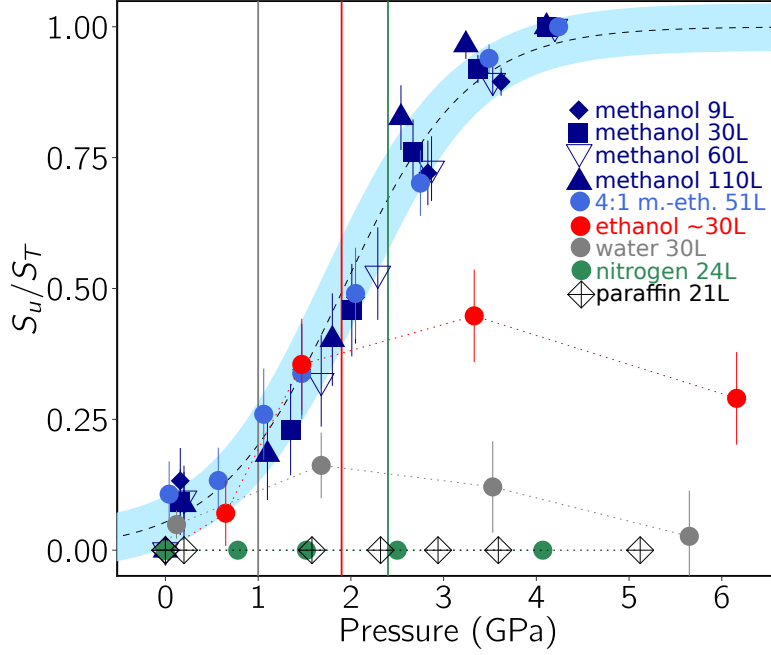


Figure 5.6 – Evolution of the detached area (S_u) over the total area (S_T) of the nanographite flakes as function of pressure for the various experiments performed (see legend). The black dashed line surrounded by light gray corresponds to a sigmoid fit the data "methanol 30L", as a guide for the eye highlighting the similar evolution found for all samples in pure methanol PTM. Vertical lines corresponds to the solidification pressures of water (in grey), ethanol (in red) and nitrogen (in green).

In the scenario that we propose, wrinkles should form for all PTMs used. Looking at the top AFM images of the samples at ambient conditions in figure 5.4, initial wrinkles exist but are not – or hardly – visible by optical microscopy after transfer on the SiO_2/Si substrate. This is most probably due to their very small, submicronic size. Thus, wrinkles may also be formed during compression in the other PTMs studied, but stay too small to be visible by simple optical inspection in the DAC, whereas the use of alcohol PTM reveals these wrinkles by enlarging them, as described.

In order to test our hypothesis, we have performed an experiment with a 48L (thickness 16 ± 3 nm — 48 ± 9 layers) nanographite flake supported directly on the diamond anvil instead of SiO_2/Si substrate (still using pure methanol as PTM). Since the compressibility of diamond is of the same order of the in-plane compressibility of graphite, a strong strain dissipation through wrinkling is not expected. Micrographs obtained are shown in figure 5.7, where no wrinkles are observed compared with the case of the SiO_2/Si substrate. Nevertheless, from 5.2 GPa, a partial detachment of the flake is observed, starting at the sample edge where methanol is more susceptible to insert under the flake. These observations are in clear agreement with our proposed explanation.

In the light of this possible scenario, it is instructive to reconsider the effect of the PTM state. In figure 5.6 for pure ethanol PTM, the ratio S_u/S_T increases with pressure before PTM solidification. Indeed, in figure 5.3 up to 1.5 GPa, observations are qualitatively similar for pure ethanol and pure methanol PTMs, while beyond ethanol solidification point (1.9 GPa), large

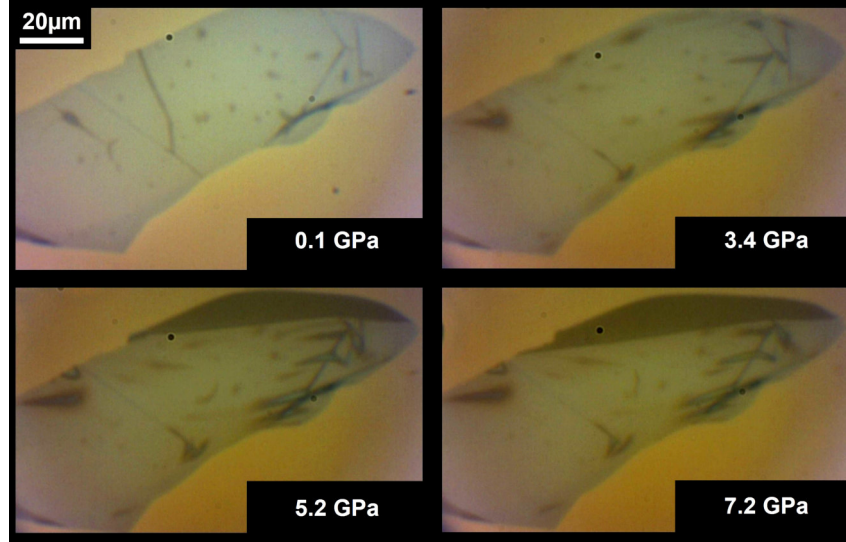


Figure 5.7 – Micrographs of a 16 ± 3 nm (48 ± 9 L) nanographite samples supported on the diamond anvil at various pressure. The PTM used was pure methanol.

wrinkles and channels are observed in the case of methanol whereas it is not observed in ethanol PTM. Considering the case of water PTM, very subtle effects are observed at the onset of the compression, before its low solidification pressure at ~ 1 GPa, see figure 5.2(b). Furthermore, it has been reported that water plays an important role in wrinkles formation in graphene [200]. Consequently, a similar mechanism of PTM insertion to the one observed for pure methanol is probably in play with these two other PTMs, although their crystallization hinders the detachment to progress.

When nitrogen is used as PTM, no sign of detachment was observed, even in the liquid PTM range as already mentioned. This may be related to the weaker interaction of nitrogen with the graphite surface, since it is a non-polar substance. Using the paraffin oil PTM, which consists in carbon chains of the type C_nH_{2n+2} ($10 < n < 14$), no wrinkles and unbinding were observed either. By the same arguments, these molecule are apolar and their interaction with the nanographite surface is expected to be weaker than for polar substances. Furthermore, the insertion of paraffin oil between the flake and substrate may be unfavoured by the large size of its molecule. Its high viscosity under pressure may also play a role.

5.5 Conclusion and Perspectives

In this chapter are presented a series of experiments on supported nanographite flakes at high pressure. Through the use of SiO_2/Si contrast-enhancing substrates and pure methanol PTM, we have observed (i) the pressure-induced formation of wrinkles in the thin graphite samples, and (ii) its total detachment from the substrate beyond ~ 4 GPa. By varying the flake thickness, the PTM and the substrate used, we were able to get insights on the observed phenomena. In the picture proposed, the compression of the substrate leads to out-of-plane strain relaxations in the flake, while the insertion of alcohol PTM in these wrinkles leads to their expansion and

finally to the sample detachment. The chemical interaction between the PTM and graphite surface seems to play an important role, since the effect is observed with alcohol PTMs while it is not observed using non-polar nitrogen and paraffin oil PTMs. The solidification of the PTM hinders the phenomenon, due to the absence of diffusion of the PTM molecules under the flake, and since the solid PTM opposes to the out-of-plane relaxations of the flake. We could not conclude on the presence of the detachment effect for water PTM, which solidifies at the very low pressure of ~ 1 GPa.

The nanographite samples studied here are intermediate between the bulk graphite and atomically thin systems such as single or bilayer graphene. Thus, their response to pressure is singular, as illustrated in figure 5.8. At the atomic scale, their perturbation due to pressure is similar to the bulk one, as they follow the same equation of state $\varepsilon_G(P) = \varepsilon_{bulk}(P)$. However, at larger scales, pressure-induced morphological changes occur. These changes, illustrated as two wrinkles in the case $n > 2$ in figure 5.8(b), are induced by the environment geometrical evolutions at high pressure. The presence of the substrate plays the preponderant role, but a solid PTM may also have strong influence, as observed in this chapter as well as in section 4.3. It is interesting to extrapolate the observation on nanographites towards supported monolayer graphene at high pressure (see figure 5.8(c)). No wrinkles or detachment have never been observed by optical inspection in that case. This can be explained by considering that the typical size of their out-of-plane displacements matches the typical curvature of the SiO_2/Si substrate ($\sim 0.4 \text{ nm}^{-1}$) [22, 201]. Consequently, a strain transfer can effectively occur from the substrate to the graphene – at least partially.

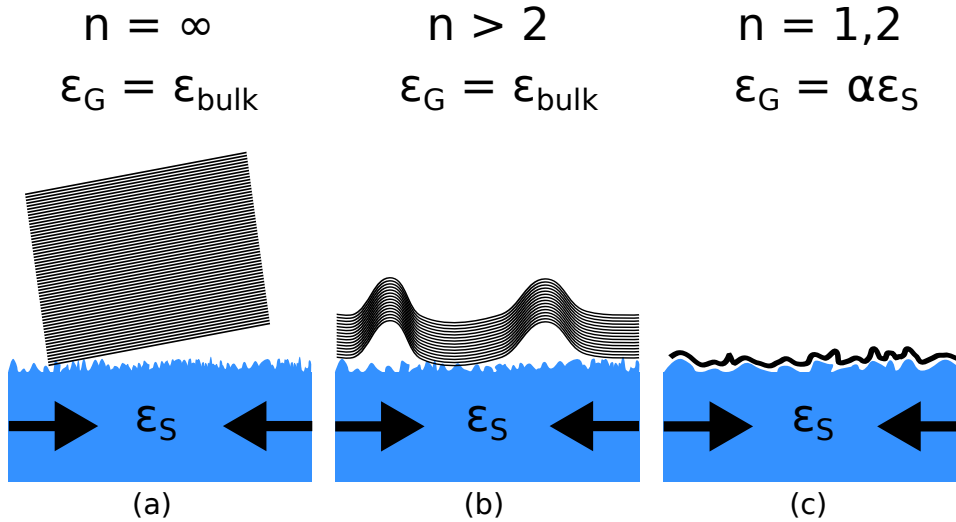


Figure 5.8 – The effect of dimensionality in supported graphene layers at high pressure. (a) $n = \infty$ corresponds to the bulk case in which the substrate has no influence. (b) corresponds to the nanographite flakes studied in this chapter ($n > 2$). In (c), for $n = 1, 2$, the bending stiffness of the system is low enough for its conformation [22, 108]. An actual strain transfer occurs from the substrate to single or bilayer graphene, such as $\varepsilon_G = \alpha\varepsilon_S$, where ε_S represents the biaxial strain at the substrate’s surface at pressure P .

The next step in this work is the modelling of the observed effects by membrane mechanics models [108]. This will allow to quantitatively describe the buckling effects, and going further in

the understanding of the pressure effect both on nanographites and atomically thin systems. In addition, experiments using helium as PTM are desirable, since the small size of helium atoms, its weak interaction with graphite and its liquid state up to 12 GPa may help to confirm or refute the proposed mechanism. Moreover, similar experiments on other few-layer 2D-systems such as MoS₂ or hBN could provide new insights on the wrinkles and detachment phenomena, since their bending rigidity and chemical interaction with the PTMs are different from the case of the thin graphite samples studied here.

Interesting perspectives arise from the observed phenomena. In the experiments presented, wrinkles are randomly distributed over the flakes surface. To go further, specifically engineered substrates [200] may be realized to produce deterministic wrinkles in graphene layers at high pressure. This could allow to spatially modulate the chemical interactions of graphene with its environment by pressure tuning, since its chemical reactivity increases with curvature [202]. Using methanol PTM, the interplay of wrinkles with the piezo-doping effect identified in chapter 3 could be studied. Finally, the observed detachment phenomenon could also have interesting applications in tribology, where the absence of mechanical contact can reduce wear of parts withstanding very high loads [17].

5.6 Summary

In this chapter, recent results obtained on supported thin graphite samples at high pressure are presented:

- The use of contrast-enhancing SiO₂/Si substrate at high pressure allowed to observe a buckling effect when alcohol PTM is used, which manifests through the pressure-induced formation of wrinkles. This is followed by the complete detachment of the flake from the substrate in liquid PTM.

- Through experiments performed with different PTM, sample thicknesses and substrates, it is shown that the detachment is not only from mechanical origin, but the state and the chemical nature of the pressure transmitting medium plays an important role. We propose a mechanism involving the intercalation of a PTM adlayer beneath the sample, promoted by wrinkles.

- Results obtained provide new insights into the mechanisms of strain relaxations in supported low-dimensional systems at high pressure, from nanographites to atomically thin graphene samples.

General Conclusion

In this work, we investigated graphene and nanographite samples at extreme pressures using *in-situ* Raman spectroscopy in diamond anvil cells. We observed that the sample's environment plays a central role in its high-pressure response. Our work focused on (i) the impact of the chemical nature and physical state of the pressure transmitting medium (PTM), and (ii) the role of the substrate on the system's response to pressure. The strategy of this study was to uncorrelate the effects of (i) and (ii).

In the first part of this work, we studied the isotopically labeled $^{12}\text{C}/^{13}\text{C}$ bilayer graphene sample at high pressure, supported on a SiO_2/Si substrate. Thanks to the isotopic substitution, it was possible to follow the Raman response of each layer independently during compression. In order to decorrelate the effects of the PTM and of the substrate, the use of the isotopic labeling is an interesting strategy since each layers reacts according to its direct environment. Our approach allowed observing a strain mismatch effect between the two graphene sheets in the solid PTM regime, while no mismatch was observed in the liquid PTM regime (nitrogen and argon were used as PTM). This singular strain asymmetry arises from the weak mechanical strain transfer contribution from the solid PTM at the top of studied bilayer system. This result highlights the mechanical effect of a solid PTM, which contributes to the pressure-induced compressive strain in graphene. Moreover, we have identified a pressure-induced doping effect when a liquid 4:1 methanol-ethanol mixture is used as PTM. Such effect is evidenced through a G-band pressure shift stronger for the top layer – in contact with the PTM – than for the bottom one – protected from it. This creates a charge concentration asymmetry between the two graphene sheets, with a stronger doping level in the top one. The mechanism and nature (*n* or *p*) of the charge transfer remains unclear, and the description of this interaction requires further investigations. We suggest that this doping effect is mediated by adsorption, and that the polarity of the adsorbed molecules plays a role. Through the experiments performed, we show that strain and doping asymmetries can be induced by extreme pressure application on multilayer graphene systems. The use of the isotope labeling was an efficient method to disentangle the mechanical and doping effects arising from the PTM. However, it does not allow to completely decorrelate the substrate and PTM effects, due to the existing coupling between the two layers.

The study of singled suspended sample is a radical solution to avoid the substrate effect, and constitutes a technical challenge. A second aspect of our work lies in experimental developments for the study of such singled *suspended* graphene samples at high pressure in the DAC. We have developped new strategies combining holed substrates and different types of graphene samples (exfoliated, as well as CVD-grown) for the loading of suspended systems in the diamond anvil cell. The PDMS dry-transfer set-up was implemented to bring the ability to prepare suspended graphene samples on-site at iLM. Two strategies have proven to be effective through proof-of-concept experiments on suspended nanographite samples. In both strategies, the sample is transferred on its support for suspension by dry PDMS-stamping, the support consisting of either (i) the diamond anvil itself, where a trench has been pre-machined by FIB, or of (ii) an

intermediate holed SiO_2/Si substrate prealably fixed on the diamond surface. In the approach (i), the diamond anvil broke after a few pressure cycles due to its structural weakening by the trench, while the approach (ii) was validated through the study of nanographite samples. For the study of thinner samples such as single layer graphene, we encountered graphene withdrawal or collapse during the PTM loading due to capillary forces. We propose the loading of helium PTM at supercritical state to overcome this problem. The development of the new portative helium loading technique at the iLM has been presented. It will bring the best conditions for the study of suspended atomically-thin samples in the near future.

Experiments were performed on suspended nanographite samples using the holed diamond technique and the intermediate holed SiO_2/Si substrate techniques, and have brought new results. The suspended nanographites system proved to be very sensitive to the solidification of the PTM, through a strong softening of the Raman signatures observed in the solid nitrogen PTM regime, while it was not observed in liquid PTM (4:1 methanol-ethanol and nitrogen at lower pressures). We explained this observation by either (i) the weak stress transfer from the solidified PTM to the nanographite, and/or (ii) a geometrical effect where the sample is pulled down by the PTM compression inside the trench due to the absence of PTM molecular diffusion in solid state. This singular observation strengthens the interest for experiments in suspended configuration. It highlights the need for a liquid PTM such as helium to investigate the intrinsic response of graphene to high hydrostatic pressures.

In the last section of the manuscript, we present preliminary results obtained on supported nanographites samples at high pressure. These samples were loaded in the DAC by PDMS-stamping on SiO_2/Si substrates prealably stucked on the diamond anvil, showing the efficiency of this approach for the study of supported samples as well. The SiO_2/Si substrate provides contrast-enhancement in order to investigate pressure-induced out-of-plane displacements of the nanographite membranes by microscope optical inspection. This revealed a pressure-induced buckling effect (formation of wrinkles) in the samples compressed in 4:1 methanol-ethanol and pure methanol PTM, followed by their total detachment from the substrate. Such behavior was not observed with other PTMs (nitrogen, water and paraffin oil) nor in solidified pure ethanol. We propose that the formation of wrinkles is mechanically induced by the substrate compression since no significant strain transfer is measured through the Raman G-band shift – showing that all the substrate's strain is dissipated in such wrinkles independantly of the PTM used. In our picture, chemical interaction with the alcohol molecules plays a significant role by enlarging the wrinkles (such as they become optically observable) and adsorbing under the nanographite sample. Such effect has never been observed in single or bilayer samples in similar conditions. This effect was not anticipated, and shows that the PTM can influence the sample-substrate interaction. By extrapolation of our results on thin graphite, we propose that a similar mechanism happens in thinner, single and bilayer systems, but at the length scale of the substrate rugosities leading to a significant – but incomplete – strain transfer from the substrate. These experiments provide new insights on the interaction of supported graphene layers with their substrate at high pressure.

From a more general point of view, we see that the concept of PTM quasi-hydrostaticity for a nanosystem at extreme pressure is to use with caution. The extreme sensibility of graphene to

the PTM could be used for PTM hydrostaticity characterization. Even more, it could be used to probe structural phase changes in compressed systems in general, through its impact of the Raman signatures of the sensitive graphene system. By deposition of graphene on the studied sample, it could be used as a sensor of transformations *e.g.* isostructural transitions, transitions between amorphous states or even liquid-liquid transitions.

Experiments on *suspended* monolayer graphene in helium PTM constitutes the logical continuation of our work, that may be later extended to other 2D-materials such as h-BN and transition metal dichalcogenides. van der Waals heterostructures [135] are particularly promising materials in that perspective. While their physical properties can be engineered by selective stacking of 2D-materials, the coupling between them could be modulated through pressure application. Our results raise question on the interaction of the PTM with the 2D constituents in heterostructures, and on the cohesion of such hybrid system at high pressure. Strain asymmetries between the constituting layers may be created through pressure application. A step further, interlayer covalent bonds could be induced by sufficiently strong pressures, with the opportunity to synthesize new nanomaterials.

Appendix

A

Raman Spectra Fitting Procedure

The fitting of the Raman bands was performed using the least-square method (Levenberg-Marquardt algorithm) implemented in specifically written R codes for our experiments. For the most difficult spectra to fit, the *fityk* software was used (also using the Levenberg-Marquardt algorithm) [203]. In both case, the procedure includes two steps: (i) background subtraction (see figure A.1(a)) and (ii) actual fitting (figure A.1(b)).

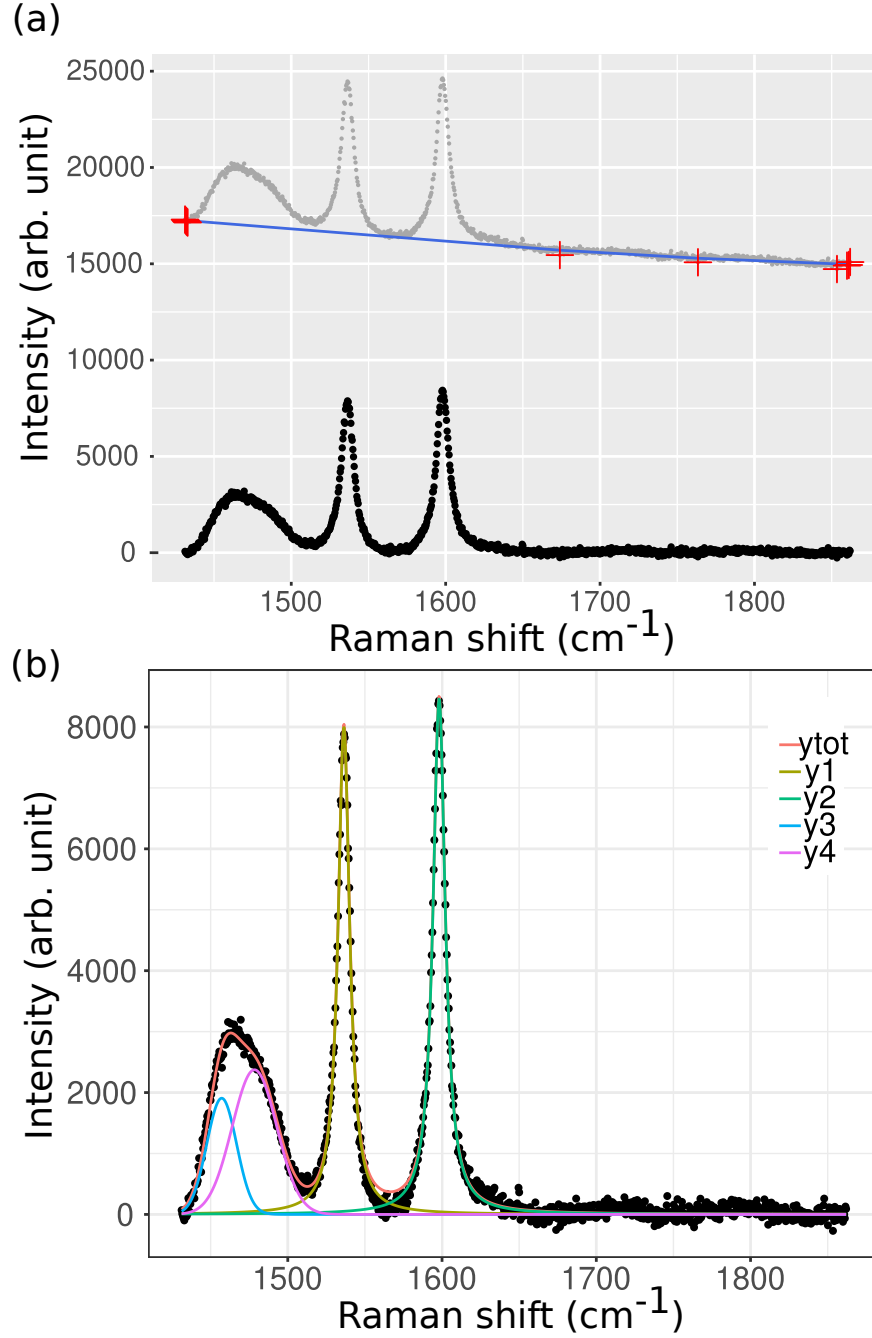


Figure A.1 – (a) The background (blue line) is subtracted from raw data (grey dots) in order to obtain the background corrected data (black dots). (b) The sum of four Lorentzian spectral lineshapes is fitted to the data by least square minimization. Two Lorentzian functions represents the 4:1 methanol-ethanol Raman feature near ~ 1450 cm⁻¹, while the two other corresponds to the two G-bands from the ¹²C and the ¹³C carbon layers of the isotopically labeled bilayer graphene sample studied during this work.

B

Isotopically Labeled Bilayer Graphene: Raman Spectra before and after the Pressure Cycle

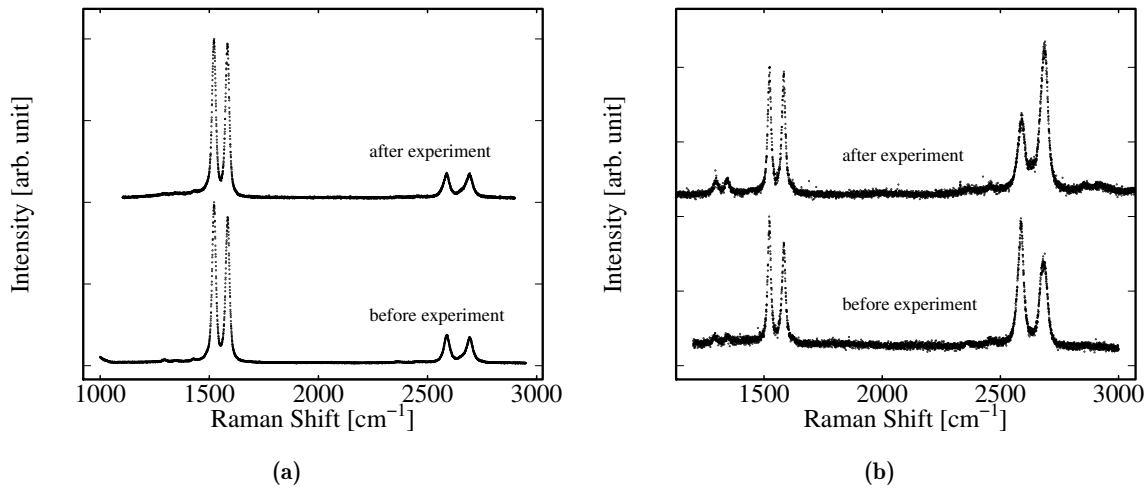


Figure B.1 – Raman spectra of samples before (bottom) and after (top) the pressure cycle in the case of (a) nitrogen PTM and (b) 4:1 methanol-ethanol PTM.

Résumé Substantiel en Langue Française

Dans ce travail, nous avons étudié sous très haute pression des échantillons de graphène et de graphite d'épaisseur nanométrique par spectroscopie Raman *in-situ*. Nous avons observé que l'environnement de l'échantillon joue un rôle central dans sa réponse à la pression. Notre travail s'est focalisé (i) sur l'impact de la nature chimique et l'état physique du milieu transmetteur de pression (PTM), et (ii) sur le rôle du substrat dans la réponse du système. Notre stratégie a consisté à décorréler le plus possible les effets (i) et (ii) afin de mieux comprendre les mécanismes en jeu.

Dans un premier chapitre, nous présentons le graphène et ses propriétés physiques, ainsi que les différents types d'empilements de feuillets de graphène. Nous décrivons la diffusion Raman appliquée au graphène, ainsi que la façon dont nous l'utilisons pour sonder *in-situ* les déformations et les effets de dopage dans nos échantillons. Enfin, nous présentons l'état de l'art des connaissances sur le graphite et le graphène sous pression extrême.

Le second chapitre est consacré aux techniques expérimentales. Nous y décrivons les méthodes de production et de transfert du graphène. Egalement, les techniques de haute pression sont décrites, centrées sur la cellule à enclumes de diamant. Le spectromètre Raman mis en place au cours de ce travail est présenté en détail, ainsi que les difficultés pratiques liées aux mesures Raman *in-situ* à haute pression.

Dans le troisième chapitre de ce manuscrit, nous exposons notre étude sous haute pression d'échantillons de graphène bi-couche $^{12}\text{C}/^{13}\text{C}$ isotopiquement modifiés, supportés sur substrats SiO_2/Si . Grâce à la substitution isotopique, il a été possible de suivre la réponse Raman de chacune des couches indépendamment pendant la compression. Afin de décorréler les effets du substrat et du PTM, le marquage isotopique est intéressant puisque la couche supérieure est en contact avec le PTM, tandis que la couche inférieure est en contact avec le substrat. Sous pression, nous avons observé une asymétrie des déformations entre les deux feuillets de graphène lorsque le PTM est solide (azote et argon au delà de leur point de solidification), alors qu'aucun découplage mécanique n'est observé dans le PTM à l'état liquide (azote et argon aux basses pressions). Le découplage mécanique observé est dû au transfert de déformation du PTM solide vers le système bi-couche étudié. Ce résultat met en évidence l'effet mécanique du PTM solide, qui contribue à la compression biaxiale induite par la pression dans le graphène. Nous avons identifié un effet de dopage pression-induit lorsque le mélange hydrostatique 4 :1 méthanol-éthanol est utilisé comme PTM. Nous avons observé cet effet à travers un décalage spectral de la bande G avec la pression plus élevé pour la couche supérieure (en contact avec le PTM) que pour la couche inférieure protégée de celui-ci. Cet effet conduit à une asymétrie de dopage entre les deux feuillets de graphène : le feuillet supérieur (en contact avec le PTM) est le plus dopé. Le mécanisme précis et la nature (*n* ou *p*) du transfert de charge restent inconnus et de nouveaux travaux sont nécessaires afin de mieux comprendre l'interaction alcool-graphène. Nous proposons que le transfert de charges se réalise par adsorption des molécules d'alcool, et que la

polarité de celles-ci joue un rôle. A travers nos expériences, nous montrons que des asymétries de déformation et de dopage peuvent être induites par l'application de hautes pressions sur des systèmes multi-couches. L'étude de cet échantillon est intéressante pour décorréler les effets provenant du substrat d'une part, et du PTM d'autre part. Cependant, elle ne permet pas de les séparer totalement en raison du couplage existant entre les deux couches.

L'étude d'échantillons de graphène en suspension est une solution radicale pour s'affranchir de l'effet du substrat, mais cela constitue un défi technique. Le quatrième chapitre présente nos développements expérimentaux pour l'étude de tels échantillons *suspendus* à haute pression dans la cellule à enclumes de diamant. Afin de suspendre et de charger ces échantillons en cellule, nous avons développé plusieurs stratégies combinant des substrats troués et des échantillons de graphène produits aussi bien par exfoliation mécanique que par croissance chimique (CVD). La technique de transfert visco-élastique par tamponnage a été mise en place pour permettre la préparation d'échantillons suspendus à l'iLM. Deux stratégies se sont avérées efficaces, et des expériences "preuves-de-principe" ont été effectuées sur des échantillons de nanographites suspendus. Dans les deux cas, l'échantillon est transféré sur le support permettant sa suspension par transfert visco-élastique. Le substrat cible est constitué soit (i) de l'enclume de diamant elle-même, où une tranchée a été usinée par un faisceau d'ions focalisé, soit (ii) d'un substrat SiO₂/Si pré-usiné et préalablement fixé sur l'enclume de diamant. Lors d'expériences préliminaires, l'enclume de diamant s'est fracturée après quelques cycles de pression, probablement en raison d'un affaiblissement structural dû à la tranchée. La seconde approche est validée par le succès d'expériences sur les échantillons de nanographite suspendus à haute pression. Pour l'étude d'échantillons très fins et fragiles comme des mono-couches ou des bi-couches de graphène, nous avons rencontré des difficultés liées à l'effondrement ou à la perte de l'échantillon lors de l'introduction du PTM, en raison des forces capillaires. Nous avons envisagé de réaliser un chargement à l'hélium supercritique afin de palier à ce problème. Nous avons contribué au développement d'une nouvelle méthode de chargement portatif à l'hélium en cours de mise en place au laboratoire. Cette méthode permettra effectivement d'étudier des échantillons de graphène suspendu dans les meilleures conditions expérimentales possibles.

Grâce aux techniques de chargement développées, nous avons obtenus des résultats préliminaires sur des échantillons de nanographites suspendus. Les techniques du diamant troué et du substrat SiO₂/Si préalablement collé sur l'enclume de diamant ont été employées pour ces expériences. Nous avons observé une grande sensibilité des échantillons de graphite mince suspendus à la solidification du PTM. Un important décalage vers le rouge des signatures Raman (bandes G et 2D₂) a été observé dans l'azote solide en comparaison avec l'évolution de la bande G dans le graphite massif. A l'inverse, l'évolution du graphite massif est mesurée lorsque le PTM est à l'état liquide (le mélange hydrostatique de 4 :1 méthanol-éthanol, et l'azote aux basses pressions). Cette observation peut s'expliquer par (i) le faible transfert de contraintes du PTM solide vers l'échantillon, et/ou (ii) par un effet géométrique lors duquel l'échantillon est étiré vers le bas, du fait de la compression du PTM sous celui-ci et de l'absence de diffusion moléculaire dans le PTM solidifié. Cette observation singulière renforce l'intérêt pour des expériences en configuration suspendue. De plus, elle démontre la nécessité d'un PTM restant liquide (tel que l'hélium) pour étudier la réponse intrinsèque du graphène sous haute pression hydrostatique.

Dans le dernier et cinquième chapitre, nous présentons des résultats obtenus sur des échantillons de nanographites *supportés* à haute pression. Pour leur chargement, nous avons employé la technique du substrat SiO_2/Si préalablement collé sur l'enclume de diamant, démontrant également son efficacité pour l'étude de systèmes supportés. Le substrat SiO_2/Si fournit un excellent contraste optique en surface. Ceci nous a permis de visualiser par microscopie optique les effets de déformation hors-plan des membranes de nanographite sous pression, tels que des plis ou des rides. En effet, nous avons observé un effet de plissement induit par la pression (formation de rides), lorsque le mélange 4 :1 méthanol-éthanol ou le méthanol pur sont utilisés comme PTM. Cet effet de plissement précède le décollement total des échantillons de leur substrat. Un tel comportement n'a été observé ni avec d'autres PTM (H_2O , azote, huile de paraffine), ni dans l'éthanol pur lorsqu'il est solidifié. Nous proposons une hypothèse selon laquelle la formation des rides est induite par la compression du substrat, puisqu'aucun transfert de déformation significatif n'est mesuré à travers le décalage spectral de la bande G avec la pression. Cela signifie que la totalité de la déformation du substrat est dissipée par la formation de ces rides dans les nanographites, indépendamment du PTM utilisé. Dans notre hypothèse, l'interaction chimique avec les molécules d'alcool joue un rôle important, révélant les rides par insertion et adsorption sous l'échantillon. Ce type d'effets n'a jamais été observé dans des échantillons de graphène monocouches ou bi-couches dans des conditions similaires. A travers cette observation, nous voyons que le PTM peut influencer l'interaction échantillon-substrat. Par extrapolation, nous supposons qu'un mécanisme similaire se produit dans les mono-couches et bi-couches de graphène, mais à l'échelle de taille des rugosités de surface du substrat. Dans ce cas, un transfert de déformation partiel du substrat au graphène est effectif. Ces expériences apportent de nouvelles informations sur l'interaction des couches de graphène supportées avec le substrat sous haute pression.

A travers nos différentes observations, nous suggérons que le concept de quasi-hydrostaticité du PTM soit utilisé avec précaution pour des échantillons d'échelle nanométrique. En effet, nous avons observé une très grande sensibilité mécanique des échantillons aux conditions non-hydrostatiques dans nos expériences, aussi bien pour le graphène bi-couche isotopiquement modifié que pour les nanographites sous haute pression. Pour finir, nous proposons comme perspectives l'étude d'autres matériaux 2D sous haute pression, ainsi que des empilements hétérogènes de ceux-ci formant des hétérostructures de Van der Waals. Cela permettra d'étudier la cohésion de ces systèmes hybrides à haute pression, ainsi que de générer d'éventuelles asymétries de déformations entre les matériaux 2D constitutifs de ces hétérostructures.

Bibliography

- [1] W. A. Bassett, “Diamond anvil cell, 50th birthday”, *High Pressure Research* **29** (2009), 163–186 (*cf.* pp. 13, 54)
- [2] D. Machon, V. Pischedda, S. Le Floch & A. San-Miguel, “Perspective: High pressure transformations in nanomaterials and opportunities in material design”, *Journal of Applied Physics* **124** (2018), 160902 (*cf.* pp. 13–15)
- [3] A. C. Torres-Dias, T. F. Cerqueira, W. Cui, M. A. Marques, S. Botti, D. Machon, M. A. Hartmann, Y. Sun, D. J. Dunstan & A. San-Miguel, “From mesoscale to nanoscale mechanics in single-wall carbon nanotubes”, *Carbon* **123** (2017), 145–150 (*cf.* pp. 13, 22, 33)
- [4] A. C. Torres-Dias, S. Cambré, W. Wenseleers, D. Machon & A. San-Miguel, “Chirality-dependent mechanical response of empty and water-filled single-wall carbon nanotubes at high pressure”, *Carbon* **95** (2015), 442–451 (*cf.* p. 13)
- [5] W. Neves, R. Alencar, R. Ferreira, A. Torres-Dias, N. Andrade, A. San-Miguel, Y. Kim, M. Endo, D. Kim, H. Muramatsu, A. Aguiar & A. Souza Filho, “Effects of pressure on the structural and electronic properties of linear carbon chains encapsulated in double wall carbon nanotubes”, *Carbon* **133** (2018), 446–456 (*cf.* p. 13)
- [6] L. Alvarez, J.-L. Bantignies, R. Le Parc, R. Aznar, J.-L. Sauvajol, A. Merlen, D. Machon & A. San Miguel, “High-pressure behavior of polyiodides confined into single-walled carbon nanotubes: A Raman study”, *Physical Review B* **82** (2010), 205403 (*cf.* p. 13)
- [7] M. Chorro, S. Rols, J. Cambedouzou, L. Alvarez, R. Almairac, J.-L. Sauvajol, J.-L. Hodeau, L. Marques, M. Mezouar & H. Kataura, “Structural properties of carbon peapods under extreme conditions studied using *in situ* x-ray diffraction”, *Physical Review B* **74** (2006), 205425 (*cf.* p. 13)
- [8] V. A. Davydov, L. S. Kashevarova, A. V. Rakhmanina, V. M. Senyavin, R. Céolin, H. Szwarc, H. Allouchi & V. Agafonov, “Spectroscopic study of pressure-polymerized phases of C 60”, *Physical Review B* **61** (2000), 11936–11945 (*cf.* p. 13)
- [9] T. Irifune, A. Kurio, S. Sakamoto, T. Inoue & H. Sumiya, “Ultrahard polycrystalline diamond from graphite”, *Nature* **421** (2003), 599–600 (*cf.* p. 13)
- [10] L. G. P. Martins, M. J. S. Matos, A. R. Paschoal, P. T. C. Freire, N. F. Andrade, A. L. Aguiar, J. Kong, B. R. A. Neves, A. B. de Oliveira, M. S. Mazzoni, A. G. S. Filho & L. G. Cançado, “Raman evidence for pressure-induced formation of diamondene”, *Nature Communications* **8** (2017) (*cf.* pp. 13, 40, 58, 71, 90, 94)
- [11] A. P. M. Barboza, M. H. D. Guimaraes, D. V. P. Massote, L. C. Campos, N. M. Barbosa Neto, L. G. Cancado, R. G. Lacerda, H. Chacham, M. S. C. Mazzoni & B. R. A. Neves, “Room-Temperature Compression-Induced Diamondization of Few-Layer Graphene”, *Advanced Materials* **23** (2011), 3014–3017 (*cf.* pp. 13, 41, 71, 90)

- [12] Z. Tao, J. Du, Z. Qi, K. Ni, S. Jiang & Y. Zhu, “Raman spectroscopy study of sp^2 to sp^3 transition in bilayer graphene under high pressures”, *Applied Physics Letters* **116** (2020), 133101 (*cf.* pp. 13, 15, 41, 71, 94, 95, 116)
- [13] C. Lee, X. Wei, J. W. Kysar & J. Hone, “Measurement of the Elastic Properties and Intrinsic Strength of Monolayer Graphene”, *Science* **321** (2008), 385–388 (*cf.* pp. 14, 22, 23)
- [14] S. Bertolazzi, J. Brivio & A. Kis, “Stretching and Breaking of Ultrathin MoS₂”, *ACS Nano* **5** (2011), 9703–9709 (*cf.* p. 14)
- [15] C. Androulidakis, E. N. Koukaras, O. Frank, G. Tsoukleri, D. Sfyris, J. Parthenios, N. Pugno, K. Papagelis, K. S. Novoselov & C. Galiotis, “Failure Processes in Embedded Monolayer Graphene under Axial Compression”, *Scientific Reports* **4** (2015), 5271 (*cf.* pp. 14, 128)
- [16] O. Frank, G. Tsoukleri, I. Riaz, K. Papagelis, J. Parthenios, A. C. Ferrari, A. K. Geim, K. S. Novoselov & C. Galiotis, “Development of a universal stress sensor for graphene and carbon fibres”, *Nature Communications* **2** (2011) (*cf.* p. 14)
- [17] D. Berman, A. Erdemir & A. V. Sumant, “Graphene: a new emerging lubricant”, *Materials Today* **17** (2014), 31–42 (*cf.* pp. 14, 141)
- [18] Z. H. Ni, T. Yu, Y. H. Lu, Y. Y. Wang, Y. P. Feng & Z. X. Shen, “Uniaxial Strain on Graphene: Raman Spectroscopy Study and Band-Gap Opening”, *ACS Nano* **2** (2008), 2301–2305 (*cf.* pp. 14, 23)
- [19] M. Ghorbani-Asl, S. Borini, A. Kuc & T. Heine, “Strain-dependent modulation of conductivity in single-layer transition-metal dichalcogenides”, *Physical Review B* **87** (2013) (*cf.* p. 14)
- [20] R. Roldán, A. Castellanos-Gomez, E. Cappelluti & F. Guinea, “Strain engineering in semiconducting two-dimensional crystals”, *Journal of Physics: Condensed Matter* **27** (2015), 313201 (*cf.* p. 14)
- [21] J. E. Proctor, E. Gregoryanz, K. S. Novoselov, M. Lotya, J. N. Coleman & M. P. Halsall, “High-pressure Raman spectroscopy of graphene”, *Physical Review B* **80** (2009) (*cf.* pp. 14, 15, 23, 38, 94)
- [22] J. Nicolle, D. Machon, P. Poncharal, O. Pierre-Louis & A. San-Miguel, “Pressure-Mediated Doping in Graphene”, *Nano Letters* **11** (2011), 3564–3568 (*cf.* pp. 14, 15, 23, 38–40, 71, 73, 89, 128, 134, 136, 140)
- [23] K. Filintoglou, N. Papadopoulos, J. Arvanitidis, D. Christofilos, O. Frank, M. Kalbac, J. Parthenios, G. Kalosakas, C. Galiotis & K. Papagelis, “Raman spectroscopy of graphene at high pressure: Effects of the substrate and the pressure transmitting media”, *Physical Review B* **88** (2013) (*cf.* pp. 14, 15, 39, 40, 71, 89)
- [24] C. Bousige, F. Balima, D. Machon, G. S. Pinheiro, A. Torres-Dias, J. Nicolle, D. Kalita, N. Bendiab, L. Marty, V. Bouchiat, G. Montagnac, A. G. Souza Filho, P. Poncharal & A. San-Miguel, “Biaxial Strain Transfer in Supported Graphene”, *Nano Letters* **17** (2017), 21–27 (*cf.* pp. 14, 15, 23, 34, 38–40, 70, 73, 77, 81, 84, 89, 128)

- [25] D. Machon, C. Bousige, R. Alencar, A. Torres-Dias, F. Balima, J. Nicolle, G. de Sousa Pinheiro, A. G. Souza Filho & A. San-Miguel, “Raman scattering studies of graphene under high pressure”, *Journal of Raman Spectroscopy* (2017) (*cf.* pp. 14, 23, 39, 40, 70, 71, 73, 77, 81, 83, 89, 128, 134)
- [26] C. Galiotis, O. Frank, E. N. Koukaras & D. Sfyris, “Graphene Mechanics: Current Status and Perspectives”, *Annual Review of Chemical and Biomolecular Engineering* **6** (2015), 121–140 (*cf.* pp. 14, 95)
- [27] Y. W. Sun, W. Liu, I. Hernandez, J. Gonzalez, F. Rodriguez, D. J. Dunstan & C. J. Humphreys, “3D Strain in 2D Materials: To What Extent is Monolayer Graphene Graphite?”, *Physical Review Letters* **123** (2019), 135501 (*cf.* pp. 15, 37, 94)
- [28] A. Jorio, M. S. Dresselhaus, R. Saito & G. Dresselhaus, *Raman Spectroscopy in Graphene Related Systems*, Wiley-VCH, 2011 (*cf.* pp. 20, 21, 24, 28, 34, 35, 77).
- [29] H. Kroto, J. R. Heath, S. O’Brien, R. Curl & R. Smalley, “C₆₀ : Buckminsterfullerene”, *Nature* **318** (1985), 162–163 (*cf.* p. 20)
- [30] S. Iijima & T. Ichihashi, “Single-shell carbon nanotubes of 1-nm diameter”, *Nature* **363** (1993), 603–605 (*cf.* p. 20)
- [31] D. S. Bethune, C. H. Kiang, M. S. de Vries, G. Gorman, R. Savoy, J. Vazquez & R. Beyers, “Cobalt-catalysed growth of carbon nanotubes with single-atomic-layer walls”, *Nature* **363** (1993), 605–607 (*cf.* p. 20)
- [32] K. S. Novoselov, A. K. Geim, S. V. Morozov, D. Jiang, Y. Zhang, S. V. Dubonos, I. V. Grigorieva & A. A. Firsov, “Electric Field Effect in Atomically Thin Carbon Films”, *Science* **306** (2004), 666–669 (*cf.* pp. 20, 25, 46)
- [33] P. Lambin, “Elastic Properties and Stability of Physisorbed Graphene”, *Applied Sciences* **4** (2014), 282–304 (*cf.* p. 22)
- [34] Y. Huang, J. Wu & K. C. Hwang, “Thickness of graphene and single-wall carbon nanotubes”, *Physical Review B* **74** (2006), 245413 (*cf.* p. 22)
- [35] L. D. Landau & E. M. Lifshitz, *Theory of Elasticity*, vol. 7, Course of Theoretical Physics, Pergamon Press, 1959 (*cf.* p. 22).
- [36] K. Cao, S. Feng, Y. Han, L. Gao, T. Hue Ly, Z. Xu & Y. Lu, “Elastic straining of free-standing monolayer graphene”, *Nature Communications* **11** (2020), 284 (*cf.* pp. 22, 103)
- [37] M. Hanfland, H. Beister & K. Syassen, “Graphite under pressure: Equation of state and first-order Raman modes”, *Physical Review B* **39** (1989), 12598 (*cf.* pp. 22, 37, 38, 40, 94, 115, 134, 136)
- [38] N. Bendiab, J. Renard, C. Schwarz, A. Reserbat-Plantey, L. Djevahirdjian, V. Bouchiat, J. Coraux & L. Marty, “Unravelling external perturbation effects on the optical phonon response of graphene: External perturbation effects on graphene optical phonons”, *Journal of Raman Spectroscopy* **49** (2018), 130–145 (*cf.* pp. 22, 25, 31, 32, 35–37, 77, 83, 87)

- [39] O. Frank, G. Tsoukleri, J. Parthenios, K. Papagelis, I. Riaz, R. Jalil, K. S. Novoselov & C. Galiotis, “Compression Behavior of Single-Layer Graphenes”, *ACS Nano* **4** (2010), 3131–3138 (*cf.* pp. 22, 23)
- [40] E. N. Koukaras, C. Androulidakis, G. Anagnostopoulos, K. Papagelis & C. Galiotis, “Compression behavior of simply-supported and fully embedded monolayer graphene: Theory and experiment”, *Extreme Mechanics Letters* **8** (2016), 191–200 (*cf.* p. 22)
- [41] T. Jiang, Z. Wang, X. Ruan & Y. Zhu, “Equi-biaxial compressive strain in graphene: Grüneisen parameter and buckling ridges”, *2D Materials* **6** (2018), 015026 (*cf.* pp. 22, 23, 128)
- [42] D. Yoon, Y.-W. Son & H. Cheong, “Negative Thermal Expansion Coefficient of Graphene Measured by Raman Spectroscopy”, *Nano Letters* **11** (2011), 3227–3231 (*cf.* pp. 22, 23, 128)
- [43] A. Castellanos-Gomez, R. Roldán, E. Cappelluti, M. Buscema, F. Guinea, H. S. J. van der Zant & G. A. Steele, “Local Strain Engineering in Atomically Thin MoS₂”, *Nano Letters* **13** (2013), 5361–5366 (*cf.* p. 22)
- [44] M. S. Brongseest, N. Bendiab, S. Mathur, A. Kimouche, H. T. Johnson, J. Coraux & P. Pochet, “Strain Relaxation in CVD Graphene: Wrinkling with Shear Lag”, *Nano Letters* **15** (2015), 5098–5104 (*cf.* p. 22)
- [45] C. Androulidakis, E. N. Koukaras, J. Parthenios, G. Kalosakas, K. Papagelis & C. Galiotis, “Graphene flakes under controlled biaxial deformation”, *Scientific Reports* **5** (2015), 18219 (*cf.* pp. 22, 23, 34)
- [46] F. Ding, H. Ji, Y. Chen, A. Herklotz, K. Dörr, Y. Mei, A. Rastelli & O. G. Schmidt, “Stretchable Graphene: A Close Look at Fundamental Parameters through Biaxial Straining”, *Nano Letters* **10** (2010), 3453–3458 (*cf.* pp. 23, 34)
- [47] N. Lindahl, D. Midtvedt, J. Svensson, O. A. Nerushev, N. Lindvall, A. Isacson & E. E. B. Campbell, “Determination of the Bending Rigidity of Graphene via Electrostatic Actuation of Buckled Membranes”, *Nano Letters* **12** (2012), 3526–3531 (*cf.* p. 23)
- [48] Y. Shin, M. Lozada-Hidalgo, J. L. Sambricio, I. V. Grigorieva, A. K. Geim & C. Casiraghi, “Raman spectroscopy of highly pressurized graphene membranes”, *Applied Physics Letters* **108** (2016), 221907 (*cf.* p. 23)
- [49] J. Zabel, R. R. Nair, A. Ott, T. Georgiou, A. K. Geim, K. S. Novoselov & C. Casiraghi, “Raman Spectroscopy of Graphene and Bilayer under Biaxial Strain: Bubbles and Balloons”, *Nano Letters* **12** (2012), 617–621 (*cf.* pp. 23, 34, 77)
- [50] G. Wang, Z. Dai, J. Xiao, S. Feng, C. Weng, L. Liu, Z. Xu, R. Huang & Z. Zhang, “Bending of Multilayer van der Waals Materials”, *Physical Review Letters* **123** (2019), 116101 (*cf.* p. 23)
- [51] T. M. G. Mohiuddin, A. Lombardo, R. R. Nair, A. Bonetti, G. Savini, R. Jalil, N. Bonini, D. M. Basko, C. Galiotis, N. Marzari, K. S. Novoselov, A. K. Geim & A. C. Ferrari, “Uniaxial strain in graphene by Raman spectroscopy: G peak splitting, Grüneisen parameters, and sample orientation”, *Physical Review B* **79** (2009) (*cf.* pp. 23, 34, 77)

- [52] R. Saito, G. Dresselhaus & M. Dresselhaus, *Physical Properties of Carbon Nanotubes*, Imperial College Press, 1998 (*cf.* p. 24).
- [53] T. Ando, T. Nakanishi & R. Saito, “Berry’s Phase and Absence of Back Scattering in Carbon Nanotubes”, *Journal of the Physical Society of Japan* **67** (1998), 2857–2862 (*cf.* p. 24)
- [54] A. C. Ferrari, J. C. Meyer, V. Scardaci, C. Casiraghi, M. Lazzeri, F. Mauri, S. Piscanec, D. Jiang, K. S. Novoselov, S. Roth & A. K. Geim, “Raman Spectrum of Graphene and Graphene Layers”, *Physical Review Letters* **97** (2006), 187401 (*cf.* pp. 24, 31)
- [55] A. H. Castro Neto, F. Guinea, N. M. R. Peres, K. S. Novoselov & A. K. Geim, “The electronic properties of graphene”, *Reviews of Modern Physics* **81** (2009), 109–162 (*cf.* pp. 24, 26)
- [56] P. R. Wallace, “The Band Theory of Graphite”, *Physical Review* **71** (1947), 622–634 (*cf.* p. 24)
- [57] K. S. Novoselov, A. K. Geim, S. V. Morozov, D. Jiang, M. I. Katsnelson, I. V. Grigorieva, S. V. Dubonos & A. A. Firsov, “Two-dimensional gas of massless Dirac fermions in graphene”, *Nature* **438** (2005), 197–200 (*cf.* pp. 24, 25)
- [58] G. Froehlicher & S. Berciaud, “Raman spectroscopy of electrochemically gated graphene transistors: Geometrical capacitance, electron-phonon, electron-electron, and electron-defect scattering”, *Physical Review B* **91** (2015) (*cf.* pp. 25, 35, 36, 87)
- [59] H. Pinto & A. Markevich, “Electronic and electrochemical doping of graphene by surface adsorbates”, *Beilstein Journal of Nanotechnology* **5** (2014), 1842–1848 (*cf.* pp. 25, 90)
- [60] A. Kaverzin, S. Strawbridge, A. Price, F. Withers, A. Savchenko & D. Horsell, “Electrochemical doping of graphene with toluene”, *Carbon* **49** (2011), 3829–3834 (*cf.* pp. 25, 90)
- [61] K. F. Mak, L. Ju, F. Wang & T. F. Heinz, “Optical spectroscopy of graphene: From the far infrared to the ultraviolet”, *Solid State Communications* **152** (2012), 1341–1349 (*cf.* p. 25)
- [62] R. R. Nair, P. Blake, A. N. Grigorenko, K. S. Novoselov, T. J. Booth, T. Stauber, N. M. R. Peres & A. K. Geim, “Fine Structure Constant Defines Visual Transparency of Graphene”, *Science* **320** (2008), 1308–1308 (*cf.* p. 25)
- [63] M. Bruna & S. Borini, “Optical constants of graphene layers in the visible range”, *Applied Physics Letters* **94** (2009), 031901 (*cf.* p. 25)
- [64] J.-C. Charlier, J.-P. Michenaud & X. Gonze, “First-principles study of the electronic properties of simple hexagonal graphite”, *Physical Review B* **46** (1992), 4531–4539 (*cf.* p. 25)
- [65] I. Brihuega, P. Mallet, H. González-Herrero, G. Trambly de Laissardière, M. M. Ugeda, L. Magaud, J. M. Gómez-Rodríguez, F. Ynduráin & J.-Y. Veuillen, “Unraveling the Intrinsic and Robust Nature of van Hove Singularities in Twisted Bilayer Graphene by Scanning Tunneling Microscopy and Theoretical Analysis”, *Physical Review Letters* **109** (2012) (*cf.* pp. 26, 31, 73)

- [66] Y. Cao, V. Fatemi, S. Fang, K. Watanabe, T. Taniguchi, E. Kaxiras & P. Jarillo-Herrero, “Unconventional superconductivity in magic-angle graphene superlattices”, *Nature* **556** (2018), 43–50 (*cf.* pp. 26, 51)
- [67] P. Y. Yu & M. Cardona, *Fundamentals of Semiconductors*, Graduate Texts in Physics, Berlin, Heidelberg: Springer Berlin Heidelberg, 2010 (*cf.* pp. 26–28, 60).
- [68] P. H. Tan, W. P. Han, W. J. Zhao, Z. H. Wu, K. Chang, H. Wang, Y. F. Wang, N. Bonini, N. Marzari, N. Pugno, G. Savini, A. Lombardo & A. C. Ferrari, “The shear mode of multilayer graphene”, *Nature Materials* **11** (2012), 294–300 (*cf.* pp. 28, 33, 60, 118)
- [69] A. C. Ferrari & D. M. Basko, “Raman spectroscopy as a versatile tool for studying the properties of graphene”, *Nature Nanotechnology* **8** (2013), 235–246 (*cf.* pp. 29, 31–33)
- [70] C.-F. Chen, C.-H. Park, B. W. Boudouris, J. Horng, B. Geng, C. Girit, A. Zettl, M. F. Crommie, R. A. Segalman, S. G. Louie & F. Wang, “Controlling inelastic light scattering quantum pathways in graphene”, *Nature* **471** (2011), 617–620 (*cf.* pp. 29, 30)
- [71] D. M. Basko, “Calculation of the Raman G peak intensity in monolayer graphene: role of Ward identities”, *New Journal of Physics* **11** (2009), 095011 (*cf.* pp. 29, 30)
- [72] N. Ferralis, “Probing mechanical properties of graphene with Raman spectroscopy”, *Journal of Materials Science* **45** (2010), 5135–5149 (*cf.* pp. 30, 34)
- [73] A. C. Ferrari, “Raman spectroscopy of graphene and graphite: Disorder, electron–phonon coupling, doping and nonadiabatic effects”, *Solid State Communications* **143** (2007), 47–57 (*cf.* pp. 30, 32, 72, 87, 102, 110)
- [74] M. Bayle, N. Reckinger, J.-R. Huntzinger, A. Felten, A. Bakaraki, P. Landois, J.-F. Colomer, L. Henrard, A.-A. Zahab, J.-L. Sauvajol & M. Paillet, “Dependence of the Raman spectrum characteristics on the number of layers and stacking orientation in few-layer graphene”, *Physica Status Solidi (b)* **252** (2015), 2375–2379 (*cf.* pp. 30, 31, 95)
- [75] M. Kalbac, A. Reina-Cecco, H. Farhat, J. Kong, L. Kavan & M. S. Dresselhaus, “The Influence of Strong Electron and Hole Doping on the Raman Intensity of Chemical Vapor-Deposition Graphene”, *ACS Nano* **4** (2010), 6055–6063 (*cf.* pp. 30, 87)
- [76] K. Kim, S. Coh, L. Z. Tan, W. Regan, J. M. Yuk, E. Chatterjee, M. F. Crommie, M. L. Cohen, S. G. Louie & A. Zettl, “Raman Spectroscopy Study of Rotated Double-Layer Graphene: Misorientation-Angle Dependence of Electronic Structure”, *Physical Review Letters* **108** (2012) (*cf.* pp. 30, 31, 73, 95)
- [77] A. Merlen, J. Buijnsters & C. Pardanaud, “A Guide to and Review of the Use of Multiwavelength Raman Spectroscopy for Characterizing Defective Aromatic Carbon Solids: from Graphene to Amorphous Carbons”, *Coatings* **7** (2017), 153 (*cf.* p. 31)
- [78] C. Thomsen & S. Reich, “Double resonant Raman scattering in graphite”, *Physical Review Letters* **85** (2000), 5214 (*cf.* p. 31)
- [79] L. Malard, M. Pimenta, G. Dresselhaus & M. Dresselhaus, “Raman spectroscopy in graphene”, *Physics Reports* **473** (2009), 51–87 (*cf.* p. 31)

- [80] S. Piscanec, M. Lazzeri, F. Mauri, A. C. Ferrari & J. Robertson, “Kohn Anomalies and Electron-Phonon Interactions in Graphite”, *Physical Review Letters* **93** (2004), 185503 (*cf.* pp. 31, 32, 35)
- [81] T. A. Nguyen, J.-U. Lee, D. Yoon & H. Cheong, “Excitation Energy Dependent Raman Signatures of ABA- and ABC-stacked Few-layer Graphene”, *Scientific Reports* **4** (2015) (*cf.* p. 31)
- [82] M. Bayle, N. Reckinger, A. Felten, P. Landois, O. Lancry, B. Dutertre, J.-F. Colomer, A.-A. Zahab, L. Henrard, J.-L. Sauvajol & M. Paillet, “Determining the number of layers in few-layer graphene by combining Raman spectroscopy and optical contrast”, *Journal of Raman Spectroscopy* **49** (2018), 36–45 (*cf.* pp. 31, 95)
- [83] J. Maultzsch, S. Reich, C. Thomsen, H. Requardt & P. Ordejón, “Phonon Dispersion in Graphite”, *Physical Review Letters* **92** (2004), 075501 (*cf.* p. 32)
- [84] L. Gustavo Cançado, M. Gomes da Silva, E. H. Martins Ferreira, F. Hof, K. Kampioti, K. Huang, A. Pénicaud, C. Alberto Achete, R. B. Capaz & A. Jorio, “Disentangling contributions of point and line defects in the Raman spectra of graphene-related materials”, *2D Materials* **4** (2017), 025039 (*cf.* pp. 32, 102)
- [85] F. Tuinstra & J. L. Koenig, “Raman Spectrum of Graphite”, *The Journal of Chemical Physics* **53** (1970), 1126–1130 (*cf.* p. 32)
- [86] A. K. Gupta, C. Nisoli, P. E. Lammert, V. H. Crespi & P. C. Eklund, “Curvature-induced D-band Raman scattering in folded graphene”, *Journal of Physics: Condensed Matter* **22** (2010), 334205 (*cf.* p. 32)
- [87] E. del Corro, L. Kavan, M. Kalbac & O. Frank, “Strain Assessment in Graphene Through the Raman 2D’ Mode”, *The Journal of Physical Chemistry C* **119** (2015), 25651–25656 (*cf.* p. 32)
- [88] M.-L. Lin, J.-B. Wu, X.-L. Liu & P.-H. Tan, “Probing the shear and layer breathing modes in multilayer graphene by Raman spectroscopy: Ultralow-wavenumber Raman spectroscopy in MLG”, *Journal of Raman Spectroscopy* (2017) (*cf.* pp. 33, 118)
- [89] L. G. Cançado, A. Reina, J. Kong & M. S. Dresselhaus, “Geometrical approach for the study of G’ band in the Raman spectrum of monolayer graphene, bilayer graphene, and bulk graphite”, *Physical Review B* **77** (2008), 245408 (*cf.* p. 33)
- [90] S. Silva-Santos, R. Alencar, A. Aguiar, Y. Kim, H. Muramatsu, M. Endo, N. Blanchard, A. San-Miguel & A. Souza Filho, “From high pressure radial collapse to graphene ribbon formation in triple-wall carbon nanotubes”, *Carbon* (2018) (*cf.* p. 33)
- [91] M. Huang, H. Yan, C. Chen, D. Song, T. F. Heinz & J. Hone, “Phonon softening and crystallographic orientation of strained graphene studied by Raman spectroscopy”, *Proceedings of the National Academy of Sciences* **106** (2009), 7304–7308 (*cf.* p. 34)
- [92] M. Lazzeri & F. Mauri, “Nonadiabatic Kohn Anomaly in a Doped Graphene Monolayer”, *Physical Review Letters* **97** (2006), 266407 (*cf.* pp. 35, 36, 87–89)
- [93] S. Pisana, M. Lazzeri, C. Casiraghi, K. S. Novoselov, A. K. Geim, A. C. Ferrari & F. Mauri, “Breakdown of the adiabatic Born–Oppenheimer approximation in graphene”, *Nature Materials* **6** (2007), 198–201 (*cf.* pp. 35, 36, 87)

- [94] M. Lazzeri, C. Attaccalite, L. Wirtz & F. Mauri, “Impact of the electron-electron correlation on phonon dispersion: Failure of LDA and GGA DFT functionals in graphene and graphite”, *Physical Review B* **78** (2008), 081406 (*cf.* pp. 35, 36, 88, 89)
- [95] A. Das, S. Pisana, B. Chakraborty, S. Piscanec, S. K. Saha, U. V. Waghmare, K. S. Novoselov, H. R. Krishnamurthy, A. K. Geim, A. C. Ferrari & A. K. Sood, “Monitoring dopants by Raman scattering in an electrochemically top-gated graphene transistor”, *Nature Nanotechnology* **3** (2008), 210–215 (*cf.* pp. 35, 87)
- [96] R. Parret, M. Paillet, J.-R. Huntzinger, D. Nakabayashi, T. Michel, A. Tiberj, J.-L. Sauvajol & A. A. Zahab, “*In Situ* Raman Probing of Graphene over a Broad Doping Range upon Rubidium Vapor Exposure”, *ACS Nano* **7** (2013), 165–173 (*cf.* pp. 35, 87–89)
- [97] Y. Almadori, G. Delport, R. Chambard, L. Orcin-Chaix, A. Selvati, N. Izard, A. Belhboub, R. Aznar, B. Jousselme, S. Campidelli, P. Hermet, R. Le Parc, T. Saito, Y. Sato, K. Suenaga, P. Puech, J. Lauret, G. Cassaboies, J.-L. Bantignies & L. Alvarez, “Fermi level shift in carbon nanotubes by dye confinement”, *Carbon* **149** (2019), 772–780 (*cf.* p. 35)
- [98] P. Puech, A. Ghandour, A. Sapelkin, C. Tinguely, E. Flahaut, D. J. Dunstan & W. Bacsa, “Raman G band in double-wall carbon nanotubes combining p doping and high pressure”, *Physical Review B* **78** (2008), 045413 (*cf.* p. 35)
- [99] M. S. Dresselhaus, A. Jorio, M. Hofmann, G. Dresselhaus & R. Saito, “Perspectives on Carbon Nanotubes and Graphene Raman Spectroscopy”, *Nano Letters* **10** (2010), 751–758 (*cf.* p. 35)
- [100] M. Lazzeri, S. Piscanec, F. Mauri, A. C. Ferrari & J. Robertson, “Phonon linewidths and electron-phonon coupling in graphite and nanotubes”, *Physical Review B* **73** (2006) (*cf.* p. 36)
- [101] D. M. Basko, S. Piscanec & A. C. Ferrari, “Electron-electron interactions and doping dependence of the two-phonon Raman intensity in graphene”, *Physical Review B* **80** (2009), arXiv: 0906.0975, 165413 (*cf.* p. 36)
- [102] J. E. Lee, G. Ahn, J. Shim, Y. S. Lee & S. Ryu, “Optical separation of mechanical strain from charge doping in graphene”, *Nature Communications* **3** (2012), 1024 (*cf.* pp. 36, 83)
- [103] N. S. Mueller, S. Heeg, M. P. Alvarez, P. Kusch, S. Wasserroth, N. Clark, F. Schedin, J. Parthenios, K. Papagelis, C. Galiotis, M. Kalbac, A. Vijayaraghavan, U. Huebner, R. Gorbachev, O. Frank & S. Reich, “Evaluating arbitrary strain configurations and doping in graphene with Raman spectroscopy”, *2D Materials* **5** (2017), 015016 (*cf.* pp. 37, 83)
- [104] L. Zhenxian, W. Lizhong, Z. Yongnian, C. Qilang & Z. Guangtian, “High-pressure Raman studies of graphite and ferric chloride-graphite”, *Journal of Physics: Condensed Matter* **2** (1990), 8083–8088 (*cf.* p. 38)
- [105] F. Balima, “Structure et porosité de systèmes lamellaires sous haute pression : cas du graphite et de la vermiculite”, PhD thesis, Université Claude Bernard Lyon 1, 2012 (*cf.* pp. 38, 40).

- [106] S. Clark, K.-J. Jeon, J.-Y. Chen & C.-S. Yoo, “Few-layer graphene under high pressure: Raman and X-ray diffraction studies”, *Solid State Communications* **154** (2013), 15–18 (*cf.* pp. 38, 40)
- [107] A. Hadjikhani, J. Chen, S. Das & W. Choi, *Supplemental Proceedings: Vol.2: Metals & Materials Society, TMS (The Minerals, Metals & Materials Society)*, John Wiley & Sons, 2012 (*cf.* p. 39).
- [108] O. Pierre-Louis, “Adhesion of membranes and filaments on rippled surfaces”, *Physical Review E* **78** (2008) (*cf.* pp. 40, 128, 136, 140)
- [109] R. S. Alencar, K. D. A. Saboia, D. Machon, G. Montagnac, V. Meunier, O. P. Ferreira, A. San-Miguel & A. G. Souza Filho, “Atomic-layered MoS₂ on SiO₂ under high pressure: Bimodal adhesion and biaxial strain effects”, *Physical Review Materials* **1** (2017) (*cf.* pp. 40, 73)
- [110] T. Pakornchote, Z. M. Geballe, U. Pinsook, T. Taychatanapat, W. Busayaporn, T. Bovornratanaraks & A. F. Goncharov, “Raman spectroscopy on hydrogenated graphene under high pressure”, *Carbon* **156** (2020), 549–557 (*cf.* p. 40)
- [111] A. Francisco-Lopez, B. Han, D. Lagarde, X. Marie, B. Urbaszek & C. Robert, “On the impact of the stress situation on the optical properties of WSe₂ monolayers under high pressure”, *Papers in Physics* **11** (2019) (*cf.* pp. 40, 96)
- [112] M. Amsler, J. A. Flores-Livas, L. Lehtovaara, F. Balima, S. A. Ghasemi, D. Machon, S. Pailhès, A. Willand, D. Caliste, S. Botti, A. San Miguel, S. Goedecker & M. A. L. Marques, “Crystal Structure of Cold Compressed Graphite”, *Physical Review Letters* **108** (2012) (*cf.* p. 40)
- [113] W. L. Mao, H.-k. Mao, P. J. Eng, T. P. Trainor, M. Newville, C.-c. Kao, D. L. Heinz, J. Shu, Y. Meng & R. J. Hemley, “Bonding Changes in Compressed Superhard Graphite”, *Science* **302** (2003), 425–427 (*cf.* p. 40)
- [114] S. Lu, M. Yao, X. Yang, Q. Li, J. Xiao, Z. Yao, L. Jiang, R. Liu, B. Liu, S. Chen, B. Zou, T. Cui & B. Liu, “High pressure transformation of graphene nanoplates: A Raman study”, *Chemical Physics Letters* **585** (2013), 101–106 (*cf.* p. 40)
- [115] F. Piazza, Kelvin Cruz, M. Monthieux, P. Puech & I. Gerber, “Raman evidence for the successful synthesis of diamane”, *Carbon* **169** (2020), 129–133 (*cf.* p. 41)
- [116] Y. Gao, T. Cao, F. Cellini, C. Berger, W. A. de Heer, E. Tosatti, E. Riedo & A. Bongiorno, “Ultrahard carbon film from epitaxial two-layer graphene”, *Nature Nanotechnology* **13** (2018), 133–138 (*cf.* p. 41)
- [117] F. Ke, Y. Chen, K. Yin, J. Yan, H. Zhang, Z. Liu, J. S. Tse, J. Wu, H.-k. Mao & B. Chen, “Large bandgap of pressurized trilayer graphene”, *Proceedings of the National Academy of Sciences* **116** (2019), 9186–9190 (*cf.* p. 41)
- [118] K. S. Novoselov, D. Jiang, F. Schedin, T. J. Booth, V. V. Khotkevich, S. V. Morozov & A. K. Geim, “Two-dimensional atomic crystals”, *Proceedings of the National Academy of Sciences* **102** (2005), 10451–10453 (*cf.* p. 47)

- [119] P. Blake, E. W. Hill, A. H. Castro Neto, K. S. Novoselov, D. Jiang, R. Yang, T. J. Booth & A. K. Geim, “Making graphene visible”, *Applied Physics Letters* **91** (2007), 063124 (*cf.* p. 47)
- [120] P. Klar, E. Lidorikis, A. Eckmann, I. A. Verzhbitskiy, A. C. Ferrari & C. Casiraghi, “Raman scattering efficiency of graphene”, *Physical Review B* **87** (2013), 205435 (*cf.* p. 47)
- [121] O. Frank, L. Kavan & M. Kalbac, “Carbon isotope labelling in graphene research”, *Nanoscale* **6** (2014), 6363 (*cf.* pp. 48, 72)
- [122] X. Li, W. Cai, L. Colombo & R. S. Ruoff, “Evolution of Graphene Growth on Ni and Cu by Carbon Isotope Labeling”, *Nano Letters* **9** (2009), 4268–4272 (*cf.* p. 48)
- [123] X. Li, W. Cai, J. An, S. Kim, J. Nah, D. Yang, R. Piner, A. Velamakanni, I. Jung, E. Tutuc, S. K. Banerjee, L. Colombo & R. S. Ruoff, “Large-Area Synthesis of High-Quality and Uniform Graphene Films on Copper Foils”, *Science* **324** (2009), 1312–1314 (*cf.* p. 48)
- [124] F. Bonaccorso, A. Lombardo, T. Hasan, Z. Sun, L. Colombo & A. C. Ferrari, “Production and processing of graphene and 2d crystals”, *Materials Today* **15** (2012), 564–589 (*cf.* p. 48)
- [125] W. Hao, C. Marichy & C. Journet, “Atomic layer deposition of stable 2D materials”, *2D Materials* **6** (2018), 012001 (*cf.* p. 48)
- [126] Y. Bleu, F. Bourquard, T. Tite, A.-S. Loir, C. Maddi, C. Donnet & F. Garrelie, “Review of Graphene Growth From a Solid Carbon Source by Pulsed Laser Deposition (PLD)”, *Frontiers in Chemistry* **6** (2018), 572 (*cf.* p. 48)
- [127] G. Bepete, E. Anglaret, L. Ortolani, V. Morandi, K. Huang, A. Pénicaud & C. Drummond, “Surfactant-free single-layer graphene in water”, *Nature Chemistry* **9** (2017), 347–352 (*cf.* p. 48)
- [128] R. Frisenda, E. Navarro-Moratalla, P. Gant, D. Pérez De Lara, P. Jarillo-Herrero, R. V. Gorbachev & A. Castellanos-Gomez, “Recent progress in the assembly of nanodevices and van der Waals heterostructures by deterministic placement of 2D materials”, *Chemical Society Reviews* **47** (2018), 53–68 (*cf.* pp. 49, 51)
- [129] A. Castellanos-Gomez, M. Buscema, R. Molenaar, V. Singh, L. Janssen, H. S. J. van der Zant & G. A. Steele, “Deterministic transfer of two-dimensional materials by all-dry viscoelastic stamping”, *2D Materials* **1** (2014), 011002 (*cf.* pp. 49, 50)
- [130] N. Morell, A. Reserbat-Plantey, I. Tsioutsios, K. G. Schädler, F. Dubin, F. H. L. Koppens & A. Bachtold, “High Quality Factor Mechanical Resonators Based on WSe₂ Monolayers”, *Nano Letters* **16** (2016), 5102–5108 (*cf.* p. 51)
- [131] F. Pizzocchero, L. Gammelgaard, B. S. Jessen, J. M. Caridad, L. Wang, J. Hone, P. Bøggild & T. J. Booth, “The hot pick-up technique for batch assembly of van der Waals heterostructures”, *Nature Communications* **7** (2016), 11894 (*cf.* pp. 51, 109)
- [132] Y. Cao, V. Fatemi, A. Demir, S. Fang, S. L. Tomarken, J. Y. Luo, J. D. Sanchez-Yamagishi, K. Watanabe, T. Taniguchi, E. Kaxiras, R. C. Ashoori & P. Jarillo-Herrero, “Correlated insulator behaviour at half-filling in magic-angle graphene superlattices”, *Nature* **556** (2018), 80–84 (*cf.* p. 51)

- [133] L. Wang, I. Meric, P. Y. Huang, Q. Gao, Y. Gao, H. Tran, T. Taniguchi, K. Watanabe, L. M. Campos, D. A. Muller, J. Guo, P. Kim, J. Hone, K. L. Shepard & C. R. Dean, “One-Dimensional Electrical Contact to a Two-Dimensional Material”, *Science* **342** (2013), 614–617 (*cf.* p. 51)
- [134] F. Cadiz, E. Courtade, C. Robert, G. Wang, Y. Shen, H. Cai, T. Taniguchi, K. Watanabe, H. Carrere, D. Lagarde, M. Manca, T. Amand, P. Renucci, S. Tongay, X. Marie & B. Urbaszek, “Excitonic Linewidth Approaching the Homogeneous Limit in MoS₂-Based van der Waals Heterostructures”, *Physical Review X* **7** (2017), 021026 (*cf.* p. 51)
- [135] A. K. Geim & I. V. Grigorieva, “Van der Waals heterostructures”, *Nature* **499** (2013), 419–425 (*cf.* pp. 51, 145)
- [136] D. J. Dunstan & I. L. Spain, “Technology of diamond anvil high-pressure cells: I. Principles, design and construction”, *Journal of Physics E: Scientific Instruments* **22** (1989), 913 (*cf.* p. 52)
- [137] R. Letoullec, J. P. Pinceaux & P. Loubeyre, “The membrane diamond anvil cell: A new device for generating continuous pressure and temperature variations”, *High Pressure Research* **1** (1988), 77–90 (*cf.* p. 52)
- [138] D. J. Dunstan, “Theory of the gasket in diamond anvil high-pressure cells”, *Review of Scientific Instruments* **60** (1989), 3789–3795 (*cf.* pp. 53–55)
- [139] R. H. Telling, C. J. Pickard, M. C. Payne & J. E. Field, “Theoretical Strength and Cleavage of Diamond”, *Physical Review Letters* **84** (2000), 5160–5163 (*cf.* p. 54)
- [140] R. Boehler & K. De Hantsetters, “New anvil designs in diamond-cells”, *High Pressure Research* **24** (2004), 391–396 (*cf.* p. 54)
- [141] M. Hanfland, K. Syassen, S. Fahy, S. G. Louie & M. L. Cohen, “The first-order Raman mode of diamond under pressure”, *Physica B+C* **139-140** (1986), 516–519 (*cf.* p. 55)
- [142] Y. Akahama & H. Kawamura, “Pressure calibration of diamond anvil Raman gauge to 310GPa”, *Journal of Applied Physics* **100** (2006), 043516 (*cf.* p. 55)
- [143] R. A. Forman, G. J. Piermarini, J. D. Barnett & S. Block, “Pressure Measurement Made by the Utilization of Ruby Sharp-Line Luminescence”, *Science, New Series* **176** (1972), 284–285 (*cf.* p. 55)
- [144] A. D. Chijioke, W. J. Nellis, A. Soldatov & I. F. Silvera, “The ruby pressure standard to 150GPa”, *Journal of Applied Physics* **98** (2005), 114905 (*cf.* p. 55)
- [145] D. Machon, V. P. Dmitriev, P. Bouvier, P. N. Timonin, V. B. Shirokov & H.-P. Weber, “Pseudoamorphization of Cs₂HgBr₄”, *Physical Review B* **68** (2003), 144104 (*cf.* p. 56)
- [146] R. J. Angel, M. Bujak, J. Zhao, G. D. Gatta & S. D. Jacobsen, “Effective hydrostatic limits of pressure media for high-pressure crystallographic studies”, *Journal of Applied Crystallography* **40** (2007), 26–32 (*cf.* pp. 56–58, 87)
- [147] S. Klotz, J.-C. Chervin, P. Munsch & G. Le Marchand, “Hydrostatic limits of 11 pressure transmitting media”, *Journal of Physics D: Applied Physics* **42** (2009), 075413 (*cf.* pp. 57, 58, 87, 118)

- [148] G. J. Piermarini, R. A. Forman & S. Block, “Viscosity measurements in the diamond anvil pressure cell”, *Review of Scientific Instruments* **49** (1978), 1061 (*cf.* p. 57)
- [149] G. J. Piermarini, S. Block & J. Barnett, “Hydrostatic limits in liquids and solids to 100 kbar”, *Journal of Applied Physics* **44** (1973), 5377–5382 (*cf.* p. 58)
- [150] L. W. Finger, R. M. Hazen, G. Zou, H. K. Mao & P. M. Bell, “Structure and compression of crystalline argon and neon at high pressure and room temperature”, *Applied Physics Letters* **39** (1981), 892–894 (*cf.* pp. 58, 82, 85, 87)
- [151] R. L. Mills, B. Olinger & D. T. Cromer, “Structures and phase diagrams of N₂ and CO to 13 GPa by X-ray diffraction”, *The Journal of Chemical Physics* **84** (1986), 2837–2845 (*cf.* pp. 58, 82, 85, 87, 137)
- [152] W. L. Vos & J. A. Schouten, “Improved phase diagram of nitrogen up to 85 kbar”, *The Journal of Chemical Physics* **91** (1989), 6302–6305 (*cf.* pp. 58, 82, 137)
- [153] H. Shimizu, H. Tashiro, T. Kume & S. Sasaki, “High-Pressure Elastic Properties of Solid Argon to 70 GPa”, *Physical Review Letters* **86** (2001), 4568–4571 (*cf.* p. 58)
- [154] M. Grimsditch, P. Loubeyre & A. Polian, “Brillouin scattering and three-body forces in argon at high pressures”, *Physical Review B* **33** (1986), 7192–7200 (*cf.* pp. 58, 87)
- [155] P. Bell & H. Mao, “Degrees of Hydrostaticity in He, Ne, and Ar Pressure-Transmitting-Media”, in: *Carnegie Institution Yearbook*, vol. 80, 1981, p. 404 (*cf.* pp. 58, 87).
- [156] M. I. Eremets, V. V. Struzhkin, J. A. Timofeev, I. A. Trojan, A. N. Utjuzh & A. M. Shirokov, “Refractive index of diamond under pressure”, *High Pressure Research* **9** (1992), 347–350 (*cf.* p. 63)
- [157] F. Medeghini, M. Hettich, R. Rouxel, S. D. Silva Santos, S. Hermelin, E. Pertreux, A. Torres Dias, F. Legrand, P. Maioli, A. Crut, F. Vallée, A. San Miguel & N. Del Fatti, “High-Pressure Effect on the Optical Extinction of a Single Gold Nanoparticle”, *ACS Nano* **12** (2018), 10310–10316 (*cf.* pp. 63, 123)
- [158] F. Medeghini, “Optics and acoustics with a single nano-object: environment effects”, PhD thesis, Université de Lyon, 2018 (*cf.* p. 63).
- [159] A. Merlen, N. Bendiab, P. Toulemonde, A. Aouizerat, A. San Miguel, J. L. Sauvajol, G. Montagnac, H. Cardon & P. Petit, “Resonant Raman spectroscopy of single-wall carbon nanotubes under pressure”, *Physical Review B* **72** (2005), 035409 (*cf.* p. 64)
- [160] B. J. Baer & M. Nicol, “High-Pressure Binary Phase Diagram of N₂-O₂ at 295 K Determined by Raman Spectroscopy”, *The Journal of Physical Chemistry* **94** (1990), 1073–1078 (*cf.* pp. 64, 114)
- [161] E. del Corro, M. Peña-Álvarez, M. Mračko, R. Kolman, M. Kalbac, L. Kavan & O. Frank, “Graphene under direct compression: Stress effects and interlayer coupling: Graphene under direct compression”, *Physica Status Solidi (b)* **253** (2016), 2336–2341 (*cf.* pp. 71, 87)
- [162] T. G. A. Verhagen, K. Drogowska, M. Kalbac & J. Vejpravova, “Temperature-induced strain and doping in monolayer and bilayer isotopically labeled graphene”, *Physical Review B* **92** (2015), 125437 (*cf.* p. 71)

- [163] P. Puech, H. Hubel, D. J. Dunstan, R. R. Bacsá, C. Laurent & W. S. Bacsá, “Discontinuous Tangential Stress in Double Wall Carbon Nanotubes”, *Physical Review Letters* **93** (2004), 095506 (*cf.* p. 71)
- [164] D. Tristant, A. Zubair, P. Puech, F. Neumayer, S. Moyano, R. J. Headrick, D. E. Tsentalovich, C. C. Young, I. C. Gerber, M. Pasquali, J. Kono & J. Leotin, “Enlightening the ultrahigh electrical conductivities of doped double-wall carbon nanotube fibers by Raman spectroscopy and first-principles calculations”, *Nanoscale* **8** (2016), 19668–19676 (*cf.* p. 71)
- [165] W. Fang, A. L. Hsu, R. Caudillo, Y. Song, A. G. Birdwell, E. Zakar, M. Kalbac, M. Dubey, T. Palacios, M. S. Dresselhaus, P. T. Araujo & J. Kong, “Rapid Identification of Stacking Orientation in Isotopically Labeled Chemical-Vapor Grown Bilayer Graphene by Raman Spectroscopy”, *Nano Letters* **13** (2013), 1541–1548 (*cf.* p. 73)
- [166] M. Kalbac, O. Frank, J. Kong, J. Sanchez-Yamagishi, K. Watanabe, T. Taniguchi, P. Jarillo-Herrero & M. S. Dresselhaus, “Large Variations of the Raman Signal in the Spectra of Twisted Bilayer Graphene on a BN Substrate”, *The Journal of Physical Chemistry Letters* **3** (2012), 796–799 (*cf.* p. 73)
- [167] J. Nicolle, “Etude du Graphène sous Pression par Spectroscopie Raman”, PhD Thesis, Université Claude Bernard Lyon 1, 2011 (*cf.* pp. 73–75).
- [168] A. Forestier, F. Balima, C. Bousige, G. d. S. Pinheiro, R. Fulcrand, M. Kalbac, D. Machon & A. San-Miguel, “Strain and Piezo-Doping Mismatch between Graphene Layers”, *The Journal of Physical Chemistry C* **124** (2020), 11193–11199 (*cf.* p. 73)
- [169] M. I. Eremets, *High Pressure Experimental Methods*, Oxford Science Publications, 1996 (*cf.* p. 74).
- [170] J. Hu & I. L. Spain, “Phases of Silicon at High Pressure”, *Solid State Communications* **51** (1984), 263–266 (*cf.* p. 75)
- [171] F. Decremps, L. Belliard, M. Gauthier & B. Perrin, “Equation of state, stability, anisotropy and nonlinear elasticity of diamond-cubic (ZB) silicon by phonon imaging at high pressure”, *Physical Review B* **82** (2010) (*cf.* pp. 77, 85, 134)
- [172] F. D. Murnaghan, “The Compressibility of Media under Extreme Pressures”, *Proceedings of the National Academy of Science* **30** (1944), 244–247 (*cf.* p. 85)
- [173] B. Olinger, “The compression of solid N₂ at 296 K from 5 to 10 GPa”, *The Journal of Chemical Physics* **80** (1984), 1309–1311 (*cf.* p. 85)
- [174] J. H. Eggert, L.-w. Xu, R.-z. Che, L.-c. Chen & J.-f. Wang, “High pressure refractive index measurements of 4:1 methanol:ethanol”, *Journal of Applied Physics* **72** (1992), 2453–2461 (*cf.* p. 85)
- [175] T.-F. Chung, R. He, T.-L. Wu & Y. P. Chen, “Optical Phonons in Twisted Bilayer Graphene with Gate-Induced Asymmetric Doping”, *Nano Letters* **15** (2015), 1203–1210 (*cf.* p. 88)
- [176] A. M. Saitta, M. Lazzeri, M. Calandra & F. Mauri, “Giant Nonadiabatic Effects in Layer Metals: Raman Spectra of Intercalated Graphite Explained”, *Physical Review Letters* **100** (2008), 226401 (*cf.* p. 88)

- [177] A. Tiberj, M. Rubio-Roy, M. Paillet, J. -R. Huntzinger, P. Landois, M. Mikolasek, S. Contreras, J. -L. Sauvajol, E. Dujardin & A. -A. Zahab, “Reversible optical doping of graphene”, *Scientific Reports* **3** (2013), 2355 (*cf.* p. 90)
- [178] A. J. Samuels & J. D. Carey, “Molecular Doping and Band-Gap Opening of Bilayer Graphene”, *ACS Nano* **7** (2013), 2790–2799 (*cf.* p. 91)
- [179] G. Trambly de Laissardière, O. F. Namarvar, D. Mayou & L. Magaud, “Electronic properties of asymmetrically doped twisted graphene bilayers”, *Physical Review B* **93** (2016), 235135 (*cf.* p. 91)
- [180] S. Berciaud, S. Ryu, L. E. Brus & T. F. Heinz, “Probing the Intrinsic Properties of Exfoliated Graphene: Raman Spectroscopy of Free-Standing Monolayers”, *Nano Letters* **9** (2009), 346–352 (*cf.* p. 94)
- [181] A. V. Soldatov, S. You, M. Mases & K. S. Novoselov, “Free standing graphene monolayer at high hydrostatic pressure”, *Abstract book, Graphene 2012* (2012) (*cf.* p. 95)
- [182] C.-T. Pan, J. A. Hinks, Q. M. Ramasse, G. Greaves, U. Bangert, S. E. Donnelly & S. J. Haigh, “In-situ observation and atomic resolution imaging of the ion irradiation induced amorphisation of graphene”, *Scientific Reports* **4** (2015) (*cf.* p. 102)
- [183] J. Chen, T. Shi, T. Cai, T. Xu, L. Sun, X. Wu & D. Yu, “Self healing of defected graphene”, *Applied Physics Letters* **102** (2013), 103107 (*cf.* pp. 102, 103)
- [184] K. Kinoshita, R. Moriya, M. Onodera, Y. Wakafuji, S. Masubuchi, K. Watanabe, T. Taniguchi & T. Machida, “Dry release transfer of graphene and few-layer h-BN by utilizing thermoplasticity of polypropylene carbonate”, *npj 2D Materials and Applications* **3** (2019), 22 (*cf.* p. 109)
- [185] B. Sprow & J. Prausnitz, “Surface Tensions of Simple Liquids”, *Transactions of the Faraday Society* **62** (1966), 1097–1104 (*cf.* p. 109)
- [186] G. Vazquez, E. Alvarez & J. M. Navaza, “Surface Tension of Alcohol + Water from 20 to 50 °C”, *Journal of Chemical & Engineering Data* **40** (1995), 611–614 (*cf.* p. 109)
- [187] M. Peña-Álvarez, E. del Corro, V. G. Baonza & M. Taravillo, “Probing the Stress Effect on the Electronic Structure of Graphite by Resonant Raman Spectroscopy”, *The Journal of Physical Chemistry C* **118** (2014), 25132–25140 (*cf.* p. 115)
- [188] R. He, T.-F. Chung, C. Delaney, C. Keiser, L. A. Jauregui, P. M. Shand, C. C. Chancey, Y. Wang, J. Bao & Y. P. Chen, “Observation of Low Energy Raman Modes in Twisted Bilayer Graphene”, *Nano Letters* **13** (2013), 3594–3601 (*cf.* p. 118)
- [189] D. J. Dunstan & W. Scherrer, “Miniature cryogenic diamond-anvil high-pressure cell”, *Review of Scientific Instruments* **59** (1988), 627–630 (*cf.* pp. 118, 119)
- [190] M. Yankowitz, S. Chen, H. Polshyn, Y. Zhang, K. Watanabe, T. Taniguchi, D. Graf, A. F. Young & C. R. Dean, “Tuning superconductivity in twisted bilayer graphene”, *Science* **363** (2019), 1059–1064 (*cf.* p. 123)
- [191] B. Han, F. Li, L. Li, X. Huang, Y. Gong, X. Fu, H. Gao, Q. Zhou & T. Cui, “Correlatively Dependent Lattice and Electronic Structural Evolutions in Compressed Monolayer Tungsten Disulfide”, *The Journal of Physical Chemistry Letters* **8** (2017), 941–947 (*cf.* p. 123)

- [192] J.-C. Blancon, M. Paillet, H. N. Tran, X. T. Than, S. A. Guebrou, A. Ayari, A. S. Miguel, N.-M. Phan, A.-A. Zahab, J.-L. Sauvajol, N. D. Fatti & F. Vallée, “Direct measurement of the absolute absorption spectrum of individual semiconducting single-wall carbon nanotubes”, *Nature Communications* **4** (2013) (*cf.* p. 123)
- [193] S. Deng, “Wrinkled, rippled and crumpled graphene: an overview of formation mechanism, electronic properties, and applications”, *Materials Today* **19** (2016), 16 (*cf.* p. 128)
- [194] J. F. Mammone, S. K. Sharma & M. Nicol, “Raman spectra of methanol and ethanol at pressures up to 100 kbar”, *The Journal of Physical Chemistry* **84** (1980), 3130–3134 (*cf.* p. 137)
- [195] P. W. Bridgman, “The Phase Diagram of Water to 45,000 kg/cm²”, *The Journal of Chemical Physics* **5** (1937), 964–966 (*cf.* p. 137)
- [196] J. W. Otto, J. K. Vassiliou & G. Frommeyer, “Nonhydrostatic compression of elastically anisotropic polycrystals. I. Hydrostatic limits of 4:1 methanol-ethanol and paraffin oil”, *Physical Review B* **57** (1998), 3253–3263 (*cf.* p. 137)
- [197] M. J. P. Brugmans & W. L. Vos, “Competition between vitrification and crystallization of methanol at high pressure”, *The Journal of Chemical Physics* **103** (1995), 2661–2669 (*cf.* p. 137)
- [198] E. Schröder, “Methanol Adsorption on Graphene”, *Journal of Nanomaterials* **2013** (2013), 1–6 (*cf.* p. 137)
- [199] A. S. Bolina, A. J. Wolff & W. A. Brown, “Reflection absorption infrared spectroscopy and temperature programmed desorption investigations of the interaction of methanol with a graphite surface”, *The Journal of Chemical Physics* **122** (2005), 044713 (*cf.* p. 137)
- [200] V. E. Calado, G. F. Schneider, A. M. M. G. Theulings, C. Dekker & L. M. K. Vandersypen, “Formation and control of wrinkles in graphene by the wedging transfer method”, *Applied Physics Letters* **101** (2012), 103116 (*cf.* pp. 139, 141)
- [201] W. G. Cullen, M. Yamamoto, K. M. Burson, J. H. Chen, C. Jang, L. Li, M. S. Fuhrer & E. D. Williams, “High-Fidelity Conformation of Graphene to SiO₂ Topographic Features”, *Physical Review Letters* **105** (2010), 215504 (*cf.* p. 140)
- [202] D. C. Elias, R. R. Nair, T. M. G. Mohiuddin, S. V. Morozov, P. Blake, M. P. Halsall, A. C. Ferrari, D. W. Boukhvalov, M. I. Katsnelson, A. K. Geim & K. S. Novoselov, “Control of Graphene’s Properties by Reversible Hydrogenation: Evidence for Graphane”, *Science* **323** (2009), 610–613 (*cf.* p. 141)
- [203] M. Wojdyr, “Fityk : a general-purpose peak fitting program”, *Journal of Applied Crystallography* **43** (2010), 1126–1128 (*cf.* p. 148)

Physical Response of Graphene Layers at Extreme Pressure

Abstract: We have studied the physical response of graphene and thin graphite (nanographites) under extreme pressure. Samples were compressed up to ~ 10 GPa using diamond anvil cells and probed by *in-situ* Raman spectroscopy, allowing to measure their in-plane strain and charge concentration during compression. Isotopically labeled $^{12}\text{C}/^{13}\text{C}$ bilayer graphene samples supported on SiO_2/Si were investigated at high pressure, allowing to measure separately the Raman response from each adjacent graphene layer. Strain and doping mismatches (asymmetries) were observed between the two layers, depending the chemical nature and the physical state of the pressure transmitting medium used for compression. New experimental methods were developed with the goal to study singled suspended graphene samples at high pressure, avoiding the effect of the substrate. One technique proved to be efficient, using sample dry-stamping transfer on pre-machined SiO_2/Si substrates fixed beforehand on the diamond anvil. Proof-of-concept experiments on suspended nanometric thin graphite samples were achieved. We optically observed an unexpected wrinkling and detachment effect by studying compressed nanographites samples supported on contrast-enhancing SiO_2/Si substrates when methanol is used as pressure transmitting medium. Our results have allowed to observe, quantify and even disentangle the different effects of the environment on the physical response of graphene under high pressure.

Keywords: Graphene, Raman spectroscopy, High pressure

Réponse Physique de Feuillet de Graphène sous Pression Extrême

Résumé : Nous avons étudié sous haute pression la réponse physique du graphène et d'échantillons de graphite mince (nanographites). Les échantillons ont été comprimés en cellules à enclumes de diamant (jusqu'à ~ 10 GPa) et sondés par spectroscopie Raman *in-situ*, afin de mesurer la déformation et la concentration de charges dans les plans de graphène pendant la compression. Nous avons étudié un système de graphène bi-couche $^{12}\text{C}/^{13}\text{C}$ isotopiquement modifié (supporté sur SiO_2/Si), permettant de mesurer séparément la réponse Raman de chaque couche à haute pression. Nous avons observé des effets d'asymétrie en terme de déformation biaxiale et de dopage entre les deux couches, qui dépendent de la nature chimique et de l'état du milieu transmetteur de pression. Nous avons développé de nouvelles méthodes expérimentales dans le but d'étudier des échantillons de graphène *suspendus* à haute pression, afin de nous affranchir de l'effet du substrat. La méthode la plus efficace est basée sur le transfert d'échantillons par tamponnage visco-élastique sur des substrats SiO_2/Si pré-usinés et préalablement fixés sur l'enclume en diamant. Des expériences préliminaires ont été réalisées sur des échantillons de nanographe suspendus à haute pression. Dans le cas de nanographites supportés sur des substrats SiO_2/Si qui améliorent le contraste optique, nous avons observé par microscopie un effet inattendu de plissement et de détachement des échantillons lorsque le méthanol est utilisé comme milieu transmetteur de pression. Nos résultats ont permis d'observer, de quantifier et même de décorréler les effets de l'environnement sur la réponse physique du graphène à haute pression.

Mots clefs : Graphène, Spectroscopie Raman, Haute pression